Quantum cascade laser spectroscopy: from trace gas detection to nonlinear optics



Tomás Henrique Passos Pinto

St Hilda's College

University of Oxford

A thesis submitted for the degree of

Doctor of Philosophy

Trinity 2018

Quantum cascade laser spectroscopy: from trace gas detection to nonlinear optics

Tomás Henrique Passos Pinto

St Hilda's College
University of Oxford

A thesis submitted for the degree of Doctor of Philosophy

Trinity 2018

Quantum cascade lasers (QCLs) are high power, narrow linewidth mid-IR lasers that are increasingly popular for trace gas sensing and nonlinear spectroscopy. This thesis demonstrates QCL based spectroscopic techniques for multi-species detection, nonlinear optics and trace gas detection, highlighting the versatility of these lasers.

Firstly, a Fabry-Perot QCL (FP-QCL) operating at 5.3 μm was used to perform multi-mode absorption spectroscopy (MUMAS) for sensing of NO and H_2O. The laser provides a spectral coverage of *ca.* 50 cm^{-1} with a time resolution down to the ms timescale. It also exhibits a frequency resolution of < 50 MHz, limited by the longitudinal mode linewidth. This was the first demonstration of MUMAS with QCLs.

Secondly, the optical purity of a single mode distributed feedback (DFB) QCL operating at 5.3 μm was determined using Lamb-dip spectroscopy and by analysing the frequency noise power spectral density (PSD). Both methods revealed the linewidth of the device is *ca.* 500 kHz, which can be reproducibly broadened up to ~ 8 MHz by applying broadband uncorrelated radio-frequency current perturbations.

Thirdly, the DFB-QCL was used in combination with an external cavity (EC) QCL to study the evolution of velocity selected coherent signals in vibrationally excited NO. The coherent signatures showed lifetimes up to 378 $\pm$ 23 ns. Maximum population transfer to the $v = 1$ level was achieved after pumping for 10 $\pm$ 0.5 μs, and the decay time of post-pumping coherent transient signals was 5.7 $\pm$ 0.3 μs at a pressure of 3 mTorr. The collisional relaxation rate of the coherent systems was determined for various buffer gases, reaching (4.28 $\pm$ 0.13) $\times 10^4$ s^{-1} $mTorr^{-1}$ with CO_2.

Lastly, a DFB-QCL was used to demonstrate intracavity Faraday modulation spectroscopy (INFAMOS), a technique for the sensitive and selective detection of radicals, using NO as a test molecule. A model that predicts the INFAMOS lineshape was presented, and the sensitivity for the detection of NO was 0.21 ppbv $Hz^{1/2}$, corresponding to a minimum detectable rotation angle of 0.16 nrad $Hz^{1/2}$, at a total pressure of 412 Torr. Optical saturation effects were observed and included in the INFAMOS model.

To my parents and my grandfather, Manuel.

Acknowledgements

There are many people without whom none of this work would be possible, either for their incredible support or for their brilliant ideas that helped me every step of the way. For both of these reasons, I am immensely grateful to Grant, but also for taking me into his group and always being ready to help, guide and provide inspiration with his enthusiasm for science. I could not possibly forget all the insightful comments about my dedication to part II students, and how entertaining they always were.

I would like to thank all the members of the Ritchie group for making an office an enjoyable place to be in. James K for his patience with me in my early states of this DPhil and all the post 6 pm rowing conversations; Katherine, Nick, James F and Luca for the lunches in the park and great group activities that were always wonderfully organized, and Jennifer for the early evening conversations when everyone else is gone. And of course, to the great Michele, whose support was essential over the last couple of years of my studies. Another thank you to all the other members and collaborators of the group: John, Graham, Pev, Gus, Xia, who have all helped either with their knowledge or banter. A special thanks to Shea and Paul in the physics department. It was productive and enjoyable to do MUMAS in collaboration with them.

I am also grateful to all the part II students who have been in the Ritchie group over the years, the office is so much quieter without them! I must thank Stella for expert figure advice and all the amazing support. And Ayush, who I have to thank for the lab company and bad jokes, but also for managing to produce a thesis with the little time he had.

I couldn't be more grateful to Emilia for all the help and motivation in the last stage of my studies. This document may have taken a lot longer to exist if it wasn't for her. And finally, I am most grateful to my parents for all their love and support. Without you, I wouldn't be where I am today.

List of publications

- S. O'Hagan, T. Pinto, P. Ewart and G. A. D. Ritchie, "Multi-mode absorption spectroscopy using a quantum cascade laser for simultaneous detection of NO and H_2O", *Applied Physics B: Lasers and Optics*, **122**, 226 (2016)
- Michele Gianella, Tomás H. P. Pinto, Xia Wu and Grant A. D. Ritchie, "Intracavity Faraday modulation spectroscopy (INFAMOS): A tool for radical detection", *The Journal of Chemical Physics*, **147**, 054201 (2017)
- Tomás H. P. Pinto, James M. R. Kirkbride and Grant A. D. Ritchie, "Broadening the optical bandwidth of quantum cascade lasers using RF noise current perturbations", *Optics letters*, **43**, 1931-1934 (2018)
- Tomás H. P. Pinto, Michele Gianella and Grant A. D. Ritchie, "Optical saturation effects in Intracavity Faraday Modulation Spectroscopy (INFAMOS)", *The Journal of Chemical Physics*, (submitted May 2018, under review)

Contents

Abstract **i**

List of publications **iv**

Abbreviations **viii**

1 Introduction **1**
1.1 QCL architecture and operating principles 3
1.2 Laser absorption spectroscopy 6
1.2.1 Line broadening mechanisms 8
1.2.2 Population transfer 11
1.3 Nonlinear spectroscopy 13
1.4 Thesis outline 15

2 Experimental considerations **18**
2.1 QCL types and operation 18
2.1.1 FP- and DFB-QCL laser housing 22
2.2 Acousto-optic modulators 23
2.3 Optical cavities 24
2.4 Spectroscopy of NO 29
2.4.1 Pressure broadening of NO spectral lines 31
2.5 Conclusion 32

3 Multi-mode absorption spectroscopy with a Fabry-Perot QCL **33**
3.1 Introduction 34
3.2 Theory 35
3.2.1 The MUMAS model 37
3.3 Experimental 39
3.4 Results 40

3.4.1 Laser mode envelope and MUMAS spectrum of NO 40
3.4.2 Measuring the mode linewidth 44
3.4.3 Multi-species sensing with FP-QCL MUMAS 46
3.4.4 Fast scan rates 47
3.4.5 Relative mode intensity changes as a function of injection current 49
3.4.6 Conclusions 51

4 Single mode QCLs: optical bandwidth and current perturbations 53
4.1 Introduction 53
4.2 Linewidth measurements via Lamb-dip Spectroscopy 57
4.2.1 Background and experiment 57
4.2.2 Results 61
4.3 Linewidth measurements via the frequency noise power spectral density 64
4.3.1 Background and experiment 64
4.3.2 Results 66
4.4 Self-heterodyne method 70
4.4.1 Background and experiment 70
4.4.2 Results 73
4.5 Conclusions 77

5 Coherent transient spectroscopy with cw-QCLs 79
5.1 Introduction 80
5.2 Theory 81
5.3 Experimental 84
5.4 Results 86
5.4.1 Coherent optical effects with a single QCL 86
5.4.2 Rapid passage effects with a velocity selected sample: R(14.5)-R(15.5) transition pair 95
5.4.3 Rapid passage effects with a velocity selected sample: R(6.5)-P(7.5) transition pair 98
5.4.4 Time resolved studies of rapid passage effects with a velocity selected sample 101
5.4.5 Time resolved rapid passage effects: signal relaxation 105
5.5 Conclusion 112

6 INFAMOS: Intracavity Faraday Modulation Spectroscopy 115
6.1 Introduction . . . 115
6.2 Theory . . . 118
6.2.1 Optical-Feedback Cavity Enhanced Absorption Spectroscopy . 118
6.2.2 Faraday effect with a static magnetic field . . . 122
6.2.3 Enhancing the Faraday rotation angle with an optical cavity . 126
6.2.4 Faraday effect with a time dependent field . . . 127
6.3 Model for the INFAMOS lineshape . . . 129
6.3.1 The effect of pressure broadening and magnetic field amplitude 133
6.4 Experimental . . . 135
6.5 Results . . . 137
6.5.1 Preliminary INFAMOS and OF-CEAS measurements . . . 137
6.5.2 INFAMOS spectra with low saturation - sensitivity analysis . 141
6.5.3 Saturation effects in INFAMOS and OF-CEAS . . . 146
6.5.4 Saturated INFAMOS lineshape model and simulation . . . 152
6.6 Conclusion . . . 156

7 Conclusions and outlook 158

A Saturated INFAMOS model 163
A.1 Lineshapes . . . 163
A.1.1 Homogeneous lineshapes . . . 163
A.1.2 Inhomogeneous lineshapes . . . 165
A.2 Unsaturated absorption and refractive index . . . 167
A.3 Saturated absorption and refractive index . . . 169
A.4 Population difference . . . 170
A.5 Summary . . . 172

Bibliography 173

Abbreviations

AC	Alternating current
AOM	Acousto-optic modulator
AR	Anti-reflective
CEAS	Cavity enhanced absorption spectroscopy
CRDS	Cavity ring-down spectroscopy
cw	Continuous wave
DAQ	Data acquisition
DC	Direct current
DFB	Distributed feedback
DFG	Difference frequency generation
DM-FRS	Dual-modulation Faraday rotation spectroscopy
EC	External cavity
FAMOS	Faraday modulation spectroscopy
FFT	Fast Fourier transform
FID	Free induction decay
FP	Fabry-Perot
FRS	Faraday rotation spectroscopy
FSR	Free spectral range
FT-IR	Fourier transform infrared spectroscopy
FWHM	Full-width at half maximum
H-FRS	Heterodyne enhanced Faraday rotation spectroscopy
HITRAN	High-resolution transmission molecular absorption database

HWHM	Half-width at half maximum
ICL	Interband cascade laser
IF	Interference filter
INFAMOS	Intracavity Faraday modulation spectroscopy
IR	Infrared
LHCP	Left-handed circular polarization
LOD	Limit of detection
MFC	Mass flow controller
MFI	Mode fractional intensity
MUMAS	Multi-mode absorption spectroscopy
NMR	Nuclear magnetic resonance
OA-CEAS	Off-axis cavity enhanced absorption spectroscopy
ODE	Ordinary differential equation
OFC	Optical frequency comb
OF-CEAS	Optical-feedback cavity enhanced absorption spectroscopy
PD	Photodiode
PSD	Power spectral density
PZT	Piezoelectric transducer
QCL	Quantum cascade laser
RF	Radio-frequency
RHCP	Right-handed circular polarization
RP	Rapid passage
SNR	Signal to noise ratio
TDLAS	Tunable diode laser absorption spectroscopy
TEC	Thermoelectric cooler
TEM	Transverse electromagnetic mode
VCSEL	Vertical-cavity surface-emitting laser
WMS	Wavelength modulation spectroscopy

Chapter 1

Introduction

Light and its interaction with matter has long fascinated mankind. Some of the first studies of light-matter interactions date back to the third century B.C., when the earliest known text on geometrical optics was written by Euclid, introducing the concept of "visual rays" together with a mathematical description of their propagation and interaction with objects to explain sight.[1] It took until two millennia later, in the 17$^{\text{th}}$ century, for Sir Isaac Newton to found the field of study of the interactions of light and matter, known as spectroscopy. The importance of spectroscopy is such, that it provides the main evidence of the existence of a universe, as pertinently observed by James Clerk Maxwell in 1873:[2]

"But in the heavens we discover by their light, and by their light alone, stars so distant from each other that no material thing can ever have passed from one to another, and yet this light, which is to us the sole evidence of the existence of these distant worlds, tell us also that each of them is built of molecules of the same kind as those which we find on earth."

The characteristics and potential uses of electromagnetic waves varies as a function of their wavelength, for example from long wavelengths used in radio navigation systems (in the cm range), to short wavelengths such as X-Rays (pm to nm range)

that find uses in medical imaging devices.[3,4] The spectral region with which this thesis is concerned is the mid-infrared (mid-IR). This region extends across a wavelength range from 3 to 8 μm (1250 - 3330 cm^{-1}), and all the studies presented hereafter are concerned with laser spectroscopy at *ca.* 5.3 μm (1900 cm^{-1}). The mid-IR region

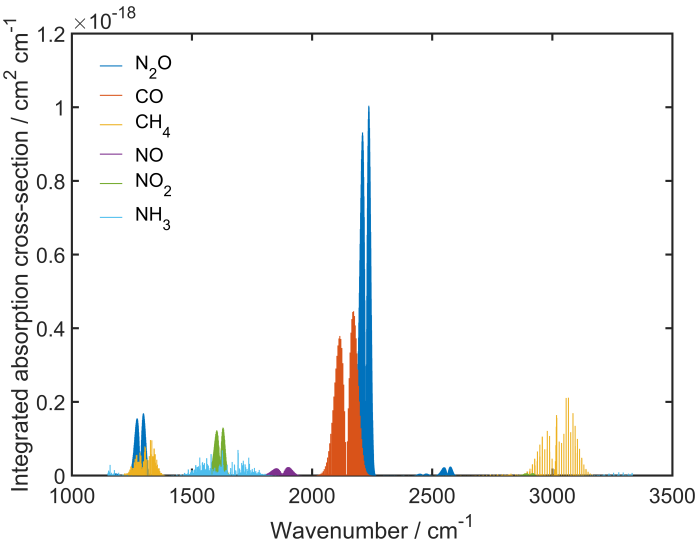


Figure 1.1: The integrated cross-section of several molecular absorbers in the mid-IR, retrieved from the HITRAN spectroscopic database.[5] The integrated cross-sections are a measure of the probability of the absorption of photons by molecular transitions, and will be discussed further in section 1.2. The cross-sections presented are of the order of 10^{-18} cm^2 cm^{-1}, often a couple of orders of magnitude larger than the cross-sections of rotational-vibrational transitions in the near-IR (between 3 μm and 0.7 μm, or 3330 - 14000 cm^{-1}).

hosts the strong fundamental bands of vibrational transitions of small (gas phase) molecules such as NO, NO_2, CH_4 or CO (see Figure 1.1), all of great importance in a variety of fields such as atmospheric science, environmental monitoring, combustion diagnostics, breath analysis and industrial process control.[6–15] The mid-IR is therefore a region of great interest for trace gas sensing applications, and can be accessed with several methods and sources for producing coherent radiation, including by difference frequency generation (DFG), lead-salt lasers, interband cascade lasers (ICLs) and quantum cascade lasers (QCLs).[11,16–19] All the studies presented herein will be based on the latter sources, QCLs.

1.1 QCL architecture and operating principles

After the theoretical prediction of stimulated emission by Einstein in 1917,[20] the first operational laser was constructed in 1960 by Maiman.[21] Since then, a variety of laser designs have emerged with the aim of covering different spectral regions or obtaining higher powers or narrower optical bandwidths. As this thesis is concerned with the mid-IR spectral region, the focus of this section will be on mid-IR semiconductor lasers, and the development and operating principles of QCLs.

The first type of mid-IR semiconductor lasers used for high-resolution trace gas sensing were lead salt diode lasers, covering a wavelength range between 3 μm and 20 μm.[18] The operating principle of these lasers is based on a p-n junction: photons are emitted due to the recombination of electrons injected through the n-type doped (conduction) band with holes in the p-type (valence) band, as shown in Figure 1.2. The wavelength of the emitted photon is determined by the size of the band gap. The operation of lead salt lasers is experimentally demanding, involving cooling to

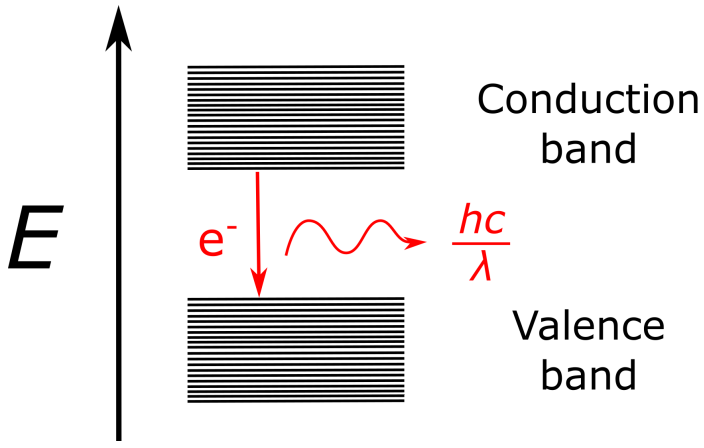


Figure 1.2: Schematic representation of the valence and conduction bands in a diode laser. Photon emission is achieved by electron-hole recombination. The energy of the photon is a function of the energy gap between the two bands.

cryogenic temperatures. The power of these devices is limited to a few mW in cw operation and their tunability is confined to narrow frequency ranges.[22] The use of different substrates for producing mid-IR p-n junction type diodes is restricted due

to the increase in the rate of Auger recombination, a process that reduces the efficiency of the device due to non-radiative relaxation of conduction band electrons, and is ascribed to the smaller p-n junction band gap required for manufacturing mid-IR devices.[23] Alternatively, the mid-IR can be accessed by DFG at the expense of a significant increase in experimental complexity of the optical and electronic components involved, but still with a low output power.[16,17] DFG is a process that involves mixing two electromagnetic waves with frequencies ν_1 and ν_2 in an appropriate dielectric medium that responds nonlinearly to high intensity radiation. The waves with frequencies ν_1 and ν_2 are known as the pump and signal radiations, respectively, and are mixed to generate a third wave (called the idler radiation) at a frequency $\nu_3 = \nu_1 - \nu_2$ where $\nu_1 > \nu_2 > \nu_3$.[24]

The construction of the first QCL by Faist *et al.* in 1994 marked a significant breakthrough in the availability of mid-IR coherent sources, two decades after Kazarinov and Suris proposed a theoretically similar light amplification mechanism.[25,26] The operating principle of QCLs is fundamentally different to that of conventional diode lasers. QCLs rely solely on one type of charge carrier, the electron, as opposed to electrons and holes in conventional diodes, to produce radiation using only the conduction band. Light emission does not rely, therefore, on a p-n junction band gap, but instead on a cascade of charge carrier transitions, between multiple energy levels E_n and E_{n-1}; these are intersub-band transitions. The sub-band energy of a QCL is determined by the thickness of nanometric sized layers of InGaAs/AlInAs that form quantum wells via spatial confinement.[19,27] The wavelength of a photon emitted from jumping between two layers, of energies E_2 and E_1, respectively, is given by

$$\frac{c}{\lambda} = \frac{E_2 - E_1}{h}. \tag{1.1}$$

A superlattice is formed with the stacking of layers of alternating thicknesses, which

typically number from 30 - 100, and thus the cascade of a single electron will produce multiple photons (see Figure 1.3).[28] This high efficiency translates into high powers, demonstrated by reports of QCLs emitting up to 1 W in cw operation at room temperature.[29]

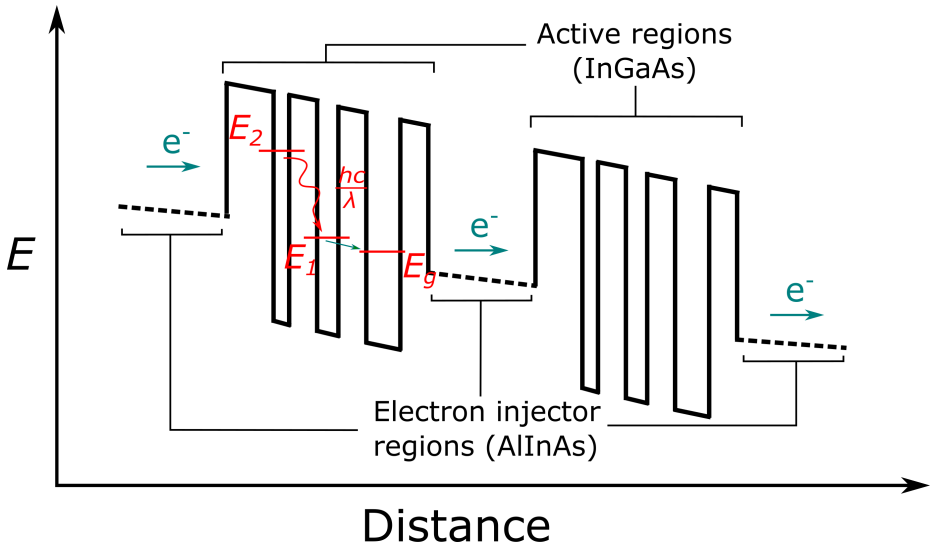


Figure 1.3: Energy diagram of the conduction band of a QCL. Two active regions and three electron injector regions are shown. The substrate of these is commonly InGaAs and AlInAs, respectively. Electron injection occurs into the upper level, generating a population inversion within each active region of the conduction band. The electrons cascade through several active regions, where photon emission occurs. The slope on the diagram is shaped by the potential applied through the superlattice. This scheme was adapted from reference 26.

The energy diagram in Figure 1.3 features three levels marked in red in the first active region. The two higher levels are labelled E_2 and E_1. Electrons are injected at E_2, and undergo radiative relaxation to E_1. A fast, non-radiative process governs the relaxation from E_1 to a lower energy level, denoted E_g, and ensures population inversion between E_2 and E_1. The electrons then tunnel into the second injection region, where the processes occurring in the first active region are repeated.

Following photon emission, the active regions of the device then act as a waveguide, and a resonator is formed within the cavity medium itself due to the high reflectivity of the gain medium facets. The resulting optical emission profile is multi-mode and

can have a bandwidth as wide as a few hundred cm^{-1}.[19] This will be discussed in more detail in Chapter 2, and wavelength selection mechanisms that allow the realization of single mode devices will be presented. The advantages QCLs offer over lead salt lasers, such as room temperature operation and high output power make these devices ideal sources for mid-IR spectroscopy.

1.2 Laser absorption spectroscopy

The transmitted intensity, I, of an incident electromagnetic wave in the weak field limit, I_0, of frequency ν, through an absorber of concentration [X] is given by the Beer-Lambert law:[30]

$$I(\nu) = I_0(\nu)e^{-\sigma(\nu)[\mathrm{X}]d}, \tag{1.2}$$

where d is the interaction distance and $\sigma(\nu)$ is the frequency dependent absorption cross section; $\sigma(\nu)$ has the units of area, and is an intrinsic property of molecular transitions. Moreover, $\sigma(\nu)$ is proportional to the probability of absorption of a photon with energy $E = h\nu$. Equation 1.2 is often presented as a function of an interaction distance independent absorption coefficient, $\alpha(\nu) = \sigma(\nu)[\mathrm{X}]$, or as a function of absorbance $A(\nu) = \alpha(\nu)d$. The latter quantity, $A(\nu)$, can be directly extracted from an absorption measurement as

$$A(\nu) = -\ln\left(\frac{I(\nu)}{I_0(\nu)}\right). \tag{1.3}$$

The interaction distance or path length is an experimental parameter, and is usually a known quantity. Furthermore, since the $\sigma(\nu)$ for mid-IR transitions of known species can be retrieved from spectroscopic databases such as HITRAN,[5] the absolute concentration of such absorbers can be quantified directly from absorption measurements. The cross section is thus a critical parameter in absorption spectroscopy.

In order to describe the physical basis of absorption, consider a molecular two-level system comprising a lower state, $|1\rangle$, and an upper state, $|2\rangle$, separated by an energy E. The probability of photon absorption, per second, is expressed as

$$\dot{P_{12}} = B_{12}\rho(\nu). \tag{1.4}$$

Here, $\rho(\nu)$ is the spectral energy density, is the energy density per unit volume per unit frequency, and B_{12} is the Einstein coefficient of induced absorption. The latter is a function of the overlap between the wavefunctions of the $|1\rangle$ and $|2\rangle$ states induced by the transition dipole moment operator.[30] The rate of population changes between the lower and upper states (with populations labelled as N_1 and N_2, respectively) as a result of photon absorption and emission is given by:

$$\dot{N_2} = (N_1 - N_2)B_{12}\rho(\nu) - N_2A_{21}, \tag{1.5}$$

where A_{21} is the Einstein coefficient for spontaneous emission and represents the contribution to upper state depopulation from this process. Several relaxation mechanisms act simultaneously, such as collisional relaxation, but these are omitted here for simplicity. If the intensity of the electromagnetic field is large enough to induce significant population changes between the lower and upper state, the Beer-Lambert law in the form presented in equations 1.2 and 1.3 is no longer applicable, and the absorption becomes nonlinear due to optical saturation. This effect will be discussed in more detail in section 1.3.1, and examples will be presented in chapters 5 and 6.

The Einstein induced absorption coefficient, B_{12}, is related to the absorption cross section via

$$\sigma_{12}(\nu) = \frac{h\nu}{c}\mathscr{V}(\nu - \nu_0)B_{12}, \tag{1.6}$$

where $\mathscr{V}(\nu - \nu_0)$ is a lineshape function centred at the centre frequency of the tran-

sition, ν_0, that satisfies the condition $\int_{-\infty}^{\infty} \mathscr{V}(\nu - \nu_0)\,\mathrm{d}\nu = 1$ assuming that the line is narrow relative to ν_0. This lineshape function is determined by the action of physical mechanisms that are responsible for broadening absorption lines in the frequency space, and these will be discussed in more detail in the following section.

A more convenient way of relating the absorption cross section to B_{12} is by integrating $\sigma_{12}(\nu)$ across all frequencies:

$$\int_0^{\infty} \sigma_{12}(\nu)\,\mathrm{d}\nu = \frac{h\nu_0}{c} B_{12}, \tag{1.7a}$$

$$\mathscr{S} = \int_0^{\infty} \sigma_{12}(\nu)\,\mathrm{d}\nu, \tag{1.7b}$$

where $\mathscr{S}$, is the integrated absorption cross-section (centred at the transition frequency, ν_0) that can be directly retrieved from the HITRAN database in units of $\mathrm{cm}^2\ \mathrm{cm}^{-1}$. This parameter is of great use as it is independent of the lineshape of the transition and only depends on the temperature.

1.2.1 Line broadening mechanisms

Line broadening mechanisms broaden the frequency distribution over which molecular absorption occurs. These can be separated into two categories, homogeneous and inhomogeneous mechanisms. The former category describes broadening mechanisms that affect all the absorber molecules equally, resulting in a Lorentzian lineshape, while inhomogeneous broadening mechanisms affect molecules to different degrees and imprint a Gaussian character to the absorption lineshape.

Molecules in the gas phase are in constant motion, moving according to the Maxwell-Boltzmann speed distribution. To describe the effect of this motion on the spectra of an absorber, consider the velocity component of a single molecule in relation to the axis of propagation of a light beam from a point source, in this case a laser beam. The velocity component of this molecule (the *observer*) along the axis

of propagation of the laser beam will cause the molecule to *observe* a Doppler frequency shift in the beam. Expanding this effect to a larger sample of absorbers with a Maxwell-Boltzmann velocity distribution, the full width at half maximum (FWHM, $\Delta\nu_D$) of its absorption lines is *inhomogeneously* broadened according to:

$$\Delta\nu_D = \nu_0\sqrt{\frac{8k_BT\ln 2}{mc^2}}. \tag{1.8}$$

The FWHM due to Doppler broadening is thus a function of the centre frequency of the transition, ν_0, the molecular mass of the absorber, m, and the temperature, T. The Doppler width for nitric oxide at room temperature and in the mid-IR ($\sim$ 5.3 μm) is *ca.* 125 MHz. As an inhomogeneous broadening mechanism, the action of Doppler broadening results in a Gaussian lineshape, often designated as a Doppler profile.

Transit time broadening is another inhomogeneous broadening mechanism, with similar origins to Doppler broadening, as it is caused by the finite time that an absorber will remain within a field due to molecular motion. The action of this broadening mechanism adds a Gaussian contribution to the absorption lineshape.[31] Consider a laser beam on resonance with a transition of an absorber. This beam has a radius of r, where r is defined as the radius within which the condition $I \geq I_0\, e^{-2}$ is satisfied, and I and I_0 are the intensity (off-beam centre) and the intensity at the centre of the beam, respectively. Transit time broadening is essentially the relaxation of an absorbing sample within the volume of the laser beam due to ground state molecules entering and excited molecules exiting the volume of the beam. For a sample of absorber with a mean thermal velocity $\bar{v}$, the FWHM is broadened due to transit time by an amount[31]

$$\Delta\nu_T = \frac{2\bar{v}}{r}\sqrt{2\ln 2}. \tag{1.9}$$

At room temperature, the transit time broadening of NO in a beam with a radius of

1 mm is $\sim$ 320 kHz. As this is almost 3 orders of magnitude smaller than Doppler broadening, transit time broadening only becomes important in Doppler-free spectroscopy (see Chapter 4).

Homogeneous broadening mechanisms may be divided into collisional (pressure) broadening and natural broadening. In the absence of all other broadening mechanisms, the latter gives the lower limit of the width of absorption lines due to Heisenberg's uncertainty principle. Let τ_{12} be the lifetime of a transition $|1\rangle \rightarrow |2\rangle$ with an energy uncertainty of ΔE. According to Heisenberg's uncertainty principle, the lifetime of a system is related to the uncertainty in its energy via

$$\Delta E \geq \frac{h}{2\pi\tau_{12}}. \tag{1.10}$$

The natural linewidth of the $|1\rangle \rightarrow |2\rangle$ transition is then given by $\Delta\nu_N = (2\pi\tau_{12})^{-1}$. All the allowed mid-IR transitions of NO in this work have natural lifetimes of hundreds of milliseconds, leading to linewidths of the order of Hz that will be neglected due to the presence of other more prominent broadening mechanisms.

The final broadening mechanism, pressure or collisional broadening is caused by the increase in the collision frequency between molecules in a gas-phase sample as a result of increasing its pressure. Collision events decrease the average lifetime of both states by facilitating the relaxation to several adjacent or lower energy states. Additionally, elastic collision processes introduce phase shifts leading to loss of coherence. Since it affects all particles equally, it is a homogeneous broadening mechanism that results in a Lorentzian shaped absorption line. The contribution of pressure broadening to the FWHM of spectral lines is described by a pressure broadening parameter, γ, that is typically 4.8 MHz Torr^{-1} for the NO transitions studied in this thesis, and is thus comparable or higher than $\Delta\nu_D$ for pressures above 26 Torr encountered in chapters 3 and 6.

The combination of Doppler and pressure broadening sees all the velocity groups within the Doppler profile of a sample to undergo broadening (see Figure 1.4), and also results in convolution of their Gaussian and Lorentzian lineshapes that characterise Doppler and pressure broadening, respectively, leading to a new absorption profile; the Voigt profile. This profile can be simulated, and its Gaussian and Lorentzian

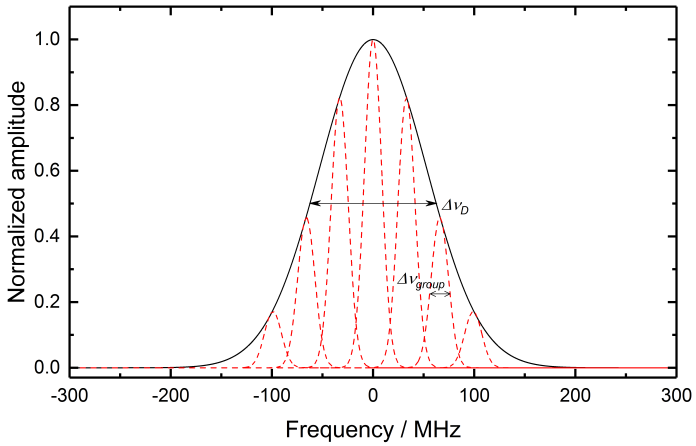


Figure 1.4: Gaussian envelope with FWHM = 125 MHz ($\approx \Delta\nu_D$ of NO at room temperature), simulating an NO absorption line at low pressure and showing multiple underlying velocity groups with $\Delta\nu_{\text{group}} = 20$ MHz. The FWHM of the velocity groups was chosen for clarity. As all molecules within the Doppler profile are equally broadened by collisions, all velocity groups become progressively wider and acquire a Lorentzian lineshape as a function of pressure. Consequently, the overall shape of the absorption line becomes a Voigt.

components numerically evaluated through several methods, including the use of complex error functions.[32]

1.2.2 Population transfer

The population of molecular eigenstates is changed upon the absorption of resonant coherent or incoherent light by a sample of gas. The rates of induced absorption and emission processes are themselves also a function of the population of the ground and upper state of a transition, as seen in Equation 1.5. In a two-level system consisting of a lower state $|1\rangle$ and an upper state $|2\rangle$, the change in upper state population,

P_2, caused by the absorption of incoherent light (and ignoring stimulated emission processes) is given by[20]

$$P_2(t) = \frac{1}{2}\Big(1 - e^{-BF(t)}\Big), \tag{1.11}$$

where B is the Einstein coefficient for induced absorption and $F(t)$ is the radiant energy per unit area (radiation fluence) up until a time t, which is a function of the time dependent radiation intensity I and is defined as

$$F(t) = \int_0^t I \mathrm{d}t. \tag{1.12}$$

Equation 1.11 shows that the maximum population transfer that can occur from absorption of incoherent light is 50%, *i.e.* population inversion in a two level system cannot be achieved with incoherent radiation pumping (see Figure 1.5).

In contrast, the population change induced in the same two level system by the absorption of coherent resonant radiation, such as that emitted by lasers, is given by

$$P_2(t) = \frac{1}{2}(1 - \cos \Omega t), \tag{1.13}$$

where $\Omega = \mu E/h$ is the Rabi frequency.[33] The Rabi frequency is a function of the magnitude of the electric field of the incident wave, E, and the transition dipole, μ.

The upper state population now varies sinusoidally with time between 0 and 1, thus population inversion can be achieved with a pulse of the correct duration; by ensuring $\Omega t = n\pi$, where n is an odd positive integer. In real systems, however, such *π-pulses* are not achievable due to phase fluctuations in the electromagnetic field, the existence of collisional relaxation mechanisms and the increase of the magnitude of induced emission processes. Due to the high intensity and optical purity of the QCLs used in the work presented herein, the population transfer to the upper state is significant enough to promote nonlinear effects that will be outlined in the following

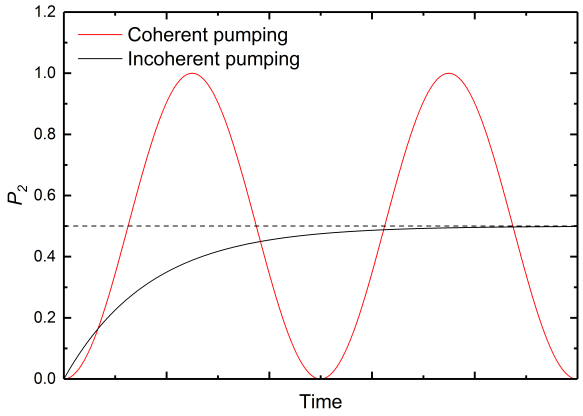


Figure 1.5: Schematic representation of the time evolution of the upper state population in a two level system, pumped by coherent and incoherent light. The maximum population transfer to the upper state is 50% using incoherent light, whereas via coherent excitation processes the upper state population varies sinusoidally between 0 and 100%.

section.

1.3 Nonlinear spectroscopy

The absorption cross section and the Beer-Lambert law neglect the effect of population changes on the excitation rate. However, the rate of change of the population of an upper state $|2\rangle$ in a two level system is a function of the population difference $\Delta N = N_1 - N_2$, as shown in Equation 1.5. When the optical pumping rate from the lower state to the upper state is comparable to the total upper state depopulation rate, an appreciable change in ΔN leads to saturation. Furthermore, the rate of radiation power absorbed per unit volume, $\dot{W}_{12}$, decreases since[31]

$$\dot{W}_{12} = h\nu B_{12}\rho(\nu)\Delta N, \tag{1.14a}$$

$$\Delta N = \frac{\Delta N_0}{1+S}, \tag{1.14b}$$

where $\rho(\nu)$ is the spectral energy density and ΔN_0 is the population difference of the two level system in thermal equilibrium. The variable S is dimensionless and is

known as the saturation parameter. S is used to modify ΔN_0 to give ΔN, where the latter is redefined as the population difference under the action of an intense field.

The saturation parameter can be written as a function of the absorption cross section, σ_{12}, the Einstein coefficient of spontaneous emission, A_{12}, and the intensity of the field, $I(\nu)$,

$$S = \frac{2\sigma_{12}I(\nu)}{h\nu A_{12}} = \frac{I(\nu)}{I_{\text{sat}}(\nu)}. \tag{1.15}$$

Here, $I_{\text{sat}}(\nu)$ is the saturation intensity, the intensity at which the rate of excitation is equal to the rate of relaxation. The frequency dependence of $I_{\text{sat}}(\nu)$ arises from the linewidth of spectroscopic transitions, which varies as a function of the broadening mechanisms. An expression for $I_{\text{sat}}(\nu)$ as a function of the frequency dependent absorption cross section, $\sigma_{12}(\nu)$, can thus be written

$$I_{\text{sat}}(\nu) = \frac{h\nu}{\sigma_{12}(\nu)\tau_2}, \tag{1.16}$$

where τ_2 is the upper state lifetime.

The saturation parameter across the profile of a broadened transition is also frequency dependent (which has a Lorentzian distribution) as:

$$S(\nu) = S_0 \frac{(\frac{\gamma}{2})^2}{(\nu - \nu_0)^2 + (\frac{\gamma}{2})^2}, \tag{1.17}$$

where γ is the FWHM of the Lorentzian profile and $S_0 = S(\nu_0)$ is the saturation parameter at the centre of the transition. S_0 can be extracted directly from the absorption coefficient and HWHM of saturated transitions in the homogeneous broadening limit, as will be demonstrated in Chapter 6. Saturation also modifies the absorption lineshape of molecular transitions, and can thus be regarded as a broadening mechanism due to the high intensity of a resonant field.

A common use of optical saturation in laser spectroscopy is for obtaining sub-

Doppler frequency resolution. Since the emission bandwidth of lasers is often narrower than the Doppler width of molecular absorbers, techniques such as spectral hole burning can be used to deplete the population of a certain velocity group of a lower state of a transition. Resolution is enhanced since the width of the population hole is approximately the linewidth of the laser. A special case of spectral hole burning is Lamb-dip spectroscopy, which will be defined in Chapter 4.

The narrow linewidth and fast tuning capability of the QCLs allow the observation of coherent transient effects. Such effects arise, in the context of this thesis, when a sample of low pressure NO is irradiated with a fast frequency chirped field across a transition, on a timescale that is short compared to its relaxation time.[34] A macroscopic polarisation that beats with the chirping field is generated, leading to the observation of oscillations that correspond to constructive and destructive interference. A more detailed discussion of the physical nature of optical coherent transient effects will be provided in Chapter 5, along with an analysis of such effects on NO transitions in the mid-IR.

1.4 Thesis outline

The next chapter of this thesis, Chapter 2, is concerned with different methodologies for wavelength selection in QCLs or for the use of these devices in absorption spectroscopy and nonlinear optics. Chapter 2 provides supporting information on the QCL types and other optical devices used, and also provides an introduction to the theory of the experimental techniques used in this work. Following Chapter 2, all subsequent chapters present studies of QCL based spectroscopic techniques.

- In Chapter 3, a multi-mode Fabry-Perot QCL (FP-QCL) operating at 5.3 μm is used to perform multi-mode absorption spectroscopy (MUMAS) for the detection of NO and H_2O. This work is the first demonstration of MUMAS with

QCLs, and was part of a collaborative effort with S. O'Hagan and P. Ewart. A simulation developed by O'Hagan *et al.* is used to accurately determine the fundamental properties of the laser device, such as the free spectral range of the cavity and the longitudinal mode width, by fitting experimentally obtained MUMAS spectra.[35]

- Chapter 4 presents a study that shows the use of different techniques for determining of the linewidth of single-mode QCLs. The target of this study is a DFB-QCL operating at 5.3 μm and the optical purity is assessed via Lamb-dip measurements and measurements of the frequency noise power spectral density (PSD). The linewidth is reproducibly measured via both methods, and broadened by perturbing the injection current with radio frequency (RF) noise. A third study on the linewidth and induced broadening is conducted using the self-heterodyne method, whereby the frequency noise is assessed by analysing the beat signal between the laser beam and a frequency shifted, time delayed version of itself.

- Following the characterisation of the optical purity of the high power, single mode DFB-QCL in Chapter 4, Chapter 5 uses this device to induce and study nonlinear optical effects in low-pressure samples of nitric oxide. These nonlinear coherent transient effects are also studied in velocity selected samples, using a EC-QCL in combination with the DFB system in a pump-probe configuration. In both cases, coherent transient effects promoted by optically induced polarisation of the medium are observed. The coherent transient signals obtained in a pump-probe configuration are simulated using a model based on a two-level and a three-level system, with the latter showing a better agreement with the measured spectra. The time evolution of the coherent systems is studied, using an acousto-optic modulator (AOM) as a fast optical switch, in order to quan-

tify the collision induced relaxation rate of these systems in low pressure gas samples.

- In Chapter 6, the intracavity Faraday modulation spectroscopy (INFAMOS) technique is introduced, using a second 5.3 μm DFB-QCL as a source. INFAMOS is a tool for the sensitive and selective detection of radical species that combines the effective path length enhancement provided by optical-feedback cavity enhanced spectroscopy (OF-CEAS) with the selectivity of Faraday modulation spectroscopy (FAMOS). INFAMOS is demonstrated with the detection of NO using a R-branch transition, and a model to predict the INFAMOS lineshapes is successfully applied. Due to the build-up of optical power in the cavity, saturation of the selected transitions occurs. These saturation effects are quantified and the INFAMOS model is modified to account for them.

- The conclusions and outlook of this thesis is presented in Chapter 7.

Chapter 2

Experimental considerations

Following the introduction to the theoretical aspects of laser spectroscopy and QCL operation provided in the previous chapter, this chapter considers the experimental apparatus and techniques that are of particular relevance for obtaining the results presented hereafter. Additionally, an introduction to the spectroscopy of NO is presented alongside a comparison between the pressure broadening of NO transitions by air and dry nitrogen. The latter subject is pertinent as dry nitrogen will be extensively used as a buffer gas in the work presented in this thesis.

2.1 QCL types and operation

In addition to the general quantum well design and operation of these devices described in the previous chapter, several wavelength selection mechanisms can be employed for obtaining QCL mid-IR radiation with the desired characteristics. The commercially available QCL chips used in this research can be placed in two categories, multi-mode and single-mode QCLs. The former possess a simpler design, using the highly reflective facets of the gain medium itself as the laser cavity.[26] The reflectivity of these facets is significant due to the large refractive index difference between the laser chip and air. The resulting emission structure consists of a comb of

modes spanning the gain profile of the device, which are equally spaced in frequency by the free spectral range (FSR), given by

$$\mathrm{FSR} = \frac{c}{2nL}. \tag{2.1}$$

Here, n is the refractive index of the gain medium and L is the physical length of the laser resonator (cavity). The laser cavity is akin to a low finesse Fabry-Perot resonator. The non-emitting rear facet of the chip is often coated with a highly reflective layer in order to minimize cavity losses. The gain profile of these devices may span tens to hundreds of cm^{-1}, thus providing a broad spectral coverage.[36] In the next chapter, such an FP-QCL device will be used to perform multi-mode absorption spectroscopy (see Chapter 3).

QCLs can also be manufactured for single mode operation. This is generally achieved by implementing one of two types of frequency selection schemes: the first consists of etching a Bragg-type diffraction grating into the cladding that coats the gain medium of the chip, while the second relies on the integration of FP-QCLs with

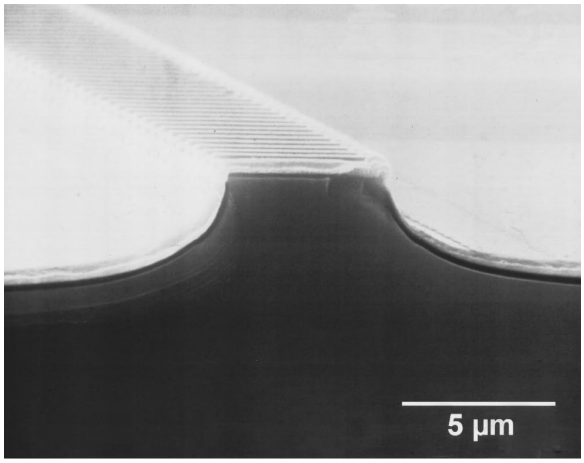


Figure 2.1: Facet of a DFB-QCL device (adapted from reference 37). The image was obtained with a scanning electron microscope.

external grating feedback cavities. After these modifications, the lasers are known as distributed feeedback QCLs (DFB-QCLs), shown in Figure 2.1, and external cavity

QCLs (EC-QCLs), respectively.[37–42]

In a DFB-QCL configuration, the longitudinal modes of the laser cavity are restricted by the etched grating. The optical feedback to the gain medium after this mode selection process results in the amplification of the single resonant mode, thus allowing the device to produce high optical purity, single mode radiation. Wavelength tuning can be achieved by changing the temperature of the device, which in turn changes the refractive index of the gain medium. To produce fast changes in the temperature of the chip, the QCL injection current can be modulated with a waveform generator. Alternatively, the temperature can be regulated using methods such as thermoelectric cooling (TEC). A drawback of this type of wavelength selection is that it restricts the spectral coverage of the device to only a few cm^{-1}.

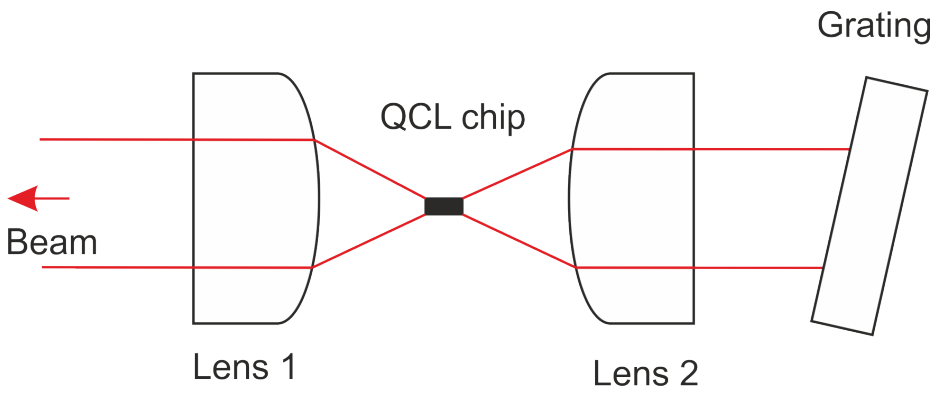


Figure 2.2: Diagram of the double-ended Littrow configuration, where lens 1 is the output lens, and lens 2 collimates the beam onto the diffraction grating. The diagram was adapted from reference 43.

The external cavity wavelength selection scheme relies on the selection of optical feedback, via a diffraction grating, to produce single mode radiation. The wavelength of EC-QCLs is tuned by altering of the position or angle of the diffraction grating, thus modifying the characteristics of the optical cavity. A schematic representation of an EC-QCL with a double-ended Littrow configuration,[44] which is the same as the Daylight Solutions 21052-MHF device used in Chapter 5, is presented in Figure 2.2. In addition to the single mode and narrow linewidth of EC-QCLs, the EC wavelength

selection scheme takes full advantage of the broad gain profile of QCLs, which can cover a few hundred cm^{-1}.[36] The complexity of the optical and mechanical systems involved, however, makes the production of this type of device more costly and more sensitive to mechanical noise sources in comparison to their DFB counterparts.

In order to measure the chirp rate (the frequency scanned per unit time) and the tuning range of the QCLs used in this thesis, a low-finesse Ge etalon with FSR = 493 MHz at 5.3 μm was used. The transmission of a frequency scanned laser through this etalon is shown in Figure 2.3. The chirp rate in the time interval shown is obtained through the average time difference between the maxima of the etalon transmission; the chirp rate extracted from the trace in Figure 2.3 is 1.64 MHz μs^{-1}. The transmission spectrum also shows that the laser frequency changes approximately linearly with the application of a triangular voltage ramp. Furthermore, an overall increase in

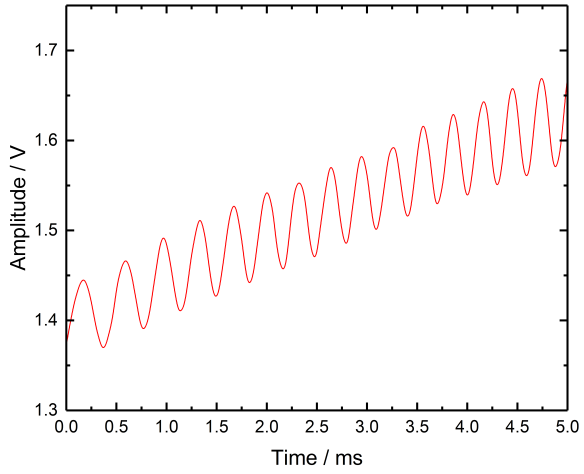


Figure 2.3: Transmission spectrum of the FP-QCL used in Chapter 3 through of a 493 MHz FSR Ge etalon. The laser is tuned by applying a 100 Hz triangular voltage ramp, yielding a chirp rate of 1.64 MHz μs^{-1}.

transmission is observed due to the increase in QCL injection current (in the up-ramp phase of the triangular waveform, in this case) necessary to produce the wavelength tuning, which in turn increases the laser power.

2.1.1 FP- and DFB-QCL laser housing

All of the DFB-QCL and FP-QCL chips used in this work are mounted in a custom-built housing that is shown in Figure 2.4. In order to control the temperature of the laser chip, a thermo-electric cooler (TEC) is attached to the copper block on which the chip is mounted. To prevent condensation on the device in cases where the selected operating temperature is below the dew point, the laser housing is hermetically sealed and evacuated. By employing a custom built laser housing, in-house

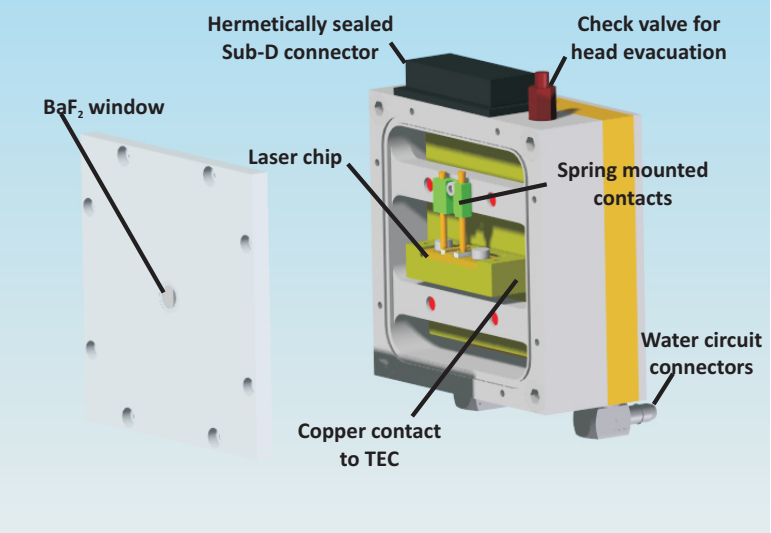


Figure 2.4: Schematic representation of the custom-built laser housing that all the DFB and FP-QCLs used in this work were mounted on.

built driver electronics and temperature controllers could be used, providing additional customization options over the operating parameter selection of the devices. Conversely, the mount and drivers of the EC-QCL system used in this work were commercial (Daylight Solutions 21052-MHF).

2.2 Acousto-optic modulators

In Chapters 4 and 5, an acousto-optic modulator (AOM) will be used as a frequency shifter and as a fast optical switch, respectively. A more detailed description of the role of the device in each of the applications will be provided in the experimental sections of the respective chapters. However, in light of the importance and the repeated use of the device in this thesis, an overview of its principles of operation is hereby presented. The mid-IR AOM (Isomet 1208-6) used here comprises an anti-

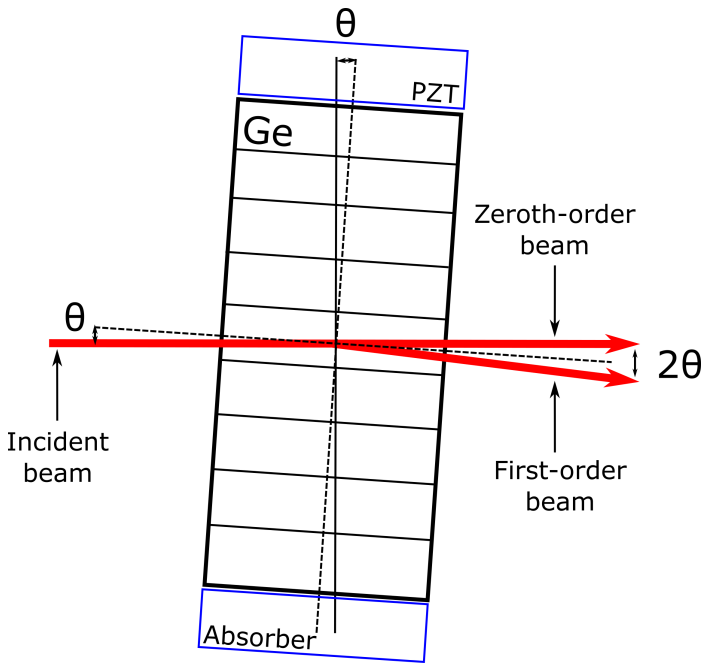


Figure 2.5: Schematic representation of the AOM used in the work presented in this thesis. The AOM is positioned at the Bragg angle, θ, with respect to the propagation direction of the incident beam. The AOM was mounted on a rotation stage (Thorlabs PR01/M) in order to optimize the angle to obtain the maximum deflection efficiency. PZT: Piezo-electric transducer.

reflection (AR) coated block of Germanium as the optical medium, through which an acoustic wave propagates. This wave is generated by a piezo-electric transducer (PZT) located at one end of the Ge crystal and is absorbed at the opposite end. This pressure wave modulates the refractive index of the crystal at the driving frequency of the PZT, which was set to 50 MHz with the driver/amplifier system (Isomet RFA151).

This process causes a 50 MHz blue-shift of the laser beam due to its interaction with the Bragg planes of the crystal (see Figure 2.5).[45] Not only is the beam frequency shifted, it is also deflected by an amount determined by the Bragg angle, which is defined as

$$\theta = \frac{\lambda f}{2V}, \tag{2.2}$$

where λ is the wavelength of the incident beam, V is the acoustic velocity of the medium and f is the frequency of the acoustic wave. The modulated beam, or first-order beam, is therefore deflected by an angle 2θ and is Doppler shifted by f. The deflection efficiency is stated by the manufacturer to be $> 80\%$, which is in good agreement with the experimental data (see Chapter 5).[46]

The final important characteristic of the AOM is its switching speed. This quantity is limited by the transit time of the acoustic wave through the waist of the incident beam within the active medium. The rise time of the first order beam is given by

$$t_{\text{trans}} = 0.65\frac{w_0}{V}, \tag{2.3}$$

where V is the acoustic velocity of the medium and w_0 is the waist of the incident beam, defined as the diameter of the beam within the limit where its intensity, I, satisfies the condition $I \geq I_0 e^{-2}$, where I_0 is the peak intensity. The switching speed of the AOM was measured at < 1 μs – see Chapter 5.

2.3 Optical cavities

Nitric oxide will be used in Chapter 6 as a test molecule for demonstrating a spectrometer aimed at the sensitive and selective detection of radicals. A key component of the spectrometer is a resonant optical cavity, and therefore an introductory discussion of these systems is pertinent. The popularity of optical cavities in trace gas sensing

applications is due to the sensitivity enhancement they provide, achieved through the extension of the effective optical path length by multiple reflections within the physical length of the cavity. Several cavity configurations exist, but this work is only concerned with the simplest linear optical cavities, formed by a pair of highly reflective plano-concave mirrors covered with a dielectric coating. The coatings are of sufficiently high optical quality that electromagnetic waves are injected through the back of one of the mirrors, and are reflected along the same path often over thousands of times before leaking out though one of the mirrors.

The main types of cavity based techniques for trace gas sensing fall into two categories: cavity ring-down spectroscopy (CRDS), developed by Deacon and O'Keefe in 1988,[47] and cavity enhanced absorption spectroscopy (CEAS), demonstrated in the following decade.[48,49] The former technique uses the change in the temporal decay of the light intensity that leaks through the cavity mirrors to obtain the concentration of an absorber, while the latter uses a measurement of the time-integrated cavity transmitted intensity as the laser wavelength is scanned.[50–55] The spectrometer introduced in Chapter 6 employs a variation of the CEAS technique known as optical feedback enhanced CEAS (OF-CEAS) that will be discussed in more detail therein, while the fundamental properties of linear optical cavities are now introduced.

In order to resonate within the cavity, an electromagnetic wave has to fulfil the condition $\nu = (kc)/(2nL)$, where L is the physical length of the cavity, k is a positive integer and n is the refractive index of the cavity medium. If this condition is fulfilled, constructive interference allows the generation of a standing wave between the two cavity mirrors and a *longitudinal mode* of the cavity is excited. The frequency separation between these longitudinal modes is known as the free spectral range (FSR), and has already been introduced in Equation 2.1. A quantity defined as the cavity finesse, $\mathscr{F}$, evaluates the ratio between the FSR and the bandwidth of the longitudinal modes of the cavity, $\Delta\nu_{\text{width}}$, as a function of the geometrical average of the reflectivity of

the cavity mirrors, R. $\mathscr{F}$ is approximately given by:

$$\mathscr{F} = \frac{\text{FSR}}{\Delta\nu_{\text{mode}}} \approx \frac{\pi\sqrt{R}}{1-R}. \tag{2.4}$$

Typical high finesse cavity mirrors in the mid-IR have $R > 0.999$, providing an enhancement to the physical length of the cavity, L, that scales proportionally to $L/(1-R)$. The finesse of a cavity with a fixed physical length is thus a measure of bandwidth as a function of mirror reflectivity, as shown in Figure 2.6. The FSR is constant, but the more stringent condition of maintaining phase over a longer path length leads to a reduction in mode width. The cavity transmission spectra shown

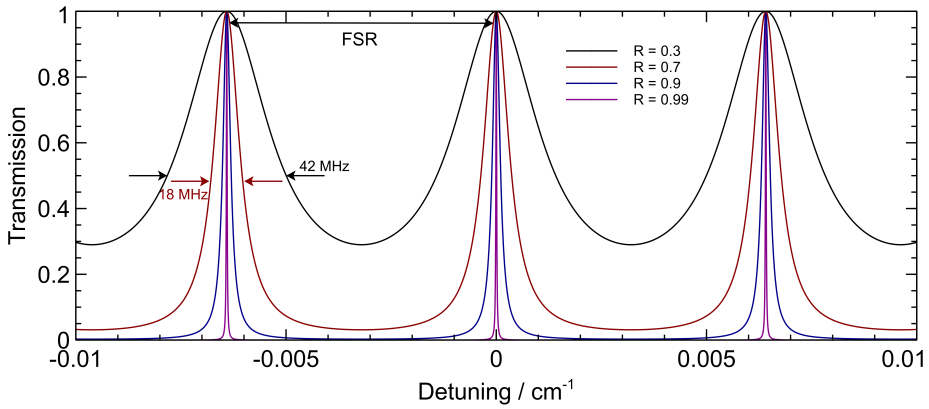


Figure 2.6: Normalized transmission of a cavity with a fixed FSR and a range of mirror reflectivities, highlighting the narrowing bandwidth due to the increase in mirror reflectivity and thus the increase in $\mathscr{F}$.

in Figure 2.6 were simulated using an Airy function of the form[56]

$$I_{\text{tr}} = \frac{I_0}{1 + \frac{4R}{(1-R)^2}\sin^2(2\pi\bar{\nu}L)}, \tag{2.5}$$

where $I_0 = 1$ is the (normalized) incident intensity and $\bar{\nu}$ is the laser detuning. The finesse also relates to the amount of power build up in the cavity, as will be highlighted later.

In addition to the resonant condition that gives rise to longitudinal modes, the

intensity distribution across a plane perpendicular to the axis of optical propagation is also quantized, giving rise to transverse electromagnetic (TEM_{mn}) modes. The

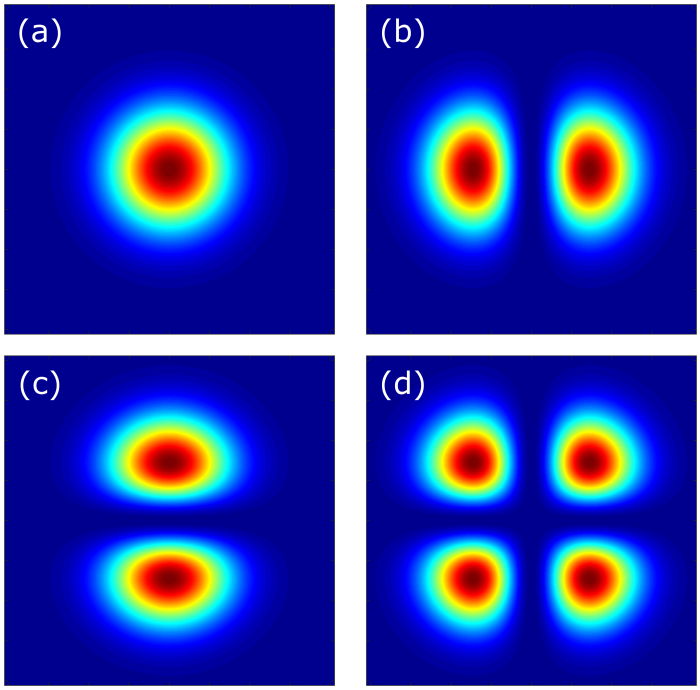


Figure 2.7: A simulation of the intensity distribution of the TEM_{00} Gaussian mode is shown in (a), while (b), (c) and (d) show intensity distributions of the TEM_{10}, TEM_{01} and TEM_{11} modes, respectively.

indices m and n define the mode order and indicate the number of nodes that exist on the x and y Cartesian coordinates, respectively, on a plane perpendicular to the axis of optical propagation. The intensity distribution profile of the lowest order TEM_{00} mode is Gaussian shaped, while higher order TEM modes are characterised by intensity profiles of the form:[57,58]

$$\psi(x,y,z) = H_m(\sqrt{2}\frac{x}{w})H_n(\sqrt{2}\frac{y}{w})\exp\left[-i\left(P(z)+\frac{k}{2q(z)}(x^2+y^2)\right)\right], \qquad (2.6)$$

where H_m and H_n are Hermite polynomials of orders m and n, respectively, and w is the beam waist, defined as the radius within which the local beam intensity satisfies the condition $I \geq I_0 e^{-2}$, where I_0 is the intensity at the centre of the beam assuming

a Gaussian intensity profile. In addition, the variables $P(z)$ and $q(z)$ are a phase shift factor and the complex beam parameter, respectively.[58] The latter defines the radius of curvature and beam waist of the intracavity field as a function of a position along the axis of propagation of the wave and is given by:

$$q(z) = \frac{i\pi w_0^2}{\lambda} + z, \tag{2.7}$$

where w_0 is the beam waist and z is a longitudinal coordinate. Finally, $k = 2\pi/\lambda$ is the wave vector number and accounts for the wavelength of the radiation. Using Equation 2.6, several cavity transverse modes are simulated and shown in Figure 2.7. Due to the wider beam waist and more complex intensity distribution, higher order TEM_{mn} modes experience larger diffraction losses than the TEM_{00} Gaussian mode.

As noted earlier, a resonant cavity acts as an optical storage device. Therefore, a final consideration must be made regarding the calculation of the local intensity of a TEM_{00} mode as a function of the circulating power in resonant optical cavities. The intensity of the Gaussian mode at any point along the cavity axis, $I_0(z)$, is given by

$$I_0(z) = \frac{2P_{\mathrm{circ}}}{\pi w^2(z)}, \tag{2.8}$$

where w is the beam waist at a point along the z axis and P_{circ}, the circulating power, can be estimated with[59]

$$P_{\mathrm{circ}} = \frac{2P_{\mathrm{out}}}{(1-R)}. \tag{2.9}$$

Here, R is the geometrical average of the reflectivity of the cavity mirrors and P_{out} is the transmitted power. The dependence of the local intensity on a radial coordinate, r, is given by

$$I(r,z) = I_0(z)e^{-2(\frac{r}{w})^2}. \tag{2.10}$$

An average *local* intracavity intensity of a Gaussian mode can thus be estimated if the output power of the resonant cavity is known, and this will be of use in studies of intracavity saturation presented in Chapter 6.

2.4 Spectroscopy of NO

Nitric oxide is the absorber used in all the work presented in this thesis, and as such it is pertinent to introduce its spectroscopic properties. The electronic ground state of NO has the molecular orbital configuration

$$\mathrm{X}\ ^2\Pi : (1\sigma)^2(2\sigma^*)^2(3\sigma)^2(4\sigma^*)^2(5\sigma)^2(1\pi)^4(2\pi^*)^1. \tag{2.11}$$

As a molecule that follows Hund's case (a), at low values of the rotational quantum number (see later), the total orbital angular momentum, L, and electron spin angular momentum, S, of NO are strongly coupled to the internuclear axis. As a consequence, these sources of angular momentum in nitric oxide are more adequately described by a new set of quantum numbers that describe the projection of angular momenta onto the internuclear axis, as shown in Figure 2.8. Λ and Σ are thus defined as the quantum numbers that describe the projection of L and S, respectively, onto the internuclear axis, while the quantum number Ω represents the total electronic angular momentum along the internuclear axis, given by $\Omega = |\Lambda+\Sigma|$.[60] The rotational angular momentum of the molecule, represented by the quantum number R, contributes to the total angular momentum of NO and the quantum number $J = \Omega+R$ gives the set of quantum numbers that most adequately describe a Hund's case (a) molecule: Λ, S, Σ, Ω and J. Finally, the nuclear spin of the ^{14}N nucleus, described by the quantum number $I = 1$, couples with J to give the total angular momentum quantum number of the molecule, F, where $F = J + I$.

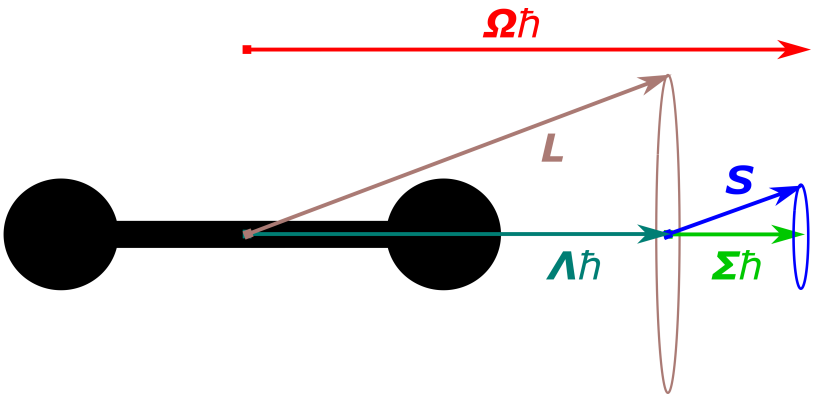


Figure 2.8: Diagram showing the contributions of orbital and electronic angular momenta and their projection onto the internuclear axis in NO.

Since $\Lambda = 1$ and $\Sigma = \pm 1/2$, the electronic ground state is divided into two electronic sub-states. These *spin-orbit* states are denoted $^2\Pi_{1/2}$ and $^2\Pi_{3/2}$, using the molecular term symbol nomenclature $^{2S+1}\Lambda_\Omega$, where $2S + 1$ is the spin multiplicity. The splitting between these two states is 123 cm^{-1}, which is less than k_BT at room temperature ($\sim$ 207 cm^{-1}) and thus both states have significant population.[61]

Within each spin-orbit manifold, another two non-degenerate states arise due to the interaction of molecular rotation and the electronic orbital angular momentum. These states are labelled as e and f, and this splitting is known as Λ-doubling. This phenomenon is responsible for the doublet structure observed in the rotationally resolved transitions within the $^2\Pi_{1/2}$ state, since the magnitude of this effect is larger than the Doppler width of NO ($\sim$125 MHz) – see Figure 2.9 for example. Notably, the splitting induced in transitions from the $^2\Pi_{3/2}$ state is significantly smaller than the Doppler width, resulting in a singlet structure.

The total angular momentum of the molecule is subjected to a final, much weaker hyperfine splitting due to coupling to the nuclear spin of ^{14}N, giving rise to 3 non-degenerate levels characterized by the quantum number F. Hyperfine splitting is usually < 1 MHz and hence is only significant in sub-Doppler spectroscopy (see Chapter 4). Transitions can occur from each of the hyperfine levels, however transitions where $\Delta I \neq 0$ are much weaker and can thus be neglected in the context of this thesis.

The spectroscopic selection rules that are relevant to this thesis are:

$$\Delta F = 0, \pm 1, \tag{2.12a}$$

$$\Delta \Omega = 0, \pm 1, \tag{2.12b}$$

$$\Delta J = 0, \pm 1, \tag{2.12c}$$

$$e \leftrightarrow e, f \leftrightarrow f, e \not\leftrightarrow f. \tag{2.12d}$$

All the rotational-vibrational transitions considered have $\Delta\Lambda = 0$, $\Delta\Omega = 0$ and $\Delta J = \Delta F = \pm 1$ ($\Delta I = 0$). Transitions with $\Delta J = 1, 0, -1$ are labelled R, Q and P branch transitions, respectively.

2.4.1 Pressure broadening of NO spectral lines

In some of the studies presented, buffering NO in another gas is necessary, either for dilution or for reducing the effects of saturation. In most cases, dry nitrogen will be used as the buffer gas. The HITRAN spectroscopic database lists self and air broadening parameters, γ_{self} and γ_{air}, respectively, but not nitrogen broadening parameters, γ_{N_2}.[5,62–65] This section examines whether it is appropriate to make the assumption that $\gamma_{\text{air}} = \gamma_{N_2}$.

Figure 2.9 shows spectra of the two Λ doublet components of the $R(6.5)_{1/2}$ transitions of NO. In a), the spectrum was obtained at a total pressure of 50 Torr, with p_{NO} = 4 mTorr buffered in air in a multi-pass cell with an optical path length of 332 cm. The spectrum is fitted with two Voigt functions, each with a fixed Gaussian component of 125 MHz (the Doppler width of NO at room temperature), from which a Lorentzian FWHM of 238 ± 1.29 MHz is extracted. According to the HITRAN database $\gamma_{\text{air}} = 4.8$ MHz Torr^{-1}, this corresponds to a total pressure of 49.6 ± 0.3 Torr, in good agreement with the experimentally measured pressure. In Figure 2.9 (b), the experimental spectrum presented in a) is overlaid with a spectrum ob-

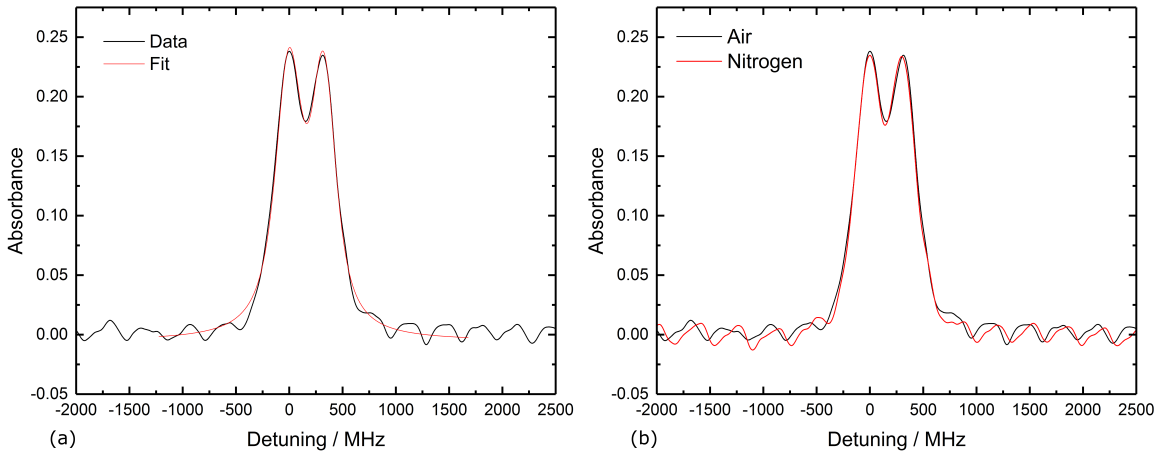


Figure 2.9: a) shows a spectrum of the $R(6.5)_{1/2}$ transitions of NO at $p_{NO} = 4$ mTorr buffered in air at a total pressure of 50 Torr, overlaid with two Voigt fits with a fixed Gaussian contribution of 125 MHz. In b), the spectrum shown in a) is overlaid with a spectrum of same transitions obtained at the same experimental conditions, using dry nitrogen as the buffer gas instead. The baseline of the spectra are affected by etalons formed between the optical components of the experimental setup (described in Chapter 5). These do not hinder the measurement of the target transitions shown or the signals studied in Chapter 5, since the latter occur at higher frequency than the etalons.

tained under the same partial and total pressure conditions, but using dry nitrogen as the buffer gas. The two spectra show excellent agreement, and so for all the work presented in this thesis it is assumed that $\gamma_{air} = \gamma_{N_2}$.

2.5 Conclusion

This chapter has presented a brief description of the types of QCLs and laser hardware used in this work. Given the central role of the mid-IR AOM used in Chapter 5, the details concerning its operation were also provided. The general properties of optical cavities were outlined, before a more detailed discussion in Chapter 6. The spectroscopy of NO was introduced, and the air and dry nitrogen broadening parameters of NO lines were compared in order to demonstrate that $\gamma_{air} = \gamma_{N_2}$. This is pertinent as dry nitrogen will be extensively used for buffering NO, and the HITRAN spectroscopic database only lists self and air broadening parameters.

Chapter 3

Multi-mode absorption spectroscopy with a Fabry-Perot QCL

In this chapter, a Fabry-Perot QCL (FP-QCL) is used to perform multi-mode absorption spectroscopy (MUMAS). MUMAS uses the output of the multi-mode laser to combine broad spectral coverage with high spectral resolution.[66] The spectrometer is used for the simultaneous detection of NO and H_2O, and the linewidth of the longitudinal modes of the QCL is extracted from simulations of the MUMAS output.[35] This work marks the first demonstration of the applicability of QCLs for MUMAS, and highlights the versatility of these coherent radiation sources with their implementation in a high spectral coverage and high resolution technique. The work presented here was done in collaboration with the Ewart group from the Physics department at Oxford University.

3.1 Introduction

Most laser based techniques aimed at the optical detection of gas phase species employ single mode devices with high optical purity. Among such techniques, tunable diode laser absorption spectroscopy (TDLAS) provides high resolution and good sensitivity with relatively low complexity for gas sensing in fields such as combustion diagnostics, environmental control and breath analysis.[67–72] A drawback, however, is that the mode-hop free tuning range of diode lasers or single mode QCLs is often limited to a few wavenumbers, and thus the detection of multiple absorbing species commonly requires multiplexing a number of laser and detector systems.[73] Spectroscopic methods that provide large spectral coverages and high resolution include (femtosecond) optical frequency combs (OFCs), but these involve the use of systems of high complexity and expensive optics.[74,75] Other methods, such as temporal correlation spectroscopic methods, provide the spectral coverage required for simultaneously sensing multiple gas species but have not been extended to the mid-IR.[76] As the absorbers commonly found in the aforementioned fields of study have their fundamental vibrational bands in the mid-IR, it would be advantageous for a broad spectral coverage, relatively inexpensive laser based sensing technique to have access to the strong absorption lines therein. The work presented in this chapter is concerned with the demonstration of a technique that offers these qualities: multi-mode absorption spectroscopy (MUMAS) using a QCL.

MUMAS was introduced in 2008 by Arita and Ewart with the detection of multiple transitions in the A band of molecular oxygen using a multi-mode diode laser.[66,77] The spectral coverage provided by the multi-mode device ($\sim$ 300 cm^{-1}) allowed the precise measurement of the temperature of oxygen samples between 300 and 500 K. In the same year, the technique was extended to the near-IR by using a diode laser pumped Er/Yb:glass laser to probe several transitions in the $v_1 + v_2$ overtone band of C_2H_2 at 1.5 μm.[78] The optical output of these multi-mode lasers provided

the high spectral resolution characteristic of single mode devices combined with the broad spectral coverage required for multi-species sensing, at the expense of higher minimum detection limits than those provided by TDLAS methods using single-mode lasers. However, for applications that do not require ultimate detection sensitivity, such as industrial process control, the multi-species sensing capabilities of MUMAS, together with the good temporal resolution of the technique, provide advantages over single-mode based techniques. More recent demonstrations of MUMAS include its use for the simultaneous detection of CO_2 and CO in engine exhaust, and for the detection of C_2H_2, N_2O and CO in a mixture.[79,80]

MUMAS has also been demonstrated in combination with sensitivity enhancement techniques such as wavelength modulation spectroscopy (WMS) and cavity enhanced absorption spectroscopy (CEAS).[81] In more recent reports, MUMAS was used with an interband cascade laser (ICL) and with a difference frequency generation source as the radiation sources for multi-species detection at *ca.* 3.3 μm and 3.7 μm, respectively, for the simultaneous detection of ammonia and methane in the former, and for the detection of methane, acetylene and formaldehyde in the latter case.[82,83] In this chapter, the extension of MUMAS to the 5 μm wavelength range is shown with the simultaneous detection of NO and water using an FP-QCL as a source.[35] MUMAS signatures were simulated and compared to the experimental data using a model developed by the Ewart group at the University of Oxford, allowing the use of MUMAS for accurately determining the optical emission properties of the multi-mode QCLs.

3.2 Theory

The operating principle of MUMAS is based upon the interaction of a single or multiple longitudinal modes of a multi-mode laser with the transitions of a gas phase absorber, as these modes are scanned in frequency. Consider a multi-mode laser

beam passing through a volume containing a gas phase absorber. The partial or total absorption of any of the laser modes causes a change in the transmitted intensity in relation to the incident intensity, producing a distinctive MUMAS *fingerprint* that is specific for an absorber being probed by a multi-mode device scanning over a target frequency range.[66] When the optical emission characteristics of the multi-mode device are known, along with the exact frequency of the transitions of the absorber, the MUMAS fingerprint can be simulated. The optical emission characteristics of a multi-mode laser that are critical for this process are the intensity envelope of the longitudinal modes, I_{env}, the mode linewidth, $\Delta\nu_{\text{width}}$, and the intermode-spacing, $\Delta\nu_{\text{mode}}$. These parameters are shown schematically in Figure 3.1 along with a representation of the MUMAS operating principle and a sample MUMAS fingerprint.

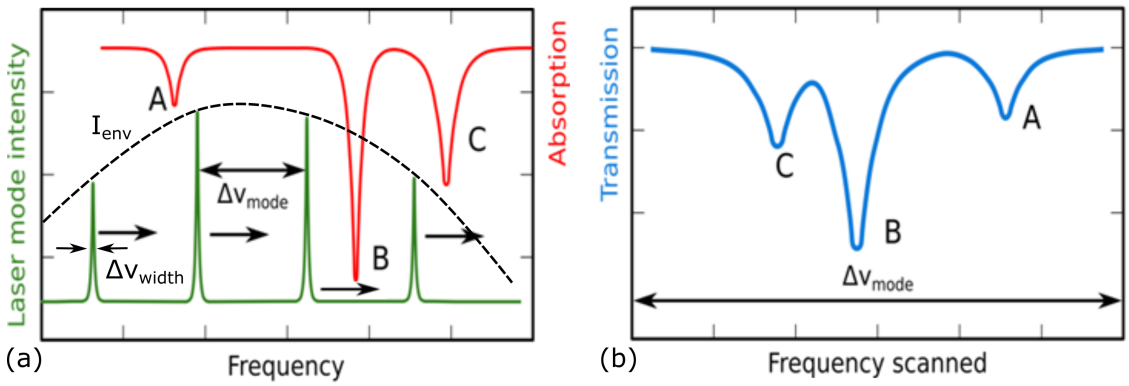


Figure 3.1: A schematic representation of a multi-mode laser emission spectrum, highlighting the intensity envelope of the longitudinal modes (I_{env}), the mode linewidth ($\Delta\nu_{\text{width}}$) and the intermode-spacing ($\Delta\nu_{\text{mode}}$) together with the transmission spectrum of an absorber, is shown in (a). (b) shows a representation of the MUMAS fingerprint resulting from scanning the modes by a frequency range equal to the intermode-spacing. The MUMAS absorption features are labelled for contrasting the different order of appearance between (a) and (b).

The MUMAS fingerprint is produced as the set of laser modes shown in Figure 3.1 (a) are simultaneously scanned across a frequency interval; in this case, the frequency interval is equal to $\Delta\nu_{\text{mode}}$. Therefore, the x-axis of a MUMAS spectrum is labelled with the detuning of the modes relative to their initial frequency. If the frequency

scan range is chosen such that it is equal to $\Delta\nu_{\text{mode}}$, then the spectral coverage of such frequency scan is equal to the full bandwidth of optical emission of the multi-mode laser.

Note that the position of the absorption features in a MUMAS spectrum is determined by the frequency of the transitions relative to the frequency of the laser longitudinal modes that are absorbed. The absorption features shown in Figure 3.1 (a) are labelled as A, B and C with the aim of establishing a comparison between the order of their appearance in the MUMAS spectrum relative to the position of the transitions on an absolute wavenumber scale. The resulting transmission spectrum (or MUMAS spectrum/fingerprint) as the longitudinal modes of the laser are simultaneously scanned is shown in (b). Clearly, the order in which the absorption features appear in a MUMAS spectrum is not the same as in a normal absorption spectrum. Furthermore, if multiple modes come into resonance with distinct transitions simultaneously, the total intensity of the light transmitted is reduced by the sum of all these interactions. In addition, the change in transmitted intensity due to the absorption of one or more modes is weighted by the mode fractional intensity (MFI), defined as the intensity of each of the modes absorbed relative to the total intensity of the beam. This point will be considered in more detail later in this chapter. An overview of the model to simulate MUMAS spectra is provided in the following subsection.

3.2.1 The MUMAS model

The MUMAS model used to predict all the spectra presented in this chapter uses the HITRAN database[65] to extract the NO transitions that fall within the spectral coverage of the multi-mode QCL, together with the laser emission spectrum, to simulate the multi-mode transmission spectrum through a sample of the gas. The HITRAN database provides the line strengths, the positions and the self and air broadening coefficients of the species of interest, assuming thermal equilibrium. In order to obtain

the laser emission spectrum, the intensity envelope is measured using a commercial FT-IR spectrometer with a resolution of *ca.* 0.5 cm^{-1} (see the next section). This experimentally measured intensity envelope is used by the computational model to estimate the maxima of the longitudinal modes of the device, which are equally separated in frequency by the free spectral range (FSR) of the laser cavity by

$$\Delta\nu_{\text{mode}} = \text{FSR} = \frac{c}{2nL}, \tag{3.1}$$

where n is the refractive index and L is length of the laser chip. The refractive index of InGaAs, the substrate of the FP-QCL, is taken as ∼3.2 at 5 μm. Therefore, using Equation 3.1 with $L = 4.3$ mm (provided by the device manufacturer),[84] the FSR of the device was initially estimated at *ca.* 11 GHz. The linewidth of the longitudinal modes, $\Delta\nu_{\text{width}}$, is smaller than the Doppler width of NO at room temperature (∼ 125 MHz) as will be shown in the results section. In line with single mode QCL devices, $\Delta\nu_{\text{width}}$ was assumed to be 1 MHz as a first approximation.[19] An Airy function ($\mathcal{L}(\nu)$) was used to generate a comb of modes with these characteristics, which was then combined with the spectral properties of the absorber to calculate the fractional multi-mode transmitted intensity ($M(\nu)$) as follows:[66]

$$M(\nu) = \frac{\int \mathcal{L}(\nu' - \nu)T(\nu')\mathrm{d}\nu'}{\int \mathcal{L}(\nu)\mathrm{d}\nu} = \frac{I_{\text{trans}}}{I_{\text{total}}}. \tag{3.2}$$

Here, $T(\nu')$ represents the frequency dependent transmission of the absorbing sample, calculated using the spectral information available in HITRAN. The resulting MUMAS fingerprint of this multi-mode device through a sample of absorber, $M(\nu)$, is thus described as the transmission function that results from the integrated absorption of all the longitudinal modes of this device, as these are detuned relative to the transmission spectrum of the absorber; *i.e.* the ratio between the intensity transmitted through an absorber, I_{trans}, and the total optical intensity, I_{total}). The output

of this model is then compared with experimentally obtained MUMAS spectra using a cross-correlation in order to obtain the initial position of the laser modes relative to the transitions of the absorber. This process is then followed by a least-squares fitting routine to determine the $\Delta\nu_{\text{mode}}$ and $\Delta\nu_{\text{width}}$ parameters with more accuracy. All the procedures described in this section were carried out using MATLAB code, in collaboration with the Ewart group at the University of Oxford, and the results will be shown in section 3.4.

3.3 Experimental

Figure 3.2 shows a schematic representation of the experimental apparatus. The multi-mode QCL used was a commercially available FP-QCL (Thorlabs QF5300CM1) operating at 5.3 μm with an optical power of 80 mW. The laser was driven by a commercial driver (ILX-Lightwave LDX3232) and the temperature of the laser chip was regulated using a custom built temperature controller. The laser modes were scanned by modulating the injection current using a function generator (TTi TG230). The output radiation was passed through an optical interference filter (Spectrogon NB-5360-078 nm) to remove some of the irregular spectral structure, and the spectrum of the resulting output was measured using an FT-IR instrument (Perkin Elmer Spectrum 100 FT-IR). The laser beam was directed to the FT-IR by a flip mirror which was retracted after these measurements were taken to allow the beam to propagate through the absorption cell and onto the detectors. The length of the frequency scan was determined by using a Ge etalon with FSR = 493 MHz at 5.3 μm. The measurement of the other laser parameters required for simulating MUMAS spectra will be outlined in the following section. The effective path length of the Herriott cell containing the samples of absorber was 26 m. The pressure in the cell was monitored using different gauges for low and higher pressures (Leybold vacuum CTR90 and

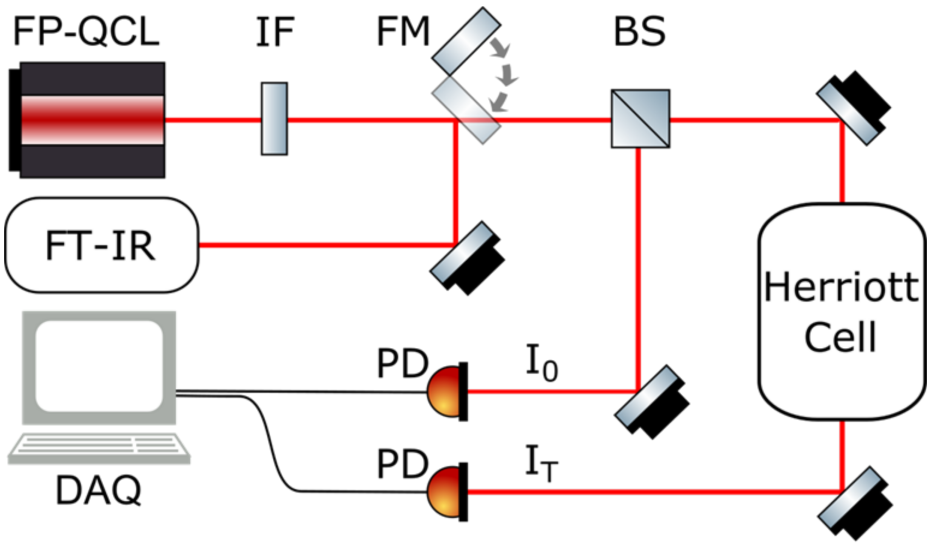


Figure 3.2: Schematic representation of the MUMAS experimental layout. The optical path lengths of the beams reflected and transmitted by the beam splitter are matched in order to remove any background absorption features, mostly caused by water in the atmosphere. IF: Interference filter; FM: Flip mirror; BS: Beamsplitter; PD: Photodiode; I_0: reference beam, used for obtaining the MUMAS fingerprint of atmospheric absorbers; I_T: intensity of the beam that is passed through the Herriott cell containing the absorbing gases, collected using a second photodiode.

600A-1000T-R12-H21X-X, respectively) with an uncertainty of 0.2 % at the lower pressures. Two photodiodes were used to monitor the reference and transmitted laser intensities (Vigo PVM-3 TE-10/MIP DC F-20 and Vigo PVI-2 TE-6/MIP DC F-20, respectively), and the resulting waveforms were digitally recorded using a digital oscilloscope (Handyscope HS4).

3.4 Results

3.4.1 Laser mode envelope and MUMAS spectrum of NO

Prior to the measurement and simulation of the MUMAS spectrum of NO, the laser intensity envelope was measured using a FT-IR spectrometer. The spectra shown in Figure 3.3 were obtained by operating the laser at a constant temperature of -15.2 °C and at currents between 913.2 mA and 988.2 mA. The effect of this current change

on the frequency of optical emission was also assessed by recording the transmission spectrum through a Ge etalon while modulating the laser driver within this current range; this yielded a total frequency scan with a range of approximately 10 GHz. The resolution of the FT-IR spectrometer (0.5 cm^{-1}) is such that the laser emission

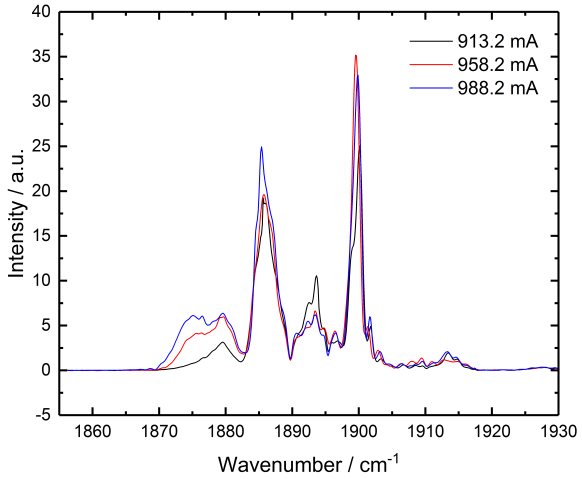


Figure 3.3: FT-IR spectra of the FP-QCL emission at a temperature of -15.2 °C and at selected currents between 913.2 mA and 988.2 mA.

spectrum looks continuous over the wavenumber interval shown in Figure 3.3, since the mode structure is not well resolved because $\Delta\nu_{\text{mode}} \approx 11$ GHz or (~ 0.37 cm^{-1}). Fortuitously, the multi-mode device could be operated in a quasi-single mode fashion by simply increasing the injection current to 1279 mA, owing to an increase in optical feedback from optics in the beam path that essentially mode-locked the laser by stimulating the emission of the most intense longitudinal mode. The transmission spectrum of the NO $R(1.5)_{1/2}$ and $R(1.5)_{3/2}$ $v = 1 \leftarrow 0$ transitions under these conditions is shown in Figure 3.4, measured at a total pressure of 2.2 mTorr of NO and with an optical path length of 26 m, along with an FT-IR spectrum of the laser emission. Figure 3.4 (b) shows the high spectral resolution provided by the laser in quasi-single mode operation: the spectrum consists of well-resolved Doppler limited features in which the splitting of the e/f Λ-doublet components within the $\Omega = 1/2$ manifold of 367 MHz is readily resolved, indicating that the width of the laser

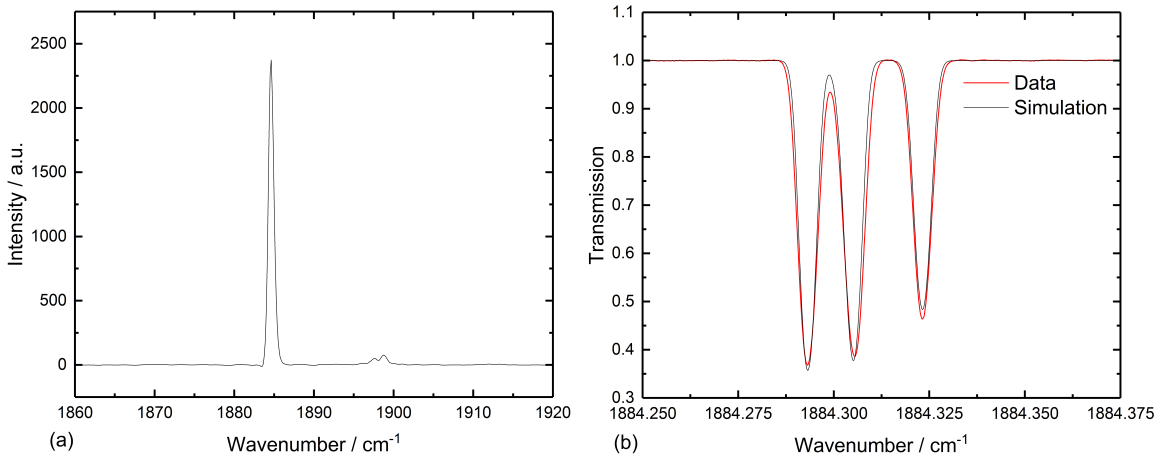


Figure 3.4: (a) shows an FT-IR spectrum of the laser emission in quasi single mode operation. The R(1.5) transition of the fundamental band of NO measured using the laser in quasi single mode operation is shown in (b).

longitudinal modes has an upper limit of about 50 MHz, considerably narrower than the nominal 0.5 cm^{-1} (15 GHz) resolution of the FT-IR spectrometer. As expected, the splitting between the e/f Λ-doublet components of the $\Omega = 3/2$ manifold at 1884.3 cm^{-1} is too small to be resolved.

Since the optical emission properties of the multi-mode device were characterised, the MUMAS fingerprint of NO of the laser in multi-mode operation can now be presented. Figure 3.5 shows the MUMAS spectrum of NO in nitrogen obtained at a total pressure of 2 Torr, with $p_{NO} = 5$ mTorr, as the laser modes are scanned across the inter-mode spacing, $\Delta\nu_{mode}$. The absorption features are the result of the interaction of several modes with a multitude of NO transitions, since NO has a congested spectrum at this wavelength due to a rotational constant of similar magnitude to $\Delta\nu_{mode}$. The spectrum shown in Figure 3.5 is overlaid with a simulation and there is good agreement. In order to obtain this simulation, the remaining laser parameters ($\Delta\nu_{mode}$ and $\Delta\nu_{width}$) had to be accurately determined in addition to the mode envelope intensity presented earlier. The most critical parameter for accurate modelling is the inter-mode spacing, and it is most accurately determined from fits of model signatures to MUMAS data of a known species recorded under known conditions of

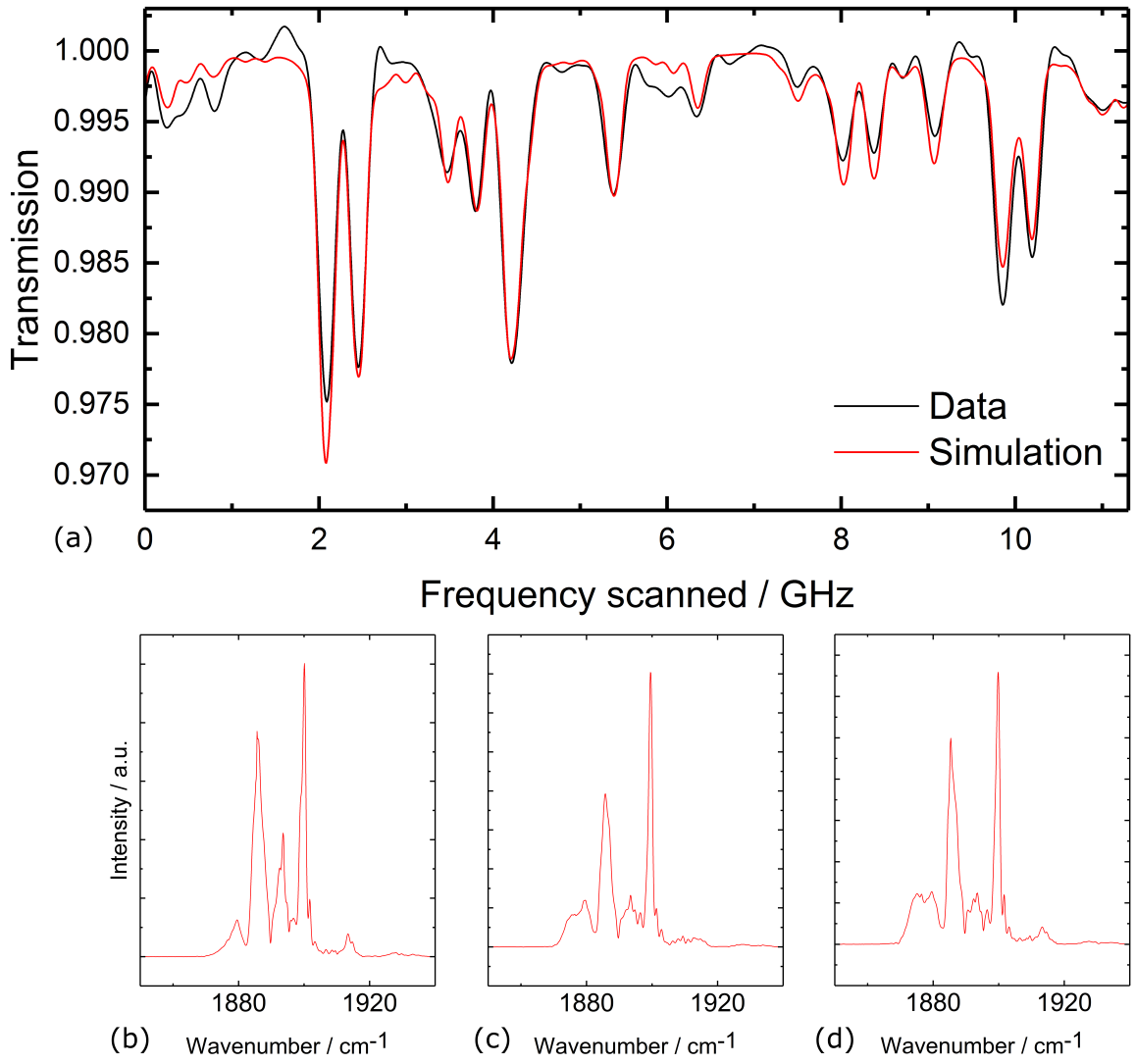


Figure 3.5: (a) shows the MUMAS spectrum of NO with fitted model spectrum. In (b), (c) and (d), the FT-IR spectra of the laser emission are shown at increasing laser injection current conditions at the start, middle and end sections of the frequency scan. The intensity envelope used to simulate this spectrum was based on a constant intensity envelope across the scan, despite the intensity increase of the lobe at the left of the spectra as a function of injection current. The effect of this phenomenon on MUMAS spectra will be discussed later in this chapter.

concentration, temperature and pressure.[85] The spectrum presented in Figure 3.5 fulfils these requirements, and all the relevant spectral information could be obtained from HITRAN. Using a nonlinear least-squares fitting routine to optimize the overlap between the simulated and the experimentally obtained MUMAS signatures, the FSR of the laser cavity was found to be 11.295 ± 0.001 GHz.

3.4.2 Measuring the mode linewidth

The final optical emission characteristic of the FQ-QCL that remains to be quantified is the mode linewidth, $\Delta\nu_{\text{width}}$. Due to the ability to fully resolve the NO $R(1.5)_{1/2}$ $v = 1 \leftarrow 0$ transition manifold, it was shown in Figure 3.4 that the mode linewidth is < 50 MHz. However, the device's $\Delta\nu_{\text{width}}$ can be more accurately determined using the MUMAS fingerprint. To do so, it is assumed that the individual longitudinal modes can be described by Lorentzian lineshapes with fixed widths. Since pressure broadened absorption lines are also described by (pressure dependent) Lorentzian lineshapes, it is impossible to distinguish how much of the total width of an individual absorption feature is due to pressure broadening as opposed to mode linewidth through the aforementioned least-squares MUMAS fitting routine. Therefore, the following method is adopted to determine $\Delta\nu_{\text{width}}$.

Several MUMAS spectra are recorded at a range of total pressures up to 152 Torr while holding a constant partial pressure of NO at 5 mTorr throughout. Dry nitrogen is used as a buffer gas in these measurements. Firstly, simulations of MUMAS spectra at the selected pressures are fitted to the data while keeping the $\Delta\nu_{\text{width}}$ parameter fixed at zero, *i.e.* assuming the width of the absorption features is solely due to pressure broadening. Figure 3.6 shows spectra recorded at total pressures of 2 Torr and 51 Torr, overlaid with fitted MUMAS simulations. The pressure is extracted

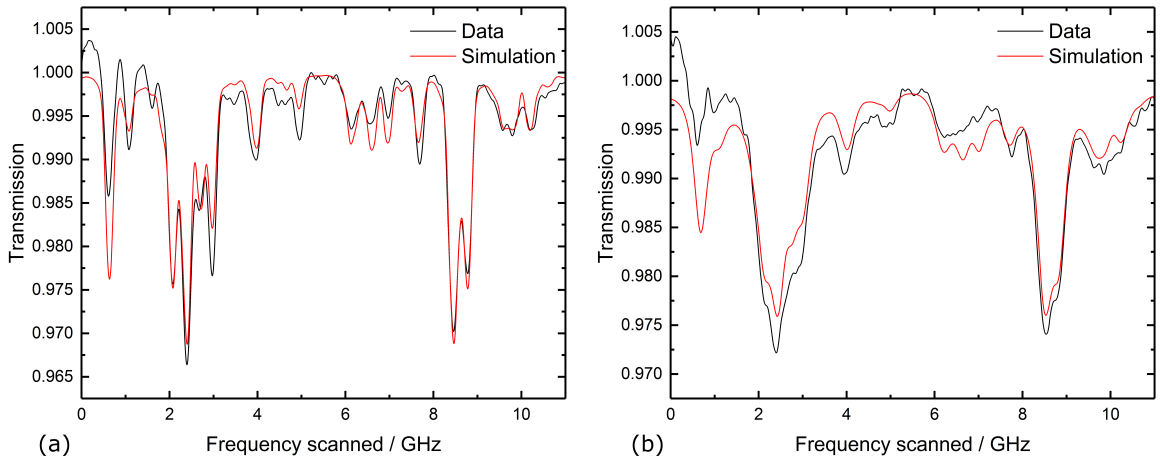


Figure 3.6: (a) shows a MUMAS spectrum of NO (with $p_{\mathrm{NO}} = 5$ mTorr), at a total pressure of 2 Torr, overlaid with a fitted MUMAS fingerprint. In (b), a MUMAS spectrum and simulation obtained at $p_{\mathrm{total}} = 51$ Torr, with the same p_{NO}, is shown.

through least squares regression fits to these data for the full range of pressures, and is plotted against the measured total pressure in Figure 3.7. The y-axis intercept is $\Delta\nu_0(p) = 7.73 \pm 0.45$ Torr. This pressure represents the buffer pressure necessary to produce the line broadening that would be caused by $\Delta\nu_{\mathrm{width}}$. It is necessary, however, to find a conversion factor that relates the zero pressure intercept to the corresponding mode-linewidth. To do so, the MUMAS fitting procedure is repeated using a fixed pressure of zero Torr and adjusting the mode-linewidth instead. A plot of pressure against mode-linewidth was then used to obtain a conversion factor of 4.76 MHz Torr^{-1} from its gradient. Hence, the mode linewidth was found to be 37.6 ± 2.2 MHz.

The mode-width was validated by fitting the MUMAS spectra at different pressures while fixing $\Delta\nu_{\mathrm{width}} = 37.6$ MHz. A plot of measured pressure against fitted pressure showed an intercept of 45 ± 495 mTorr, which is effectively zero due to the measurement uncertainty. With all optical emission properties of the multi-mode device pinned down, the use of the FP-QCL for MUMAS can now be further explored.

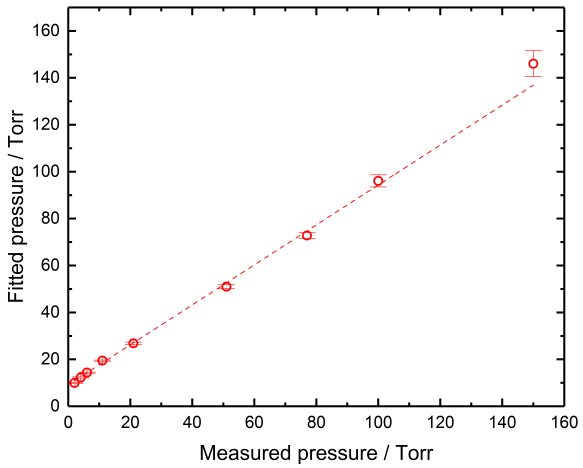


Figure 3.7: Plot of measured pressure versus the pressure extracted from the fits to the MUMAS data.

3.4.3 Multi-species sensing with FP-QCL MUMAS

The spectral coverage of MUMAS is perhaps its main attractive feature, together with the possibility for multi-species detection. To demonstrate the multi-species detection ability of MUMAS with a QCL, laboratory air was admitted to the Herriott cell in addition to NO. Figure 3.8 (a) shows a MUMAS spectrum of NO, with $p_{\mathrm{NO}} =$ 5 mTorr, obtained prior to admitting air to the cell in (b). The laboratory air had a recorded relative humidity of 24.6% at a temperature of 26 °C. Therefore, the 10 Torr of air admitted into the Herriott cell to produce the spectrum shown in (b) contained waver vapour at a partial pressure of $p_{\mathrm{H_2O}} = 83$ mTorr. Upon the addition of water, two distinct absorption features appear at approximately the centre of the frequency scan. The clear difference between the spectra in (a) and (b) illustrates the potential for MUMAS to distinguish a background interferent, in this case water, since additional information on the target species being detected is provided in the form of additional absorption features at other positions during the scan. Furthermore, since the spectroscopic information of common interferents can be found in suitable databases, HITRAN in this case, the spectra can be simulated and the relative contribution of different species to a MUMAS signature can be assessed,

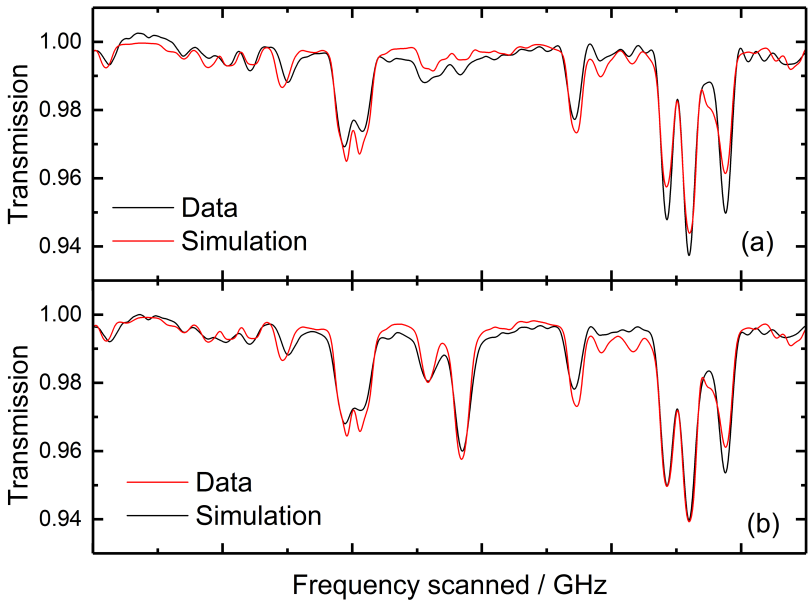


Figure 3.8: (a) MUMAS spectrum of NO at 5 mTorr overlaid with a fitted simulation. (b) MUMAS spectrum of NO ($p_{\mathrm{NO}} = 5$ mTorr) with 10 Torr of laboratory air. At this total pressure, with a relative humidity of 24.6% and a temperature of 26 °C, the laboratory air introduced in the Herriott cell contains water at a partial pressure of $p_{\mathrm{H_2O}} = 83$ mTorr. This spectrum is overlaid with a simulation of MUMAS of NO and water.

provided the optical emission characteristics of the source are well known.

3.4.4 Fast scan rates

All the MUMAS spectra shown up until now were obtained with frequency scans over the inter-mode spacing by modulating the laser current with a triangular waveform at a rate of 100 Hz. In this case the resulting chirp rate is 1.1 MHz $\mu\mathrm{s}^{-1}$, assuming all longitudinal modes are tuned at the same rate. Faster chirp rates across the frequency range $\Delta\nu_{\mathrm{mode}}$ would offer a time resolution advantage, and several frequency scanning schemes have successfully been applied to QCLs in order to obtain chirp rates several orders of magnitude faster, including applying higher frequency waveforms or injection current pulses (see Chapter 5). Figure 3.9 shows MUMAS spectra, and best fit simulations, recorded over a range of 6 GHz at scan rates of 100 Hz and 10 kHz, respectively. Both spectra are an average of 100 sweeps, and so (b) was

obtained within a significantly shorter time interval. The small differences in the

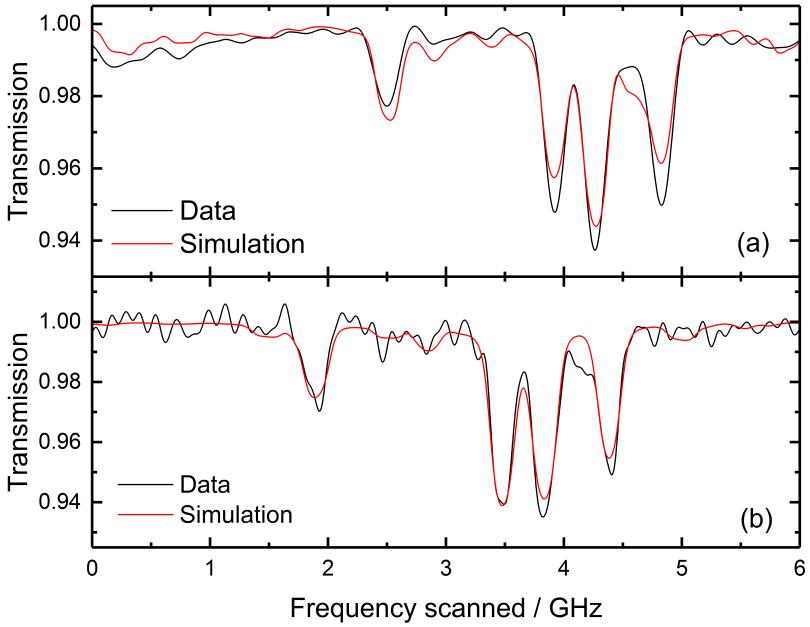


Figure 3.9: A MUMAS spectrum of NO, obtained at a total pressure of 5 mTorr and a scan rate of 100 Hz, is shown in (a). In (b), a MUMAS spectrum of NO obtained at the same total pressure, but faster scan rate (10 kHz), is shown. The slight difference in the measured spectra is due to changes in the laser operating conditions between (a) and (b).

relative absorption between features in the slow and fast scans can be accounted for by the slight change in laser temperature and current operating conditions, which in turn affect $\Delta\nu_{\text{mode}}$, necessary for the removal of transients that occurred at the start of the frequency scan in the spectrum shown in Figure 3.9 (b).

The scan range is reduced to 6 GHz instead of $\Delta\nu_{\text{mode}}$ ($\sim$ 11 GHz) due to limitations imposed by the drive electronics. This range is sufficiently wide to include the cluster of absorption features at *ca.* 4 GHz, but the multi-species detection capabilities of the technique become more limited. The spectra obtained at these distinct scan rates show that the frequency resolution is not affected by higher scan rates, and thus FP-QCL devices can be used to obtain MUMAS spectra with a higher temporal resolution than previously shown in this chapter. The maximum scan rate used was 50 kHz, however the scan range in this case was reduced to only 2 GHz. Despite

the loss of spectral coverage, increasing the temporal resolution of MUMAS this way would be advantageous in process control applications, where fast response times are necessary for studying rapidly changing molecular concentrations.

3.4.5 Relative mode intensity changes as a function of injection current

The final aspect that requires consideration concerning the application of QCLs to MUMAS is the fluctuation of the mode envelope intensity during the frequency scan. The model used to simulate the MUMAS spectra takes as an input the mode envelope intensity that is an average over a set injection current conditions; *e.g.* the average of the emission spectra shown in Figure 3.3. As the relative intensity of the longitudinal modes changes as a function of injection current, the mode fractional intensity (MFI) mentioned in the theory section will also change, and is a possible explanation to the overestimation or underestimation of the model total intensity attenuation in the event of total or partial absorption (see the features around 4 GHz in Figure 3.9 (a)), for example).

To demonstrate this effect, consider a model multi-mode laser emission spectrum consisting of three longitudinal modes scanning over the $R(6.5)_{1/2}$ and $R(6.5)_{3/2}$ transitions of NO in the weak field limit; *i.e.* no optical saturation effects are considered. The optical emission parameters of this model device, $\Delta\nu_{\text{mode}}$ and $\Delta\nu_{\text{width}}$, are taken as 11 GHz and 37 MHz, respectively, in agreement with the measured parameters of the FP-QCL. Figure 3.10 shows how the MUMAS spectra are modified by changes in the relative intensity of the longitudinal modes, *i.e.* changes in the MFI.

The MUMAS spectrum shown in Figure 3.10 (b) is obtained by scanning the modes in (a) by the $\Delta\nu_{\text{mode}}$ of the model device. In (c), the relative intensity of longitudinal modes is changed with respect to (a), resulting in a decrease in total transmission from $\approx$0.96 to $\approx$0.93 of the spectral feature at 4 GHz due to absorption

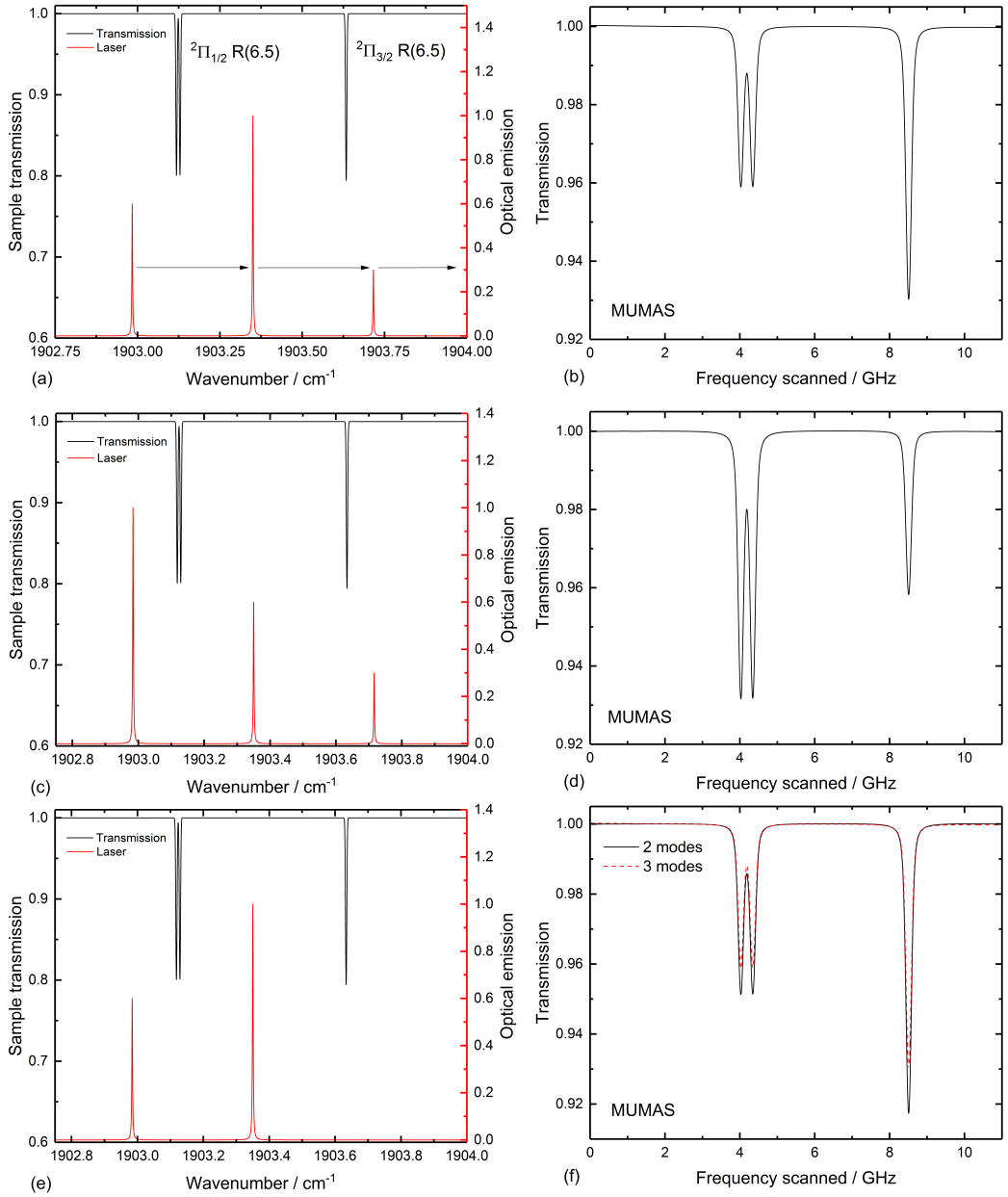


Figure 3.10: (a) shows a model laser emission spectrum consisting of three longitudinal modes of different peak intensities, along with the frequency dependent transmission through a 1 m long sample of NO at 5 mTorr. (c) and (e) present the same information as (a), but with different mode relative intensity and total intensity, respectively. The MUMAS spectra that result from scanning the modes by $\Delta\nu_{\text{mode}}$ (as shown by the arrows in (a)) are displayed in (b), (d) and (f). The spectrum in (f) highlights the effect of changing the total emission intensity by using only the two lower wavenumber modes when these have the same relative intensity as in (a).

of the highest intensity mode by the $R(6.5)_{1/2}$ transition. The laser emission spectrum in (e) is nearly identical to (a), except that the highest wavenumber mode is removed, and so the total optical emission intensity is changed. By scanning the laser spectrum shown in (e) by $\Delta\nu_{\text{mode}}$, a MUMAS spectrum that possesses features with the same relative transmission (between the two absorption features), but less total transmission than (b) is obtained. This shows that changes in the total emitted intensity, even by the increase or decrease of the intensity of longitudinal modes that are not absorbed, may cause discrepancies between the measured and simulated MUMAS spectra. It is therefore highly likely that the discrepancies between the experimental data and the simulations presented in this chapter are primarily due to the evolution of the mode envelope intensity as the injection current changes during the frequency scans across $\Delta\nu_{\text{mode}}$ (see Figure 3.3).

3.4.6 Conclusions

The work presented in this chapter demonstrates the applicability of FP-QCLs as multi-mode sources for multi-species detection with high temporal resolution using MUMAS. The technique was demonstrated with the detection of multiple transitions of NO over a bandwidth of *ca.* 50 cm $^{-1}$, limited by the transmission of an interference filter. The simultaneous detection of NO and H_2O from laboratory air demonstrated the multi-species sensing capabilities of the technique. A MUMAS model was successfully used to predict the transmission fingerprint, showing the potential of cost-effective high-resolution broadband spectroscopy in the mid-IR with commercially available QCL devices despite the relative intensity changes in the longitudinal mode envelope during the frequency scan. Finally, it has been shown that MUMAS data can be obtained at high scan rates, up to 50 kHz, at the expense of a reduction in spectral coverage, in order to enable gas sensing with short measurement times important for applications in rapidly changing environments or for active process con-

trol. While in this chapter the optical emission characteristics of a multi-mode device were determined, the subsequent chapters are concerned with the determination of the optical characteristics of single mode devices and their applications in nonlinear spectroscopy and trace gas sensing.

Chapter 4

Single mode QCLs: optical bandwidth and current perturbations

4.1 Introduction

Single mode QCLs as mid-IR sources have gained popularity in the last two decades finding applications in areas such as high resolution spectroscopy, nonlinear optics and trace gas sensing.[27,86,87] This is due to their high optical emission power (usually in the hundreds of mW), narrow linewidths (typically a few MHz or less), and near room-temperature operation.[19] High resolution spectroscopic techniques such as saturation spectroscopy (see Chapter 1) benefit from these narrow linewidths, and are tools for establishing accurate frequency markers and laser stabilisation.[88,89] The high coherence and intensity of the electric field produced by these sources also allows the observation of coherent transient effects when the laser frequency is swept over a strong molecular transition of a velocity selected sample on a timescale that is short compared to its relaxation time.[90–92] These nonlinear optical effects, some of

which are investigated in Chapter 5 of this thesis, include Rabi cycling and coherent transient effects such as rapid passage (see later), and are highly dependent on the linewidth of the laser that prepares the velocity selected sample. Coherent effects are suppressed with the excitation of a wider range of velocity groups, as will be shown later in this thesis.

The theory underpinning the calculation of the fundamental limit of the linewidth of a laser, $\delta\nu$, was first presented by Schawlow and Townes[93]. The following expression, realised by Henry[94], extended the original Schawlow-Townes calculation to diode lasers:

$$\delta\nu = \frac{v_g^2 h\nu\alpha\alpha_m n_{sp}}{4\pi P_0}(1+\alpha_e^2), \tag{4.1}$$

where v_g is the electron group velocity, α represents the cavity losses, α_m the mirror losses and n_{sp} is the spontaneous emission factor. The terms α_e and P_0 are the Henry linewidth enhancement factor (that accounts for refractive index fluctuations) and the laser output power, respectively. In contrast to diode lasers, the linewidth of QCLs is largely unaffected by refractive index variations at the peak of the gain spectrum since electron density fluctuations in the gain medium are negligible[26], hence α_e is close to zero. The limit for the QCL linewidth predicted by Equation 4.1 was thus reformulated by Yamanishi *et al.* in the last decade, incorporating a better description of the specific mechanisms that govern the linewidth of QCLs. Yamanishi's theory is based on the rate equation analysis of a three-level system of the QCL active region as represented in Figure 4.1.[95] From this model, a new expression emerged for the QCL linewidths:

$$\delta\nu = \frac{1}{4\pi}F_R\frac{N_3}{(N_3-N_2)_{th}}\frac{(h\nu)\gamma_{photon}^2}{P_{int}}(1+\alpha_e^2), \tag{4.2}$$

where F_R is a spontaneous emission enhancement factor, P_{int} is the internal power and γ_{photon} is the photon decay rate. This model, along with frequency noise measurements

by Bartalini *et al.*, have demonstrated that the intrinsic linewidth of QCLs is lower than the limit predicted by the Shawlow-Townes model, dropping as low as a few hundred Hz.[96] Fluctuations in the injection current, however, are the main contributor to the broadening of this linewidth to the MHz level in non-stabilised devices.[97,98]

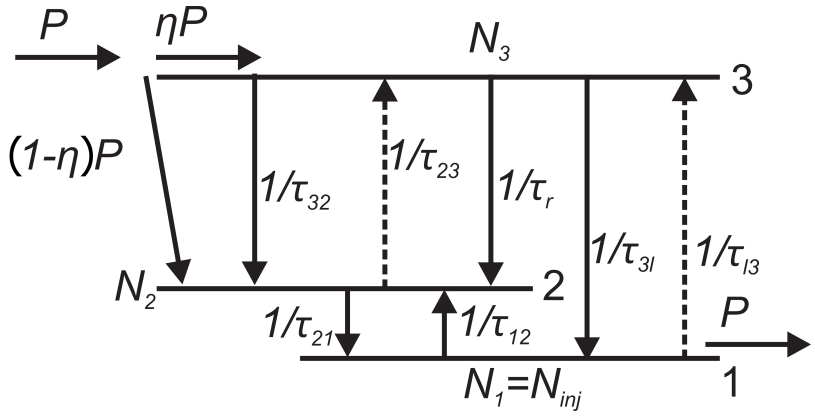


Figure 4.1: Energy level diagram of the 3-level system of the active region of a QCL gain medium, reproduced from[95]. The relaxation time constants between levels are denoted by τ, each level's electron population by N_i, where i represents the level, P is the net rate of electrons in and out of the system and η is the coupling efficiency into the highest level.

The spectral purity of the laser emission is a critical property that has far reaching implications on the sensitivity of laser based spectrometers. For trace gas sensing, high fidelity QCLs have been implemented in a range of optical cavity techniques such as off-axis cavity enhanced absorption spectroscopy (OA-CEAS), cavity ring-down spectroscopy (CRDS) and optical-feedback cavity enhanced absorption spectroscopy (OF-CEAS).[50,71,99–103] While resonant cavity techniques like OF-CEAS provide the highest sensitivities in general, OA-CEAS retains attractive features relating to practicality, including robustness, ease of alignment, frequency resolution and compactness.[49] These are a consequence of a modus operandi for OA-CEAS which requires a dense, random mode structure from which to generate a smooth time-integrated cavity transmission spectrum as the laser frequency is scanned. Such attributes are particularly pertinent for example, in the construction of in-line breath sensors where

rapidly varying flows occur.[69] A drawback of OA-CEAS, however, is that it is a low signal technique (because the cavity is non-resonant) and therefore the high powers of cw QCLs are beneficial. In such instruments the intensity noise arising from the residual mode structure is often the sensitivity limiting factor and is most apparent with narrow linewidth lasers. Strategies to reduce the residual mode noise in these non-resonant techniques have included dithering the laser frequency or the cavity length; the latter usually achieved using a piezo-electric transducer.[104] An alternative method for improving the sensitivity of OA-CEAS was demonstrated by Ciaffoni *et al.*, who showed that the introduction of random frequency fluctuations induced by mixing broadband radio-frequency (RF) noise with the driving current of a VCSEL operating at 764 nm resulted in residual mode noise suppression.[105] Similarly, Manfred *et al.* have shown that the sensitivity of a QCL based OA-CEAS spectrometer was enhanced by nearly an order of magnitude by employing the same current perturbation scheme.[106] The residual mode noise suppression resulting from perturbation of the injection current is due to laser linewidth broadening, making it clear that tuned linewidth sources are advantageous in a laser spectrometer of this type. While this enhancement has been predicted theoretically[107], the actual impact of broadband RF perturbations on QCL linewidth requires further investigation.

The linewidth of QCLs has been experimentally determined in several ways, including two-sample (Allan) variance[108], by analysing the noise power spectral density (PSD) of optical emission[97,98] (using the side of a molecular transition as a frequency discriminator) and by Lamb-dip spectroscopy[92,109]. In this chapter, the linewidth of a QCL operating at ~ 5.3 μm is measured via Lamb-dip spectroscopy on a low pressure sample of NO and by analysing the frequency noise power spectral density of the system using a Ge etalon as a frequency discriminator. The impact of RF noise perturbations on the linewidth of a QCL is quantified, and the ability to control the extent of the line broadening by amplifying the noise by different factors is demon-

strated. Another established method for performing linewidth measurements, the self heterodyne technique, will also be presented. This method relies on splitting a laser beam and analysing the beat signal between the two resulting beams after one is frequency shifted and time delayed relative to the other.[110,111] It finds its most common applications in the characterisation of diode systems operating in the near-IR, and its extension to the mid-IR has been hindered by the difficulty in producing optical delay lines of sufficient length. The self-heterodyne technique will also be used to study the effects of applying RF current perturbations to the laser injection current, and the results will be compared with those obtained with the Lamb-dip and frequency noise PSD techniques.

4.2 Linewidth measurements via Lamb-dip Spectroscopy

4.2.1 Background and experiment

The maximum resolution achievable in a low pressure sample in the gas phase is often limited the Doppler width of the sample, and thus the spectroscopic measurement of the linewidth of a cw-QCL, that is of the order of a few MHz, cannot be achieved by conventional direct spectroscopy. To circumvent this problem, saturation spectroscopy, introduced in Chapter 1, is put into practice in the form of Lamb-dip spectroscopy. To introduce Lamb-dip spectroscopy, consider a monochromatic wave, with wave vector $\boldsymbol{k}$, traversing a gas sample along an axis $\boldsymbol{z}$. Only molecules moving with a velocity component along this axis, v_z, such that the Doppler-shifted frequency falls within the Doppler broadened profile of the sample, will interact with the field.[31]

The Doppler shifted resonance frequency of these molecules is thus given by

$$\nu_0' = \nu_0\Big(1 \pm \frac{v_z}{c}\Big). \tag{4.3}$$

In the presence of an intense field coupling a lower state $|1\rangle$ to an upper state $|2\rangle$, significant changes in population difference $\Delta N = N_2 - N_1$ can be induced. If the spectral bandwidth of this field is small compared to the Doppler width of the sample, only the small selection, or subset, of velocity groups will be affected by this population change, in what can be described as *hole burning*. This concept is shown pictorially in Figure 4.2.

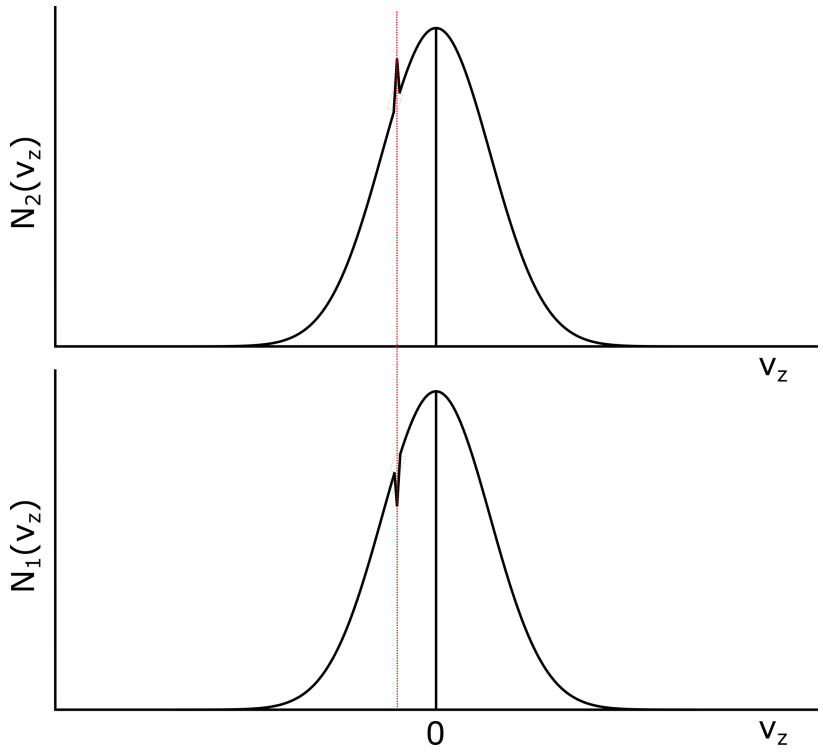


Figure 4.2: Hole burnt in the population density of a lower state N_1 accompanied by an increase in population density of the same velocity group in N_2. The FWHM of the hole will be approximately the laser linewidth if collisional broadening is small in comparison.

Probing such a hole would be impossible with direct absorption spectroscopy with a single cw laser, but by splitting the output of a single source into a strong

pump beam and a weak *probe* beam, as seen in Figure 4.5, the laser is able to serve both functions simultaneously. As the two beams propagate in opposite directions with identical frequency, they interact with mirror image velocity groups across the Doppler profile (see Figure 4.3). The Lamb-dip is then observed as a hole at the line centre, when the two beams interact with the same velocity subset, $v_z = 0$.

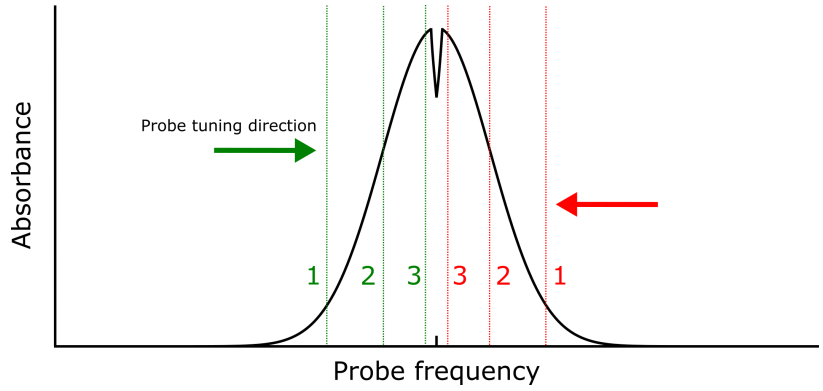


Figure 4.3: In green, the probe frequency position relative to a Doppler profile as it is swept. The pump laser (red) burns a hole in a velocity group of the same speed and opposite direction.

The depth of the hole in the population density at the line centre ($\nu = \nu_0$) can be described in terms of a saturation parameter, S, introduced in Chapter 1, by the relation:

$$\Delta N_0(v_z) - \Delta N(v_z) = \Delta N_0(v_z)\frac{S_0}{1+S_0}, \tag{4.4}$$

where S_0 is the saturation parameter at the line centre. Neglecting coherence effects, the change in absorption coefficient that is observed by the weak probe beam in a strong pump field can be modelled as

$$\alpha(\nu) = \alpha_0(\nu)\left[1 - \left(1 - \frac{1}{\sqrt{1+S_0}}\right)\mathscr{L}\right], \tag{4.5}$$

where $\alpha_0(\nu)$ is the unsaturated absorption coefficient at the line centre and $\mathscr{L}$ is a lineshape function that is determined by the experimental conditions.

The FWHM of the Lamb-dip encodes the information necessary to extract the linewidth of the laser. The shape of the dip results from the convolution between the sub-Doppler absorption profile of the transition and the lineshape of the laser. Further broadening contributions from residual collisional broadening and transit time broadening will affect the width and shape of the dip, but can be calculated and removed to yield the laser linewidth.[112]

The experimental procedures described in this chapter were conducted on a single mode cw distributed feedback (DFB) QCL (Maxion M575AH-NS). As shown in Figure 4.4, the laser is driven by a custom designed driver, and its driving current is mixed with broadband (50 kHz to 500 MHz) RF noise (RFDesignUK, Noise Brick - NB 3) via a bias tee, which can be amplified up to +25 dB (Mini-circuits MHF model).

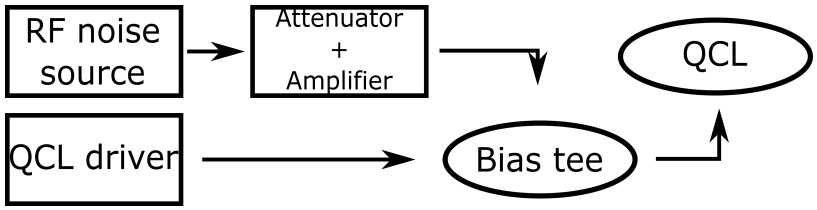


Figure 4.4: Schematic representation of the current noise mixing electronics.

As presented in Figure 4.5, a CaF_2 window is used to split the laser beam into a strong pump beam and a weak probe beam containing about 95% and 5% of the laser output power, respectively. The two beams then counter propagate through a 73 cm long cell with a crossing angle of 0.2°. This angle was chosen in order to avoid excessive optical feedback, which can perturb the frequency tuning rate of the free running laser. The laser frequency is scanned by applying a triangular voltage ramp to the driver by the means of a function generator (TTi TG230). The probe beam is detected by a photodiode (VIGO PVMI-3TE-10.6). The DFB QCL probes the $R(6.5)_{1/2}$ $v = 1 \leftarrow 0$ transition of the electronic ground state of NO at 1900.07 cm^{-1} and at a total gas pressure of 50 mTorr. Individual spectra are then averaged using

a MATLAB routine.

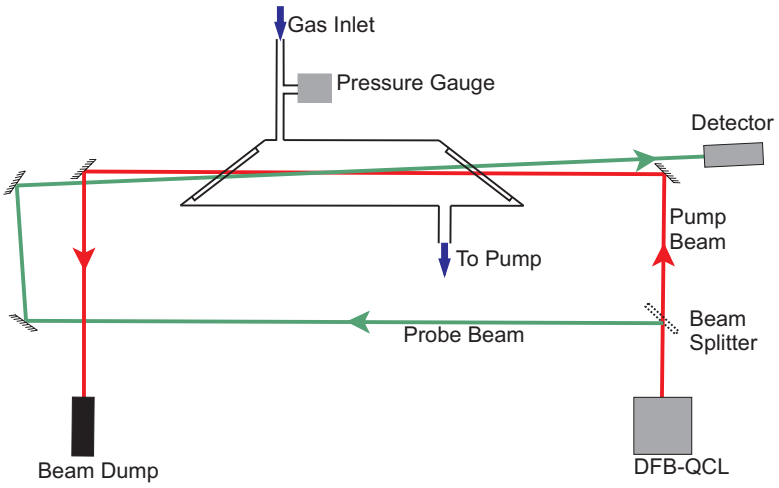


Figure 4.5: Lamb-dip experimental scheme. The cell is fitted with CaF_2 windows, and another window of this material is used to split the laser beam into a strong pump beam and a weak probe beam.

4.2.2 Results

The laser is tuned to the $R(6.5)_{1/2}$ $v = 1 \leftarrow 0$ transition of the electronic ground state of NO which presents the doublet structure shown in Figure 4.6 due to Λ-doubling. In addition, hyperfine coupling with the nuclear spin of nitrogen (I = 1) will be responsible for further splitting of each Λ component into six hyperfine components, from which only the three strongest are observable and saturable with the laser intensity available. The hyperfine interaction is weak, so the splitting between the most widely separated hyperfine components is only 540 kHz for the e Λ-component and 1.26 MHz for the f Λ-component, resulting in a single dip in both cases.

The Doppler profiles are subtracted from the spectrum and the Lamb dip of the e component is shown in the main part of Figure 4.7 along with fits to the data obtained with and without RF perturbation of the laser injection current. For the unperturbed case the data are fit with the sum of three Lorentzian functions. These functions are

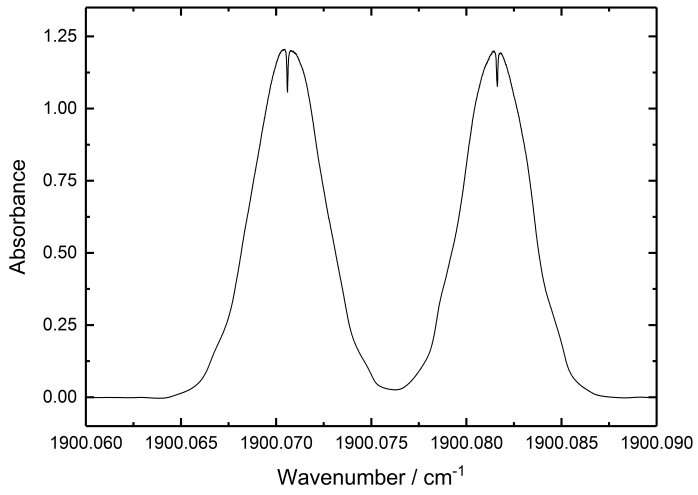


Figure 4.6: Full range of the frequency scan over the R(6.5)$_{\frac{1}{2}}$ $v = 1 \leftarrow 0$ transition of NO. The low frequency noise present on the profiles is caused by residual optical feedback due to the spatial proximity of the counter-propagating pump and probe beams, and is absent if either of the beams is blocked.

of equal width and centered at the position of each hyperfine component, which yield a FWHM of 1.56 ± 0.17 MHz. The spectra are averaged 100 times, and the error is obtained from the standard deviation of the width of all individual sweeps. The measured FWHM includes contributions from collisional broadening, which is 240 kHz at 50 mTorr of NO (with $\gamma_{\text{self}} = 4.9$ MHz Torr^{-1}),[65] transit-time broadening of $\sim$ 320 kHz with a beam radius of 1 mm, and residual Doppler broadening of 320 kHz (since the beam crossing angle is not zero). Removing these contributions yields a linewidth of 680 ± 170 kHz. The Lamb-dips are retrieved at a chirp rate of 0.15 MHz μs^{-1}, and so a time of 11.5 μs is taken to traverse the dip FWHM of 1.73 MHz; this establishes a lower limit for the observation time.

As seen in Figure 4.7, by perturbing the injection current with the RF noise device coupled to a +20 dB gain amplifier, the linewidth increases to 3.67 ± 0.23 MHz. The evolution of the width as a function of noise is provided further on in this chapter (see Figure 4.12). Notably, while the lineshape without RF noise should have both Gaussian and Lorentzian contributions owing to the laser being affected by both white and 1/f noise, and thus be described by a Voigt profile, it is found that a Lorentzian

function returns a better fit to the unperturbed lineshape. As broadband RF noise is added to the injection current, the Lamb-dip profile becomes progressively more Gaussian; this is expected since the added noise is white, bandwidth limited and hence not statistically correlated.[105]

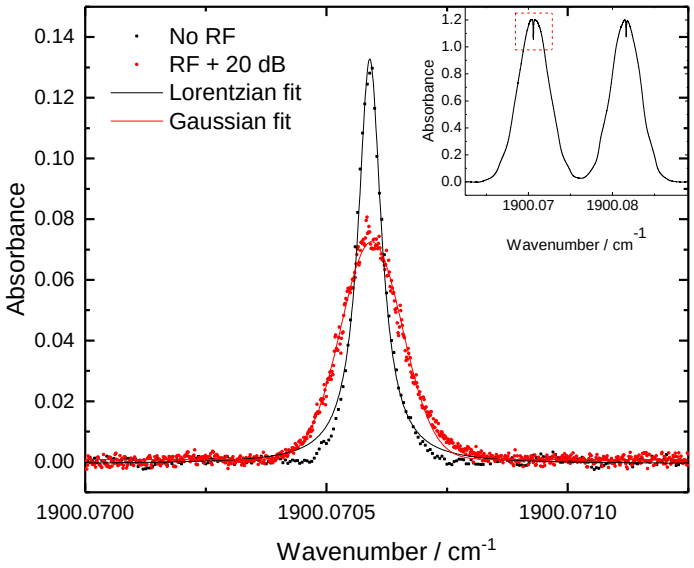


Figure 4.7: Lamb dips with Lorentzian and Gaussian fits for the cases of unperturbed injection current and with the application of RF noise (+20 dB) respectively.

Using Lamb-dip spectroscopy to obtain sub-Doppler resolution and hence measure the laser linewidth proves to be an effective method, and shows evidence of spectral bandwidth broadening by RF current perturbations. However, this method involves a reasonably complex experimental setup which requires the careful co alignment of counter-propagating beams, and is restricted to lasers with sufficient optical power to reach saturating intensities. A technique with less stringent experimental demands is presented in the following section, for which the high intensity requirement is also alleviated.

4.3 Linewidth measurements via the frequency noise power spectral density

4.3.1 Background and experiment

This section presents a technique that allows the measurement of RF current perturbed and unperturbed QCLs using the frequency noise power spectral density (PSD) of optical emission. The theory, originally developed by Di Domenico *et al.*,[97] requires a PSD measurement that can be obtained with a simple experimental setup with which the optical bandwidth of the laser can be determined over any accessible timescale. To obtain the frequency noise PSD, a mechanism for converting optical frequency fluctuations into measurable fluctuations is necessary. This has previously been achieved by tuning the laser frequency onto the side of a pressure broadened molecular transition[96]; in this work, the side of a fringe of a low finesse etalon is employed.

The PSD can be split into two regions that contribute either to the linewidth or the wings of the laser spectrum. This separation is defined by the line represented in Figure 4.8, known as the β-separation line, given by $8\ln 2f/\pi^2$, where f is the Fourier frequency. The region that contributes to the linewidth, defined by $S_{\delta\nu}(f) > 8\ln 2f/\pi^2$, is a region of high modulation index β. Conversely, the region where $S_{\delta\nu}(f) < 8\ln 2f/\pi^2$ is a low modulation index region and only contributes to the wings of the lineshape.

The laser lineshape can be obtained via the autocorrelation function, $\Gamma_E(\tau)$, calculated using the frequency noise PSD of the optical electric field ($E(t)$) measured experimentally. This function is determined by employing the theory developed by Di Domenico *et al.*, using the following relation:[97]

$$\Gamma_E(\tau) = E_0^2 e^{i2\pi\upsilon_0\tau} e^{-2\int_0^\infty S_{\delta\nu}(f)\frac{\sin^2(\pi f\tau)}{f^2}\mathrm{d}f}, \tag{4.6}$$

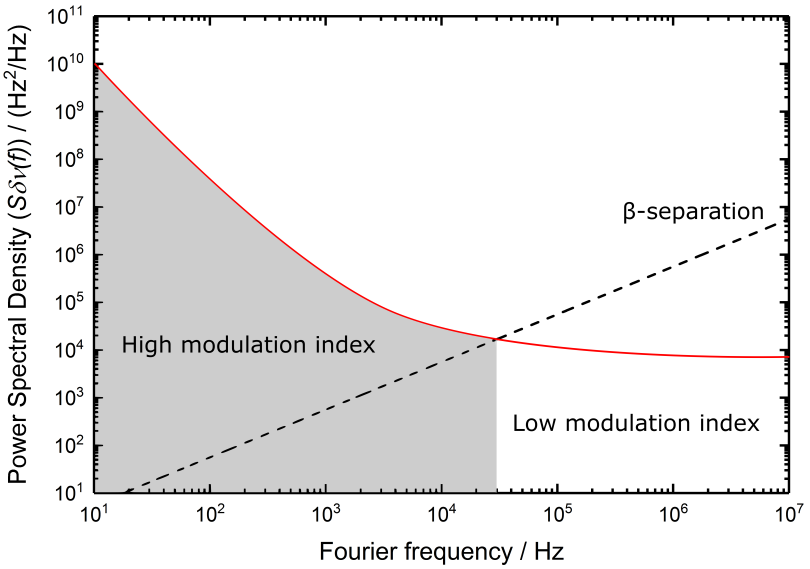


Figure 4.8: Schematic of an optical frequency noise PSD, with the β-separation line represented as the dashed line. The shaded, high modulation index region contributes to the linewidth while the low modulation index region, where the PSD drops below the β-separation line, only contributes to the wings of the lineshape.

where E_0 is an electric field amplitude factor and $\delta\nu$ represents the laser frequency deviation around its centre value. The computation of the laser lineshape is realised, according to the Wiener-Khintchine theorem, by Fourier transforming the autocorrelation function:

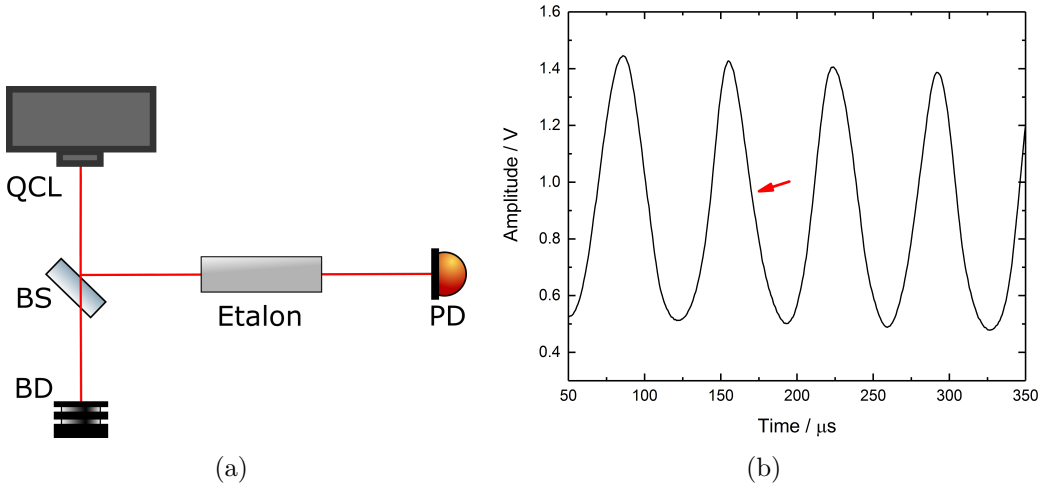
$$S_E(\nu) = 2\int_{-\infty}^{\infty} e^{-i2\pi\nu\tau}\Gamma_E(\tau)\mathrm{d}\tau. \tag{4.7}$$

For calculating the laser lineshape at a given observation time, a low frequency cutoff, f_c, is established as the lower limit of integration at the Fourier frequency that corresponds to $1/t_{obs}$, where t_{obs} is the observation time. A useful approximation to the laser linewidth can be direcly extracted from the geometric area under the frequency noise PSD, using the following expression:

$$\mathrm{FWHM} = \sqrt{8\ln 2 A} \tag{4.8}$$

where A is the area under the high modulation index region of the $S_{\delta\nu}(f)$ spectrum,

as shown in Figure 4.8. This simple relation, along with the autocorrelation analysis of the frequency noise PSD spectra allow the calculation of linewidths and lineshapes at similar observation times as those obtained via Lamb-dip spectroscopy.



(a) (b)

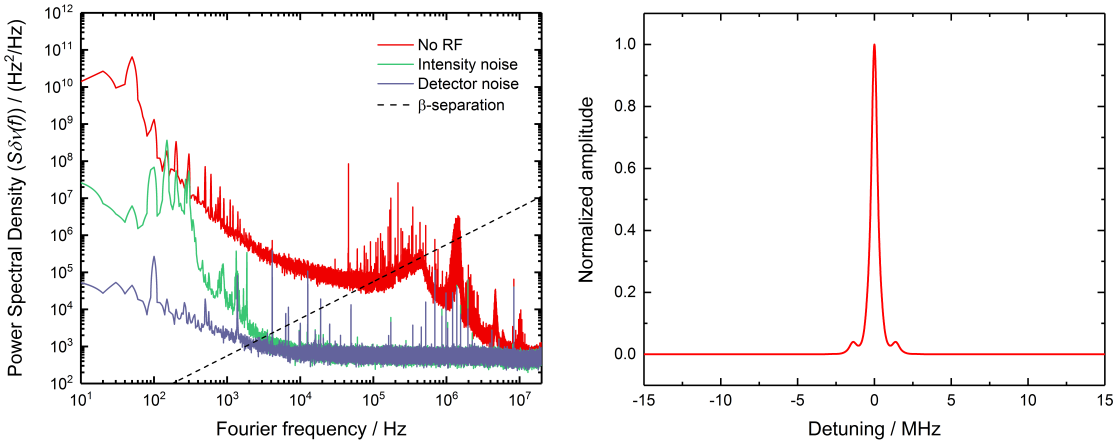
Figure 4.9: (a) Experimental scheme of the PSD measurement. BS - beamsplitter, BD - beam dump, PD - Photodiode ;(b) Ge etalon raw transmission spectrum as the laser is scanned. The arrow indicates the level at which the laser remains during the acquisition of the frequency noise PSD.

The experimental setup of this technique is shown in Figure 4.9 (a). The etalon used as a frequency discriminator is a low finesse Ge etalon with FSR = 493 MHz, and a typical transmission spectrum from which an amplitude to frequency conversion factor of 163.9 ± 8.5 MHz V^{-1} is extracted is shown in b). After passing through the etalon, the laser beam is collected onto a 20 MHz bandwidth photodiode (VIGO PVMI-3TE-10.6) and recorded using an oscilloscope (LeCroy Wavesurfer 400 MHz). The PSD is then generated using a standard MATLAB Fourier transform routine and amplitude to frequency conversion factor mentioned above.

4.3.2 Results

The frequency noise PSD measured for the unperturbed laser is presented in Figure 4.10 (a). The intensity noise is obtained by repeating the measurement procedure

without a frequency discriminator, while the detector noise is obtained simply by blocking the laser beam. The lineshape of the unperturbed laser is computed, using Equations 4.6 and 4.7, and shown in Figure 4.10 (b). The integration was performed employing a low frequency cutoff of 200 Hz, which corresponds to an observation time of 5 ms, in order to be consistent with the exclusion of flicker noise.[98] In the unperturbed case, the calculated laser lineshape has a FWHM of 460 ± 40 kHz, which is in reasonable agreement with the width extracted from the Lamb-dip measurements. The two sidebands separated from the central line by *ca.* 1.5 MHz could be a result of the frequency noise that follows the β-separation line between 100 kHz and 400 kHz, which could cause leaking of power to the wings of the lineshape. Again, the lineshape is best fit by a Lorentzian function with a smaller Gaussian contribution, consistent with the Lamb-dip observations.

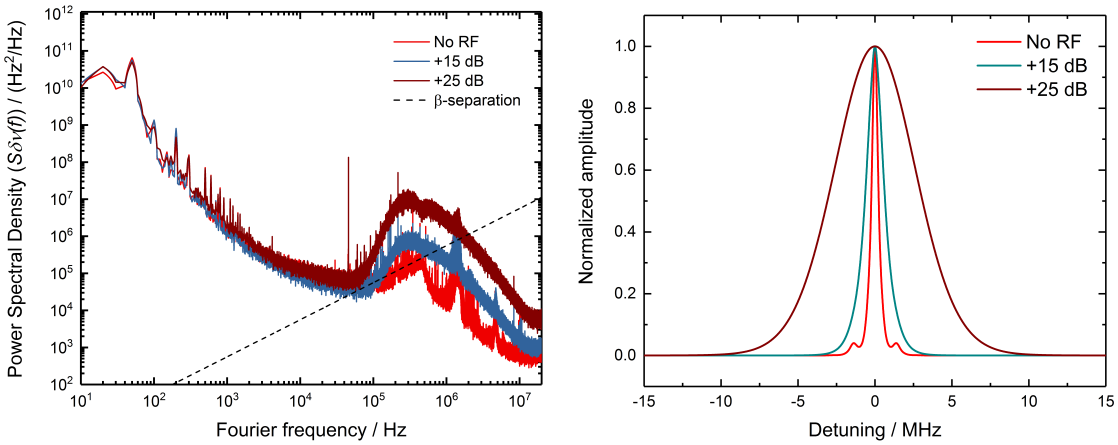


(a) (b)

Figure 4.10: (a) Frequency noise PSD, $S_{\delta\nu}(f)$, measurement of the unperturbed laser, along with the intensity noise and detector noise PSDs. The β-separation line separates the high and low frequency regimes at the point of intersection with the PSD; (b) Laser lineshape simulated via the frequency noise PSD spectrum presented in (a).

Figure 4.11 (a) shows how the optical PSD of the unperturbed laser is modified by RF current perturbations, producing an increase in frequency noise up to a factor of 100 centered at 300 kHz. The resulting lineshapes are presented in Figure 4.11 (b). The Lorentzian-like lineshape of the unperturbed laser quickly evolves to become

more Gaussian once the injection current is perturbed by RF noise, following the same trend as the Lamb-dip measurements. The evolution of the linewidth as a function of RF gain level is presented in Figure 4.12, showing a steady linewidth increase up to 6.26 ± 0.34 MHz at +25 dB gain.



(a) (b)

Figure 4.11: (a) Frequency noise PSD measured for a range of RF perturbation gains; (b) Laser lineshapes simulated via the frequency noise PSD spectra presented in a) for a range of RF perturbation gains.

As previously mentioned, the linewidth measured via Lamb-dip spectroscopy has a lower limit of observation time of 11.5 μs. To simulate the lineshape at the same observation time using the PSD, a low frequency cutoff of *ca.* 100 kHz would have to be implemented. In the unperturbed case, imposing such a limit causes problems due to its close proximity to the low modulation index region. However, as RF noise is added, higher frequencies will enter the high modulation index region as they move above the β-separation line, allowing the 100 kHz cutoff to be implemented in data above +15 dB gain. A comparison between the linewidth with a 200 Hz or a 100 kHz cutoff at $>$ +15 dB revealed only a negligible change in the FWHM. Such comparison is not possible in the unperturbed case for the reason mentioned above. However, using the approximation presented in Equation 4.8, an approximate linewidth in the unperturbed case can be obtained by integrating the frequency noise using a low

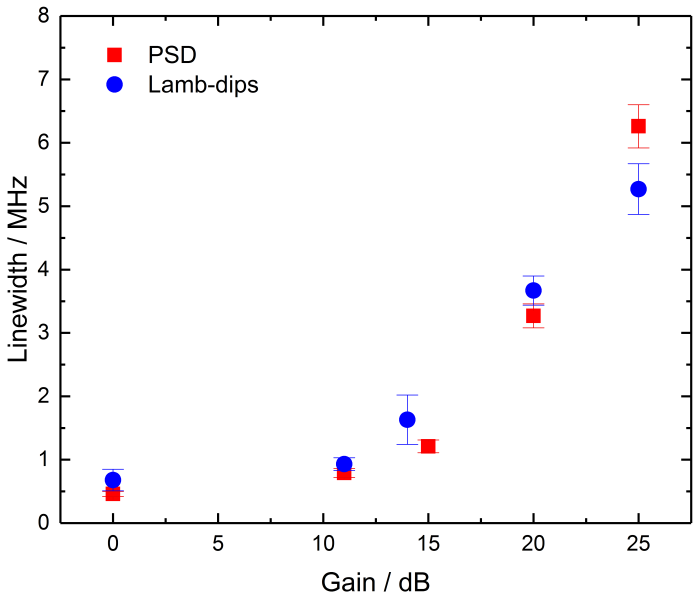


Figure 4.12: Laser linewidths for unperturbed and perturbed injection currents as measured by the two distinct techniques.

frequency cutoff of 100 kHz; a linewidth of $\sim$ 500 kHz is thus obtained. This is in good agreement with both the linewidth of 460 $\pm$ 60 kHz acquired through the Fourier transform method using a 200 Hz cutoff, as well as with the Lamb-dip observations. From this, it can be concluded that the linewidth of the QCL with a 5 ms observation time is nearly identical to that with a 11.5 μs observation time, since the frequency noise drops below 10^6 (Hz^2/Hz) at 1 kHz Fourier frequency, corresponding to an observation time of 1 ms.

Using the PSD rather than Lamb-dip spectroscopy for measuring laser linewidths has the clear advantage of allowing the computation of the linewidth at different observation times by adjusting the low frequency cutoff of integration, while only requiring a single measurement. However, both techniques reveal that the QCL linewidth can be reliably tuned within the range of a few MHz by simply adjusting the level of RF current perturbation.

4.4 Self-heterodyne method

4.4.1 Background and experiment

In this section, the self-heterodyne method, an established technique for linewidth measurements of telecommunication semiconductor lasers first developed by Okoshi *et al.* is extended to QCLs.[113] The technique measures the phase noise of an optical field by employing a Mach-Zehnder type interferometer to convert an optical field's phase noise into intensity noise.[111] The name of the technique originates from its use of a single radiation source and a beamsplitter to create two separate beam paths that are then subsequently recombined to produce a beat signal. One of the paths includes an acousto-optic modulator (AOM) that induces a frequency shift, Ω, to the beam that traverses it, while the other path contains an optical delay line that introduces a time delay, τ_d, between the two beams. These two *arms* of the experiment are depicted in Figure 4.13 as 1 and 2 (frequency shift and time delay, respectively).

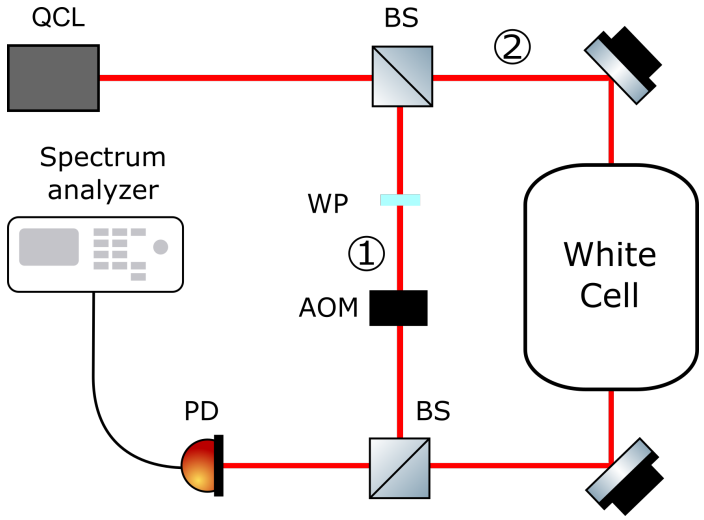


Figure 4.13: Experimental setup of the self-heterodyne interferometer. BS - 50/50 Ge beamsplitters; WP - 1/2 Waveplate; AOM - Acousto-optic modulator; PD - photodiode. The total path length added by the White cell is 20 m. The beam path that contains the AOM is referred to as the *AOM arm* while the beam path that contains the White cell is referred to as the *cell arm*.

The self-heterodyne experiment was performed using the same DFB-QCL system

as the other experiments described in this chapter, operated at approximately the same temperature and current conditions as mentioned above. The beam is split by a 50/50 Ge beamsplitter, and the transmitted part is passed through a White cell which introduces a path length difference of 20 m, while the reflected part of the beam is frequency shifted by 50 MHz by an AOM (Isomet AOM (1208-6-4M)). The frequency shifted and the time delayed beams are then recombined at a second 50/50 Ge beamsplitter and collected by a 1 GHz bandwidth AC coupled photodiode. The power spectral density of the beat signal is then monitored using a spectrum analyser (HP 4395A).

When the two arms of the interferometer, labelled 1 and 2 in Figure 4.13, are recombined, the total electric field incident on the detector, E_T, is the sum of both electric fields:[110,114,115]

$$E_T = E_1(t) + E_2(t) = E_0 e^{i\Omega t} + \alpha E_0(t + \tau_d), \tag{4.9}$$

where α is a factor that accounts for the fact that the two fields may have different amplitudes. As mentioned previously, the phase or frequency fluctuations are converted into intensity fluctuations that generate a photocurrent that depends only on the intensity correlation of the laser field, given by:

$$G^{(2)}_{E_T}(\tau) = \langle E_T(t) E^*_T(t) E_T(t+\tau) E^*_T(t+\tau) \rangle. \tag{4.10}$$

Here, τ is the lag between the total electric fields. The combination of Equation 4.9 with Equation 4.10 yields the following autocorrelation function, after simplification, for a white frequency noise dominated spectrum:[110]

$$G^{(2)}_{E_T}(\tau) = E_0^4 \Big[(1+\alpha^2)^2 + 2\alpha^2 \cos(\Omega\tau) e^G \Big], \quad G = \begin{cases} -S_0 \tau_c, & \text{if } \tau_c < \tau_d \\ -S_0 \tau_d, & \text{if } \tau_c > \tau_d \end{cases}, \tag{4.11}$$

where τ_c is the coherence time of the laser. S_0 is the white noise (flat) spectrum and thus a constant that is related to the coherence time of the laser. The Fourier transform of this auto-correlation function is the observable measured via the self-heterodyne method. An analytical expression can be used for modelling the observed self-heterodyne signal in this (white noise only) case:

$$S(\omega) = (1+\alpha^2)^2\delta(\omega) + 2\alpha^2 e^{-S_0\tau_d}\delta(\omega-\Omega) + 2\alpha^2\frac{2S_0}{(S_0)^2+(\omega-\Omega)^2}\times \left[1 - e^{-S_0\tau_d}\Big(\cos[(\omega-\Omega)\tau_d] + \frac{S_0}{\omega-\Omega}\sin[(\omega-\Omega)\tau_d]\Big)\right]. \tag{4.12}$$

The observed self-heterodyne spectrum is thus highly dependent on both τ_c and τ_d. If $\tau_c > \tau_d$, the phases of the fields of both arms are partially correlated and the spectrum presents a delta function feature at the AOM modulation frequency, Ω. Conversely, if $\tau_c < \tau_d$ the power shifts from the delta function to the Lorentzian shaped pedestal until the spectrum becomes fully Lorentzian.[114] In the latter case, if the spectrum consists only of a Lorentzian, the linewidth can be extracted directly from the HWHM at -3 dB. To illustrate this dependence on τ_c and τ_d, Figure 4.14 shows simulations of the output of the self-heterodyne interferometer as a function of delay arm length. The simulations are obtained by performing a numerical Fourier transformation of Equation 4.11.

Although not including the significant $1/f$ contribution to the QCL frequency noise spectrum, Equation 4.11 highlights the main impediment to using the self-heterodyne technique to measure the linewidth of QCLs. With laser linewidths of the order of a few MHz or less, prohibitively long optical delay lines (in the mid-IR), of the order of $>$ 300 m are necessary to approach the $\tau_c < \tau_d$ regime. In this work, despite operating in a regime where $\tau_c \gg \tau_d$, the self-heterodyne spectra show a pedestal that is not predicted by the model presented in this section.

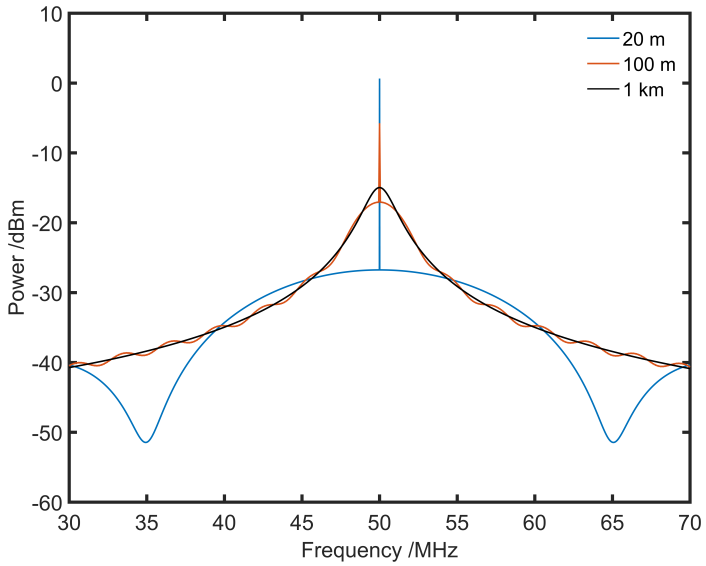
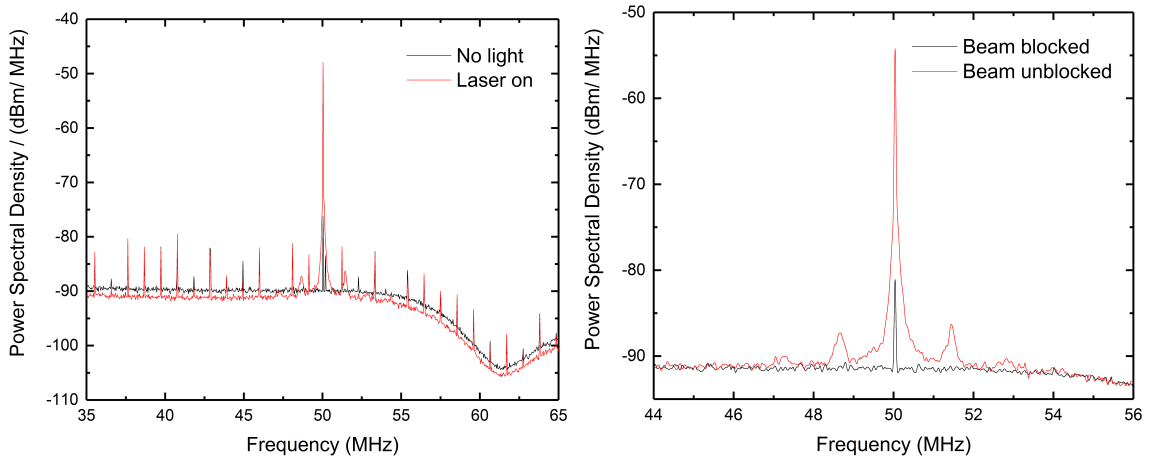


Figure 4.14: Output of the self-heterodyne technique simulated by performing a numerical Fourier transformation of Equation 4.11. A linewidth of 1 MHz was used, and the simulation was repeated for 20 m, 100 m and 1 km delay arms with $\Omega = 50$ MHz in all cases. The sharp feature at the centre of the spectrum disappears as the path length of the delay arm increases, as expected.

4.4.2 Results

Figure 4.15 show the PSD obtained via the self-heterodyne beat of the laser in unperturbed operation. The spectra are the result of 20 averages obtained over *ca.* 1 minute. The data presented in Figure 4.15 (b) is the same as that presented in (a), after the removal of the sharp periodic artefacts with a MATLAB routine. These artefacts, which were present in all spectra, are a consequence of detector noise. The baseline slope observed in (b) is caused by the drop in the spectrum analyser response at *ca.* 62 MHz, as evidenced in (a), by its persistence when the light is blocked.

A path length difference of 20 m between the cell arm and the AOM arm introduces a time delay of 67 ns between the two beams. Comparing this with the coherence time of the laser of 2 μs, assuming an unperturbed linewidth of the order of 500 kHz, it is evident that because $\tau_c \gg \tau_d$ the two waves are still largely correlated. Consequently, the PSD of the beat signal returns a sharp feature at 50 MHz that corresponds to the AOM driving frequency and thus the frequency difference between the two waves.



(a) (b)

Figure 4.15: (a) Optical emission PSD measured by the self-heterodyne method, and background signal obtained simply by blocking the light to the detector - both of these before a MATLAB post-processing routine; (b) Same spectra as (a), after post-processing.

When one or both arms are blocked, the residual feature that remains at 50 MHz as seen in Figure 4.15 (b) is caused by the pick-up of the AOM driving frequency by the electrical equipment.

The present mathematical model shows limitations for investigating self-heterodyne signals with $\tau_c \gg \tau_d$, thus it is impossible to extract a linewidth from the spectra in Figure 4.15 through simulations. However, sideband-like features appear at *ca.* 1.3 MHz either side of the AOM carrier frequency, consistent with the simulation of the free-running laser linewidth shown in section 4.3. Such features are the result of noise present at frequencies above $1/\tau_d$ ($\sim$ 15 MHz), that exceed the detection bandwidth of 20 MHz of the system used in the previous section. Figure 4.16 reveals that these sidebands broaden and eventually merge as RF current noise is mixed with the laser driving current, suggesting that the laser is responsive to current fluctuations at frequencies $>$ 15 MHz. The HWHM at -3 dB of these signals at +20 dB RF noise gain, however, returns a value of $<$ 1 MHz; much smaller than the value obtained using the other techniques. This is a consequence of the rejection of a large portion of the

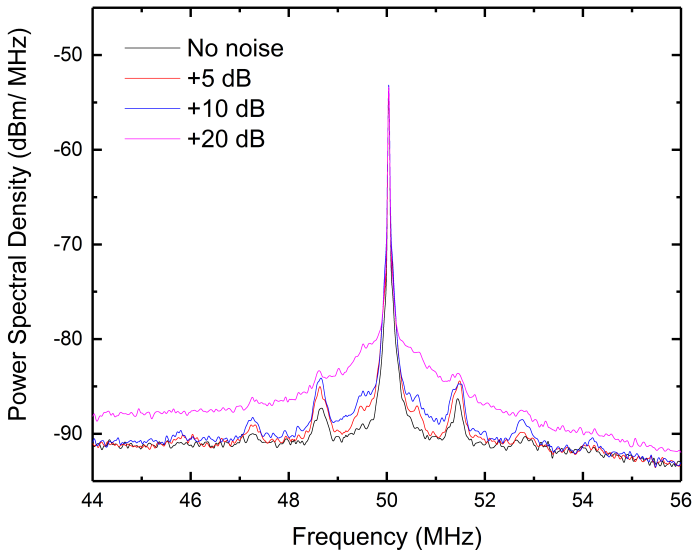


Figure 4.16: Comparison between the self-heterodyne PSD with different noise injection gains. As RF noise is injected the spectral features observed around 50 MHz broaden, consistent with the linewidth broadening quantified earlier in this chapter.

noise spectrum at < 15 MHz.

For comparison Figure 4.17, shows the self-heterodyne beat of the unperturbed laser obtained by removing the bias-tee. The smoother, sideband free spectrum indicates that the mathematical model presented for linewidth measurements via the self-heterodyne method may not have $\tau_c < \tau_d$ as an essential requirement. More theoretical studies would be required to devise a model that incorporates such experimental conditions, but it remains interesting that the -3 dB width of the pedestal is of the order of a few hundred kHz, which is in reasonable agreement with the linewidth measurements performed with the two previous methods.

Although it was not possible to quantitatively determine the linewidth of a QCL via the self-heterodyne method due to short delay lines and relatively high coherence times, the method provided an insight into the response of the system to high frequency current fluctuations and how it was affected by RF current noise. It also opens the door to further investigation in this $\tau_c \gg \tau_d$ regime, as the result in Figure 4.17 defies the predictions of the current mathematical model.

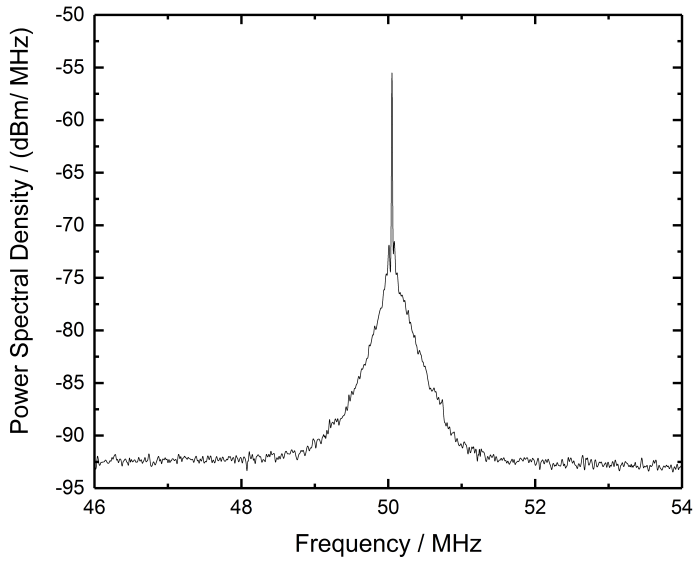


Figure 4.17: Self-heterodyne PSD without RF current perturbations and without the bias-tee. A pedestal with a -3 dB HWHM of a few hundred kHz is present, as well as a sharp feature at 50 MHz that results from residual coherence between the delay arm and the frequency shift arm.

The self-heterodyne technique is more readily applicable in the near-IR, where long delay lines are possible due to the availability of low loss optical fibre. This is demonstrated by the self-heterodyne measurements shown in Figure 4.18. These were obtained with a DFB laser diode (NEL NLK1U5EAAA) operating at 1654 nm with a 1 km optical fibre delay line and frequency shift of 80 MHz. No sharp feature is observed at 80 MHz, indicating that the beams of both arms of the experiment are not correlated. A linewidth of *ca.* 1.7 MHz is determined from the -3 dB HWHM. This linewidth is broadened up to *ca.* 10 MHz with +40 dB RF current noise.

These measurements show that the self-heterodyne method has been successfully implemented and is adequate for measuring both the linewidth of near-IR laser diodes, and the broadening caused by RF noise current perturbations in these systems. Although a definitive measurement of the unperturbed QCL linewidth through this method was not achieved, the similarity between the measurement shown in Figure 4.17 and Figure 4.18 is encouraging, and opens doors for further investigation of this technique as an alternative QCL linewidth measurement method.

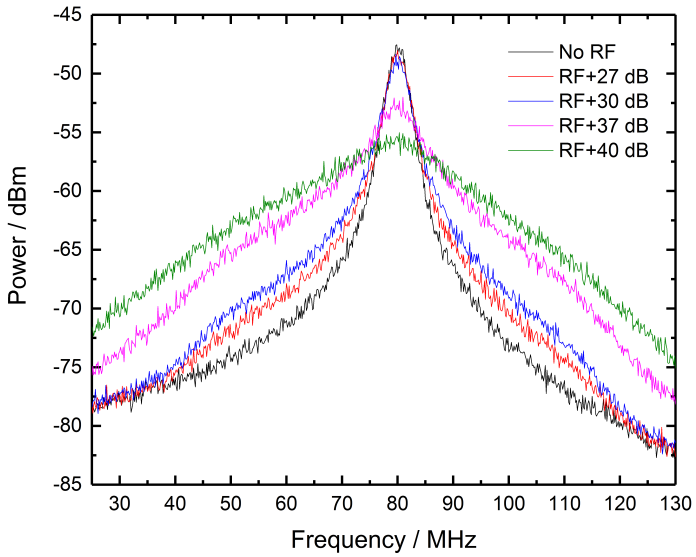


Figure 4.18: Self-heterodyne linewidth measurements performed on a DFB laser diode operating at 1654 nm with a 1 km optical fibre delay line and a frequency shift of 80 MHz. Self-heterodyne spectra of the same system under RF current perturbations are also shown.

4.5 Conclusions

The linewidth of a DFB-QCL can be reproducibly measured using both the Lamb-dip and frequency noise PSD techniques and modified by perturbing the injection current with RF noise. The extent of broadening has been quantified through both these methods. A drawback of using Lamb dip spectroscopy is that in order to measure the laser linewidth at a different observation time, the laser chirp rate has to be changed and a new set of experiments is needed, while a single noise PSD measurement is enough for simulating the lineshape at a variety of observation times simply by changing the low frequency cutoff. A third technique, known as the self-heterodyne method, was used to determine the linewidth of the QCL. The coherence time of the laser greatly exceeded the delay time, and thus according to the current mathematical models the linewidth of the laser cannot be directly extracted this way. Interestingly, a -3 dB HWHM of a few hundred kHz was observed in the self-heterodyne measurements of the free-running laser, consistent with the Lamb-dip and

PSD measurements, and shows promises that this method may become applicable to QCLs in the near future. The self-heterodyne technique was also sensitive to the injection of RF noise to the laser current. The ability to tune the laser linewidth is of great use as a sensitivity enhancement method in OA-CEAS based trace gas sensors.

Chapter 5

Coherent transient spectroscopy with cw-QCLs

In the previous chapter, the frequency noise spectral density and linewidth of a single mode DFB-QCL were quantified, showing that the device has a sufficient spectral purity to make it a good source for mid-IR high-resolution spectroscopy and nonlinear optics. This chapter is concerned with nonlinear optical effects induced in low-pressure samples of nitric oxide by high power cw-QCLs, namely coherent transients. Such studies find potential applications in the investigation of fundamental processes of light-matter interaction or for the preparation of molecules in selected excited states.[116] The latter may be used to gain an insight into a number of physical properties of molecular systems such as collision induced relaxation and sample polarisation loss. Two sets of experiments will be presented: the first set explores nonlinear effects induced by a single QCL, while the second will focus on the observation of coherent properties when probing a velocity selected sample in a 2 QCL pump and probe experiment. A model based on the optical Bloch equations will be used to simulate the time evolution of the coherence of a two photon coherent transient signal.

5.1 Introduction

Coherent transient effects were first seen in nuclear magnetic resonance (NMR), prior to being observed in the optical region. In NMR, these effects were described as spin echoes upon the application of high power radiofrequency pulses by Hahn in 1950.[117] In the optical domain, analogous effects were observed in the form of optical nutation and free induction decay (FID). The former is the cycling of *population* between two states that are coupled by a coherent electromagnetic field, otherwise known as Rabi cycling. Conversely, free induction decay in the optical region results from the interaction between the electromagnetic field driving a transition and the macroscopic *polarisation* induced in the medium by the same field. These two effects are concurrent, and hence coherent transient spectroscopy may be defined as the observation of the influence on an electromagnetic field of a coherently created transient population and polarisation.[118]

The early studies of optical coherent transient effects relied on rapidly chirping a molecular transition out of resonance with an optical field by using the Stark effect. Such experiments were realised by Brewer and Shoemaker, who used a CO_2 laser (operating at $\sim$ 10 μm) to probe NH_2D and $^{13}CH_3F$ transitions that were rapidly swept off resonance.[119] Frequency tunable lasers were later employed by Genack and Brewer to produce the same coherent effects.[120] Here, the frequency of a cw dye laser was chirped through transitions in I_2 vapour, using the resulting coherent effects to investigate elastic and inelastic collision mechanisms. With the development of frequency swept semiconductor lasers, Li *et al.* observed FID in the near-IR in a low pressure sample of Rb.[121]

Coherent transient effects have also been studied in the mid-IR by using cw-QCLs, due to their high power and tunability. Examples include the observation of coherent structures in OCS by McCormack *et al.*, using a QCL operating at 10 μm, or in velocity selected samples of NO by Walker and Kirkbride *et al.*, employing the same

5 μm QCLs used in this work in a pump-probe configuration.[122–124] Moreover, pulsed QCLs capable of achieving higher chirp rates of the order of MHz ns^{-1} have also been used to study coherent transient effects in N_2O, NO and ethylene by Duxbury *et al.*[90,91,125]

In this work, coherent transient effects will be induced in low pressure samples of NO using both current pulses, slower frequency sweeps, and optical pulses prepared using an AOM. In the context of this chapter, the FID signals will be referred to as *rapid passage* (RP) signals, since their occurrence relies on the condition that the laser field is swept through resonance on a timescale that is short compared to the relaxation time of the system. The theory regarding the physical nature of these coherent transient effects will be outlined in the next section, and the experimental data compared to a model developed by Kirkbride *et al.*[124] This model will be used to describe the time evolution of system coherence as a function of physical parameters such as the laser intensity, frequency chirp rate and the total pressure of the absorber.

5.2 Theory

The coherent transient effects presented in this chapter are the product of the interaction of the laser electric field with a macroscopic polarisation induced in low pressure samples of NO. The theoretical framework that describes the time evolution of this type of system was initially formulated by Bloch to describe the analogous FID structures observed in NMR, and was later adapted to the optical regime.[126,127]

Consider a two level system, with a lower state $|1\rangle$ and an upper state $|2\rangle$, coupled by a coherent driving field $\boldsymbol{E}$. The equations that describe the time evolution of the

population and the macroscopic polarisation of this system, known as the Maxwell-Bloch equations, are:[126,128]

$$\dot{\rho}_{11} = i(\Omega\rho_{21} - \Omega^{\rho}_{12}) + \frac{\rho_{22}}{T_1}, \tag{5.1a}$$

$$\dot{\rho}_{22} = i(\Omega^{\rho}_{12} - \Omega\rho_{21}) - \frac{\rho_{22}}{T_1}, \tag{5.1b}$$

$$\dot{\rho}_{12} = i\Omega(\rho_{22} - \rho_{11}) - i\Delta\rho_{12} - \frac{\rho_{12}}{T_2}. \tag{5.1c}$$

Here, $\Omega = \mu_{21}E_0/\hbar$ is the Rabi frequency,[33] where μ_{21} is the transition dipole moment and E_0 is the magnitude of the driving electric field, and $\Delta = \omega - \omega_{21}$ is the detuning from the $|1\rangle \rightarrow |2\rangle$ transition frequency. T_1 and T_2 are the longitudinal and transverse relaxation times of the sample polarisation, respectively. The variables denoted as ρ_{mn} are the elements of the density matrix representation of the system, which takes the form:

$$\boldsymbol{\rho} = \begin{pmatrix} \rho_{11} & \rho_{12} \\ \rho_{21} & \rho_{22} \end{pmatrix}. \tag{5.2}$$

The diagonal elements, ρ_{mm}, are the probability of the system being in the state $|m\rangle$, whereas the off-diagonal elements of the matrix give the coherence between the levels of the system.

A new set of variables is introduced to describe the system in terms of the real and imaginary parts of the coherence and the population inversion: $u = \rho_{21} + \rho_{12}$, $v = i(\rho_{21} - \rho_{12})$ and $w = \rho_{22} - \rho_{11}$, respectively. A new set of differential equations based on these variables can thus be written :[24]

$$\dot{u} = \Delta v - \frac{u}{T_2}, \tag{5.3a}$$

$$\dot{v} = 2\Omega w - \Delta u - \frac{v}{T_2} \tag{5.3b}$$

$$\dot{w} = -\frac{(w - w_{eq})}{T_1} - 2\Omega v, \tag{5.3c}$$

where w_{eq} is the population inversion at equilibrium. These variables obey the conservation law $u^2 + v^2 + w^2 = 1$. This system of differential equations can be used to create a pictorial description of the time evolution of both the coherence and the population inversion with a Bloch sphere (see Figure 5.1). To better describe the time

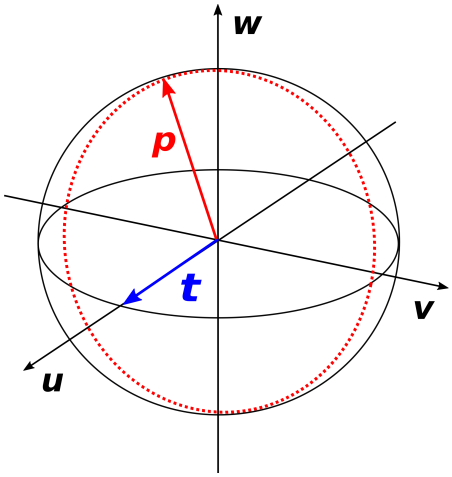


Figure 5.1: Bloch sphere representation of the coherence and population inversion of a two level system, coupled by a resonant field, as a function of time. The blue vector represents the torque that is applied to the system, while the red vector corresponds to the macroscopic polarisation and population inversion induced in the sample. The dashed line represents the path traced by the vector $\boldsymbol{p}$ on the surface of the sphere, and thus the time evolution of the system.

evolution of the system, consider a torque vector, $\boldsymbol{t}$, that symbolises an on-resonance field driving the $|1\rangle \rightarrow |2\rangle$ transition (shown in blue in Figure 5.1). Along with it, a vector that represents the macroscopic polarisation and population inversion of the sample $\boldsymbol{p} = u(t)\hat{i} + v(t)\hat{j} + w(t)\hat{k}$ is shown in red. The time evolution of the system, described by its equation of motion, is thus a cross product:

$$\dot{\boldsymbol{p}} = \boldsymbol{t} \times \boldsymbol{p}. \tag{5.4}$$

The time evolution of the vector $\boldsymbol{p}$, $\dot{\boldsymbol{p}}$, is represented in Figure 5.1 as the red circle

traced on the surface of the sphere due to the action of the torque vector $\boldsymbol{t}$.

In the case of a three level system in a pump and probe configuration ($|1\rangle \rightarrow |2\rangle \rightarrow |3\rangle$), as will be shown later (see Figure 5.12), the set of equations that describe the time evolution of the coherence and population inversion, equivalent to 5.1, are as follows:[129]

$$\dot{\rho}_{11} = \frac{i\Omega_{12}}{2}(\rho_{12} - \rho_{21}) + \rho_{22}\gamma_{22}, \tag{5.5a}$$

$$\dot{\rho}_{22} = \frac{i\Omega_{12}}{2}(\rho_{21} - \rho_{12}) + \frac{i\Omega_{23}}{2}(\rho_{23} - \rho_{32}) - \rho_{22}\gamma_{22}, \tag{5.5b}$$

$$\dot{\rho}_{33} = \frac{i\Omega_{23}}{2}(\rho_{32} - \rho_{23}) - \rho_{33}\gamma_{33}, \tag{5.5c}$$

$$\dot{\rho_{12}} = -i(\Delta_{12} - i\gamma_{12})\rho_{12} + i\Omega_{12}(\rho_{22} - \rho_{11}) - i\rho_{13}\Omega_{32}, \tag{5.5d}$$

$$\dot{\rho_{23}} = -i(\Delta_{23} - i\gamma_{23})\rho_{23} + i\Omega_{23}(\rho_{33} - \rho_{22}) + i\rho_{13}\Omega_{21}, \tag{5.5e}$$

$$\dot{\rho_{13}} = -i(\Delta_{12} + \Delta_{23} - i\gamma_{13})\rho_{13} + i\Omega_{12}\rho_{23} - i\rho_{12}\Omega_{23}. \tag{5.5f}$$

In these equations, the γ_{mn} ($m \neq n$) and γ_{mm} represent the decoherence between levels and the population decay, respectively. The latter can be neglected since the population decay process is several orders of magnitude longer than the decoherence time. Ω_{12} and Δ_{12} are the pump field Rabi frequency and detuning from resonance, while Ω_{23} and Δ_{23} are the Rabi frequency and the detuning of the probe field. The set of equations in 5.5 will be used to model a three-level rapid passage signal obtained experimentally in section 5.4.2; before that, a description of the experimental setup is provided in the following section.

5.3 Experimental

Figure 5.2 shows a schematic representation of the experimental configuration. Two sets of experiments will be presented in this chapter. These are two colour studies that utilise both the EC-QCL (Daylight Solutions 21052-MHF) and the DFB-QCL

(Maxion M575AH-NS) shown, and single colour studies in which only the DFB-QCL is used. All experiments, unless stated otherwise, are conducted in a multi-pass cell comprised of four planar mirrors, based on the design developed by Linnartz *et al.*,[130] with a total path length of 332 cm. The cell is fitted with a turbo-molecular pump (Turbovac 361c) and is able to achieve background pressures < 1 mTorr. In the

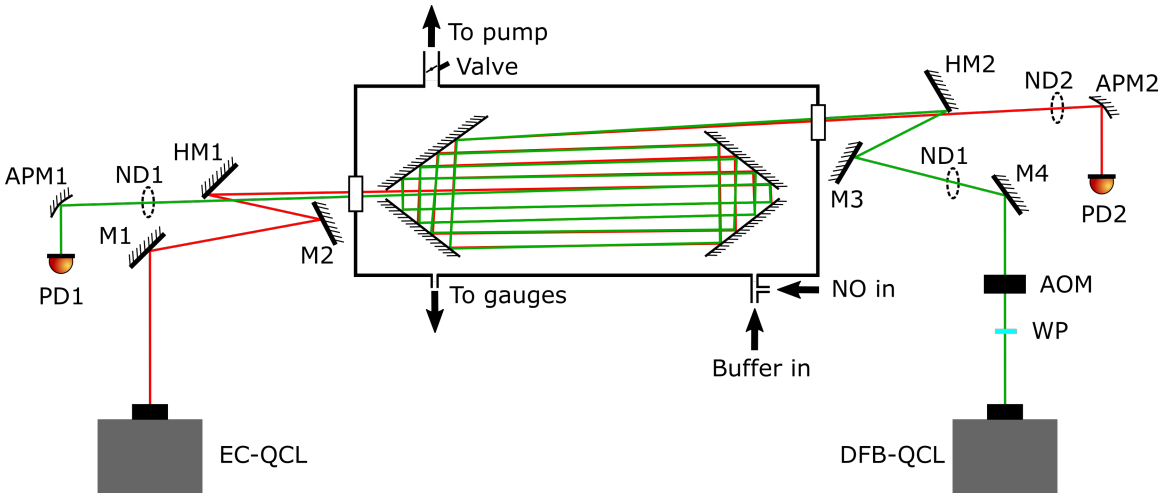


Figure 5.2: Schematic diagram of the experimental setup used for the experiments described in this chapter. APM1 and APM2: Parabolic mirrors 1 and 2; M1-M4: Beam steering mirrors; HM1 and HM2: Half-mirrors 1 and 2; PD1 and PD2: Photodiode 1 and 2; AOM: Acousto-optic modulator; WP: Waveplate ($\lambda/2$); ND1 and ND2 are neutral density filters aimed at attenuating the pump and probe beams before these reach the detectors. Both neutral density filters were placed after the multi-pass cell, unless stated otherwise. The half mirrors were used in order to reduce the crossing angle and thus maximise the spatial overlap between the counter-propagating beams. The multi-pass cell represented has a total path length of 332 cm. Where specified, a 72 cm single-pass cell was used instead.

two colour case, the beams counter-propagate in the cell with a small crossing angle ($< 0.2°$) and are collected by the photodiodes PD1 and PD2 (VIGO PVMI-3TE-10.6 and VIGO PVMI-2TE-6, respectively). The DFB-QCL beam is passed through an acousto-optic modulator (AOM) (see Chapter 2), and the first order beam used in all the experiments. The frequency of the DFB-QCL is scanned by applying a voltage ramp to an in-house built low noise driver using a function generator (TTi TG330). Conversely, the frequency of the EC-QCL is swept by applying a voltage ramp to a

piezoelectric transducer (PZT) that controls the position of the diffraction grating within the laser external cavity. The total gas pressure is regulated by keeping a constant flow using two mass-flow controllers (MFCs, Tylan FC-260) and adjusting the pumping speed with a butterfly valve. One of the MFCs is connected to a cylinder of 100% NO, while the other is connected (when applicable) to a selected buffer gas cylinder (all gases supplied by BOC gases). The data are recorded using a digital oscilloscope (LeCroy WaveSurfer 44 MXs-A) and all post-processing and averaging routines are performed using custom MATLAB code.

5.4 Results

5.4.1 Coherent optical effects with a single QCL

All single laser experiments described in this section were performed using the DFB-QCL. Figure 5.3 shows an example (single-sweep) transmission spectrum obtained by scanning over the $R(6.5)_{1/2}$ $v = 1 \leftarrow 0$ transition of NO, with a chirp rate of 0.7 MHz μs^{-1}, a scan rate of 40 Hz, a total pressure of NO of 5 mTorr and a laser power of 120 mW. The spectrum presents a doublet structure since the frequency splitting between the e and f components of this transition is 331 MHz, larger than the Doppler width of NO at room temperature ($\sim$ 125 MHz). The undulatory structure seen in the baseline is the result of a small etalon caused by stray reflections inside the multi-pass cell. This etalon did not constrain the observation of the nonlinear coherent effects described in this chapter.

A significant increase in signal fluctuation is observed when the laser approaches resonance with transitions from either Λ-doublet component of the $\Omega = 1/2$ transition manifold. This effect can be clearly identified by comparing the standard deviation of the signal measured while keeping the laser on resonance with the e component transition, on the side of the same transition or off resonance, as is shown in Figure 5.4

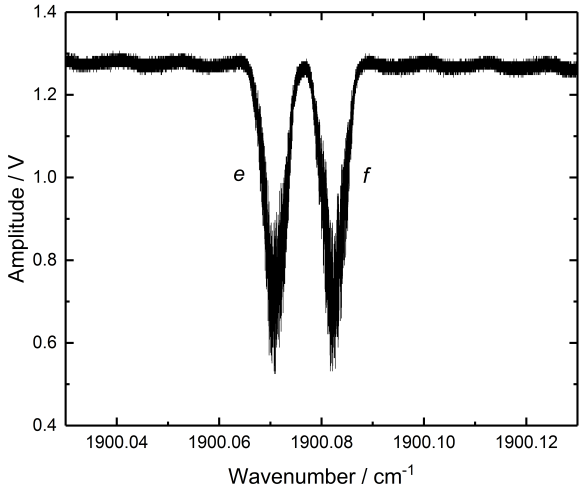


Figure 5.3: Transmission spectrum of the $R(6.5)_{1/2}$ $v = 1 \leftarrow 0$ transition of NO. The spectrum was not averaged in order to highlight the difference between the baseline noise and the noise at the centre of each Λ-doublet component of the $R(6.5)_{1/2}$ transition.

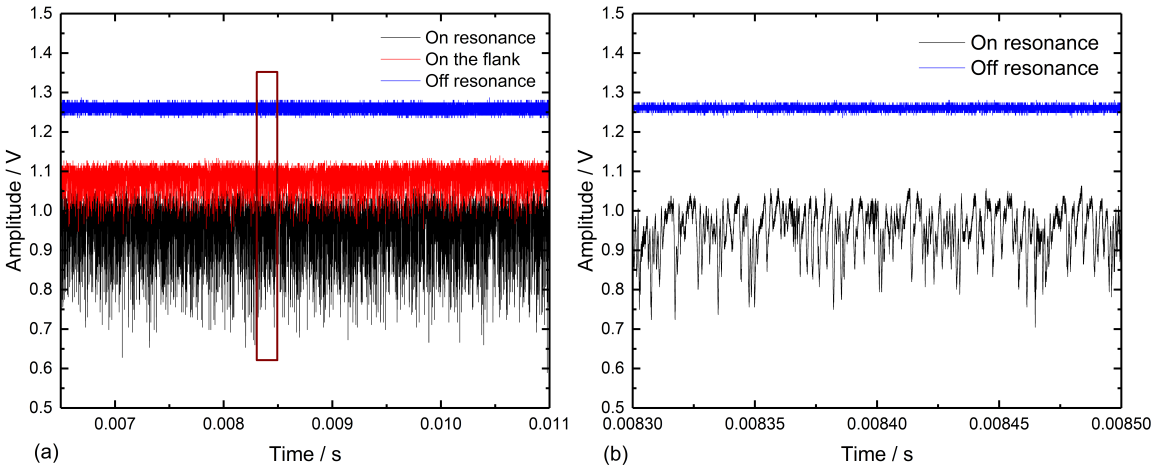


Figure 5.4: (a) Multi-pass cell transmission as the laser frequency is kept on resonance, on the flank and off resonance with the e component of the R(6.5) $v = 1 \leftarrow 0$ transition of NO. A zoomed in section of (a) is shown in (b), showcasing the random "dipping" structure of the noise induced by resonance.

(a); the amplitude normalised standard deviation of the fluctuations, σ_n, is 6.1×10^{-2} V, 2.1×10^{-2} V and 4.9×10^{-3} V, respectively. A possible explanation for the difference in σ_n of over an order of magnitude when the laser is on resonance, would be the conversion of laser frequency noise to intensity noise, similar to the work shown in the previous chapter. However, this is not the case since fluctuations caused by frequency noise conversion would be more prominent on the side of the transition where $(\mathrm{d}I/\mathrm{d}\nu)$ is largest. These fluctuations have a different origin and will hereafter be referred to as *on-resonance fluctuations*.

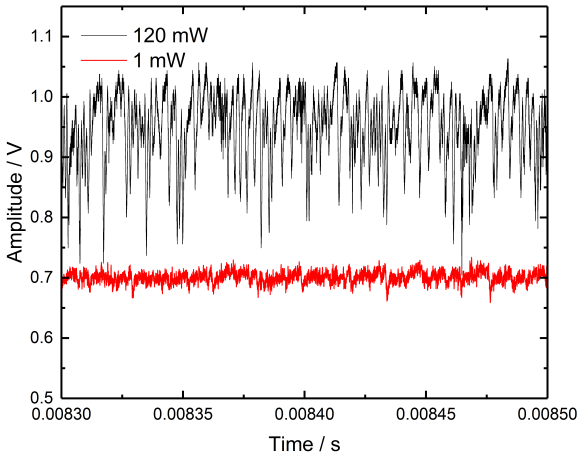


Figure 5.5: Comparison of the sample transmission when the laser is resonant with the e component of the $\mathrm{R}(6.5)_{1/2}$ $v = 1 \leftarrow 0$ transition of NO, with optical powers of 120 mW and 1 mW.

To investigate the cause of these fluctuations, the beam entering the cell was attenuated using a reflective ND filter (Thorlabs NDIR20B) that reduced the laser power from 120 mW to *ca.* 1 mW. The laser was then tuned to the e component of the $\mathrm{R}(6.5)_{1/2}$ transition and the transmission was measured. The result is shown in Figure 5.5. The reduction of σ_n from 6.1×10^{-2} V with 120 mW to 1.3×10^{-2} V with 1 mW reveals that these on-resonance fluctuations are dependent on the laser power, which is consistent with a nonlinear response of the medium. Furthermore, the suppression of on-resonance fluctuations can also be achieved by increasing the chirp rate of the laser, as shown in Figure 5.6. In this case, on-resonance fluctuations

are removed by essentially low-pass filtering; the spectrum is recorded at the same sample rate, but the frequency of the laser is swept faster.

To further investigate the influence of the laser power on this sample of low pressure NO, consider the absorbance spectra of the $R(6.5)_{1/2}$ transition, obtained at a total pressure of 5 mTorr and laser powers of 1 and 120 mW, shown in Figure 5.6. The absorbance at the line centre of either Λ doublet component in the 1 mW spectrum is 0.77 ± 0.01, in good agreement with the maximum absorbance of 0.73 predicted via the Beer-Lambert law, using the cross-sections available in the HITRAN database.[65] A spectrum of the same transitions with a laser power of 120 mW is recorded at a faster chirp rate in order to remove the on-resonance fluctuations for clarity. A reduction in absorbance of approximately 10% between the 1 mW spectrum and the 120 mW spectra is observed. This reduction is due to optical saturation.

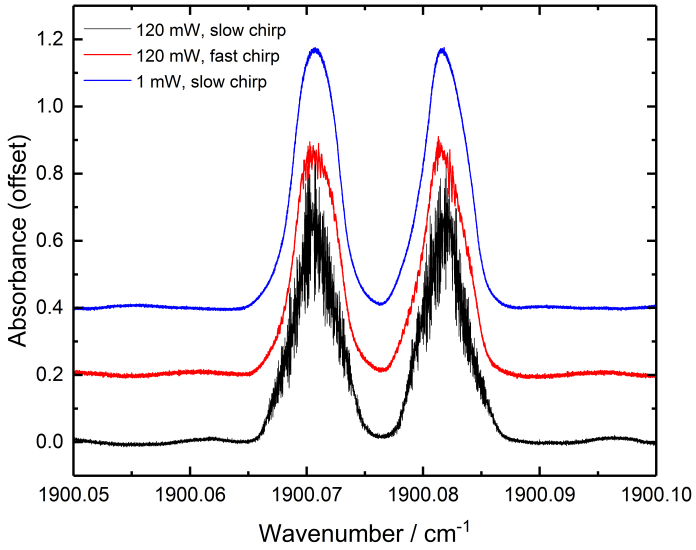


Figure 5.6: Direct absorption spectrum of the $R(6.5)_{1/2}$ transition of the NO fundamental band taken at different laser powers and chirp rates. The total pressure of NO was 5 mTorr, and the chirp rates used were 0.9 MHz μs^{-1} and 3.4 MHz μs^{-1}. The absorbances of the faster chirp rate and lower power spectra are offset 0.2 and 0.4, respectively, for clarity.

While the reduction of the absorbance of the sample (or the increase of the transmitted intensity) is explained by optical saturation, the on-resonance fluctuations are

not. To test if these are caused by coherent effects, the high power spectra are investigated by keeping the laser on resonance with the $R(6.5)_{1/2}$ transition for a time period > 20 μs, and subsequently tuning the laser off-resonance with a chirp rate of 37.1 MHz μs^{-1} by applying a sawtooth voltage ramp to the QCL driver. The resulting single-sweep transmission spectra are shown in Figure 5.7. In (a), the large fluctuations observed before 0 μs are equivalent to the fluctuations observed in the low pressure, high power spectrum shown in Figure 5.5. A fast oscillatory structure is present immediately after the laser is detuned from resonance, as demonstrated by the two sweeps shown in (b). Taking sweep 1 as an example, the frequency of the

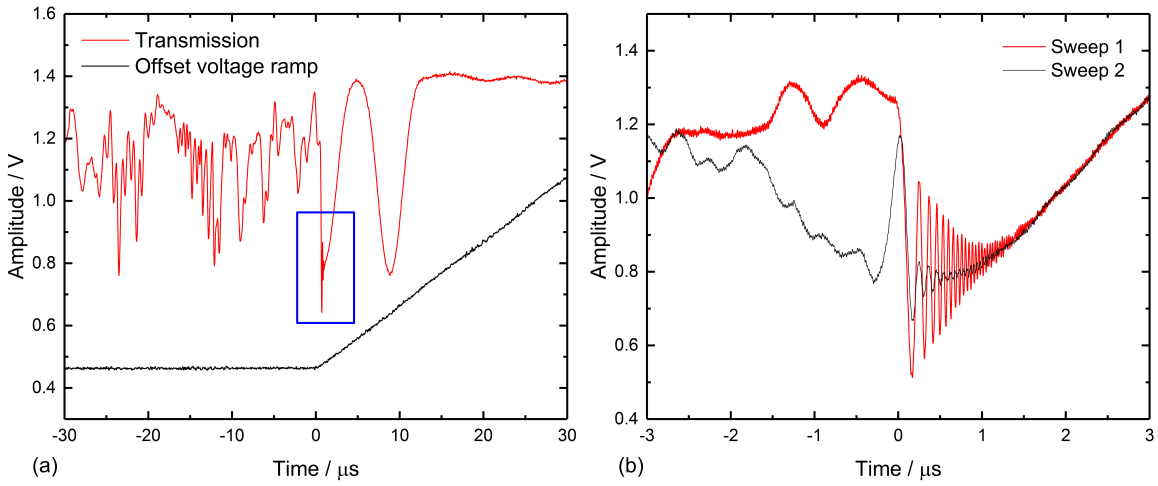


Figure 5.7: (a) shows the multi-pass cell transmission as the laser is kept on resonance with the f component of the NO $R(6.5)_{1/2}$ transition and is detuned by applying a voltage ramp to the driver. In (b), two selected zoomed in scans over the region highlighted in (a) reveal oscillatory structures resembling rapid passage. These highlight the fluctuation of the duration and amplitude of the oscillations. All spectra were recorded at a total pressure of 4 mTorr of NO.

oscillations at $t > 0$ μs increases from *ca.* 7 MHz at the start to over 20 MHz after 1 μs. These oscillatory structures correspond to a beat between a macroscopic polarisation in the NO sample with the chirping laser field, and are thus an example of rapid passage. The oscillatory structures in (b) also persist over each scan (obtained every 10 ms with a 100 Hz scan rate), however with fluctuating amplitudes and durations of between *ca.* 0.5 μs and 1.5 μs. These amplitude and duration fluctuations are

the result of the random nature of the initial conditions for the sample polarisation, which is due to the continuous pumping of the $R(6.5)_{1/2}$ transition. The on-resonance effects observed prior to ramping the laser current can be separated in terms of high and low transmission: when the transmission is high, a large fraction of the sample macroscopic polarisation beats constructively with the laser field. Conversely, the low transmission sections of the on-resonance fluctuations correspond to destructive interference between the laser field and the sample polarisation.

The reproducibility of the nonlinear events described so far is limited by the initial conditions of sample polarisation and excited state population at the start of the voltage ramp, t_0, over which the selected experimental conditions offer no control. Similar nonlinear effects have been observed using pulsed and cw-QCLs, such as rapid passage oscillations in the spectra of low pressure gases,[131,132] but these employ chirp rates of the order of a few MHz ns^{-1}, while the spectrum in Figure 5.7 (a) was obtained by chirping the laser some 2 orders of magnitude more slowly, at only *ca.* 37 MHz μs^{-1}. For achieving chirp rates in the MHz ns^{-1} range, a voltage pulse was applied to the laser chip by mixing said pulse with a slow current ramp through a bias tee, using the same configuration presented in Figure 4.2 of Chapter 4. The sudden change in current passing through the chip induces rapid Joule heating that increases the chirp rate by several orders of magnitude. Figure 5.8 shows a schematic representation of the frequency change of the QCL upon the application of a current pulse.

To demonstrate the frequency excursion caused by applying a voltage pulse to the QCL chip, a 36 ns long pulse with an amplitude of -1.5 V was applied to the laser as it is down-chirped at 77 MHz μs^{-1} over the transmission fringes of a Ge etalon with a FSR = 493 MHz (see Figure 5.9). For all the following single laser experiments, an AC coupled, 1 GHz bandwidth detector was used. After the application of the pulse at t_0, at phase (1), the frequency at time t_0 returns to the (higher) frequency that it

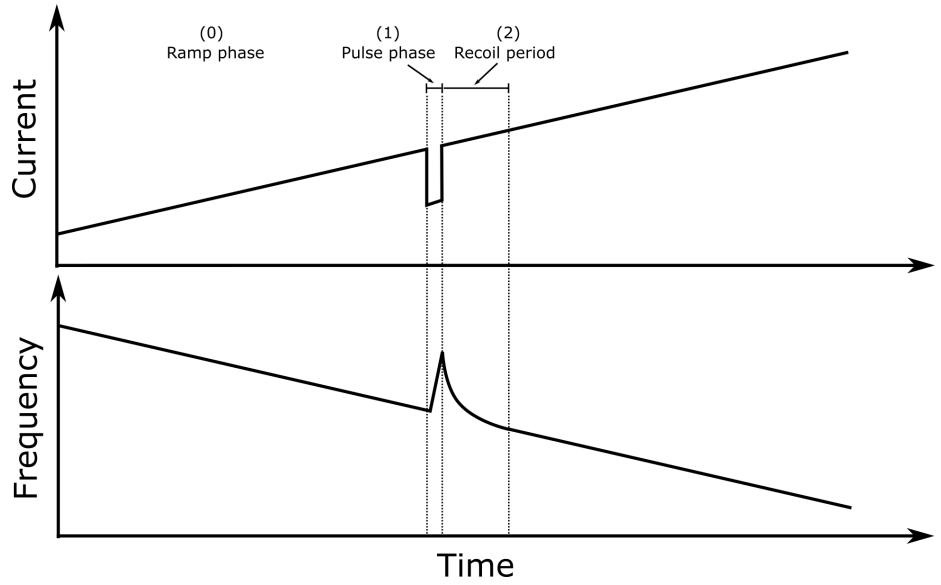


Figure 5.8: Top: the current ramp with a pulse applied to the laser chip, generated by applying a voltage pulse via a bias tee. The bottom panel presents the frequency change induced by the current pulse. The pulse induces a fast frequency up-chirp in phase (1), which is followed by a recoil period in (2) whereby the frequency scan resumes down-chirping approaching the same rate as phase (0).

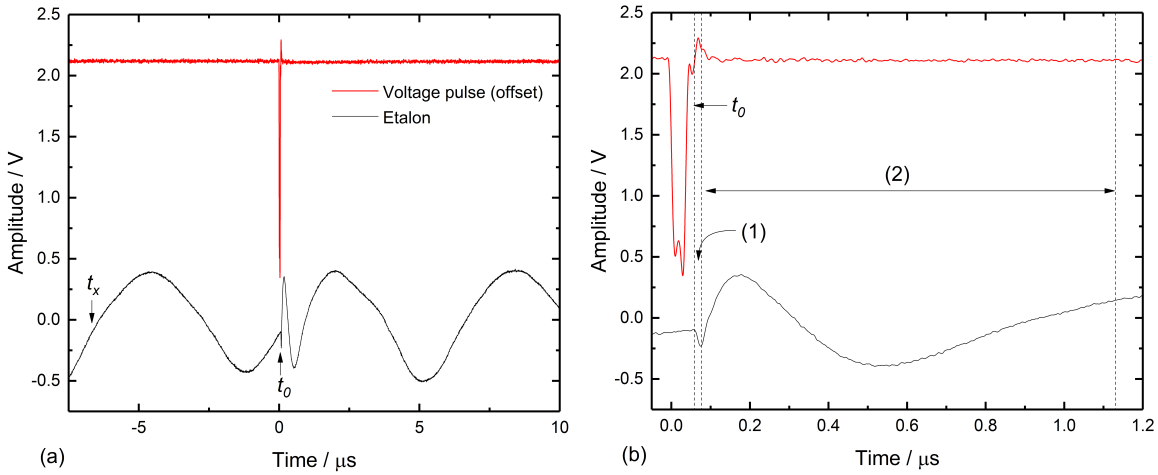


Figure 5.9: (a) shows the effect of applying a pulse to the laser chip using an etalon transmission spectrum. The same data, zoomed in around the pulse, is shown in (b). The noise observed on the voltage pulse at the rising and falling edges of the square wave is due to electrical noise. The time delay of *ca.* 50 ns between the pulse falling edge t_0 and the sharp change in the etalon transmission spectrum is due to the optical path length ($\sim$ 17 ns) and the electronic delays.

had earlier in the scan, at the time point t_x. In the recoil period, marked as phase (2), the frequency rapidly scans over the region between t_x and t_0,, and the chirp rate progressively slows down until it returns to the same value as the pre-pulse chirp rate.

Figure 5.10 (a) shows the transmission spectrum of the $R(6.5)_{1/2}$ transition at a total pressure of 4 mTorr as the laser frequency is down-chirped. A 36 ns long voltage pulse is applied at the centre of the e component transition and the laser frequency is rapidly up-chirped to the high-frequency flank of the f component, then slowly recoils towards the same chirp rate and sweep direction than at $< t_0$. The splitting between the two Λ components is 331 MHz, and this frequency range is covered within 21 ns yielding an average chirp rate in that time interval of 15.7 MHz ns^{-1}.

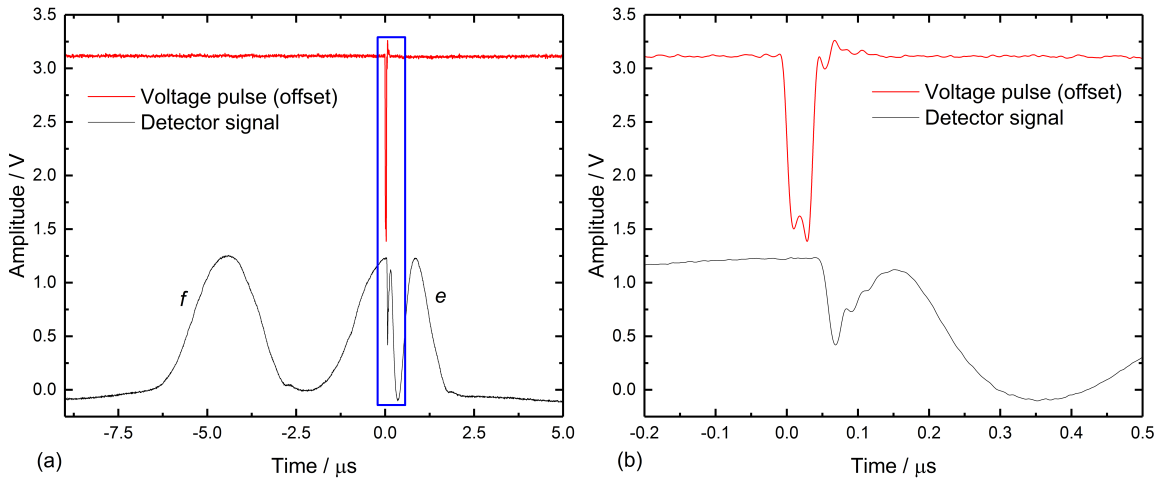


Figure 5.10: The spectrum of the $R(6.5)_{1/2}$ transition at a total pressure of 4 mTorr, with a pulse applied at the centre of the e component of the Λ doublet is shown in (a). The region shortly after the pulse is magnified and shown in (b). Here it should be noted that the y-axis represents the response of the AC detector in Volts, as it is a direct measurement of the multi-pass cell transmission, and does not represent the absorbance of the sample.

The slower recoil probes the f component of the transition, and an oscillatory structure is clearly present in the spectra. This structure is a rapid passage signal induced by the fast frequency up-chirp of the laser field, and becomes more prominent as the total pressure of the sample is increased to 22 mTorr (see Figure 5.11). At this pressure, the sample becomes optically thick (*i.e.* the laser beam is almost fully

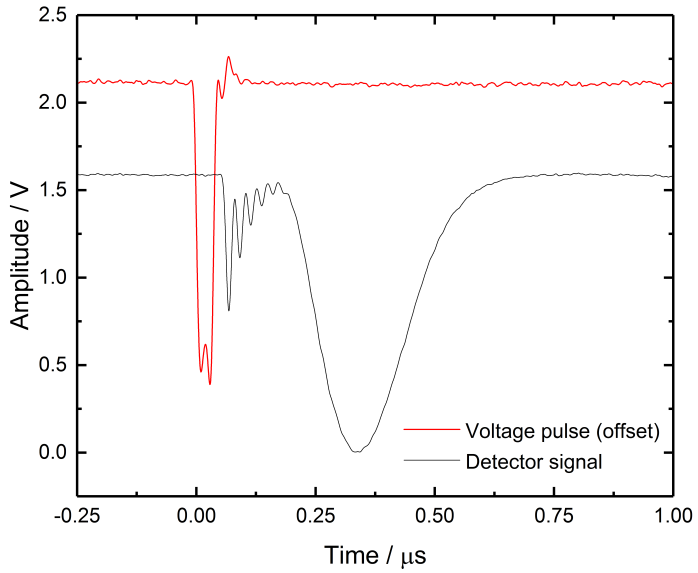


Figure 5.11: Spectrum of the f component of the R(6.5) $\Omega = {}^1/_2$ transition of NO with the recoil of a pulse at a total pressure of 22 mTorr. The pulse is applied while on resonance with the e component of the Λ doublet. The plateau of the AC detector response indicates the sample is optically thick and completely absorbs the beam.

attenuated) and increasing the pressure further made it impossible to observe the induced macroscopic polarisation beat. It is clear that the use of a voltage pulse allows the observation of coherent transient effects in NO, with the macroscopic polarisation induced by rapid passage being probed by the recoil region of the pulse. Moreover, the oscillations observed in Figures 5.10 (b) and 5.11 occur at the same frequency (*ca.* 43 MHz), and the difference in amplitude is solely due to the higher number density of NO in the latter.

By applying a voltage pulse to the laser driver, similar rapid passage effects to those observed with a single on-resonance laser can be achieved due to average chirp rates of the order of a few MHz ns^{-1}. Rapid passage effects similar to those described in this section can also be produced with much slower chirp rates by probing a velocity selected sample, as will be discussed in the following section.

5.4.2 Rapid passage effects with a velocity selected sample: R(14.5)-R(15.5) transition pair

The occurrence of rapid passage in a velocity selected sample is investigated by adding a second QCL to the experiment in order to pump a narrow velocity group to the first vibrationally excited level of NO. The experiment employed an EC-QCL and a DFB-QCL, using a counter-propagating beam configuration as shown in the experimental section, and a 72 cm single pass cell rather than a multi-pass cell. In this case, the EC-QCL was tuned to the centre of the f component of the $R(14.5)_{1/2}$ $v = 1 \leftarrow 0$ transition at *ca.* 1923.5 cm^{-1}, while the DFB-QCL scanned over the f component of the $R(15.5)_{1/2}$ $v = 2 \leftarrow 1$ transition at *ca.* 1894.9 cm^{-1}. An energy level diagram of the *ladder-like* pump-probe configuration is shown in Figure 5.12 (a). Figure 5.12 (b) shows the transmission spectrum of a single probe laser scan over the $R(15.5)_{1/2}$ $v = 2 \leftarrow 1$ transition of NO as a triangular voltage ramp is applied to the current driver. The voltage up-ramp region marked with (1) corresponds to a frequency down-ramp, while the region marked with (2) corresponds to a frequency up-ramp. The sharp structures occurring at the two regions marked with rectangles in Figure 5.12 (b) are caused by transient absorption by the velocity selected vibrationally excited sample of NO (see the inset – a clear oscillating structure is present). A

MATLAB routine was subsequently used to remove the background and average multiple spectra. The procedure involved restricting the width of the frequency scan to a narrower window around the transient signal, and removing the effects of probe laser jitter by overlapping the minima of the transient signals between all sweeps. Thus, the rapid passage spectrum shown in Figure 5.13 was obtained by scanning over the f component of the $R(15.5)_{1/2}$ $v = 2 \leftarrow 1$ transition of NO, at a total pressure of 20 mTorr, in a frequency down-ramp with a chirp rate of 22.6 MHz μs^{-1}. The pump beam and probe beam powers were 50 mW and 70 mW, respectively. The

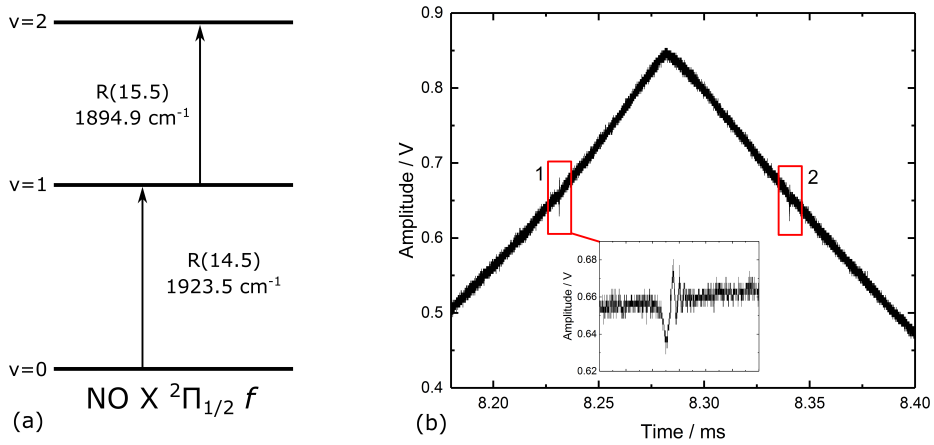


Figure 5.12: (a) The ladder state configuration and the transitions used in the initial two-colour rapid passage experiment. (b) The transmission spectrum of the probe beam as a triangular voltage ramp use to scan over the $R(15.5)_{1/2}$ $v = 2 \leftarrow 1$ transition of NO. The inset shows a rapid passage oscillation found in the laser current up-ramp.

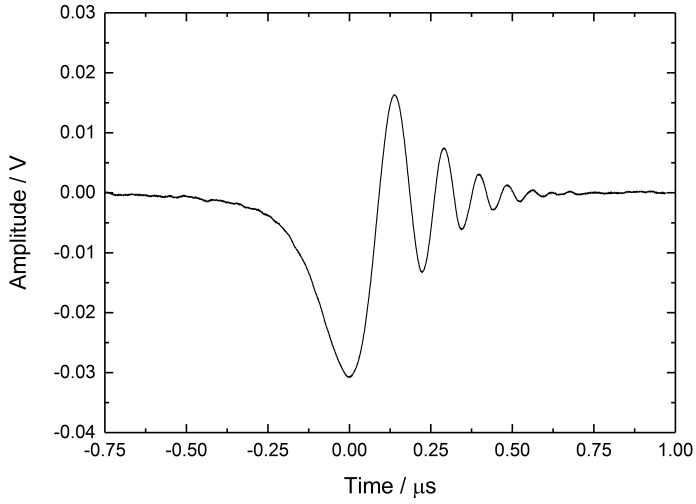


Figure 5.13: Coherent transient signal from the f component of the $R(15.5)_{1/2}$ $v = 2 \leftarrow 1$ transition of NO, 100 scans average.

oscillatory structure is the beat signal between the macroscopic polarisation induced by scanning over the $R(15.5)_{1/2}$ $v = 2 \leftarrow 1$ transition on a timescale that is short compared to the relaxation time of the system (rapid passage), analogously to the coherent nonlinear phenomena presented in the previous section. The chirp rates required to observe rapid passage effects on a velocity selected sample are much lower than those required to produce rapid passage on a Doppler broadened sample; in the previous section, the chirp rate used in the pulsed experiments was 3 orders of magnitude larger than that used to obtain the signal in Figure 5.13.

The measured rapid passage signals are the sum of the precession of the induced macroscopic polarisation of all hyperfine components of the $v = 2 \leftarrow 1$ transition, whose frequency splitting changes as a function of Λ component, spin-orbit state and total angular momentum of the transition. The f component of the $\Omega = 1/2$ spin-orbit state was selected since the magnitude of the hyperfine splitting is the lowest of the transitions with an angular momentum quantum number $J = 15.5$.

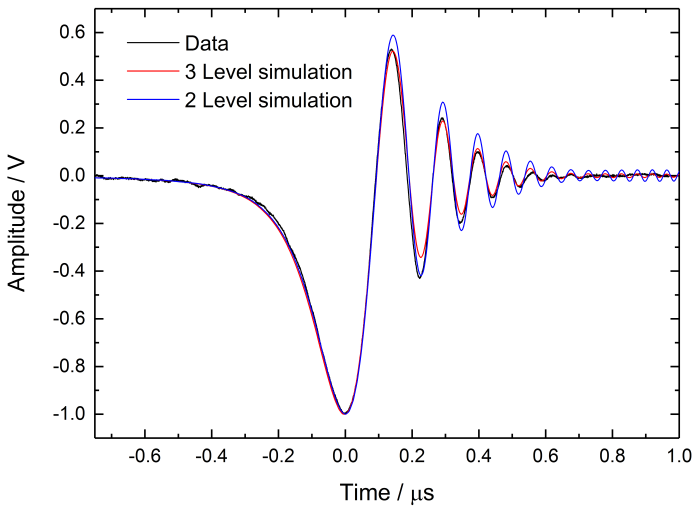


Figure 5.14: Rapid passage spectrum shown in Figure 5.13 overlaid with simulations using a 2 level and 3 level system model. The latter model provides a more adequate fit to the experimental data.

The rapid passage signal in Figure 5.13 is shown again in Figure 5.14 and is overlaid with simulations developed by Kirkbride *et al* for solving the optical Bloch equations

both for a ladder-like 3 level system (see Equations 5.5) and for a 2 level system.[124] A MATLAB program was used to solve the ODEs, using as input parameters the chirp rate of the probe laser (21.3 MHz μs^{-1}) (the pump laser was kept on resonance with the R(14.5) transition), the linewidth of both lasers (pump: 2 MHz, probe: 0.5 MHz), the laser powers (P_{pump} = 50 mW, P_{probe} = 70 mW), the total pressure (20 mTorr), and the self broadening parameters of both transitions with the respective Einstein A coefficients (retrieved from HITRAN).[65] Using the experimental conditions as input parameters for both simulations, the time evolution of the coherent system is accurately described, and the model based on a 3-level system produces a better fit to the data. The 2-level simulation underestimates the dephasing time of the rapid passage oscillations since it neglects all decay mechanisms which are not vibrational relaxation directly to the ground state.

5.4.3 Rapid passage effects with a velocity selected sample: R(6.5)-P(7.5) transition pair

In preparation for the time-resolved studies presented in the next section (*vide infra*), a pair of stronger transitions is chosen to increase the signal to noise ratio of the velocity selected coherent transient signals. The DFB-QCL was tuned to the $R(6.5)_{1/2}$ $v = 1 \leftarrow 0$ transition of NO at 1900.1 cm^{-1} with a power of 160 mW, while the EC-QCL probed the $P(7.5)_{1/2}$ $v = 2 \leftarrow 1$ transition at 1821.3 cm^{-1}. Additionally, a multi-pass cell with a total path length of 332 cm (see Figure 5.2) was used. The rapid passage spectrum shown in Figure 5.15 was obtained using this configuration, scanning over the e component of the Λ-doublet with a total pressure of 4 mTorr, continuous pumping to the intermediate level, and a chirp rate of 9.5 MHz μs^{-1}.

In order to establish which of the two Λ-doublet components will be used in the time resolved studies, consider the spectra in Figure 5.16, showing spectra obtained at

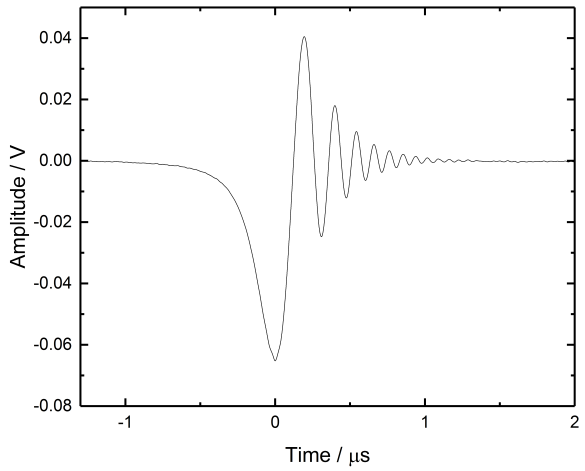


Figure 5.15: Rapid passage spectrum of the P(7.5) $v = 2 \leftarrow 1$ transition of NO, obtained at a chirp rate of 9.5 MHz μs^{-1} with a total pressure of 4 mTorr, and 100 averages.

a chirp rate of 13.3 MHz μs^{-1} of both e and f components of the $P(7.5)_{1/2}$ $v = 2 \leftarrow 1$ transition manifold. This comparison is made in order to determine if the different hyperfine splitting between the e and f components of this transition (0.6 MHz and 1.2, respectively) contribute to the dephasing time and amplitude of these oscillatory structures. Again, the pump laser is kept on resonance with the fundamental transition of the ladder state, *i.e.* molecules are continuously pumped to the $v = 1$ level. The oscillatory structure present in the two spectra are fit with the following equation:

$$A(t) = A_0 e^{-t\kappa} \sin(\mu t^2 + \phi), \tag{5.6}$$

where A is the amplitude of the signal, κ is the decay constant of the oscillation, μ is the laser chirp rate and ϕ is a phase adjustment constant. The t^2 term is used to account for the increasing frequency of the rapid passage signature as the laser frequency is swept away from resonance with the target transition. The pressure of NO for the e component spectrum was 3 mTorr, while the f component spectrum was obtained at a pressure of 4 mTorr. The maximum amplitude of the first oscillation in both the spectra shown in Figure 5.16, relative to the signal baseline of each spectra,

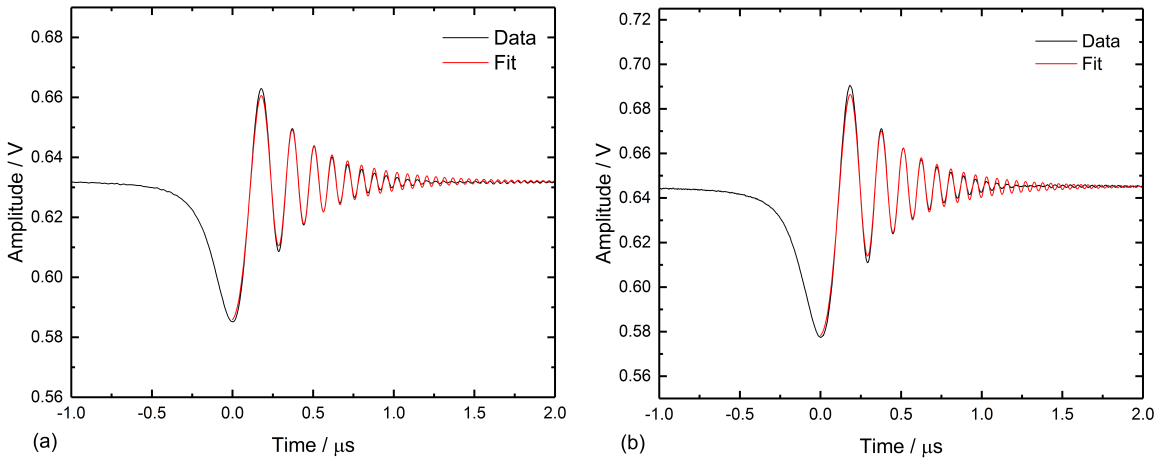


Figure 5.16: (a) shows the rapid passage spectrum of the e component of the P(7.5) $v = 2 \leftarrow 1$ transition, obtained at a chirp rate of 13.3 MHz μs^{-1} and a total pressure of 3 mTorr. In (b), the rapid passage spectrum of the f component of the same transition is shown, obtained at the same chirp rate and at a total pressure of 4 mTorr. Both spectra are the result of 130 averaged scans.

differ by *ca.* 45%. This difference is caused by the different pressure between the two spectra, as well as the error on the pressure gauge, equivalent to the smallest division on its scale of ±1 mTorr. The half-lives of the coherent oscillatory structures of 372 ± 17 ns and 378 ± 23 ns for the e and f components, respectively, are within error of each other. These lifetimes are over a factor of 2 longer than the lifetimes reported by Kirkbride *et al.* probing the same transition pair of NO at similar chirp rates and a total pressure of 50 mTorr.[124] Given the similar decay times and amplitudes of the two signals shown in Figure 5.16, the e component was chosen for all time-resolved measurements in this chapter owing to the smaller splitting between its most distant hyperfine components.

The method for producing 3-level rapid passage signals described in this section relies on continually pumping into the intermediate state by keeping the pump laser on resonance. By continuously pumping to the first vibrationally excited state, information regarding the pumping time required to reach maximum population transfer can not be obtained. This issue is addressed by controlling the duration of the optical pump pulse, as described in the next section.

5.4.4 Time resolved studies of rapid passage effects with a velocity selected sample

In the work presented in this section, an AOM was used as an optical switch in order to time-resolve the pumping process which prepares the $v = 1$ level, as well as to gain an insight into the relaxation of coherent transient signals. In order to study the evolution of rapid passage signals as a function of pumping time, the relative amplitudes of the first rapid passage oscillation (of the same transition pair) occurring a delay time, τ, after the optical pulse rise, were used. The pulse duration was controlled by using the first-order AOM beam as the pump beam. By switching the AOM off, the pump beam generated by the DFB-QCL was deflected away from the multi-pass cell. The time τ represents the time difference between the optical pump pulse rise and the time at which the probe laser (the EC-QCL) sweeps through the velocity selected sample in the $v = 1$ level. A schematic representation of this process is presented in Figure 5.17. The frequency jitter of the EC-QCL causes fluctuations in τ between scans,

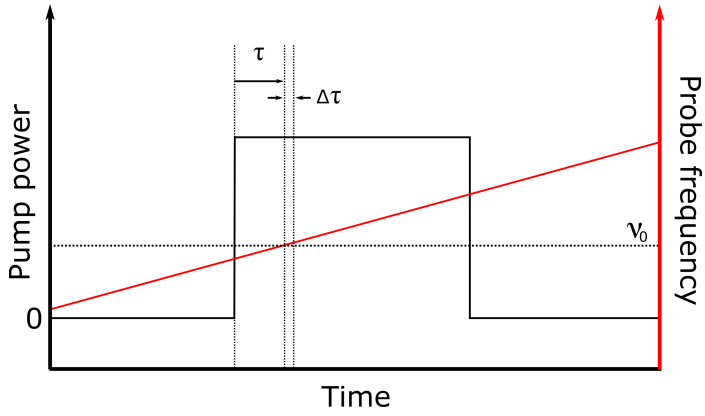


Figure 5.17: Schematic representation of the optical pumping to the intermediate level and the probe laser frequency scan. τ represents the time delay between the optical pulse rise and the probe laser sweeping through resonance with the e component of the $P(7.5)_{1/2}$ transition manifold of NO, and $\Delta\tau$ represents the tolerance in τ within which the shots will be averaged together.

as the EC-QCL will sweep through resonance of the hot band transition at varying time delays after the pump pulse rise. To ensure that only spectra that correspond

to the same selected interval τ are averaged together, a MATLAB script was used to find rapid passage minima in a region $\tau \pm \Delta\tau$ (in Figure 5.17). The $\Delta\tau$ used for all spectra presented hereafter was 0.1 μs. The resulting rapid passage spectra at two distinct τ delays are shown in Figure 5.18. The spectra are obtained by probing the e

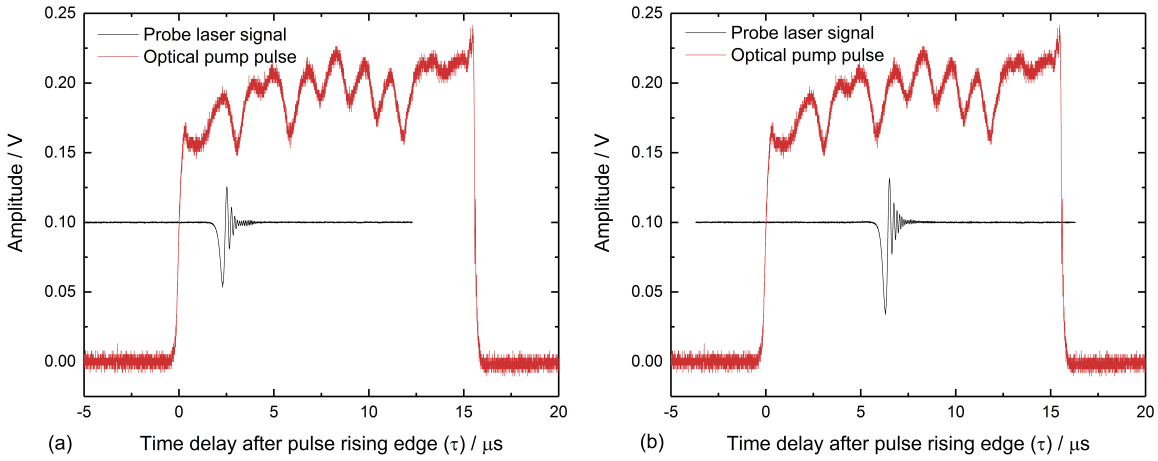


Figure 5.18: In (a), the rapid passage signal obtained by scanning over the P(7.5) $v = 2 \leftarrow 1$ transition of NO at a chirp rate of 7.8 MHz μs^{-1} with $\tau = 2.3$ μs is presented. The total pressure was 3 mTorr of pure NO. Under identical conditions, the rapid passage spectrum of the same transition with $\tau = 6.3$ μs is shown in (b). In both spectra an optical pump pulse is shown for clarity. The spectra were averaged 20 times.

component of the $P(7.5)_{1/2}$ $v = 2 \leftarrow 1$ transition of NO with a chirp rate of 7.4 MHz μs^{-1}, at a total pressure of 3 mTorr and averaging 20 scans.

In both figures, a measurement of the optical pump pulse is also shown for clarity. The pump pulse consists of a single sweep acquired simultaneously with the dataset. The pulse length fluctuations are of the order of a few nanoseconds and were thus disregarded due to the small magnitude in comparison with the τ delays used in this study. The intensity fluctuations observed during the pump pulse are caused by the coherent effects described earlier in this chapter, when using a single QCL to study the nonlinear response of the optical medium (see Figure 5.7). Figure 5.19 shows the rapid passage spectra obtained at a series of time delays, using the conditions described for the spectra shown in Figure 5.18. A three fold increase in amplitude

of the first rapid passage oscillation from 2.1×10^{-2} V at $\tau = 0.3$ μs to 6.3×10^{-2} V at $\tau = 5.3$ μs is an indicator of the increasing population of the intermediate state within this time interval. The evolution of the amplitude of the first rapid passage

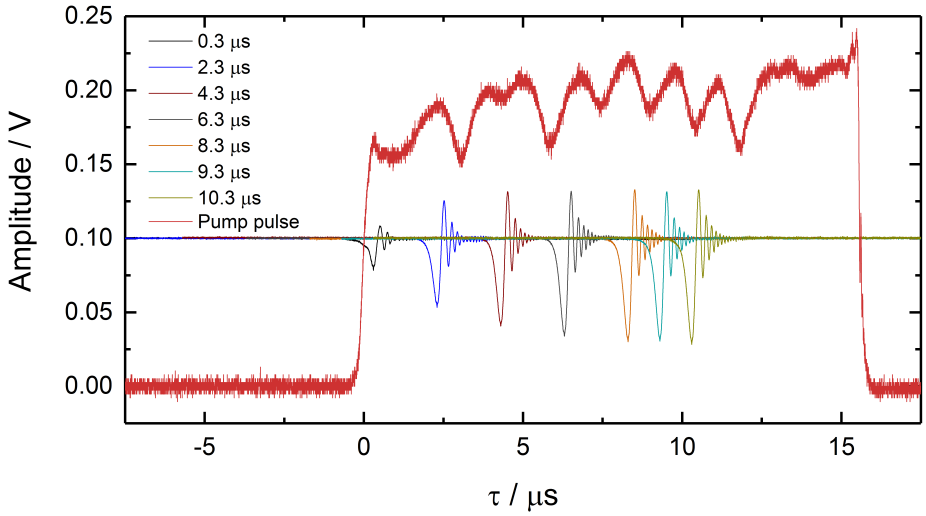


Figure 5.19: Rapid passage signals obtained by sweeping over the P(7.5) $v = 2 \leftarrow 1$ transition of NO at a chirp rate of 7.8 μs^{-1} for a range of τ between 0 and 11 μs. The total pressure was 3 mTorr of pure NO. All spectra presented were averaged 20 times.

oscillation as a function of τ is shown in Figure 5.20. The data are overlaid with a function of the form

$$y = y_0 + A(1 - e^{-\tau/t_r}), \tag{5.7}$$

where y_0 is an offset, A is a factor that determines the value that the function approaches asymptotically $(y_0 + A)$, and t_r is the rise time. Using this function, the maximum value approached asymptotically by the amplitude of the rapid passage signals was extracted, which in these experimental conditions was $(7.3 \pm 0.2) \times10^{-2}$ V. It can be seen that after 10 μs the rapid passage amplitude reaches a value within 3% of the maximum. This time delay is thus regarded as the minimum optical pumping time for reaching the maximum population transfer to the $v = 1$ level, τ_{steady}.

At a total pressure of 3 mTorr the collision rate between NO molecules is $\kappa_{\text{col}} = 2.76 \times 10^4$ s^{-1}, leading to an average period between collision events of *ca.* 36 μs.

This collision period is longer than both the pulse length $\tau_{\text{pulse}} = 15$ μs and τ_{steady}, hence the probability of a single collision event (per molecule) during the pulse is < 1. The probability of molecular collisions, $P_{\text{col}}(x, \lambda)$, is given by a Poisson distribution of the form

$$P_{\text{col}}(x, \lambda) = \frac{\lambda^x e^{-\lambda}}{x!}, \tag{5.8}$$

where x is the number of collision events and λ is the average number of collision events in a selected time interval, given by the product of the event rate and an observation time. If τ_{steady} is chosen as the observation time, then $\lambda = \kappa_{\text{col}}\tau_{\text{steady}}$.

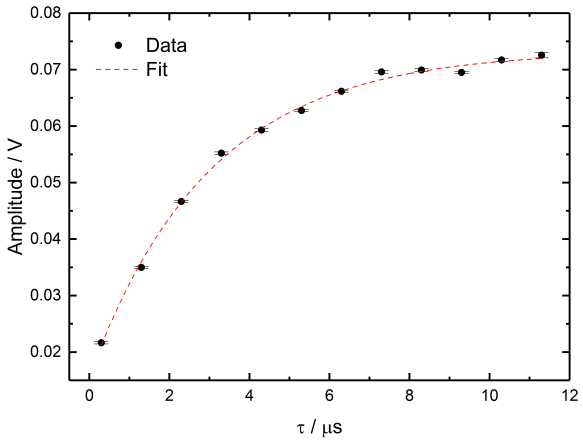


Figure 5.20: Evolution of the amplitude of the signals produced by rapidly sweeping over the e component of the $P(7.5)_{1/2}$ $v = 2 \leftarrow 1$ transition of NO at several time delays (τ) after an optical pump pulse. Constructed from the data presented in Figure 5.19.

With $\kappa_{\text{col}} = 2.76 \times 10^{-2}$ μs^{-1} and $\tau_{\text{steady}} = 10$ μs, the probability of a single collision per molecule is $P_{\text{col}}(1, \lambda) = 21\%$. Multiple collisions can occur, but the probabilities sum up to only *ca.* 3%. Therefore, the total collision probability per molecule at 3 mTorr within a 10 μs window of observation is 24%. Due to this significant collision probability during τ_{steady}, optical pumping to within 3% of the maximum population transfer to the $v = 1$ level is achieved with a considerable contribution of dampening by collision events.

5.4.5 Time resolved rapid passage effects: signal relaxation

The time reference provided by the falling edge of the optical pump pulse can be used for studying the relaxation of these coherent systems. Here, τ is redefined as the time delay between the pulse falling edge and the maximum amplitude of the first rapid passage oscillation. A 10 μs long optical pulse pumping the e component of the

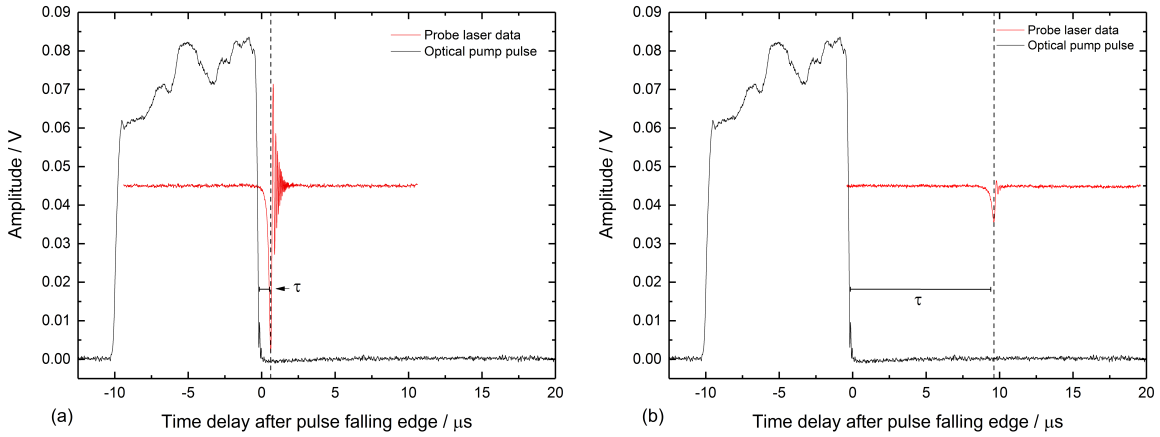


Figure 5.21: (a) The rapid passage spectrum of the $P(7.5)_{1/2}$ $v = 2 \leftarrow 1$ transition of NO taken 0.6 μs after the optical pump pulse falling edge. The spectrum shown in (b) presents the rapid passage spectrum of the same transition, obtained 9.6 μs after the pump pulse falling edge. Both spectra were obtained at a total pressure of 3 mTorr, a chirp rate of 15 MHz μs^{-1} and 20 averaged scans. The time delay between the pulse falling edge and the first rapid passage oscillation is represented as τ in both cases.

$R(6.5)_{1/2}$ transition is chosen for the studies presented in this section and again an example optical pump pulse (single sweep) is shown for clarity in all cases. Figure 5.21 presents rapid passage spectra obtained by scanning over the e component of the $P(7.5)_{1/2}$ transition of NO, with a chirp rate of 15 MHz μs^{-1}, at two distinct time delays τ. The total pressure of the sample was 3 mTorr in both cases.

Both a decrease in amplitude of the first rapid passage oscillation, as well as a dampening of the oscillatory structure as a function of τ, are seen. Figure 5.22 shows several rapid passage spectra obtained under the same conditions (3 mTorr, 15 MHz μs^{-1}, 20 averages) with increasing τ. The rapid passage spectrum obtained at $\tau = 0.6$ μs was fit using Equation 5.6, yielding an oscillation decay time of 307 $\pm$ 25 ns. This

result is consistent with the rapid passage decay time obtained in the permanent pumping case of 372 ± 17ns (shown in Figure 5.16 (a)). The 66 ns difference in decay

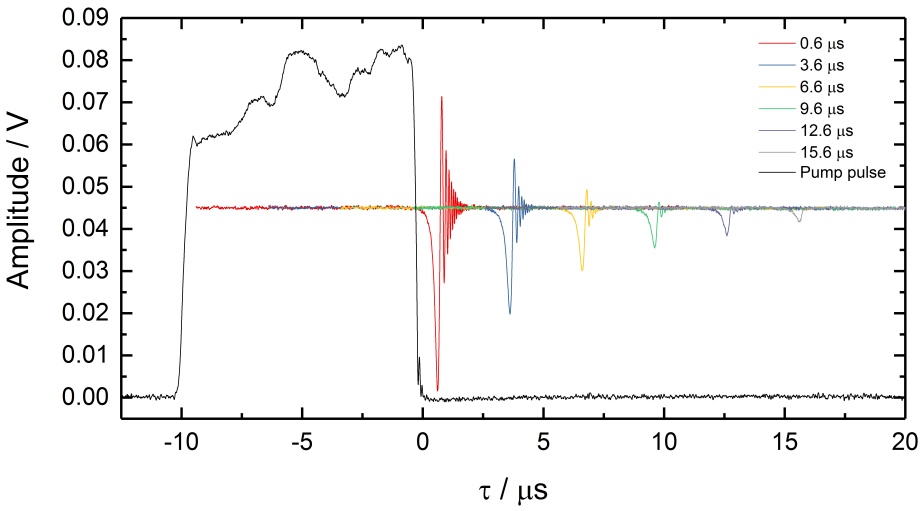


Figure 5.22: Rapid passage spectra, obtained at increasing τ under the same experimental conditions as the spectra shown in Figure 5.21. An optical pump pulse is shown for clarity.

time is explained by dependence of rapid passage signals on the chirp rate of the probe laser; higher chirp rates have been shown to reduce the decay time of the rapid passage oscillatory structures.[124] The chirp rate in the spectra shown in Figure 5.16 (a) is 13.3 MHz μs^{-1}, while in the spectra shown in Figure 5.22 the chirp rate is 15 MHz μs^{-1}.

Figure 5.23 shows the evolution of the amplitude of the first rapid passage oscillation as a function of τ. The data are overlaid with an exponential decay fit of the form:

$$y = y_0 + Ae^{-\tau k}, \tag{5.9}$$

where y_0 is the amplitude offset, A is the initial amplitude and k is the decay constant of the amplitude of the first rapid passage oscillation. The fit in Figure 5.23 yields a decay constant $k = 0.176 \pm 0.004$ μs^{-1} and a lifetime $t_{life} = 1/k = 5.65 \pm 0.15$ μs. Despite the short timescale at which the decay of rapid passage oscillations occurs in comparison to the average time between collisions at a total pressure of 3 mTorr

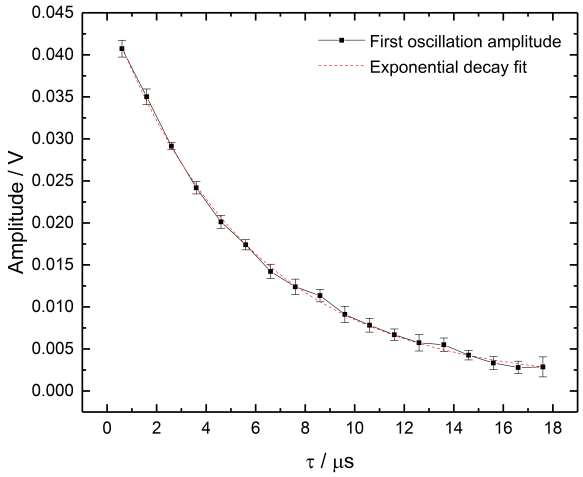


Figure 5.23: Evolution of the maximum amplitude of rapid passage oscillations as a function of τ, produced using the spectra shown in Figure 5.21.

(*ca.* 36 μs), the loss of signal as a function of τ is still governed by this process. Collision events are responsible for the relaxation of the population in the $v = 1$ level across rotational levels in this vibrational state, a process that is faster than the vibrational relaxation of the system due to the smaller energy gaps between rotational states. The oscillatory structure is also lost due to the loss of coherence of the system due to the effect of collisions, an effect that becomes more prominent as τ increases. Collisions also increase the velocity distribution of the vibrationally excited sample, further contributing to the relaxation of the rapid passage signals. The effect of probing broader velocity distributions will be studied in more detail at the end of this chapter.

The effect of chirp rate on the decay of the coherent transient signals was assessed by measuring the evolution of these signals as a function of τ, under the same conditions as the spectra shown in Figure 5.21, using chirp rates of 15 MHz μs^{-1} and 4.1 MHz μs^{-1}. The comparison between the maximum amplitude decay with these different chirp rates is shown in Figure 5.24. The initial amplitude of the rapid passage oscillations clearly decreases as a function of chirp rate and this is due to the reduction of the pumping time of the velocity selected sample to $v = 2$ as the

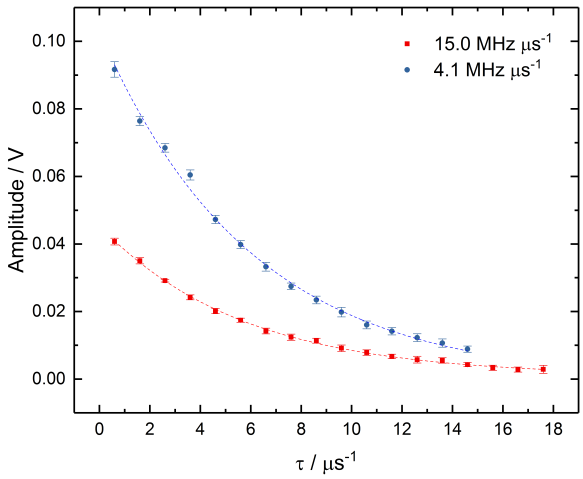


Figure 5.24: Evolution of the maximum amplitude of rapid passage oscillations as a function of τ, probing the same transition pair and using the same total pressure, but at two different chirp rates.

chirp rate increases. It was shown in Figure 5.20 that maximum population transfer to $v = 1$ occurs after 10 μs. Assuming a velocity selected sample with FWHM = 500 kHz, the time taken for the probe laser to traverse this sample with a chirp rate of 4.1 MHz μs^{-1}, is 0.12 μs. This timescale is much shorter than that necessary to achieve maximum population transfer, and it is reduced even further by increasing the chirp rate to 15 MHz μs^{-1}. However, the rapid passage signal amplitude decay constants have the same value ($k \approx 0.17$ μs^{-1}). It can therefore be concluded that although the initial amplitude of the coherent systems is dependent on the chirp rate of the probe laser, the relaxation rate of these systems is not.

The contribution of collisional energy transfer to the relaxation of the system was studied by increasing the total pressure in the gas cell and measuring the amplitude of the rapid passage signals as a function of τ. The pressure was increased by adding buffer gas through a second MFC while keeping a constant flow of NO. This guarantees that the concentration of NO remains constant throughout the measurements. A series of increasing pressures with pure NO was not realized since the medium became optically thick at pressures above 8 mTorr. Instead, the procedure is demonstrated using CO_2 as a buffer gas, with a partial pressure of NO of 3 mTorr. Figure 5.25

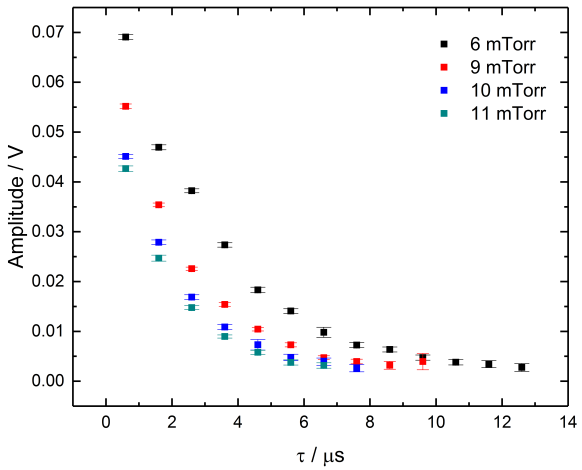


Figure 5.25: Evolution of the maximum amplitude of rapid passage oscillations as a function of τ, for a range of total pressures obtained by buffering 3 mTorr of NO in CO_2.

shows the maximum amplitude of the first rapid passage oscillation for a range of τ at various total pressures. The decay time at the total pressure of 6 mTorr is 3.21 $\pm$ 0.19 μs, and decreases to 1.96 $\pm$ 0.13 μs at a total pressure of 11 mTorr. The buffering process was repeated using a variety of buffer gases while keeping the partial pressure of NO at 3 mTorr. Figure 5.26 shows the decay constants as a function of buffer gas pressure for He, N_2O, CO_2 and N_2. The partial pressure and the rapid passage decay constant of pure NO were subtracted from all datasets in order to determine the relaxation rate constants for each buffer gase. For each pressure series measurement a linear fit is shown and the slope of the linear fits corresponds to the collisional relaxation rate induced by each buffer, and is presented in table 5.1. The main aspect that governs the collisional relaxation rate is the collision frequency, Z_w, given by[133]

$$Z_w = \sigma_{\mathrm{col}} \bar{c}_{\mathrm{rel}} \frac{N}{V}, \tag{5.10}$$

where σ_{col} is the collisional cross-section, $\bar{c}_{\mathrm{rel}}$ is the relative mean speed of the molecules,

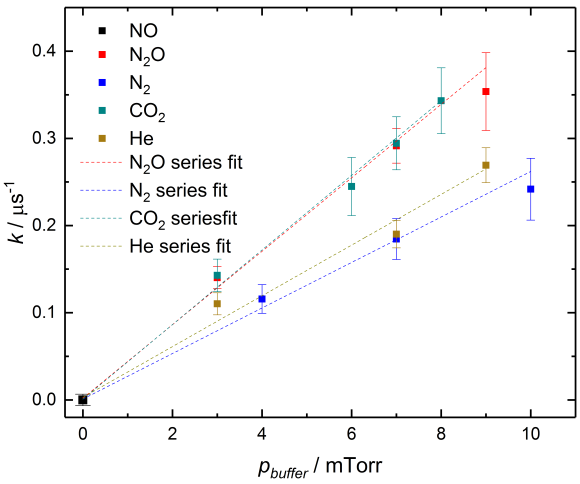


Figure 5.26: Rapid passage decay constants obtained for different buffer gases as a function of buffer gas pressure. For all the data presented, a partial pressure of NO of 3 mTorr was used.

N is the number of molecules and V is the sample volume. $\bar{c}_{\mathrm{rel}}$ is given by

$$\bar{c}_{\mathrm{rel}} = \left(\frac{8k_BT}{\pi\mu}\right)^{1/2}, \tag{5.11}$$

where T is the temperature and μ is the reduced mass.

It can be seen immediately from Figure 5.26 that N_2O and CO_2, induce faster relaxation than N_2 and He, which have comparable relaxation rate constants. The similarities of the rate constants for N_2 and He are consistent with their hard sphere collision rates, indicating that the intermolecular forces and inelastic energy transfer play little or no role. In the case of N_2O and CO_2 (whose collision frequencies with NO are similar to those of N_2 and He) the marked increase in relaxation rate reflects the increased interaction potentials and the possibility of more vibrational energy transfer. N_2O, CO_2 are more polarizable than He, N_2 and in the case of N_2O there is a dipole-dipole interaction with NO.

A collisional relaxation rate constant of 4.8×10^3 s^{-1} mTorr^{-1} is extracted using the air broadening parameter for the pump transition available on HITRAN.[65] Assuming $\gamma_{air} = \gamma_{N_2}$ (see Chapter 2), the measured collisional relaxation rate of the coherent

Table 5.1: Table presenting the relaxation rates of the coherent transient signals, calculated from the amplitude decay of spectra obtained from buffering low pressure samples of NO in a variety of gases. The σ_{col} values for N_2, CO_2 and He are 0.43 nm^2, 0.52 nm^2 and 0.27 nm^2, respectively.These were retrieved from reference 133. For the Z_w calculations, $T = 298$ K was assumed.

Buffer gas	Collisional relaxation rate / s^{-1} $mTorr^{-1}$	Z_w / s^{-1} $mTorr^{-1}$
N_2	$(2.61 \pm 0.14)\times10^4$	9.20×10^3
N_2O	$(4.21 \pm 0.20)\times10^4$	—
CO_2	$(4.28 \pm 0.13)\times10^4$	1.06×10^4
He	$(2.91 \pm 0.24)\times10^4$	1.19×10^4

signals in nitrogen is approximately a factor of ~ 5 larger than the database value. However, depopulation of the intermediate state is not the only process responsible for the decay of rapid passage signals, as the velocity selected sample of NO ($v = 1$) molecules also undergoes velocity redistribution due to collisions. An indicator of velocity redistribution is the widening of the first rapid passage oscillation obtained at different τ delays after switching off the pump pulse. In Figure 5.27, the signal obtained at $\tau = 0.6$ μs is compared to that obtained at $\tau = 12.6$ μs, with a total pressure of 3 mTorr of pure NO and a chirp rate of 15 MHz μs^{-1}. The FWHM of the first oscillation feature is 2.9 MHz at $\tau = 0.6$ μs, which broadens to 4.0 ± 0.1 MHz at $\tau = 12.6$ μs.

For studying the effect of velocity redistribution on the amplitude decay of the rapid passage signals independently of collisional relaxation processes, a sample with a broader velocity distribution was prepared by broadening the linewidth of the pump laser with RF noise, using the noise injection system described in the previous chapter. Figure 5.28 shows rapid passage spectra obtained by continuously pumping the e component of the $R(6.5)_{1/2}$ $v = 1 \leftarrow 0$ transition and probing the P-branch transition of the ladder state. The total pressure of NO is 3 mTorr and the chirp rate is 7 MHz μs^{-1}. From the previous chapter, it is known that using this RF noise injection system with a +14 dB gain doubles the linewidth of the pump laser from approximately

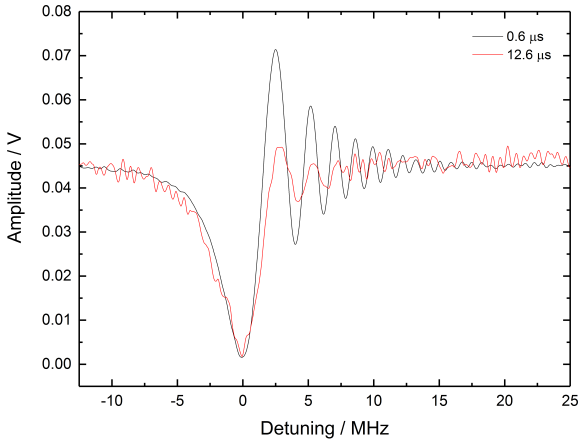


Figure 5.27: Rapid passage spectra obtained at $\tau = 0.6$ μs and $\tau = 12.6$ μs, overlaid for clarity. The signal obtained at the latter τ displays a wider first oscillation feature due to the partial thermalisation of the velocity distribution in the intermediate state.

500 kHz to 1 MHz. The width of the first oscillation sees only a marginal increase by doubling the width of the velocity selected group in the $v = 1$ level, while the amplitude of the first oscillation decreases by 20% and the oscillatory structure is significantly dampened. It can thus be said that the decay of these coherent signals is determined by both loss of population in the $v = 1$ level and velocity dephasing, with the latter contributing more significantly to the loss of the oscillatory structure.

5.5 Conclusion

The high power and narrow linewidth of two single-mode QCLs has been exploited to observe nonlinear coherent optical processes on samples of low pressure NO. Coherent effects were observed by keeping a DFB-QCL on resonance with the e component of the $R(6.5)_{1/2}$ transition of NO at low pressure and subsequently detuning the laser from resonance. Single laser rapid passage effects were also induced in Doppler broadened samples of NO by using a current pulse to tune the laser frequency with a fast chirp rate of 15.7 MHz ns^{-1}, demonstrating the ability for controlled single laser production of coherent signals. The narrow linewidth of the DFB device allowed

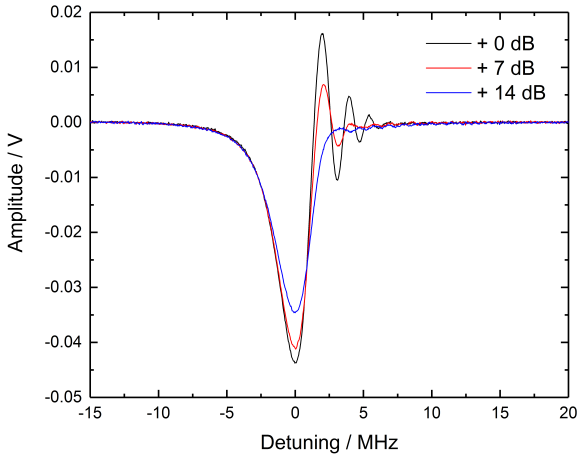


Figure 5.28: Rapid passage spectra obtained by perturbing the current of the pump laser with RF noise at different gains. By doubling the linewidth of the pump laser, the width of the first rapid passage oscillation increases from 2.6 MHz to 3.2 MHz, and the oscillatory structure is greatly dampened after 0 MHz detuning.

pumping of a narrow velocity group, which was probed by a second laser (EC-QCL). In this case, rapid passage signals were observed with chirp rates of the order of a few MHz μs^{-1}, and these signals were simulated using a model based on a two-level and a three-level system. The latter model produced a more adequate fit to the observations. The rapid passage signatures obtained from the pump-probe experiments had lifetimes up to 378 $\pm$ 23 ns. An optical switch (AOM) was successfully implemented in the pump laser to characterise the timescale of optical pumping to the $v = 1$ intermediate state and the collision dependent relaxation of coherent transient signals. Maximum population in the $v = 1$ level was achieved after pumping for 10 $\pm$ 0.5 μs, and the decay time of post-pumping coherent transient signals was 5.7 $\pm$ 0.3 μs. The collisional relaxation rate constants for these coherent signals was also investigated for a variety of buffer gases, reaching (4.28 $\pm$ 0.13) $\times 10^4$ s^{-1} $mTorr^{-1}$ with CO_2. Broadening the optical emission bandwidth of the DFB-QCL allowed an investigation of coherence loss due to velocity dephasing by pumping a broader velocity group to the intermediate level. Broadening the velocity distribution of the molecules pumped to the $v = 1$ level from 500 kHz to 1 MHz resulted in an increased width of the first

rapid passage oscillation and in the coherence collapse of the subsequent oscillatory structure.

Chapter 6

INFAMOS: Intracavity Faraday Modulation Spectroscopy

6.1 Introduction

In this final results chapter, a DFB-QCL will be incorporated into a cavity enhanced spectrometer for the sensitive and selective detection of radicals. In fields such as medicine, atmospheric chemistry or combustion, the need for instruments capable of quantifying the presence of gases in trace concentration has driven spectroscopists to develop techniques that more effectively reject all types of noise. Some species that play pivotal roles in these fields are paramagnetic molecules (radicals), such as HO_2, NO_3, NO, or OH, and are present at very low concentrations ($<$ ppbv).[70,134–139] The limiting factor for the development of sensors that can quantify these radicals may sometimes be the presence of other species at much higher concentrations, including water or carbon dioxide. Litfin *et al.* showed that a significant sensitivity enhancement compared to direct absorption spectroscopy can be achieved by making use of the Faraday effect, which in gas-phase samples is specific to paramagnetic species.[140] The selectivity offered by this technique circumvents the spectral interference prob-

lem for radical sensing, and is the basis of the method that will be presented in this chapter, INtracavity FAraday MOdulation Spectroscopy (INFAMOS).[141]

Faraday rotation can be described as the rotation of the plane of polarisation of a linearly polarised wave propagating through an optically active sample within a magnetic field. As mentioned above, only paramagnetic samples can influence light in this way, meaning that either in the absence of a sample or with a diamagnetic sample, no signal will be produced. By modulating the magnetic field and measuring the intensity modulated signal with a lock-in amplifier, the influence of low frequency ($1/f$) noise can be minimised. For this purpose, several modulation schemes have been implemented including magnetic field modulation (AC-FRS),[140,142,143] magnetic field and wavelength (dual) modulation (DM-FRS),[144] and heterodyne-enhanced modulation (H-FRS).[145]

Modern Faraday rotation spectrometers can reach angular sensitivities of the order of 1 nrad within a 1 Hz measurement bandwidth.[146,147] The limit of detection (LOD) of a spectrometer of this type, in terms of number density of a given species, will depend on a number of factors such as the interaction length with said species, the transition probed, and the magnetic field strength. Optical cavity based techniques offer an increased interaction length with the absorber and are attractive in combination with Faraday rotation techniques due to the cumulative property of the Faraday rotation angle over multiple round-trips.[146,148,149] However, a stable cavity output is the main technical challenge for the implementation of a lock-in detection scheme in a cavity enhanced spectrometer. In other words, to produce an INFAMOS signal, a stable output for a time period long enough for the lock-in amplifier to demodulate the signal is necessary. Optical-feedback locking is an ideal candidate for this purpose, as its application in cavity enhanced absorption spectroscopy provides a stable output on a single transverse mode.[102,150–152] Using this locking technique, the laser can be frequency locked to a resonant longitudinal mode of an external optical cav-

ity. The best known application of this optical feedback effect is in cavity-enhanced absorption spectroscopy (OF-CEAS).[102,150–154] A discussion of the underlying theory of OF-CEAS will be provided in the next section.

The INFAMOS spectrometer can be generically described as the combination of a Faraday modulation and an OF-CEAS spectrometer.[141] Along with OF-CEAS, the theory of Faraday modulation spectroscopy (FAMOS) and an introduction to a model for the INFAMOS lineshape will also be provided. The INFAMOS technique will be demonstrated by probing rovibrational transitions in the R-branch of nitric oxide with a QCL emitting at 5.3 μm.

The NO radical is an ideal test molecule for demonstrating INFAMOS, because its spectroscopic properties are well documented and it is stable in a nitrogen atmosphere. The detection of NO via the Faraday effect dates back to at least 1982,[155] and there are numerous reports on the sensitive detection of NO based on absorption spectroscopy. Nelson *et al.*[156] used a pulsed QCL within a 210 m multi-pass cell and reported a LOD of 0.12 ppbv $\mathrm{Hz}^{-1/2}$, while Moeskops *et al.*[157] used a shorter 76 m multi-pass cell to probe the P(7.5) transition with wavelength modulation spectroscopy (WMS) and reached a detection limit of 0.2 ppbv in 30 s. Kosterev *et al.*[158] employed a cw quantum cascade laser (QCL) in the same spectral region to detect NO using cavity ring-down spectroscopy (CRDS), and achieved a LOD of 0.7 ppbv in 8 s. Also based on CRDS, Stsiapura *et al.*[159] achieved 2 ppbv $\mathrm{Hz}^{-1/2}$ in 0.1 s with an external cavity QCL, while Heinrich *et al.*[68] demonstrated a remarkable LOD of 7 pptv in 70 s with a CO sideband laser. Recently, De *et al.*[101] claimed a detection limit of 70 pptv $\mathrm{Hz}^{-1/2}$ also using CRDS.

A final consideration must go to the observation of saturation effects in the INFAMOS spectra at low pressures (< 400 Torr). The combination of the optical power build-up in the cavity, the high output power (*ca.* 50 mW) provided by the QCL device and the strong absorption cross sections in the mid-IR mean that saturation can

significantly impact the INFAMOS lineshape. Similar effects have been previously observed in Faraday rotation experiments involving DC magnetic fields in atomic vapours and in noble gas discharges between pressures of 1 – 10 Torr and laser intensities up to 1 W cm^{-2},[160,161] but not in Faraday rotation spectra of gas-phase molecular samples. A more detailed description of saturation effects in INFAMOS is provided at the end of the chapter, and saturation is added to the INFAMOS lineshape model. The simultaneously acquired saturated OF-CEAS spectra are also used as a supporting material for extracting saturation parameters for a range of total pressures.

6.2 Theory

6.2.1 Optical-Feedback Cavity Enhanced Absorption Spectroscopy

Stray reflections that propagate back into the laser facet are a common occurrence in laser spectroscopy, and have long been known to adversely affect the operation of semiconductor devices. Early studies of optical feedback by Bogatov *et al.*, using a mirror (whose surface was parallel to the laser facet) to reflect the external field, showed that the coherence characteristics of a laser operated under such conditions were altered.[162] More studies using a similar experimental configuration, notably by Lang and Kobayashi, improved the understanding of the physical phenomena that govern semiconductor laser emission under different amounts of phase-matched light.[163] They observed that when optical feedback is supplied within the gain of the device, the power and frequency of the scanning laser will present anomalous jumps when compared to the same laser in a free running condition. These deviations are due to the external field acting as injection seeding and stimulating emission with similar properties to said field. This property of optical feedback allows the use of

the output of an external optical cavity to maintain the laser on resonance with said cavity for a time (> 1 ms) sufficient for INFAMOS operation.

OF-CEAS was initially developed by Morville *et al.*, using the *resonant* optical feedback provided by a V-shaped high-finesse optical cavity.[102] The V-shape configuration of the system was adopted to ensure that the light reflected directly from the first cavity mirror – the *non-resonant* feedback – would not return to the laser facet. When on resonance with a longitudinal mode of the cavity, an intracavity field builds up. When this resonant field reaches the laser facet, it stimulates emission at its frequency and thus "locks" the laser to the longitudinal mode of the cavity.[55,150]

The bandwidth of the resonant field is narrower than the free running laser linewidth, and longitudinal cavity mode bandwidths of the order of 10s of kHz are common for high finesse optical cavities. As a result of the high spectral purity of the feedback field, the linewidth of the laser is narrowed, the injection efficiency into the cavity increases, and the intracavity power builds up. As the laser frequency is scanned through the longitudinal modes of the cavity, separated by the free spectral range, $\Delta\nu_{cav}$,

$$\Delta\nu_{cav} = \frac{c}{2nL}, \tag{6.1}$$

where n is the refractive index of the medium and L is the physical length of the cavity, a comb-like structure emerges as the laser goes into and out of resonance with the modes. This comb-like structure can then be used to probe molecular absorbers in the cavity.

Figure 6.1 shows the typical transmission of an optical-feedback cavity, along with an illustration of the frequency locking. Most models relating the free running laser frequency to the feedback-coupled laser frequency were developed based on a V-shaped cavity design, such is the case of the model developed by Morville *et al.*[55] However, the INFAMOS spectrometer is based on a linear cavity design, for which a model for the frequency of a feedback-coupled QCL was developed by Manfred *et*

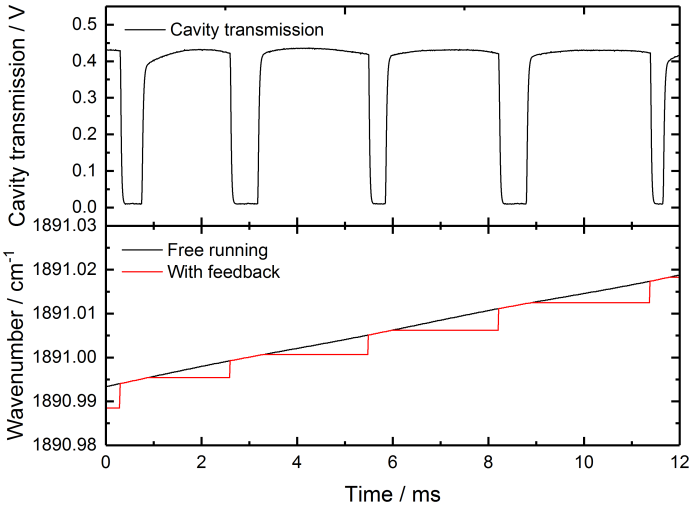


Figure 6.1: The top panel shows the typical cavity transmission spectrum as the laser is swept across several cavity longitudinal modes. The bottom panel shows the (simulated) frequency scan as a function of time. When on resonance with the cavity, the frequency of the laser remains locked to a mode for some time until it sharply unlocks towards the next cavity mode.

al.[100] This model is the basis of the theoretical description presented in this section. The free running, ν_0, and feedback coupled, ν_{fb}, frequencies are related by:

$$\nu_0 = \nu_{fb} + \frac{\sqrt{\beta}(1-R_0)c}{2\pi l n_0 \sqrt{R_0}} \left[\mathrm{Re}(h_{fb}) \sin\left(\frac{4\pi\nu_{fb}L'}{c} + \Phi\right) - \mathrm{Im}(h_{fb}) \cos\left(\frac{4\pi\nu_{fb}L'}{c} + \Phi\right) \right]. \tag{6.2}$$

The remaining variables are the feedback rate, β, the reflectivity of the laser facet, R_0, the laser cavity length, l, the refractive index of the gain medium, n_0, the laser to cavity distance, L', and the feedback transfer function, h_{fb}. For effectively locking the laser to optical feedback, the physical length of the cavity and the laser to cavity length must be matched (see Figure 6.2). This is done so the phase of the feedback matches that of optical emission at the laser facet. Consequently, a phase factor, Φ, is required in order to account for small path differences. The two main parameters that are not intrinsic to the QCL chip and can be used to control the quality of the optical

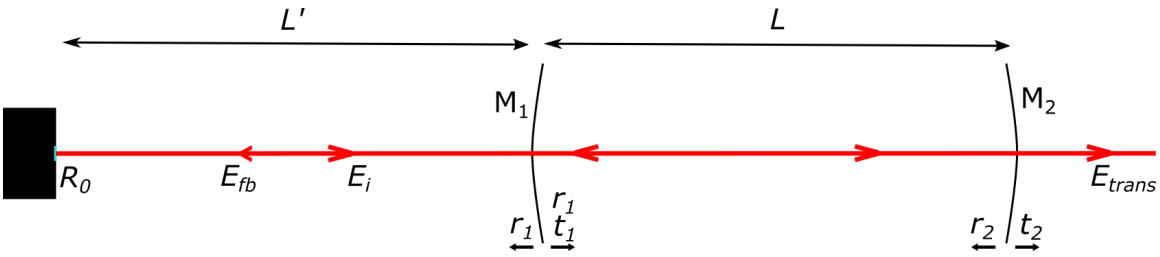


Figure 6.2: Scheme illustrating the injection of light into a linear resonant cavity. M_1 and M_2 represent the first and second cavity mirrors, and r_i and t_i represent the reflection and transmission coefficients of i^{th} mirror. R_0 is the reflectivity of the laser facet, L' and L are the laser to cavity distance and the cavity length, respectively.

feedback process are the feedback rate and the transfer function. The feedback rate is simply the ratio of the feedback power and the optical emission power at the laser facet. The transfer function, however, describes the modification of properties of the field, such as the phase and intensity, due to the action of the optical cavity. The transfer function for the *resonant* field returning to the laser facet is given by

$$h_{fb} = \frac{(1-R)\sqrt{R}\exp(-(2ik+\alpha)L)}{1-R(-(2ik+\alpha)L)}, \tag{6.3}$$

where R is the geometrical mean reflectivity of the cavity mirrors and is related to the reflection coefficient r by $R = |r|^2$ and to the transmissivity, T, by $T = (1-R)$ (in the case of lossless mirrors). The variable k is the wave vector defined as $k = 2\pi/\lambda$, α represents the cavity losses, and L is the cavity length. The total feedback reaching the laser facet, however, includes a non-resonant term that is proportional to $\sqrt{R}$ that arises from a back reflection from the first cavity mirror. Details on how this contribution is controlled are provided in the experimental section. A schematic representation of a linear cavity is presented in Figure 6.2 and highlights the variables used in Equation 6.3. Equation 6.4 was derived by Manfred[164] using the analysis by Davis[58] for the field leaking back through M_1 (see Figure 6.2)

$$E_{fb} = E_i\left[t_1^2 r_2 \exp\Big(-(2ik+\alpha)L\Big) + t_1^2 r_1 r_2 \exp\Big(-2(2ik+\alpha)L\Big) + ...\right], \tag{6.4}$$

where E_i is the incident electric field. t_i and r_i represent the transmission and reflection coefficients at each i^{th} cavity mirror, respectively.

Through a similar procedure, a transfer function that describes the transmitted field at the mirror M_2 can be derived. For a phase matched resonant cavity, this function takes the form:[100]

$$h_{trans} = \frac{E_{trans}}{E_0} = \frac{T\ \exp(-(2ik+\alpha)\frac{L}{2})}{1 - r_1 r_2\ \exp(-(2ik+\alpha)L)}, \tag{6.5}$$

where E_0 is the incident electric field. The presence of a molecular absorber reduces the amplitude of the transmitted field, resulting in an attenuation of the measured intensity of

$$\frac{I_\alpha}{I_i} = |h_{trans}|^2 = \frac{T^2\ \exp(-\alpha L)}{(1 - R\ \exp(-\alpha L))^2}. \tag{6.6}$$

An expression can then be written explicitly in terms of the absorption coefficient, α, thus allowing its determination by comparing the transmitted intensity with an absorber present with that of the empty cavity:

$$\alpha = \frac{(1-R)}{L}\left(\sqrt{\frac{I_o}{I_\alpha}} - 1\right). \tag{6.7}$$

This expression will be used to generate the OF-CEAS spectra that are acquired simultaneously with the INFAMOS spectra.

6.2.2 Faraday effect with a static magnetic field

The selectivity of INFAMOS towards paramagnetic species stems from its use of the Faraday effect. As mentioned previously, the Faraday effect consists of the rotation of the plane of polarisation of a linearly polarised wave as it traverses a magnetically induced birefringent medium.

In order to describe the physical origin of the Faraday effect, consider the basic

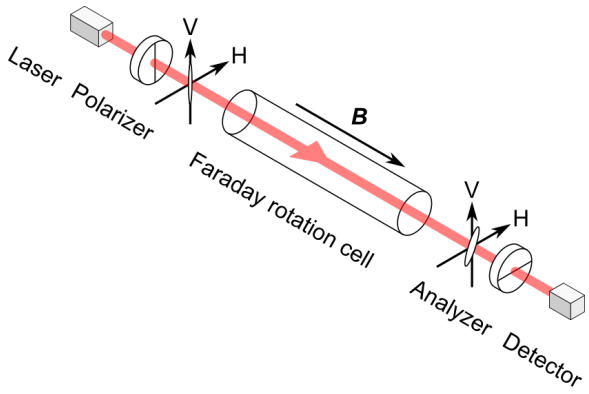


Figure 6.3: Scheme showing the experimental setup of a Faraday rotation spectrometer, consisting of a laser, a polariser before the optically active medium, a polarisation analyser (at $\sim 90°$with respect to the first polariser) after it and a detector.

Faraday rotation spectrometer shown in Figure 6.3. An electromagnetic wave experiences both attenuation and phase shift if its frequency is in the vicinity of a molecular transition. Furthermore, the presence of a magnetic field will lift the degeneracy of energy levels with magnetic quantum number M_J, that belong to a rotational state with total angular momentum quantum number J. Each of these subtransitions will have its own centre frequency and intensity, now offset by the action of the Zeeman effect by:[165]

$$\Delta\nu = \frac{B}{2\pi}((M \pm 1)g' - Mg), \tag{6.8}$$

where g' and g are the g-factors of the upper and lower state, respectively.

A linearly polarised electromagnetic wave can be treated as the combination of two circularly polarised components, left-hand (LHCP) and right-hand (RHCP) circularly polarised, each interacting independently with the aforementioned sets of subtransitions. LHCP interacts only with the $\Delta M_J = +1$ set, while RHCP interacts only with the $\Delta M_J = -1$ set. This results in different refractive indices and attenuations as a function of polarisation; magnetic circular birefringence (MCB) and magnetic circular dichroism (MCD), respectively. Figure 6.4 shows an example of how this splitting can produce magnetically induced birefringence in a sample by highlighting

the different phase shifts of the two circular polarisations. This phase shift difference is responsible for the rotation of the plane of polarisation of the wave.

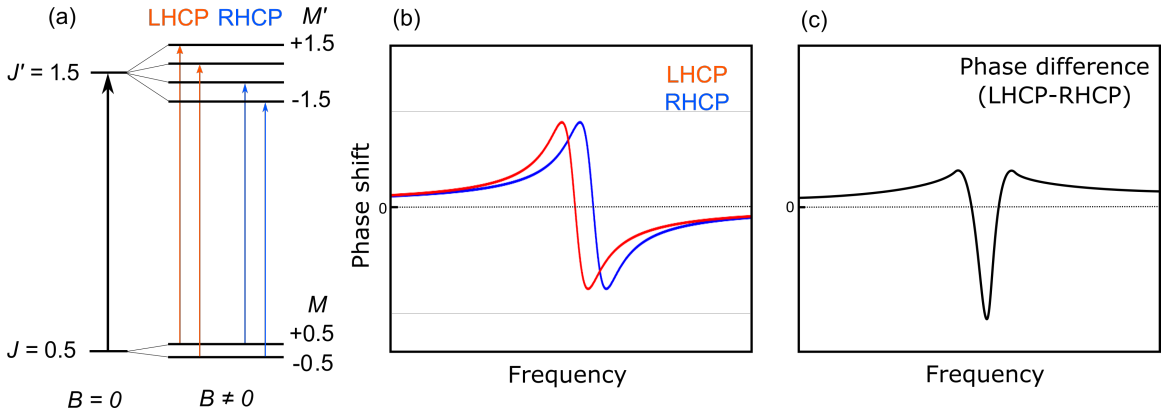


Figure 6.4: (a) Schematic representation of the splitting of a transition with total angular momentum $J = 0.5$ due to the action of a magnetic field: the Zeeman effect. (b) Total phase shift experienced by the LHCP and RHCP waves (ϕ^L and ϕ^R) for a range of frequencies in the vicinity of the transition in (a) with an applied magnetic field. (c) Phase shift difference, proportional to the Faraday rotation angle (see Equation 6.9).

The Faraday rotation angle, θ, can thus be obtained from the phase difference between the two LHCP and RHCP, ϕ^{L} and ϕ^{R}, components of the wave:

$$\theta = \frac{\phi^{\mathrm{L}} - \phi^{\mathrm{R}}}{2}. \tag{6.9}$$

An identical relation involving the attenuation of the two polarisations yields the dichroism

$$\mathscr{D} = \frac{\delta^{\mathrm{L}} - \delta^{\mathrm{R}}}{2}, \tag{6.10}$$

where δ^{L} and δ^{R} represent the attenuation of the LHCP and RHCP waves, respectively. Note that dichroism and birefringence are not independent phenomena, and similarly to absorption and dispersion, are connected via the Kramers-Kronig relations.[166]

The signal measured by a static field Faraday rotation spectrometer such as the

one depicted in Figure 6.3, assuming weak birefringence ($\theta \ll 1$), weak dichroism ($\mathscr{D} \ll 1$) and a polarisation analyser with a good extinction ratio ($\xi \ll 1$) is given by[141]

$$\begin{aligned} \mathcal{S} &= \mathcal{G}I\left[\xi + \beta^2 + \epsilon^2/2 - 2\beta^2\bar{\delta} + 2\beta\theta + 2\epsilon\mathscr{D} + \mathscr{D}^2\right], \\ &= \mathcal{S}_0 + \delta\mathcal{S} \end{aligned} \tag{6.11}$$

where the variables are an intrumental factor, $\mathcal{G}$, the intensity of the wave, I, the uncrossing angle of the analyser, β, and the average attenuation factor for the two circular polarisations, $\bar{\delta}$. The uncrossing angle, which describes the angle between the polarisation plane of the wave through the first polariser plus 90° and the polarisation analyser, is assumed to be small ($\beta < 5°$). The remaining parameter, ϵ, describes the amount of ellipticity of the field before the sample and is also assumed to be small ($\epsilon \ll 1$). The signal component represented by $\mathcal{S}_0 = \mathcal{G}I(\xi + \beta^2 + \epsilon^2/2)$ does not depend on the laser frequency or the magnetic field, and is thus the light that reaches the detector without any interaction: the baseline signal. The signal variation term, $\delta\mathcal{S}$, includes all the frequency dependent terms:

$$\delta\mathcal{S} = \mathcal{G}I(-2\beta^2\bar{\delta} + 2\beta\theta + 2\epsilon\mathscr{D} + \mathscr{D}^2). \tag{6.12}$$

Due to the $2\beta\theta$ contribution to the signal variation, it can be said that the Faraday rotation signal is proportional to β in the small angle approximation. The total noise includes contributions from laser intensity noise (proportional to $\beta^2 I$), quantum (shot) noise (proportional to $\beta\sqrt{I}$), and detector noise (independent of I and β).[147] If all the noise sources affecting a Faraday rotation instrument are known, the β that provides the best signal to noise ratio (SNR) can be computed.[143] Alternatively, it can be determined experimentally.

6.2.3 Enhancing the Faraday rotation angle with an optical cavity

The INFAMOS technique uses the extended interaction length with the sample by the means of an optical cavity in order to enhance the angular sensitivity of the system. This possibility was highlighted by Jacob *et al.*[146] by showing that the Faraday rotation angle, θ, scales with the (effective) interaction path length according to

$$\theta = \mathcal{V}LB, \tag{6.13}$$

where L is the path length, B is the magnitude of the magnetic field and $\mathcal{V}$ is the Verdet constant. This constant describes the strength of the Faraday effect for a given substance and has units of rad G^{-1} cm^{-1}, and is also wavelength and temperature dependent.

The path enhancement provided by a linear optical cavity, with finesse $\mathscr{F} \approx \sqrt{R}\pi(1-R)^{-1}$ can be described by the relation[141,146,148]

$$\theta_{cav} = \frac{2\mathscr{F}}{\pi}\theta. \tag{6.14}$$

For a cavity with mirrors of equal reflection coefficients $r_1 = r_2 = 0.9995$, a significant enhancement of the Faraday rotation angle by a factor of *ca.* 4000 can be achieved. However, additional losses caused by the medium or by the transverse profile of the electromagnetic field may reduce the effective path length of the optical cavity below this limit. This effective path length can be determined by calibrating the spectrometer before measurements, either with an absorber of known concentration (for example 100 % CO_2), or by measuring the ring-down time of the cavity.

6.2.4 Faraday effect with a time dependent field

A Faraday rotation spectrometer employing a static magnetic field is susceptible to noise at all frequencies, including at lower frequencies where it is significantly larger due to the flicker noise contribution. A common way of rejecting low frequency noise is by mixing the signal with a carrier wave at higher frequency, which has been successfully implemented into several Faraday modulation (FAMOS) spectrometers.[142,144,167] The simplest modulation scheme consists of modulating the magnetic field with a sinusoidal wave in a similar manner to wavelength modulation spectroscopy (WMS). Doing so modulates the transitions in time, making the measured Faraday rotation signal ($\mathcal{S}$) time-dependent.

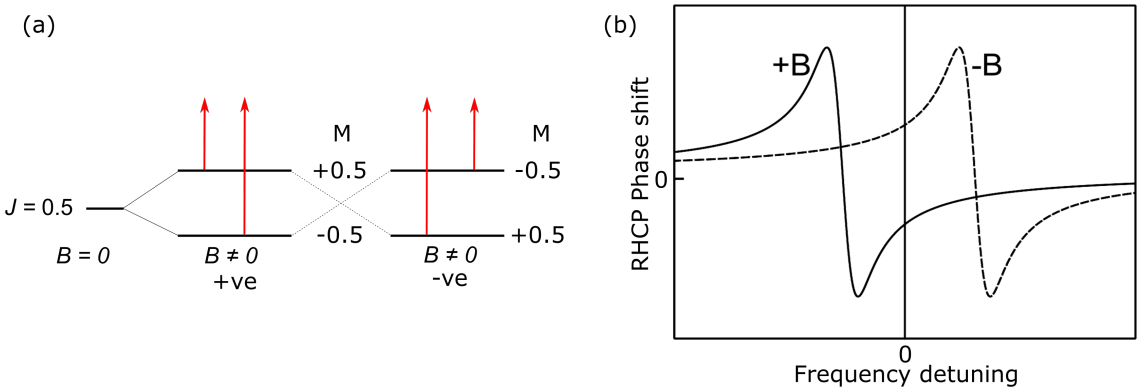


Figure 6.5: (a) Energy level diagram for a hypothetical transition with total angular momentum J with and without an alternating magnetic field. The M states swap in energy as the sign of the magnetic field changes. (b) As the magnetic field is sinusoidally modulated, the phase shift experienced by each circular polarisation state oscillates around the centre frequency of the transition with maximum splitting at the fields $+B$ and $-B$. Only the RHCP wave phase shift is represented for clarity.

The time dependence of the magnetic field, B, can be described in terms of the angular frequency of modulation, Ω, as

$$B(t) = B_0 \cos(\Omega t), \tag{6.15}$$

where B_0 is the maximum magnetic field amplitude. The output of a lock-in amplifier set to detect the first harmonic of an intensity modulated Faraday rotation signal $\mathcal{S}$ is proportional to the first Fourier coefficients Θ_1, $\mathfrak{D}_1$ and $\mathfrak{D}_1^{(2)}$ of the Fourier series representation of $\theta(t)$, $\mathscr{D}(t)$ and $\mathscr{D}^2(t)$[141,168]

$$X = \mathcal{G}I\left(\beta\ \mathrm{Re}[\Theta_1] + \epsilon\ \mathrm{Re}[\mathfrak{D}_1] + \mathrm{Re}[\mathfrak{D}_1^{(2)}]/2\right). \tag{6.16}$$

The real part of Θ_1 can be obtained numerically by evaluating the Faraday rotation angle θ as a function of time for a range of frequencies near a molecular transition. Consider θ and $\mathscr{D}$ at a fixed point in frequency in a sinusoidally varying magnetic field. In such a field, these two quantities will also become time dependent: $\theta(t) = \theta_0 \cos(\Omega t)$ and $\mathscr{D}(t) = \mathscr{D}_0 \cos(\Omega t)$ with first harmonics of $\Theta_1 = \theta_0/2$ and $\mathfrak{D}_1 = \mathscr{D}_0/2$. The final term of Equation 6.16 disappears, as $\mathfrak{D}_1^{(2)} = 0$, and as such the lock-in amplifier output becomes a direct measurement of the Faraday rotation angle and the dichroism. Equation 6.16 can thus be simplified to:

$$X = \frac{\mathcal{G}I}{2}[\beta\theta_0 + \epsilon\mathscr{D}_0]. \tag{6.17}$$

The Faraday rotation signal scales with the uncrossing angle β, but as previously mentioned in the case of a static magnetic field, the laser intensity noise and shot noise contributions are proportional to β^2 and β, respectively. Consequently, the optimum uncrossing angle still takes a small value $\beta < 5°$. Note also that the dichroism term ($\epsilon\mathscr{D}_0$) is independent of β but scales with the amount of ellipticity of the polarisation state, ϵ.

6.3 Model for the INFAMOS lineshape

The Faraday modulation spectrum of a selected molecular transition of a paramagnetic species can be calculated using Equation 6.9, for which the phase shifts and attenuations of the LHCP and RHCP waves need to be computed. The following analysis is appropriate for NO in the electronic ground state, a molecule that adheres to Hund's case (a). The B field lifts the degeneracy of a rotational energy level with total angular momentum J, and splits it into $2J+1$ substates with quantum number $M_J = -J, -J+1, ..., J-1, J$. Now consider a transition $J \rightarrow J'$ where the degeneracy of the $M_{J'}$ states is also lifted by the Zeeman effect. If the magnetic field is applied longitudinally to the propagation of the electromagnetic wave coupling the two states, only $M_J \rightarrow M_{J'} = M_J \pm 1$ transitions are allowed. Since a LHCP wave will only interact with the $M_J \rightarrow M_{J'} = M_J + 1$ set and a RHCP wave with the $M_J \rightarrow M_{J'} = M_J - 1$ set, the two polarisations will experience different phase shifts ($\phi^{L/R}$) which are described as follows:[141]

$$\begin{aligned} \phi^{\mathrm{L}} &= \frac{\mathscr{N}\mathscr{S}L}{2} \sum_{M=-J}^{J} \bar{S}_{\mathrm{M}}^{+}\, \chi(\mathscr{W}_{M}^{+}, \mathscr{V}) \\ \phi^{\mathrm{R}} &= \frac{\mathscr{N}\mathscr{S}L}{2} \sum_{M=-J}^{J} \bar{S}_{\mathrm{M}}^{-}\, \chi(\mathscr{W}_{M}^{-}, \mathscr{V}). \end{aligned} \tag{6.18}$$

The summation pre-factor includes the integrated absorption cross section, $\mathscr{S}$, available in the HITRAN database[65], the molecular number density, $\mathscr{N}$, and the interaction path length, L, all of which are constant for a given transition and a set of selected experimental conditions. The total phase shift of a polarisation state is the sum of the phase shifts induced by the individual $M_J \rightarrow M_{J'} = M_J \pm 1$ transitions. These have different intensities relative to the total intensity, represented by $\bar{S}_{\mathrm{M}}^{+}$ for a $M_J \rightarrow M_J + 1$ transition, which can be expressed through the Wigner 3-j symbol

as follows:

$$\bar{S}_M^+ = 3 \begin{pmatrix} J' & 1 & J \\ -(M+1) & 1 & M \end{pmatrix}^2 . \tag{6.19}$$

For the evaluation of the Wigner 3-j symbols, an existing MATLAB algorithm was used. The final variable of equations 6.18 is the normalised dispersive lineshape, χ, which corresponds to the imaginary part of the scaled complementary error function w, evaluated in MATLAB.[169] The input parameters of this function are the Doppler normalised detuning, $\mathscr{W}_M^+$, and the Voigt parameter, $\mathscr{V}$. The latter can be calculated from the Gaussian and Lorentzian HWHM, γ_G and γ_L, respectively, via

$$\mathscr{V} = (\sqrt{\ln 2}/\gamma_G)\gamma_L, \tag{6.20}$$

where γ_G remains constant at constant temperature (298 K is assumed) and γ_L, the pressure dependent collisional broadening term, can be calculated for a selected transition and total pressure using the collisional broadening parameters available in the HITRAN database.[65] The Doppler normalised detuning, $\mathscr{W}_M^+$, is evaluated as follows:

$$\mathscr{W}_M^+ = \frac{\sqrt{\ln 2}}{\gamma_G} \left\{ \nu - \left[\nu_0 - \left((M+1)g' - Mg \right) \mu_B B \right] \right\}, \tag{6.21}$$

where ν_0 is the centre of the transition in the zero-field case, μ_B is the Bohr magneton, and B is the magnetic field amplitude.

The attenuations experienced by the LHCP and RHCP waves are determined using 6.18:

$$\begin{aligned} \delta^{\mathrm{L}} &= \frac{\mathscr{N}\mathscr{S}L}{2} \sum_{M=-J}^{J} \bar{S}_{\mathrm{M}}^+ \, \eta(\mathscr{W}_M^+, \mathscr{V}) \\ \delta^{\mathrm{R}} &= \frac{\mathscr{N}\mathscr{S}L}{2} \sum_{M=-J}^{J} \bar{S}_{\mathrm{M}}^- \, \eta(\mathscr{W}_M^-, \mathscr{V}). \end{aligned} \tag{6.22}$$

In this case, the absorptive lineshape, η, is used instead of the dispersive one. This lineshape function uses the same parameters as described for the calculation of the phase shifts, but uses the real part of the scaled complementary error function w.

Table 6.1: Parameters for the simulation of the $R(3.5)_{3/2}$ transition of NO. a: assumed value; c: calculated value.

Parameter		Value			Unit	Ref.
angular momentum	J	3.5	$\rightarrow$	4.5		
g-factor	g	0.163	$\rightarrow$	0.0937		[165]
Zeeman splitting	$\mu_B g$	7.6×10^{-6}	$\rightarrow$	4.3×10^{-6}	cm^{-1}/G	c
molecular mass	m	4.9815×10^{-26}			kg	c
integrated cross-section	$\mathscr{S}$	4.6454×10^{-20}			$cm^2\,cm^{-1}$	[65]
transition frequency	ν_0	1890.913			cm^{-1}	[65]
pressure-broadening param.	γ	8.13×10^{-5}			$cm^{-1}/Torr$	[65]
Doppler width (HWHM)	γ_G	2.13×10^{-3}			cm^{-1}	c
Lorentzian width (HWHM)	γ_L	4.07×10^{-3}			cm^{-1}	c
Voigt parameter	$\mathscr{V}$	1.57				c
pressure	p	50			Torr	a
temperature	T	298			K	a
magnetic field	B	1000			G	a
concentration		1			ppb	a

Consider the X $^2\Pi_{3/2}R(3.5)$ $v = 1 \leftarrow 0$ transition of NO at *ca.* 1891 cm^{-1}, which will be the main subject of the experimental studies presented in this chapter. For the hypothetical conditions shown in Table 6.1, the attenuation and phase shifts experienced by each of the circular polarisation states are calculated for each $M \rightarrow M \pm 1$ transition for the static field case. With that intention, MATLAB code was used to compute the Wigner 3-j symbols and the lineshape functions χ and η. The results are presented in Figure 6.6. In (a), the Zeeman splitting of the M states is shown along with the individual $M \rightarrow \pm 1$ transitions. The panels labelled (b) and (d) show the phase shift and the attenuation that are caused by each of the individual transitions, respectively. The sum of all phase shift and attenuation contributions result in the polarisation rotation angle and total attenuation shown in the panels (c)

and (e), respectively. In this simulation, the magnetic field of 1000 G was chosen to maximise the splitting of the M sublevels, and the parameters $\beta = 5°$ and $\epsilon = 0.01$ were chosen.

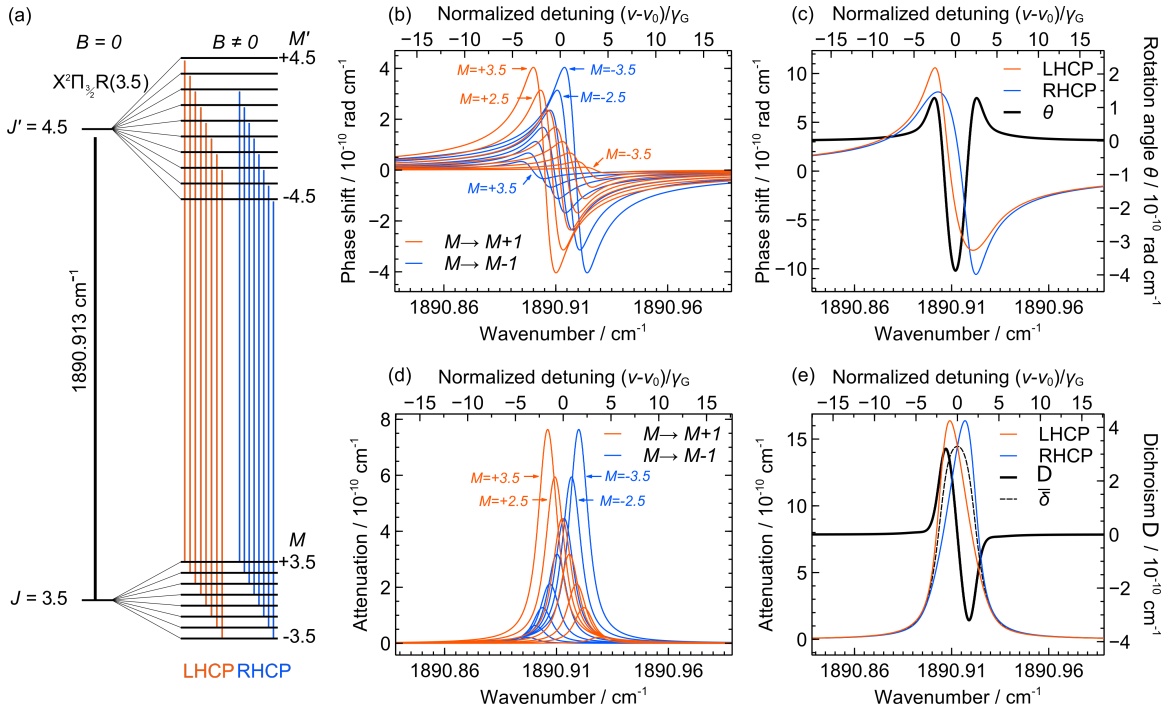


Figure 6.6: (a) Energy level diagram for the $R(3.5)_{3/2}$ $v = 1 \leftarrow 0$ transition of NO, highlighting the Zeeman splitting of the M states. (b) Phase shifts of each circular polarisation state induced by each individual $M \rightarrow M \pm 1$ transition. (c) Total phase shift experienced by a LHCP and RHCP wave, and phase shift difference, θ. (d) Attenuation to each circular polarisation state induced by each individual $M \rightarrow M \pm 1$ transition. (e) Sum of all attenuation contributions to both polarisation states, and the resulting dichroism $\mathscr{D}$ and average attenuation $\bar{\delta}$.

It is important, however, to compare the expected Faraday rotation angle with a static field with the output of the lock-in amplifier. To do so, the measured signal variation $\delta\mathcal{S} = \mathcal{G}I(-2\beta^2\bar{\delta} + 2\beta\theta + 2\epsilon\mathscr{D} + \mathscr{D}^2)$ (Equation 6.12) as a function of absorption, MCB and MCD is computed with the choice of $\beta = 873\,\text{mrad} = 5\,°$ and $\epsilon = 0.01$. In this example, $\mathscr{D} \sim 10^{-10} \ll \epsilon$ and therefore $\mathscr{D}^2 \ll 2\epsilon\mathscr{D}$. The $\mathscr{D}^2$ term in Equation 6.12 can thus be neglected. Next, the lock-in amplifier output, X, given by Equation 6.16, is simulated for the $R(3.5)_{3/2}$ $v = 1 \leftarrow 0$ transition of NO using

the same conditions as for the simulation shown in Figure 6.6. The result is shown in Figure 6.7. The signal shapes are nearly identical with a small difference at the line

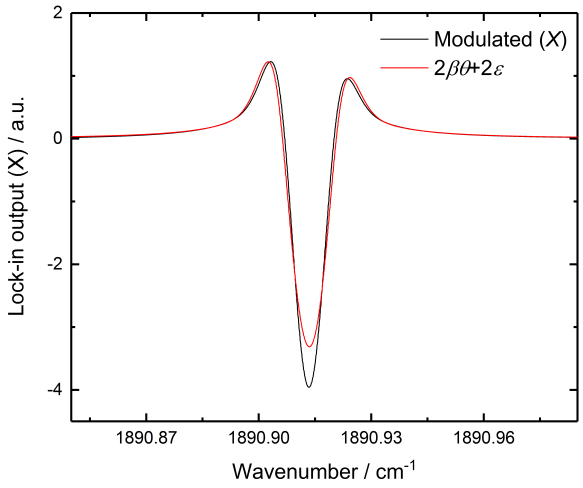


Figure 6.7: Simulated lock-in output X (with a modulated magnetic field), obtained by evaluating the first Fourier coefficients of the Faraday rotation angle θ and the dichroism $\mathscr{D}$ using Equation 6.16, compared to the signal expected with a static field.

centre owing to the large amplitude of the magnetic field (1000 G). The INFAMOS spectrometer operates with much more modest field strengths ($<$ 300 G), at which the discrepancy between the two signals is small.

6.3.1 The effect of pressure broadening and magnetic field amplitude

The Faraday rotation signal shows a strong dependence on both the total pressure and the amplitude of the magnetic field. Figure 6.8 (a) shows the simulated signal amplitude at the line centre of the $\mathrm{R}(3.5)_{3/2}$ $v = 1 \leftarrow 0$ transition at a range of pressures and magnetic fields. The general trend is that a stronger magnetic field produces larger signals. This is due to the proportionality between the Faraday rotation angle and the phase shift difference, $\phi_L - \phi_R$, between LHCP and RHCP waves. Within the range of magnetic field amplitudes used in this work, the phase shift difference at the $\mathrm{R}(3.5)_{3/2}$ $v = 1 \leftarrow 0$ transition centre increases linearly as a

function of B.

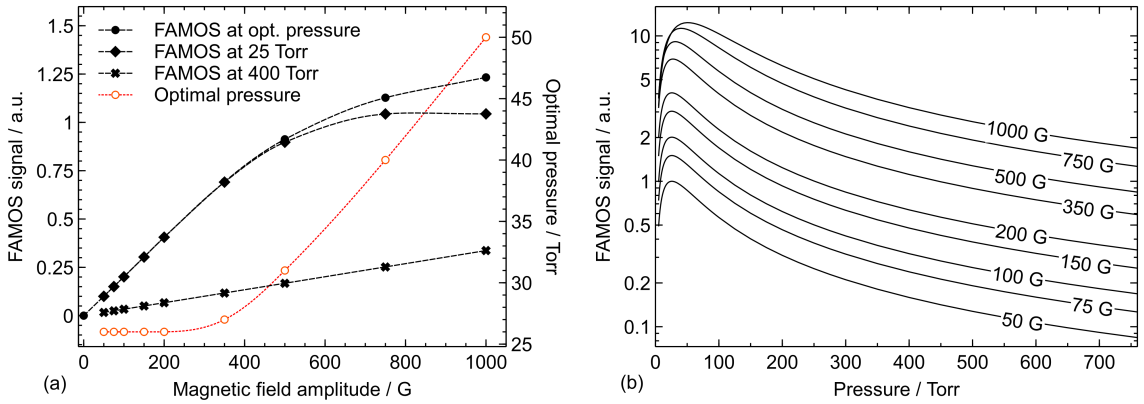


Figure 6.8: (a) The evolution of the Faraday rotation signal (FAMOS) at the line centre as a function of magnetic field amplitude. (b) The evolution of the FAMOS signal as a function of total pressure for a range magnetic field amplitudes.

Figure 6.8 (b) shows the FAMOS signal for a range of pressures for various magnetic field amplitudes, highlighting the maxima at *ca.* 25 Torr which shifts towards *ca.* 50 Torr for larger fields. Since the magnetic field amplitudes used in this work are in the $B < 200$ G limit, 25 Torr is the optimum pressure. At higher pressures, the signal gradually decreases due to collisional effects. The broadening of the dispersive lineshapes χ will increase the overlap between all the individual $M \rightarrow M \pm 1$ transitions, thus countering the effect of having a large magnetic field. It should be noted however that the INFAMOS spectrometer is more suited for measurements of pressure broadened lines, as its frequency resolution is limited by the FSR of the optical cavity. A 78 cm long cavity has a frequency resolution of 192 MHz, which is larger than the Doppler width of NO at room temperature ($\sim$ 125 MHz). For this reason, the majority of the spectra presented in this chapter were acquired at higher total pressures, sacrificing a large INFAMOS signal for more spectral points.

6.4 Experimental

Figure 6.9 shows a schematic representation of the INFAMOS spectrometer. A DFB-QCL (Maxion M575AY) operating in cw mode is the source. The laser emits up to 100 mW of optical power, within a range of 1883 – 1894 cm^{-1} and is driven by a home-built driver. As a requirement for the operation of the linear optical-feedback cavity,[100] an iris, onto which the laser is focused by a parabolic mirror, is placed after an optical delay line with the aim of spatially filtering out non-resonant optical feedback, ensuring that the resonant feedback returning from the cavity is always dominant. The piezo mounted mirror (MPZ) before the cavity is responsible for fine adjustment of the laser to cavity distance to ensure optimum spatial phase matching of the feedback field into the laser. After a mode-matching lens and a polariser, two highly reflective dielectric coating mirrors (Los Gatos Research, R = 0.9998) comprise the cavity, which is situated within the core of a solenoid. A beam splitter (Thorlabs BSW510) separates the cavity output into two paths that are simultaneously collected by detectors D1 and D2. The first photodetector, D1 (Vigo System S.A. PVI-2TE-6/VPDC-20I), is placed after a polarisation analyser (LOT-QuantumDesign SIR3-5) at an uncrossing angle $\beta \approx 2°$. The output of D1 is demodulated by a lock-in amplifier (Stanford Research Systems SR830) which in turn drives the solenoid with an amplified (QSC Audio RMX 4050 HD) 7.5 kHz sine wave. The second photodetector, D2 (Vigo System S.A. PVMI-3TE-10.6-MIPDC-F-20), monitors the cavity output simultaneously, and produces an OF-CEAS spectrum.

Trace concentrations of NO are achieved by mixing two different flows, the first being a calibrated 15 ppmv NO in nitrogen gas mixture (BOC gases) and the second dry nitrogen (BOC gases). The two flows were controlled by two mass flow controllers (Tylan FC-260), combined, and passed through the cavity. The total pressure is chosen by maintaining a constant gas inflow of NO and N_2 and restricting the outflow with a valve. The total pressure increases until these two flows equilibrate. The oscil-

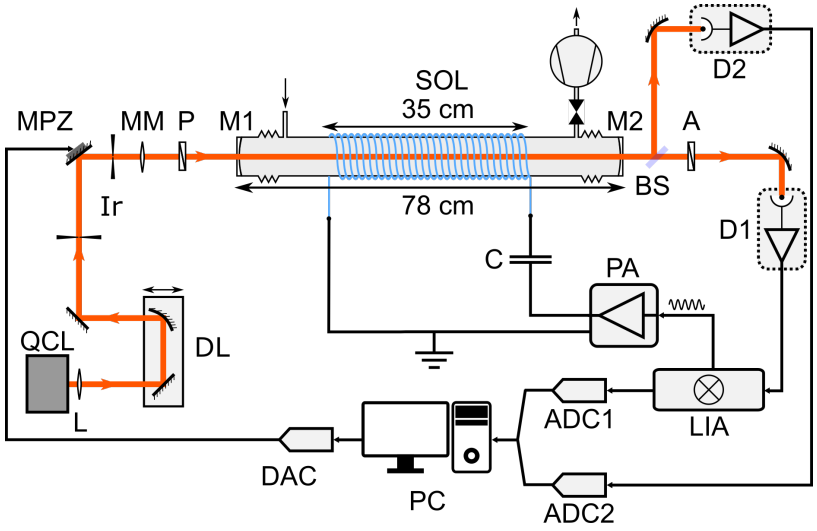


Figure 6.9: Schematic diagram of the INFAMOS spectrometer. QCL: Quantum Cascade Laser; L: Collimating lens; DL: Optical delay line; Ir: Iris; MPZ: Piezo mounted mirror; MM: Mode matching lens; P: Polariser; M1 and M2: Cavity mirrors 1 and 2; SOL: Solenoid; BS: Beam splitter; A: Analyser; D1 and D2: Detectors 1 and 2; LIA: Lock-in amplifier; PA: Audio amplifier; ADC1 and 2: Analog to digital converter 1 and 2; DAC: Data acquisition card.

lating magnetic field that is applied longitudinally to the optical cavity is generated by a water cooled solenoid capable of producing magnetic fields of strengths up to 240 G.[141] The solenoid is connected in series with a home-made capacitor to produce a circuit with a resonance frequency of 7.5 kHz.

The laser frequency is slowly (<5 Hz repetition rate) scanned through the cavity modes by applying a current modulation to the driver with a function generator (Rigol, DG 1022). The beam collected at the detector D1, shown in Figure 6.9, is represented as $\mathcal{S}$ in Equation 6.11 and depends on the Faraday rotation angle, θ. This signal is demodulated by the lock-in amplifier at the modulation frequency of the magnetic field and with a low-pass filter time constant, t_c, of 100 μs. A 24 dB/octave low-pass filter roll-off was selected, yielding a measurement bandwidth for a single-scan spectrum of 780 Hz.[170] The settling time, t_s, the time required to correctly demodulate the signals, is $t_s \approx 10t_c$ with this filter roll-off setting, and therefore approximately 1 ms with the selected t_c. A stable cavity output can only

be maintained during a mode for a time of *ca.* 4 ms, establishing an upper limit to t_s.

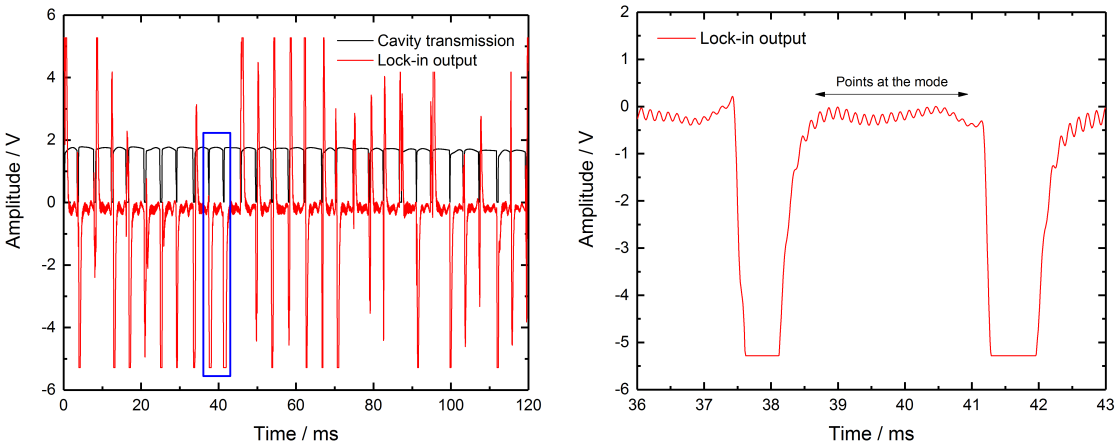
The output of the lock-in is acquired by an analog-to-digital acquisition card at a sampling rate of 100 kSa/s, and the same card is used to digitise the output of detector D2. The digitised waveforms are simultaneously recorded using a LabVIEW (National Instruments) program, which is also used to measure the asymmetry of the cavity modes and ensure these remain symmetrical by applying a corresponding correction to the piezo transducer MPZ.[100]

6.5 Results

6.5.1 Preliminary INFAMOS and OF-CEAS measurements

Figure 6.10 shows the typical cavity transmission overlaid with the lock-in amplifier output without the presence of any molecular absorber. As outlined in section 1.2.1, the cavity's mode structure is characterised by sudden transmission changes due to the locking and unlocking to different longitudinal modes. Figure 6.10 (a), shows that the effect of the cavity transmission structure on the lock-in output is the production of transients of random shape and magnitude at the start and end of each cavity locking period, which need to be removed to produce an INFAMOS spectrum.

The spectra in Figure 6.11 (a) show the raw single-sweep data, obtained at a total pressure of 6 Torr, with a NO mixing ratio of 1.7 ppm in N_2 and a magnetic field amplitude of 79 G. The bottom panel shows the lock-in output sweeping over the $R(3.5)_{3/2}$ $\nu = 1 \leftarrow 0$ transition of NO and highlights the step-like structure of the INFAMOS signal, a consequence of the free spectral range of the optical cavity. For extracting the INFAMOS signal from the lock-in output, a MATLAB routine is used to post-process the raw data. Here, a gate is centred on each mode with the aim of excluding the transients caused by the sudden changes in cavity transmission, and the



(a) (b)

Figure 6.10: Typical raw cavity transmission and lock-in amplifier output spectra. The sharp transients on the lock-in output coincide in time with the locking and unlocking of the frequency from cavity modes.

gated signal is then averaged. The length of the gate is given by the duration of the region labelled as "Points at the mode" in Figure 6.10 (b). The INFAMOS spectrum presented in Figure 6.11 (b) is obtained by processing the raw signal shown in Figure 6.11 (a). After the removal of the transients and averaging the points at each mode, the resulting INFAMOS signal presents a similar shape to the second derivative of a conventional absorption signal.

Interestingly, the top panel of Figure 6.11 (a) shows no decrease in cavity transmission as the laser is tuned over the $R(3.5)_{3/2}$ $\nu = 1 \leftarrow 0$ transition of NO, despite the clear signal observed in the INFAMOS spectrum. According to HITRAN,[65] this transition has an integrated absorption cross-section of $\mathscr{S} = 4.8 \times 10^{-20}$ cm^{-1}/(molecule^{-1} cm^{-2}) which corresponds to an absorption coefficient at the line centre (at a total pressure of 6 Torr) of $\alpha \approx 3 \times 10^{-6}$ cm^{-1}. Therefore, according to Equation 6.7, the transmitted intensity should decrease by over a factor of 2 due to this absorption line (in a 78 cm long cavity with $R = 0.9995$). To investigate the cause of this discrepancy between the measured and theoretical cavity transmission, two OF-CEAS spectra of the same NO transition were recorded using laser powers of 35 mW and 6 mW, while

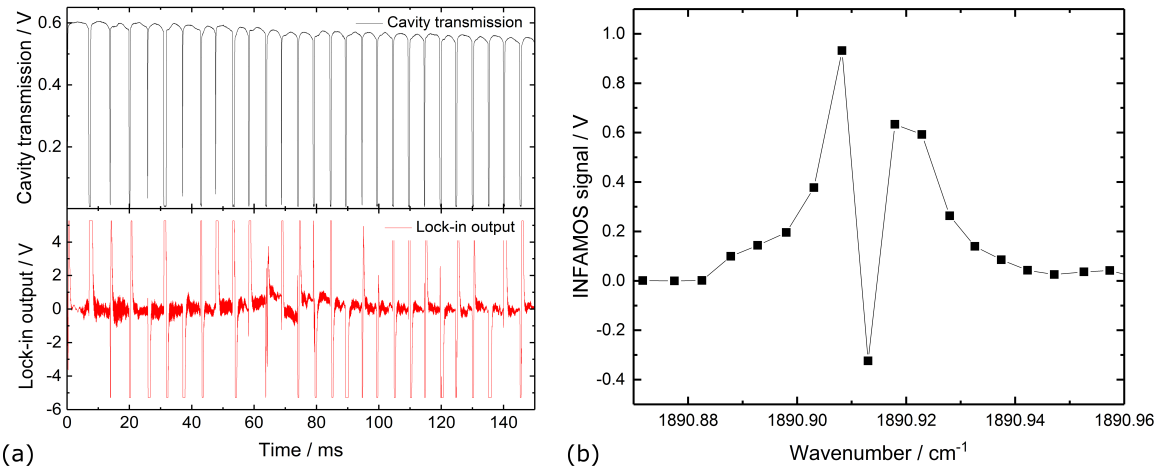


Figure 6.11: (a) The top panel shows the optical cavity transmission, while the bottom panel shows the simultaneously recorded lock-in output with a magnetic field amplitude of 79 G and an NO:N_2 gas mixture at a total pressure of 6 Torr. (b) INFAMOS spectrum obtained from the gating the lock-in output data shown in (a).

keeping the total pressure and NO:N_2 mixing ratio constant. These spectra, along with their raw cavity transmission, are shown in Figure 6.12. The laser power was reduced from 35 mW in (a) and (c) to 6 mW in (b) and (d) by using a polariser placed before the optical cavity. The absorption coefficient of the transitions shown increases markedly from (c) to (d). This is consistent with the optical saturation of the transitions. Saturation effects in both INFAMOS and OF-CEAS will be discussed in more detail at the end of this chapter.

Since the feedback ratio, and consequently the mode locking time, are significantly decreased by reducing the power of the laser reaching the optical cavity, using this technique to remove saturation makes INFAMOS impractical. This becomes obvious by comparing the locking time of the laser in the raw cavity transmission spectra between Figure 6.12 (a) and (b); with 35 mW the modes are $\sim$ 2.5 ms wide, while at 6 mW they are only $\sim$ 0.5 ms wide. At lower power, the time on resonance is insufficient for the lock-in to demodulate the signal and extract INFAMOS spectral points. An alternative way in which to produce saturation-free spectra is to increase the vibrational relaxation rate by raising the total pressure. Therefore, all measurements

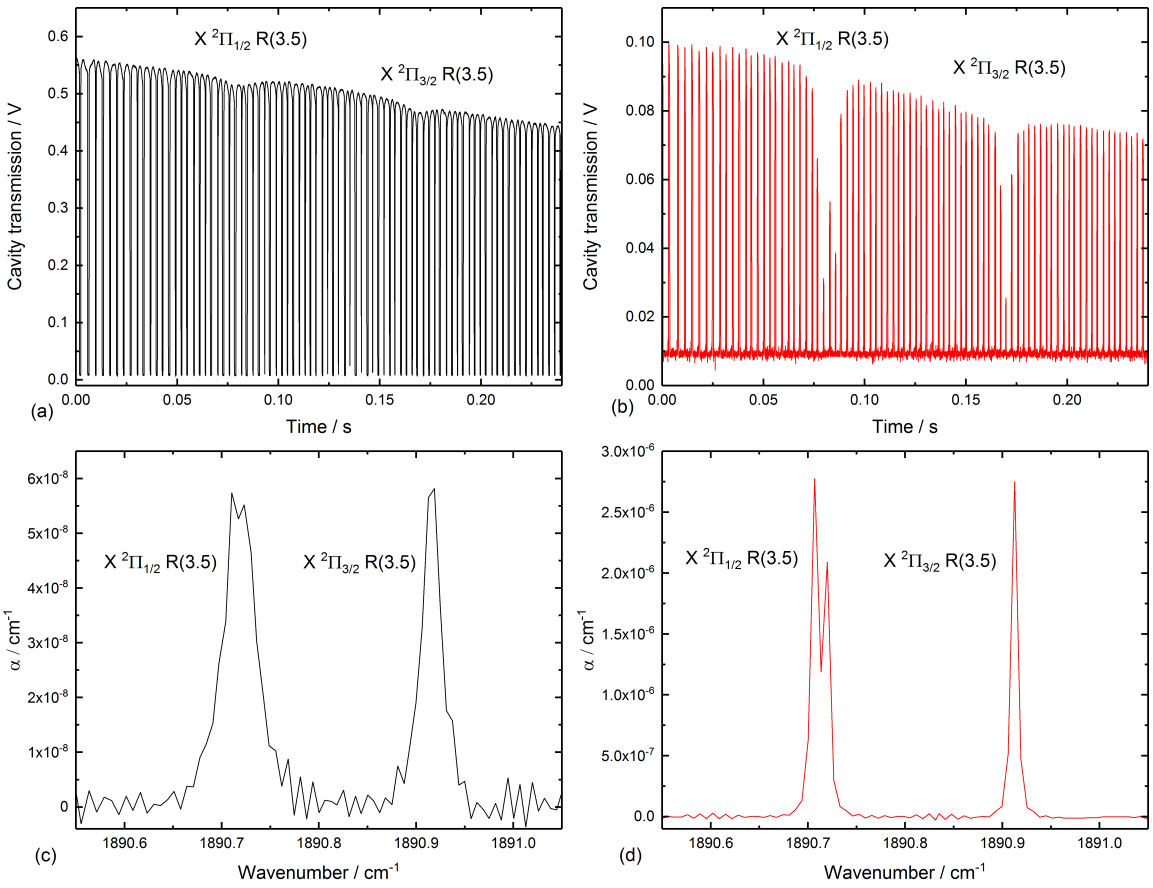


Figure 6.12: (a) and (b) show the raw cavity transmission as the laser is scanned over the $R(3.5)_{1/2}$ and $R(3.5)_{3/2}$ transitions of NO. Both spectra were recorded at a total pressure of 21 Torr and NO concentration of 1 ppmv. The laser power reaching the cavity is 35 mW in (a) and 6 mW in (b). (c) and (d) are the processed OF-CEAS spectra produced from (a) and (b), respectively, and reveals that the power reduction increases the measured absorption coefficient in (d).

shown in the next section were obtained at pressures > 200 Torr.

6.5.2 INFAMOS spectra with low saturation - sensitivity analysis

Figure 6.13 shows INFAMOS spectra obtained by scanning over the $R(3.5)_{3/2}$ $v = 1 \leftarrow 0$ transition of NO with a magnetic field amplitude of 85 G and a laser power of 35 mW. The spectrum in (a) was obtained at 237 Torr with an NO mixing ratio of 110 ppbv in N_2. It is overlaid with a simulation based on the model presented in section 6.3; despite the reasonably good agreement between the model and the data, a total pressure of $\sim$ 280 Torr had to be used in the simulation to obtain the correct signal width. This 18% discrepancy was also confirmed by the simultaneously obtained OF-CEAS measurement. The overestimation of the signal amplitude at the line centre, also in Figure 6.13 (a), is due optical saturation effects of the NO transition. This phenomenon is also responsible for the overestimation of the measurement pressure, since saturation also causes the broadening of spectral lines (see later).

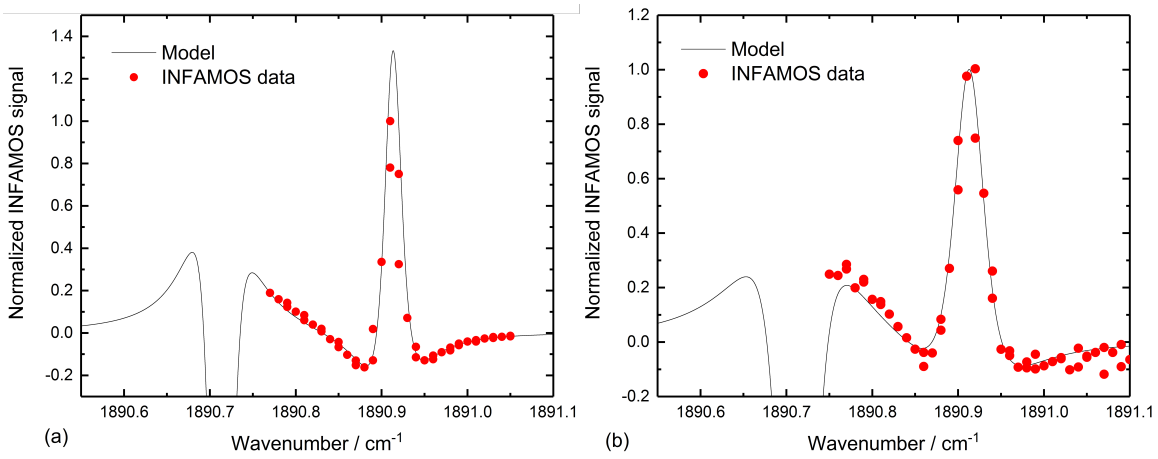


Figure 6.13: INFAMOS spectra of the $R(3.5)_{3/2}$ transition of NO. (a) Was obtained at a total pressure of 237 Torr and 110 ppbv, while (b) was taken at a total pressure of 426 Torr and 38 ppbv. The magnetic field amplitude was 85 G in both cases, and the overlaid simulation shows the vicinity of the transition, including the $R(3.5)_{1/2}$ transition at lower wavenumber. Both spectra were averaged 100 times.

The spectrum shown in Figure 6.13 (b) was taken at a higher total pressure (426 Torr) by increasing the flow rate of N_2 into the cavity, lowering the NO:N_2 mixing ratio to 38 ppbv. The signal to noise ratio (SNR) is poorer at the measurement taken at 426 Torr than at 237 Torr, which can be explained by the dependence of the INFAMOS signal on pressure shown in Figure 6.8, as well as by the lower concentration of NO. There is however a good agreement between the model and the experimental data, and the experimentally measured total pressure and that used in the simulation. The good agreement between the measured and simulated INFAMOS lineshapes at 426 Torr is a result of the reduction of optical saturation effects.

Now that the conditions at which the INFAMOS lineshape can be successfully modelled have been identified, the sensitivity of the technique is investigated. To assess the ultimate sensitivity of the instrument, an analysis of the temporal stability of the system is required. With OF-CEAS type spectrometers, maximum sensitivity can be achieved without large amounts of averaging; typically within a few hundred averaged scans.[55] The Allan-Werle variance analysis is a widely accepted method for determining the temporal stability of this type of instrument in the spectroscopy community.[171] This statistical method is based on the analysis of the variance of a measurement as a function of a range of averaging times, which are plotted on a log-log scale – the Allan-Werle plot. Therefore, the minimum of this plot corresponds to the number of averages, or averaging time, required to minimise the measurement variance. Approximately 70 000 INFAMOS signals were recorded and the amplitude of a single longitudinal cavity mode was monitored in order to produce an Allan-Werle plot, shown in Figure 6.14.

The plot reveals that a gradual improvement occurs down to a bandwidth 0.4 Hz, where the minimum is reached at *ca.* 130 averages. Between 1 and 11 averages, corresponding to a measurement bandwidth of approximately 10 Hz, the plot shows white noise (390 nV $Hz^{-1/2}$) behaviour. The detector and shot noise levels are also

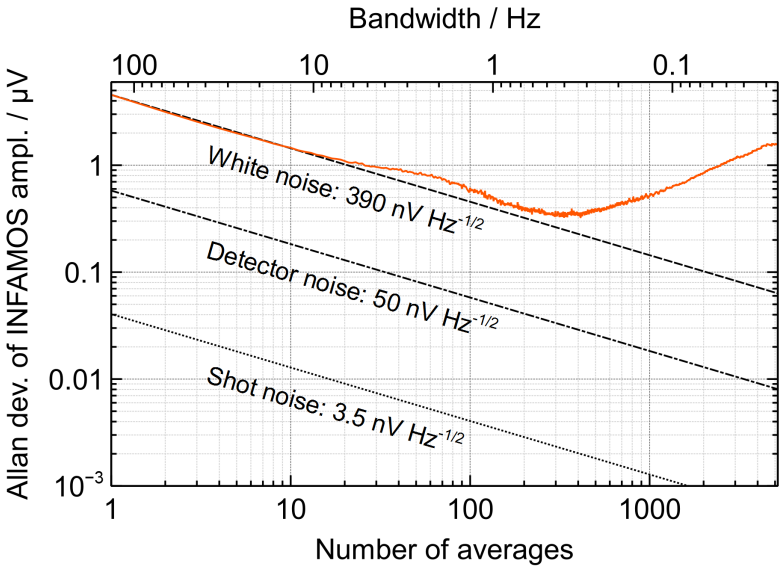


Figure 6.14: Allan-Werle plot that quantifies the noise of the INFAMOS system with measurement bandwidths under 100 Hz. The PSD of the detector noise is assumed to be flat within this bandwidth range.

shown in Figure 6.14. Shot noise has a flat PSD, while detector noise includes a frequency dependent 1/f component. However with measurement bandwidths < 100 Hz around a modulation frequency of 7.5 kHz, the latter noise source can also be considered frequency independent. An important consideration regarding the stability of the instrument must be made: the optimum averaging time showed day-to-day variations depending on conditions such as changes in room temperature and cavity alignment. The shot noise level was calculated using

$$i_{shot} = \sqrt{2eVG}, \tag{6.23}$$

by measuring the voltage output of the detector with the cavity on resonance ($V = 3.8$mV) and using the transimpedance gain of the device, $G = 10^4$ V A^{-1}. The value obtained was $i_{shot} = 3.5$ nV Hz$^{-1/2}$. The experimentally measured noise level is above the detector noise level by a factor of 8 and above the shot noise by a factor of *ca.* 110. There is thus a significant margin for improvement if the cavity were to be

mechanically stabilised.

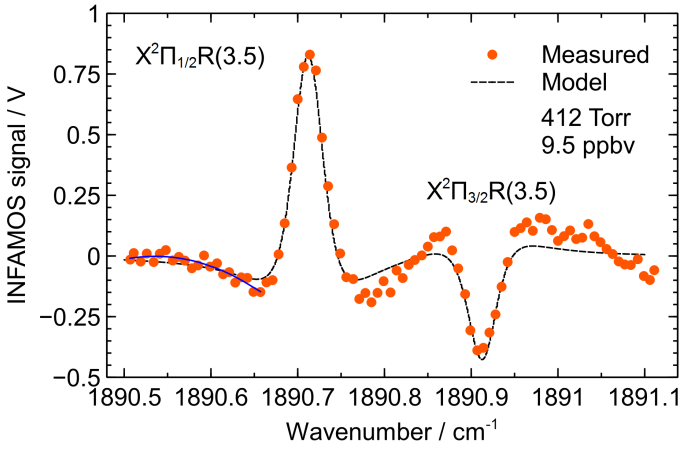


Figure 6.15: INFAMOS spectrum taken at a total pressure of 412 Torr, 9.5 ppbv NO concentration and magnetic field amplitude 98 G. The spectrum shows the $R(3.5)_{1/2}$ and $R(3.5)_{3/2}$ transitions of NO, and is the result of 170 averages, which corresponds to a measurement bandwidth of 0.77 Hz.

The limit of detection of INFAMOS was attained by preparing a low concentration sample of NO in nitrogen (9.5 ppbv) and taking an SNR measurement. The spectrum shown in Figure 6.15 was taken at a total pressure of 412 Torr in order to avoid saturation effects and at a field amplitude of 98 G. The maximum of the $R(3.5)_{1/2}$ transition was used, as at pressures above *ca.* 150 Torr the e and f components of the Λ doublet of this transition merge due to pressure broadening effects, making the absorption and Faraday rotation signals larger than the adjacent $R(3.5)_{3/2}$ transition. To determine the noise, the standard deviation of the residuals of a parabola fitted to the data points at < 1890.65 cm^{-1} of the spectrum was used. The value obtained was 0.0191, which compared to the maximum of the spectrum at 1.02, yielded a SNR of 54 and a limit of detection (at SNR = 1) of 0.18 ppbv. For these conditions, the Faraday rotation angle per unit length computed at the maximum point of the INFAMOS spectrum (at the centre of the $R(3.5)_{1/2}$ transition for 0.18 ppbv) gives an angular sensitivity of the system of 4×10^{-12} rad cm^{-1}; for a single pass through the 35 cm

Table 6.2: Comparison of performances of recently reported (IN)FAMOS systems.

$\theta_{\min}$ $\frac{\text{nrad}}{\sqrt{\text{Hz}}}$	L cm	B G	$\mathcal{V}_{\min}$ $\frac{10^{-12}\,\text{rad}}{\text{cm G}\,\sqrt{\text{Hz}}}$	$2\mathcal{F}/\pi$	LOD NO $\frac{\text{ppbv}}{\sqrt{\text{Hz}}}$	Trans.	Ref.
0.16	35	98	0.047	4,000	0.21	R	this work
7.1	45	223	0.71	–	0.53	Q	Wang *et al.*[167]
13	45	212	1.4	–	0.36	Q	Zhang *et al.*[147]
16	44	156	2.3	–	0.76	Q	Lewicki *et al.*[142]
18	15	141	8.5	–	20.7	R	Wang *et al.*[145]

long field region, $\theta_{min} = 0.14$ nrad. However, the measured angle is amplified by the cavity finesse according to Equation 6.14. The measured angle, θ_{cav}, is therefore 0.56 μrad.

With 170 averaged scans and a measurement bandwidth of 0.77 Hz, the bandwidth-normalized LOD is 0.21 ppbv $\text{Hz}^{-1/2}$ or, in terms of the Faraday rotation angle, $\theta_{min} = 0.16$ nrad $\text{Hz}^{-1/2}$ per pass. Along with the measurement bandwidth, for comparing the performance of INFAMOS with similar Faraday rotation systems, the interaction path length and the amplitude of the magnetic fields must also be considered. The sensitivity will also depend on the species measured, as well as on the total pressure. An ideal parameter for comparing different measurements is the Verdet constant $\mathcal{V}$ defined in Equation 6.13. Although this quantity is independent of the magnetic field amplitude and the interaction length, it is still influenced by the total pressure and is heavily dependent on the chosen transition (e.g., P, Q or R branch and angular momentum J). Taking the experimental conditions $B = 98$ G and $L = 35$ cm, the minimum detectable Verdet constant defined as

$$\mathcal{V}_{min} = \frac{\theta_{min}}{LB}, \tag{6.24}$$

can thus be determined for the INFAMOS system: $\mathcal{V}_{min} = 4.7 \times 10^{-14}$ rad cm^{-1} G^{-1} $\text{Hz}^{1/2}$. Table 6.2 compares the sensitivity of the INFAMOS spectrometer with other Faraday rotation spectrometers for the detection of NO. Taking the system reported

by Zhang *et al.*[147], despite having a larger $\mathcal{V}_{min}^{\text{Zhang}} = 1.4 \times 10^{-12}$ rad cm^{-1} G^{-1} Hz$^{1/2}$ by approximately a factor of 30, the LOD was LOD$^{\text{Zhang}} = 0.36$ ppbv Hz$^{-1/2}$. This can be explained by the fact that Zhang *et al.* probed a Q branch transition (X $^2\Pi_{3/2}$ Q(1.5)), which is known to provide a larger Faraday effect by a factor of ≈ 6, and also by the lower total measurement pressure of 80 Torr.[145]

6.5.3 Saturation effects in INFAMOS and OF-CEAS

This section presents a quantitative description of saturation effects observed in INFAMOS and OF-CEAS. The INFAMOS spectrometer produces two simultaneous outputs, the raw cavity transmission and the Faraday rotation signal (lock-in amplifier output). This is, in itself, a useful tool for quantifying saturation effects since, as previously mentioned, OF-CEAS spectra can be obtained from typical cavity transmission spectra such as the one shown in Figure 6.16. The transmission maxima in

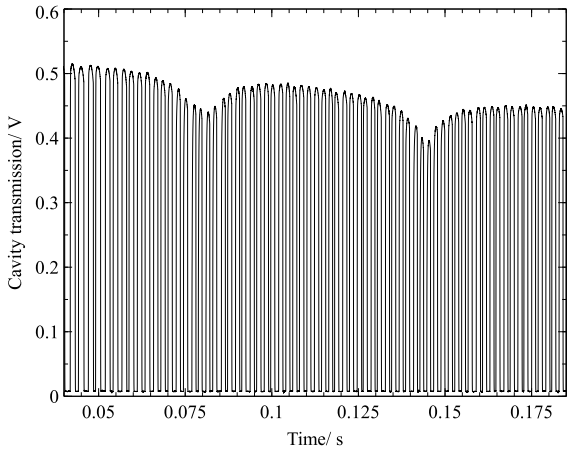


Figure 6.16: Raw cavity transmission on a frequency up-sweep, monitored during the acquisition of an INFAMOS spectrum. The raw cavity transmission in a single sweep across the R(3.5)$_{1/2}$ and R(3.5)$_{3/2}$ $v = 1 \leftarrow 0$ transitions of NO, at a repetition rate of 5 Hz, a total pressure of 50 Torr and a mixing ratio of 0.22 ppmv in dry nitrogen.

Figure 6.16 appear at the times during the scan that the laser is on resonance with a cavity longitudinal mode. Taking the amplitude at each point, OF-CEAS spectra such as shown in Figure 6.17 can be constructed since the absorption coefficient, α,

can be related to the cavity transmission using Equation 6.7:

$$\alpha = \frac{(1-R)}{L}\left[\sqrt{\frac{T_0}{T}} - 1\right] \tag{6.25}$$

where T and T_0 are the transmission with and without the presence of an absorber, respectively. Since the length L is known, the *apparent* mirror reflectivity are inferred (see later) from a unsaturated absorption of a sample of known concentration.

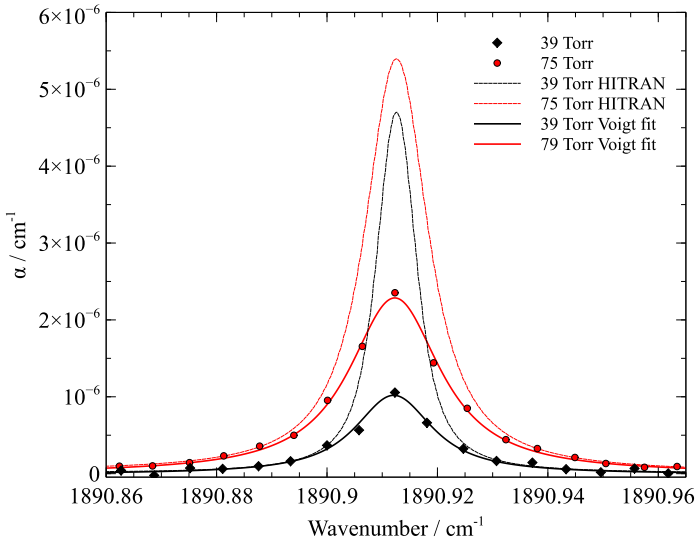


Figure 6.17: OF-CEAS spectra of the R(3.5)$_{3/2}$ $v = 1 \leftarrow 0$ transition of NO taken at two different total pressures of 39 and 75 Torr with $p_{NO} = 0.94$ ppmv, overlaid with simulations generated using the HITRAN database, for demonstrating the pressure dependence of absorption characteristic of saturation. Both spectra were obtained with the same cavity transverse mode. Voigt fits to the experimental data are also shown.

Figure 6.17 shows the measured absorption coefficient, $\alpha(\nu)$, obtained for two samples of NO at total pressures of 39 and 75 Torr and a mixing ratio of 940 ppbv in N_2. Under these conditions, the Lorentzian widths calculated using the HITRAN pressure broadening parameters are 187 MHz and 360 MHz respectively. However, fitting these spectra with a Voigt profile with a fixed FWHM Gaussian component of 126 MHz (the Doppler width of NO at 298 K), the full width of the Lorentzian components extracted for the 39 Torr and 75 Torr transitions is 471 ± 22 MHz and

567 ± 15 MHz. This marked increase in linewidth is a signature of optical saturation. In addition, it can be seen that the absorption at the line centre is at least a factor of 2 smaller than expected. A saturation parameter at the line centre calculated via the homogeneous width of the transitions, $S_{0,\gamma}$, can then be extracted using the relationship[31]

$$\gamma_S = \gamma_0 \sqrt{1 + S_{0,\gamma}}, \tag{6.26}$$

where γ_S is the saturated homogeneous width and γ_0 is the unsaturated homogeneous width. Applying this treatment to the spectra obtained at 39 Torr and 75 Torr yields $S_{0,\gamma} = 5.3$ and $S_{0,\gamma} = 1.5$, respectively. A similar procedure can be followed for calculating the saturation parameter at the line centre using the absorption coefficients, $S_{0,\alpha}$, via

$$\alpha_S = \frac{\alpha_0}{1 + S_{0,\alpha}}. \tag{6.27}$$

The saturation parameters extracted this way from the spectra recorded at lower and higher pressures are $S_{0,\alpha} = 3.5$ and $S_{0,\alpha} = 1.3$, respectively. Note that it is common for the parameters $S_{0,\gamma}$ and $S_{0,\alpha}$ to have different values, as α is affected by saturation at both homogeneous and inhomogeneous broadening limits whereas γ is only dependent on homogeneous broadening mechanisms.[31] The comparison between these parameters as a function of pressure is shown in Figure 6.18 and as expected, saturation effects decrease as the total pressure and hence the relaxation rate of the system increase. Qualitatively, it can be seen that closer to the inhomogeneous broadening limit $S_{0,\gamma}$ is larger than $S_{0,\alpha}$, since only the Lorentzian component of the Voigt profile is fitted to obtain the former parameter. At the higher pressure limit, the relative sizes of the two parameters is inverted and the assumption that the system is homogeneously saturated becomes more adequate, making $S_{0,\gamma}$ more appropriate for quantifying saturation in the homogeneously broadened limit.

The saturation intensity determined using the relaxation rate constant of 4.5 s^{-1}

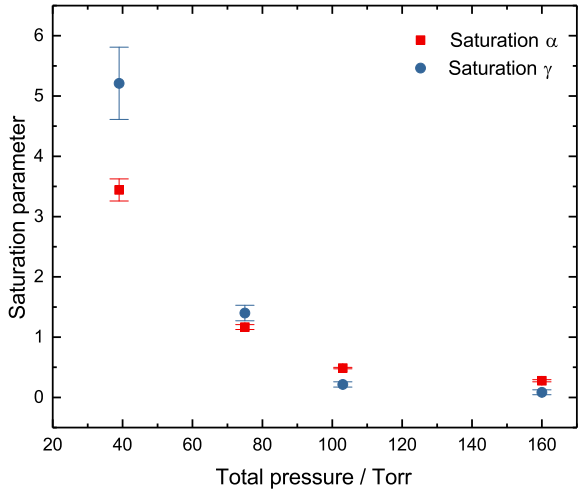


Figure 6.18: Saturation parameters calculated using homogeneous widths and absorption coefficients for the NO $^2\Pi_{3/2}$ R(3.5) transition. All data were taken at constant intensity and using the TEM_{10} mode.

Torr^{-1}, at a pressure of 75 Torr and an absorption cross-section of $\sigma_0 = 2.24 \times 10^{-18}$ cm^2, is $I_0^{sat} \approx 5.6$ W cm^{-2}. Assuming collisional relaxation to be the only relaxation mechanism would result in an overestimation of S_0 by a factor of ≈ 45, indicating that other contributions to the total relaxation rate play a significant role. With cavity mirrors with a radius of curvature of 0.5 m, the beam waist of the Gaussian mode in the cavity is *ca.* 1.2 mm, leading to a transit-time of about 5 μs and a saturation intensity $I_0^{sat} = 3.4$ kW cm^{-2}. Since the beam diameter almost doubles at the mirrors, this transit-time relaxation mechanism becomes slower and yields a saturation intensity of *ca.* 1 kW cm^{-2}. The total relaxation time can then be seen as a combination of the effects mentioned above, along with pressure induced velocity changing collisions and rotational energy transfer within the upper vibrational state.

The final aspect which influences the degree of saturation in the spectrometer is the transverse cavity mode (TEM) used. Aside from the change in intensity distribution within the cavity that comes with a higher TEM mode, the effective path length, and hence the finesse, will also be reduced due to increased diffraction losses. This

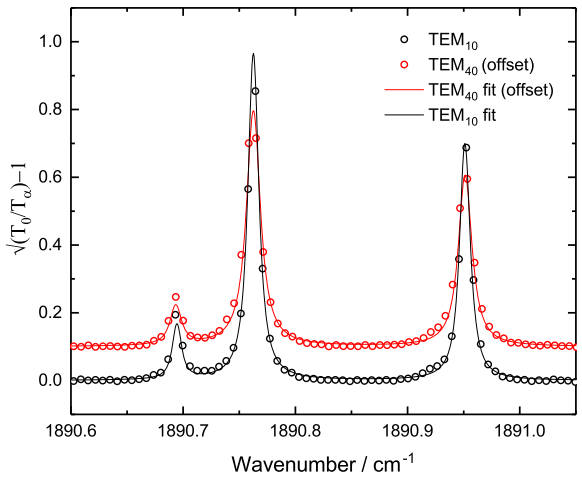


Figure 6.19: OF-CEAS spectra of pure CO_2 observed with the TEM_{10} and TEM_{40} cavity modes at 41 Torr and 56 Torr total pressure respectively. The spectrum acquired with the TEM_{40} mode is offset by 0.1 for clarity.

effect can be verified with spectra of a species at known concentration that does not saturate under the same experimental conditions. To demonstrate this effect, a sample of 100% CO_2 (BOC gases) is chosen as it absorbs in the same spectral region as the NO $R(3.5)_{3/2}$ transition, but its transitions have considerably lower absorption cross sections; the $(1\ 1^1\ 0) \leftarrow (0\ 0^0\ 0)$ P(15) transition of $^{16}O^{12}C^{18}O$, the strongest in the spectrum shown in Figure 6.19, has a cross section of $\sigma_0 = 2.3 \times 10^{-24}$ cm^2 which is $\approx 10^6$ times lower than the aforementioned NO transition. Saturating these transitions would require intensities on the order of MW cm^{-2}. The difference in ratio of cavity transmission with absorber, T_α, to cavity transmission without absorber, T_0, shown in Figure 6.19, is a manifestation of effective path length reduction due to higher diffraction losses with the higher order mode, resulting in an apparent reduction of mirror reflectivity from ≈ 0.9998 to ≈ 0.9997.

It is important to assess the degree of saturation in each individual case taking into consideration that the effective path length may also be altered, hence calibrating the spectrometer either with a non-saturable species of known concentration at the same experimental conditions or taking an empty-cavity CRDS measurement, is vital.

In INFAMOS, optical saturation effects influence the lineshapes differently. The

spectra shown in Figure 6.20 compare saturation effects in INFAMOS to those seen in OF-CEAS. These data were taken with samples of NO mixed in nitrogen with a volume fraction of 110 ppbv and 602 ppbv at 237 Torr and 42 Torr, respectively, and a magnetic field amplitude of 85 G.

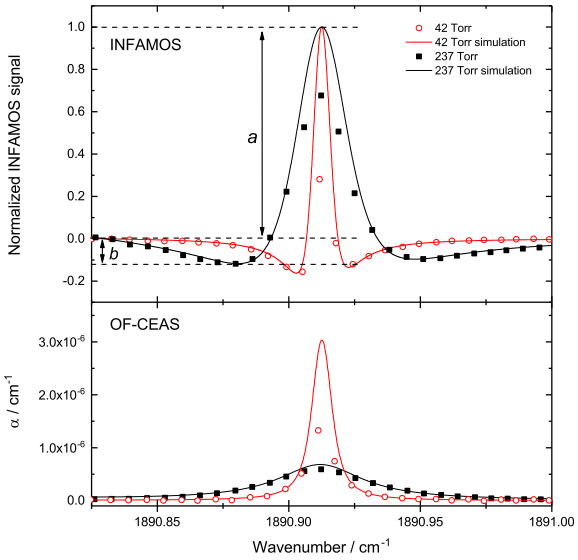


Figure 6.20: Top panel: INFAMOS spectra of the NO $R(3.5)_{3/2}$ $v = 1 \leftarrow 0$ transition at 42 Torr and 237 Torr overlaid with simulations using an unsaturated lineshape model for INFAMOS; Bottom panel: OF-CEAS spectra acquired simultaneously, overlaid with simulations using pressure broadening parameters and cross-sections from HITRAN.

By overlaying the spectra taken at different pressures with simulations based on the model for unsaturated INFAMOS,[141] a clear discrepancy is seen between the experimental data and the simulations in Figure 6.20. This discrepancy can be qualitatively described as a change in the ratio between the amplitude of the signal at line centre (a) and the amplitude of the lobes (b) - a change in *aspect ratio* of the signal. The centre:lobe amplitude ratio of the simulated lineshapes, represented in Figure 6.20 as the ratio a/b, using the left lobe for all comparisons, increases from 6.7 at 42 Torr to 8 at 237 Torr. The measured spectra, however, underestimate this ratio by approximately a factor of 4 and a factor of 2, respectively, and approach the simulated values at higher pressures.

6.5.4 Saturated INFAMOS lineshape model and simulation

After identifying the effects of optical saturation in OF-CEAS and INFAMOS, the model for the INFAMOS lineshape presented earlier was adapted in order to include such effects. The saturated INFAMOS model focuses on the homogeneous broadening limit for pressures 150 – 400 Torr. In order to introduce the saturated INFAMOS model the notation presented in section 6.3 is modified for simplicity, and a variable q, that takes the values of $q = +1$ for LHCP and $q = -1$ for RHCP, is introduced. The derivation of the equations shown in this section can be found in the appendix.

Consider the unsaturated absorption of a circularly polarised wave in the presence of a magnetic field at frequency ν, $\alpha_q(\nu)$, for a transition $|J\rangle \rightarrow |J'\rangle$. The absorption consists of the sum of the contributions from all allowed sub-transitions $|J, M\rangle \rightarrow |J', M'\rangle$,

$$\alpha_q(\nu) = \mathscr{N}\mathscr{S}\mathscr{M}_q(\nu), \tag{6.28}$$

where $\mathscr{N}$ is the molecular number density and $\mathscr{S}$ is the integrated absorption cross-section. $\mathscr{M}_q$ is the absorptive lineshape function, given by

$$\mathscr{M}_q(\nu) = 3 \sum_{M,M'} \begin{pmatrix} J' & 1 & J \\ -M' & q & M \end{pmatrix}^2 \eta(\nu; \nu_0^{MM'}), \tag{6.29}$$

where η is the absorptive lineshape function for a single $|J, M\rangle \rightarrow |J', M'\rangle$ transition centred at $\nu_0^{MM'}$ due to the action of a magnetic field. $\nu_0^{MM'}$ is given by:

$$\nu_0^{MM'} = \nu_0 + (g'M' - gM)\frac{\mu_B B}{hc}. \tag{6.30}$$

Here, ν_0 is the transition centre in the zero-field case, g, g' are the g-factors of the lower and upper states, and B is the magnetic field strength.

The energy separation between $|J, M\rangle$ and $|J, M+1\rangle$ for $B = 100$ G is sim-

ply $g\mu_B B/(hc)$ and takes values in the range $0.0001\,\mathrm{cm}^{-1}$ – $0.001\,\mathrm{cm}^{-1}$ for g values between 0.02 and 0.2. Doppler (FWHM = $0.00425\,\mathrm{cm}^{-1}$) and pressure broadening contributions are significantly larger and therefore there is a strong overlap between the lineshapes of each sub-transition, η, so that any given laser frequency ν will probe virtually all sub-transitions simultaneously. Clearly then, if the intensity is large enough, the populations of *all* the upper and lower states change due to optical pumping.

To begin with, it is assumed that the pressure is large enough that no spectral hole burning occurs, *i.e.* the number of molecules in a given state, and with a velocity component v along the axis of propagation a wave, is given by the Maxwell-Boltzmann distribution (homogeneous limit). This greatly simplifies the rate equations for the populations of the upper and lower states of the transition. There are then two extreme cases that can be considered. In the first case, no relaxation among the lower sub-states , $|J, M\rangle$, is assumed, nor among the upper sub-states, $|J', M'\rangle$; the laser beam alters the population of the lower, N_{JM}, and upper, $N_{J'M'}$, states of each sub-transition independently. Each sub-transition then has its own population difference (and saturation parameter). The net (observed) lineshape then consists of the weighted sum of all the individual lineshapes, where the weights include not only the different transition moments of each sub-transition (given by the Wigner $3j$ symbols), but also the sub-transition-specific population difference. In the second case, instantaneous relaxation among the lower sub-states and among the upper sub-states is assumed, such that the population is distributed evenly across all the lower (upper) sub-states, $N_{JM} = N_J/g_J$ ($N_{J'M'} = N_{J'}/g_{J'}$). The net lineshape is then given by Equation A.30, but scaled by a factor common to all sub-transitions, $p_q(\nu)$. Due to this factor, the saturated absorption then becomes

$$\alpha_q = \mathscr{N}\mathscr{S}p_q(\nu)\mathscr{M}_q(\nu), \tag{6.31}$$

with the fractional population given by

$$p_q(\nu) = \frac{1}{1 + S_q(\nu)}, \tag{6.32}$$

and the saturation parameter

$$S_q(\nu) = \frac{I}{I_q^{\text{sat}}(\nu)} = \pi\gamma S_0 \mathscr{M}_q(\nu), \tag{6.33}$$

where S_0 is the saturation parameter at the line centre and I is the local intensity.

Often, an alternative saturation intensity, I_0^{sat}, is defined as the irradiance required to halve the measured absorption at the centre of the transition in the zero-field, high-pressure limit. In this limit,

$$I_0^{\text{sat}} \sim \frac{1}{\sigma_0 \tau}, \tag{6.34}$$

where σ_0 is the absorption cross-section at the transition centre and τ is the lifetime of the upper state. As mentioned previously, the collisional vibrational relaxation rate constant for NO ($v = 1$) is *ca.* 4.5 s^{-1} Torr^{-1}. At 75 Torr, for example, this corresponds to an upper state lifetime of *ca.* 3 ms which should be regarded as an upper limit for the system's relaxation time since, as discussed in the previous section, other contributions such as transit time and rotational energy transfer reduce the lifetime further.

Equation A.30 can be modified in the following way to give the dispersive lineshape function of a $|J\rangle \rightarrow |J'\rangle$ transition, $\mathscr{M}'_q$,

$$\mathscr{M}'_q(\nu) = 3 \sum_{M,M'} \begin{pmatrix} J' & 1 & J \\ -M' & q & M \end{pmatrix}^2 \chi(\nu; \nu_0^{MM'}), \tag{6.35}$$

where χ is the dispersive lineshape for a single $|J, M\rangle \rightarrow |J', M'\rangle$ transition centred at the Zeeman-shifted transition centre $\nu_0^{MM'}$. Using equations A.36 to 6.35, the

saturated refractive index and absorption coefficient for a circular polarisation q can be expressed as:

$$n_q(\nu) = 1 + \frac{1}{4\pi\nu} \frac{\mathscr{N}\mathscr{S}\mathscr{M}'_q(\nu)}{1 + \pi\gamma S_0 \mathscr{M}_q(\nu)} \tag{6.36}$$

$$\alpha_q(\nu) = \frac{\mathscr{N}\mathscr{S}\mathscr{M}_q(\nu)}{1 + \pi\gamma S_0 \mathscr{M}_q(\nu)}. \tag{6.37}$$

The resulting phase-shift for a polarisation q is then given by:

$$\phi_q(\nu) = \text{const} + \frac{\mathscr{N}\mathscr{S}L}{2} \frac{\mathscr{M}'_q(\nu)}{1 + \pi\gamma S_0 \mathscr{M}_q(\nu)}. \tag{6.38}$$

The model for the saturated phase-shift allows the Faraday rotation angle to be computed via Equation A.53 using S_0 as a free parameter. A reasonable agreement between the predicted saturated INFAMOS signal with $S_0 = 0.3$ and the measurement at 237 Torr is achieved in Figure 6.21. The spectrum presented in this figure is the same as in Figure 6.13 (a). The overlap is good in the central region of the feature. The model took into account the $^2\Pi_{1/2}$ doublet transition at $\sim 1890.7\,\text{cm}^{-1}$, which at 237 Torr gives a significant contribution to the refractive index in the spectral range of Figure 6.21. Nevertheless, there is a significant discrepancy towards the left side of the spectrum, for which a number of factors could be responsible.

Firstly, the on-axis longitudinal magnetic field of a solenoid with a radius much smaller than its length is relatively homogeneous within the solenoid, but falls off to zero outside of it. The NO molecules thus experience a non-uniform magnetic field, a fact that was not taken into account in the model. Secondly, the intensity (irradiance) of the laser beam is dependent on the position within the cavity. This leads to position-dependent rates of optical pumping and, thus, to a spatially dependent saturation parameter. To some extent this phenomenon is mitigated by the thermal motion of the molecules. Finally, even though Voigt lineshapes are used,

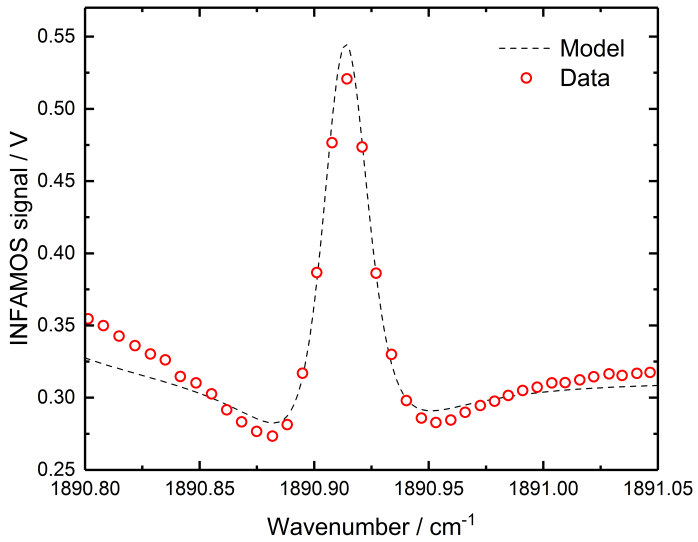


Figure 6.21: INFAMOS spectrum obtained at 237 Torr and a magnetic field amplitude of 85 G overlaid with a simulation produced using the saturated INFAMOS model.

the model was derived in the limit of homogeneous broadening and therefore does not include inhomogeneous saturation mechanisms. Despite these factors, the saturation parameter computed with a least-squares fitting procedure to the INFAMOS spectrum in Figure 6.21 is $S_0 = 0.3$, and is in good agreement with the parameter calculated from OF-CEAS ($S_0 < 0.5$ at *ca.* 160 Torr) using the models for saturated absorption spectroscopy. The saturation intensity of this NO transition under the selected experimental conditions is $I_0^{sat} = 1.5$ kW cm^{-2}, corresponding to an excited state relaxation time of 30 μs. This short upper state lifetime is consistent with a significant transit-time contribution to the molecular relaxation.

6.6 Conclusion

A technique that combines FAMOS with the enhanced path length provided by an optical-feedback cavity was demonstrated with the INFAMOS technique. The difficulties associated with extracting INFAMOS signals and their dependence on the magnetic field amplitude and pressure were demonstrated. The detection limit of

NO is 0.21 ppbv $Hz^{-1/2}$, which corresponds to a minimum detectable Verdet constant $\mathcal{V} = 4.7 \times 10^{-14}$ rad cm^{-1} G^{-1} $Hz^{-1/2}$ and a minimum detectable Faraday rotation angle of 0.16 nrad $Hz^{-1/2}$. The sensitivity of the instrument can be readily improved for the detection of NO by probing the X $^2\Pi_{3/2}$ Q(1.5) transition at 1875.8 cm^{-1}.[142] Moreover, the integrated absorption cross section of this Q-branch transition is lower than the R-branch transition studied in this chapter, and thus the Q-branch transition's saturation intensity is higher. This would allow measurements at lower pressure, resulting in a combined effect of signal improvement of at least one order of magnitude. The effects of saturation in INFAMOS and OF-CEAS were explored, and the saturation parameters for different sets of experimental conditions were determined via the OF-CEAS spectra and by using a new model that predicts the saturated INFAMOS lineshape. In the latter case, S_0 was used as a free parameter to obtain the best fitting simulation to an INFAMOS spectrum obtained at a total pressure of 237 Torr. The saturation parameter obtained using this method was $S_0 = 0.3$, in good agreement with the value extracted from the OF-CEAS measurements. In summary, the INFAMOS technique was presented as a robust, sensitive and selective method for radical detection which has significant potential for further improvements in its sensitivity.

Chapter 7

Conclusions and outlook

Quantum cascade lasers are versatile coherent sources of high power mid-IR radiation. This thesis focused on demonstrating the applicability of these laser sources for the sensitive and selective detection of trace gases. The thesis also presented studies on the emission bandwidth of these laser devices, and strategies to manipulate it. Additionally, the use of QCLs for preparing and probing coherent molecular systems was investigated.

Firstly, the multi-species sensing capabilities of QCLs was demonstrated using a multi-mode Fabry-Perot (FP) QCL to perform multi-mode absorption spectroscopy (MUMAS) for the simultaneous detection of NO and H_2O. The full bandwidth of the FP-QCL of *ca.* 50 cm^{-1}, together with the narrow mode width of < 50 MHz and mode spacing of *ca.* 11 GHz allowed the device to achieve a broad spectral coverage with a good time resolution (< 1 ms) while retaining the frequency resolution of a single mode laser. Despite the changes in the intensity envelope of the laser emission as the injection current was tuned, a MUMAS model was successfully implemented for the prediction of the multi-mode fingerprint of NO and H_2O with the FP-QCL. This result highlights the reproducibility and robustness of FP-QCLs as sources for MUMAS. Multi-mode QCLs provide an economical alternative to com-

plex and expensive systems such as high-resolution FT-IR spectrometers or optical frequency combs (OFCs), and future research could see these laser devices finding applications in real-time plasma diagnostics, combustion diagnostics and/or environmental monitoring. In real time plasma diagnostics, the time resolution of the system demonstrated in this work could be advantageous for the accurate determination of rotational and vibrational temperatures, and for identifying non-equilibrium systems. This is of particular interest for the control of plasma etching processes widely used in the semiconductor fabrication industry.

The second results chapter (Chapter 4) was concerned with single mode QCLs. Several techniques were used to determine the spectral purity of the optical emission from these devices. The linewidth of a free running DFB-QCL was quantified using Lamb-dip spectroscopy and frequency noise power spectral density (PSD) analysis. Both methods were in good agreement and revealed a linewidth of *ca.* 500 kHz. The introduction of radio-frequency (RF) noise into the system by mixing it with the laser injection current proved to be a reliable and reproducible method for broadening the linewidth of the device by up to an order of magnitude. The self-heterodyne technique, a popular technique for measuring the linewidth of telecommunications laser diodes, was also presented as a candidate for quantifying the linewidth of QCLs. Interestingly, the resulting self-heterodyne spectra presented structures that are not predicted by the theoretical models with a short delay time, and show sensitivity to linewidth broadening via injection of RF noise. The extension of this technique to QCLs could be demonstrated by using longer delay lines ($\gg$ 20 m) based on low-loss multi-pass cells. Furthermore, with the improvement of the availability and quality of mid-IR optics, this technique could provide an attractive alternative for determining the coherence properties of single mode QCLs.

Chapter 5 presented spectroscopic studies on coherent transient effects induced in low pressure samples of NO. Initially, the DFB-QCL laser characterised in Chapter 4

was used to identify on-resonance coherence effects on a low pressure sample of NO, such as the interaction of an induced macroscopic polarisation with the on-resonance field. A current pulse was then applied to the cw-DFB-QCL via a bias-T in order to achieve a rapid frequency chirp of the order of a few MHz ns^{-1}, sufficient to generate controllable coherent transient effects with a single QCL in a non-velocity selected profile of NO. A second set of experiments focused on the study of the coherent transient spectroscopy of velocity selected samples. In this case, an EC-QCL was added in order to prepare a narrow velocity group in the $v = 1$ level that was subsequently probed by the DFB-QCL tuned to the ladder-state hot band transition. The transient signals were compared with simulations of the time evolution of the two-photon coherent system performed using the optical Bloch equations for a two and a three level system. The three level system based simulation was found to provide a more accurate description of the damping of the oscillatory coherent structures. The final investigation in this chapter focused on time resolved studies of the development and decay of velocity selected rapid passage signals, using an acousto-optic modulator (AOM) as an optical switch to generate an optical pump pulse. Maximum population transfer to $v = 1$ in the selected conditions occurred after optically pumping a low pressure (3 mTorr) sample of NO for *ca.* 10 ± 0.5 μs. Additionally, the amplitude of coherent systems after the application of a fixed length optical pump pulse was investigated in order to obtain their relaxation time; in case of a 3 mTorr sample of NO, this relaxation time was 5.7 ± 0.3 μs. The evolution of the relaxation time as a function of the total pressure was also studied by mixing NO with a variety of buffer gases. From these measurements, the collisional relaxation constants of the coherent signals were extracted for all gases, and reach a maximum value of $(4.28 \pm 0.13) \times 10^4$ s^{-1} $mTorr^{-1}$ with CO_2. In the future, a deeper understanding of the coherence properties of the molecular systems described in this chapter can be achieved by using frequency locking mechanisms in order to narrow the linewidth of the pump or the

probe lasers. These mechanisms could include electrical noise cancellation or locking to high-finesse external cavities. In addition, collisional relaxation constants could be determined for gases other than NO with strong absorption bands in the mid-IR using the pump and probe configuration with a fast optical switch, as described in the final section of Chapter 5.

Lastly, intracavity Faraday modulation spectroscopy (INFAMOS) with a DFB-QCL was presented in Chapter 6. The technique combined optical-feedback cavity enhanced absorption spectroscopy (OF-CEAS) and Faraday modulation spectroscopy (FAMOS) for the sensitive and selective detection of radical species. The technique was demonstrated using samples of nitric oxide buffered in nitrogen as a test system, probing R-branch transitions at 5.3 μm. The sensitivity of the technique for NO detection was 0.21 ppbv $Hz^{1/2}$ at a total pressure of 412 Torr, and a simulation for the prediction of the INFAMOS lineshape was successfully implemented. The build up of intracavity power generated peak intensities up to 1 kW cm^{-2} sufficient to produce optical saturation of the NO transitions; clear evidence of saturation is demonstrated in the INFAMOS spectra at low pressure. Saturation was incorporated into the INFAMOS model for the limit of homogeneous broadening, and the saturation parameters as a function of total pressure were calculated from the simultaneously acquired OF-CEAS spectra. The saturation parameter extracted from the saturated INFAMOS simulation, $S_0 = 0.3$, was in good agreement with the saturation parameter calculated from OF-CEAS at a total pressure of 237 Torr. In the future, several measures can be taken to improve the sensitivity of the INFAMOS technique, including reducing saturation by using a V-shaped cavity configuration or tuning to transitions that exhibit larger magnetically induced birefringence; in the case of NO, probing Q-branch transitions could improve the sensitivity by approximately a factor of 7.[141] Moreover, INFAMOS could find applications for sensing of other radicals that play important roles in fields such as atmospheric chemistry, for example HO_2. The

work in this chapter has shown the applicability of QCLs for the sensitive detection of trace gas species using optical cavities, and therefore completing these demonstrations of the versatility of these lasers for studies that require a wide range of qualities: from broad spectral coverage to narrow linewidths and high sensitivity and selectivity.

Appendix A

Saturated INFAMOS model

This appendix presents the derivation of the model used to predict the lineshape of saturated INFAMOS signals in section 5.4 of Chapter 6.

A.1 Lineshapes

A.1.1 Homogeneous lineshapes

When a transition is probed by monochromatic light, the dependence of the *absorption coefficient*, α, and of the *refractive index, n*, on the wavenumber, ν, is described by a pair of *lineshape functions*. One can distinguish between two cases: (a) if all the molecules in the sample have the same lineshape (e.g. due to collisional broadening), the transition is said to be *homogeneously broadened*; (b) if the lineshape varies among the molecules in the sample (e.g. due to the Doppler effect), the transition is said to be *inhomogeneously broadened*. Assume a plane wave of the form

$$\vec{E}(z,t) = \hat{\vec{E}} \exp\left[-\mathrm{i}k\tilde{n}z\right] \exp\left[2\pi\mathrm{i}\nu ct\right] \tag{A.1}$$

propagating through the gaseous sample, with $\hat{\vec{E}}$ the polarisation vector, $k = 2\pi\nu$ the magnitude of the wave vector, and $\tilde{n}$ the complex refractive index. With a classical model (damped oscillating dipoles, see for example chapter 3 in reference 31) it is possible to derive the forms of the real and imaginary part of the complex refractive index for a collection of identical molecules,

$$n \doteq \Re[\tilde{n}] = 1 - \mathscr{X}\frac{1}{\pi}\frac{\nu - \nu_0}{(\nu - \nu_0)^2 + \gamma^2} \tag{A.2}$$

$$\kappa \doteq -\Im[\tilde{n}] = \mathscr{X}\frac{1}{\pi}\frac{\gamma}{(\nu - \nu_0)^2 + \gamma^2}, \tag{A.3}$$

where γ is the Lorentzian width (HWHM), ν_0 is the transition (resonance) frequency, and $\mathscr{X}$ (let us call it the transition strength) is a property of the transition under investigation which includes the transition moment and the population of the upper and lower states. By defining the *homogeneous lineshape functions*,

$$\mathscr{L}'(\nu;\nu_0) = -\frac{1}{\pi}\frac{\nu - \nu_0}{(\nu - \nu_0)^2 + \gamma^2} \tag{A.4}$$

$$\mathscr{L}(\nu;\nu_0) = \frac{1}{\pi}\frac{\gamma}{(\nu - \nu_0)^2 + \gamma^2}, \tag{A.5}$$

Equations (A.2) and (A.3) can be written more compactly as

$$n = 1 + \mathscr{X}\mathscr{L}'(\nu;\nu_0) \tag{A.6}$$

$$\kappa = \mathscr{X}\mathscr{L}(\nu;\nu_0). \tag{A.7}$$

The real part of $\tilde{n}$ [(A.6)] is just the ordinary refractive index, whereas the imaginary part, κ [(A.7)], can be linked to the absorption coefficient through the Beer-Lambert law,

$$|\vec{E}(z,t)|^2 \sim I\exp\left[-2k\kappa z\right] \doteq I\exp\left[-\alpha z\right], \tag{A.8}$$

yielding

$$\alpha = 4\pi\nu\mathscr{X}\mathscr{L}(\nu;\nu_0). \tag{A.9}$$

Notice that since $\mathscr{L}$ [(A.5)] is area-normalized to unity, its peak amplitude is inversely proportional to the width:

$$\mathscr{L}(\nu_0;\nu_0) = \frac{1}{\pi\gamma}. \tag{A.10}$$

A.1.2 Inhomogeneous lineshapes

If the molecules possess velocity v parallel to the probe beam, then the lineshapes are frequency-shifted by the Doppler-shift,

$$\nu_{\mathrm{D}} = \nu_0\frac{v}{c}. \tag{A.11}$$

If $\mathscr{G}(\nu_{\mathrm{D}})\mathrm{d}\nu_{\mathrm{D}}$ indicates the fraction of molecules with Doppler-shift between ν_{D} and $\nu_{\mathrm{D}} + \mathrm{d}\nu_{\mathrm{D}}$, where $\mathscr{G}(\nu_{\mathrm{D}})$ is the Maxwell-Boltzmann velocity distribution,

$$\mathscr{G}(\nu_{\mathrm{D}})\mathrm{d}\nu_{\mathrm{D}} = \sqrt{\frac{1}{\pi}}\frac{\sqrt{\ln 2}}{\gamma_{\mathrm{D}}}\exp\left[-\left(\frac{\sqrt{\ln 2}}{\gamma_{\mathrm{D}}}\nu_{\mathrm{D}}\right)^2\right]\mathrm{d}\nu_{\mathrm{D}}, \tag{A.12}$$

then the refractive index and absorption coefficient become

$$n(\nu) = 1 + \mathscr{X}\int\mathscr{L}'(\nu;\nu_0+\nu_{\mathrm{D}})\mathscr{G}(\nu_{\mathrm{D}})\mathrm{d}\nu_{\mathrm{D}} \tag{A.13}$$

$$\alpha(\nu) = 4\pi\nu\mathscr{X}\int\mathscr{L}(\nu;\nu_0+\nu_{\mathrm{D}})\mathscr{G}(\nu_{\mathrm{D}})\mathrm{d}\nu_{\mathrm{D}}. \tag{A.14}$$

By writing $\mathscr{X}$ outside of the integral it is implied that the transition strength of a molecule does not depend on its velocity; *i.e.* no spectral hole burning (Bennett holes) occurs. This is not true at very low pressures where the population difference of a specific velocity group can be altered by strong optical pumping (*e.g.* Lamb dip spectroscopy). The integrals in (A.13) and (A.14) can be written with the scaled

complementary error function w[32] as, respectively,

$$\chi(\nu;\nu_0) \doteq -\frac{\sqrt{\ln 2}}{\gamma_\mathrm{D}}\frac{1}{\sqrt{\pi}}\Im\left[w\left(\frac{\sqrt{\ln 2}}{\gamma_\mathrm{D}}\left(\nu-\nu_0+\mathrm{i}\gamma\right)\right)\right] \tag{A.15}$$

$$\eta(\nu;\nu_0) \doteq \frac{\sqrt{\ln 2}}{\gamma_\mathrm{D}}\frac{1}{\sqrt{\pi}}\Re\left[w\left(\frac{\sqrt{\ln 2}}{\gamma_\mathrm{D}}\left(\nu-\nu_0+\mathrm{i}\gamma\right)\right)\right], \tag{A.16}$$

where γ_D is the Doppler-width (HWHM),

$$\gamma_\mathrm{D} \doteq \nu_0\sqrt{\frac{2k_\mathrm{B}T\ln 2}{mc^2}}, \tag{A.17}$$

with T the temperature and m the mass of the molecule. The absorptive lineshape, η, is the well known *Voigt function*, and χ is its dispersive counterpart. The refractive index and absorption coefficient thus become

$$n(\nu) = 1 + \mathscr{X}\chi(\nu;\nu_0) \tag{A.18}$$

$$\alpha(\nu) = 4\pi\nu\mathscr{X}\eta(\nu;\nu_0). \tag{A.19}$$

Because both $\mathscr{L}$ and $\mathscr{G}$ are normalised to unit area, so is η (since it is a convolution of $\mathscr{L}$ and $\mathscr{G}$).

With a magnetic field present, the absorptive and dispersive lineshapes of a transition $|J,M\rangle \rightarrow |J',M'\rangle$[1] are Zeeman-shifted compared to the zero-field case and centred at

$$\nu_0^{MM'} = \nu_0 + (g'M' - gM)\frac{\mu_\mathrm{B}B}{hc}, \tag{A.20}$$

where g, g' are the g-factors of the lower and upper states, respectively. The refractive index and absorption coefficient then become weighted sums of contributions from

[1] J is the angular momentum, and M is the projection of the angular momentum on the axis of the magnetic field. The remaining quantum numbers (*e.g.* vibrational state) are omitted for clarity.

each allowed transition,

$$n(\nu) = 1 + \mathscr{X} \sum_{M,M'} \bar{w}^{MM'} \chi(\nu; \nu_0^{MM'}) \doteq 1 + \mathscr{X}\mathscr{M}'(\nu) \tag{A.21}$$

$$\alpha(\nu) = 4\pi\nu\mathscr{X} \sum_{M,M'} \bar{w}^{MM'} \eta(\nu; \nu_0^{MM'}) \doteq 4\pi\nu\mathscr{X}\mathscr{M}(\nu), \tag{A.22}$$

where $\bar{w}^{MM'}$ is the relative intensity of the transition $|J, M\rangle \to |J', M'\rangle$ and

$$\sum_{M,M'} \bar{w}^{MM'} = 1. \tag{A.23}$$

A.2 Unsaturated absorption and refractive index

The *line strength*, $\mathscr{S}$, for an electric dipole transition $|J\rangle \to |J'\rangle$ without any external magnetic field is defined in[62] as (in SI units),

$$\mathscr{S} \doteq \frac{2\pi^2\nu_0}{3hc\epsilon_0} \frac{\mathscr{N}_J}{\mathscr{N}} \left[1 - \frac{g_J}{g_{J'}} \frac{\mathscr{N}_{J'}}{\mathscr{N}_J}\right] \mathscr{R}, \tag{A.24}$$

where $\mathscr{N}_{xJ}$, $\mathscr{N}_{x'J'}$ are the population number densities in thermodynamic equilibrium (TDE) at $T = 298\,\mathrm{K}$,

$$\mathscr{N}_J = \mathscr{N} \frac{g_J e^{-\frac{E_J}{k_\mathrm{B}T}}}{Q(T)}, \tag{A.25}$$

$g_J, g_{J'}$ are the statistical weights, $\mathscr{N}$ is the molecular number density, $\mathscr{R}$ is the total dipole transition moment, and Q is the partition sum. The (unsaturated) absorption coefficient, α, in TDE at the temperature T is then simply

$$\alpha(\nu) = \mathscr{N}\mathscr{S}\eta(\nu; \nu_0). \tag{A.26}$$

With a magnetic field present, the states $|J\rangle$ split into sub-states $|J, M\rangle$. The observed absorption at the frequency ν is then the sum of the contributions from all

sub-transitions $|J, M\rangle \rightarrow |J', M'\rangle$,

$$\alpha_q(\nu) = \mathscr{N}\mathscr{S} \sum_{M,M'} w_q^{MM'} \eta(\nu; \nu_0^{MM'}). \tag{A.27}$$

How much each sub-transition contributes to the total absorption depends on two factors: Firstly, the population of the upper and lower state; Secondly, the transition moment for the specific sub-transition. For circularly polarised light propagating along the field axis, the transition moments for the sub-transition $|J, M\rangle \rightarrow |J', M'\rangle$ are of the form $|\langle J', M'|\mu_q|J, M\rangle|^2$, where $q = +1$ for a LHCP wave, $q = -1$ for a RHCP wave, and μ_q ($q = \pm 1$) are the spherical components of the dipole moment operator. Since the selection rules for μ_{+1} and μ_{-1} are different, two different absorption values depending on the polarisation of the wave are obtained. Assuming all sub-states $|J, M\rangle$ with the same J quantum number to be equally populated,

$$\mathscr{N}_{JM} = \frac{\mathscr{N}_J}{g_J} \quad \forall M, \tag{A.28}$$

and with the Wigner-Eckart theorem, one can show[168] that the weights, $w_q^{MM'}$, for a rovibrational transition take on the form

$$w_q^{MM'} = 3 \begin{pmatrix} J' & 1 & J \\ -M' & q & M \end{pmatrix}^2, \tag{A.29}$$

where the term in parentheses is the Wigner $3j$ symbol. The sum in (A.27) is then of the form (A.22). The absorptive lineshape function, $\mathscr{M}$,

$$\mathscr{M}_q(\nu) = 3 \sum_{M,M'} \begin{pmatrix} J' & 1 & J \\ -M' & q & M \end{pmatrix}^2 \eta(\nu; \nu_0^{MM'}), \tag{A.30}$$

and the dispersive lineshape function, $\mathscr{M}'$,

$$\mathscr{M}'_q(\nu) = 3 \sum_{M,M'} \begin{pmatrix} J' & 1 & J \\ -M' & q & M \end{pmatrix}^2 \chi(\nu; \nu_0^{MM'}). \tag{A.31}$$

can thus be written.

A.3 Saturated absorption and refractive index

The above is valid if the populations of the states are in thermodynamic equilibrium. This is not the case in the regime of optical saturation, where *saturated populations* can be introduced:

$$N_J(\nu) = \mathscr{N}_J f_J(\nu), . \tag{A.32}$$

Here, it is still assumed that all the sub-states $|J, M\rangle$ are equally populated. This implies the assumption that there are very fast relaxation processes between states with the same x and J quantum numbers. The factor $f_J(\nu)$ accounts for the depletion (or population) of the state and is unity in TDE. To obtain the saturated absorption and refractive index, the TDE populations, $\mathscr{N}_J$, must be substituted in Equation (A.24) with the saturated populations, N_J [(A.32)]. Hence, the following substitution must be carried out

$$\mathscr{S} \to \mathscr{S} \frac{N_J(\nu)\left[1 - \frac{g_J}{g_{J'}} \frac{N_{J'}(\nu)}{N_J(\nu)}\right]}{\mathscr{N}_J\left[1 - \frac{g_J}{g_{J'}} \frac{\mathscr{N}_{J'}}{\mathscr{N}_J}\right]}. \tag{A.33}$$

With $E_{J'} - E_J \approx 1900\,\mathrm{cm}^{-1}$ and $k_\mathrm{B}T \approx 200\,\mathrm{cm}^{-1}$, the fractional term in the brackets in the denominator of (A.33) can be neglected (see (A.25)), and from (A.32) the following equation is obtained:

$$\mathscr{S} \to \mathscr{S} \cdot \left[f_J(\nu) - \frac{g_J}{g_{J'}} \frac{\mathscr{N}_{J'}}{\mathscr{N}_J} f_{J'}(\nu)\right]. \tag{A.34}$$

With the definition,

$$p(\nu) \doteq \left[f_J(\nu) - \frac{g_J}{g_{J'}} \frac{\mathscr{N}_{J'}}{\mathscr{N}_J} f_{J'}(\nu) \right], \tag{A.35}$$

and after carrying out the substitution (A.34) in (A.27) we have with (A.30),

$$\alpha_q(\nu) = \mathscr{N}\mathscr{S}p(\nu)\mathscr{M}_q(\nu). \tag{A.36}$$

Comparison of (A.36) with (A.22) yields

$$\mathscr{X} = \frac{1}{4\pi\nu}\mathscr{N}\mathscr{S}p, \tag{A.37}$$

and from (A.21) and (A.37), the refractive index is

$$n_q(\nu) = 1 + \frac{1}{4\pi\nu}\mathscr{N}\mathscr{S}p(\nu)\mathscr{M}'_q(\nu). \tag{A.38}$$

A.4 Population difference

Assuming a 2-level system, the rate equation for $N_J = \mathscr{N}_J f_J$ is

$$\mathscr{N}_J \dot{f}_J = -\mathscr{B}I\mathscr{N}_J p\mathscr{M}_q + \mathscr{A}\mathscr{N}_{J'} f_{J'}, \tag{A.39}$$

where $\mathscr{A}$ and $\mathscr{B}$ are the Einstein coefficients (in the appropriate units), and I is the irradiance (power per unit area) of the wave. It is also assumed that the total number of molecules in both upper and lower state with optical pumping is the same as without pumping in TDE:

$$N_J + N_{J'} = \mathscr{N}_J + \mathscr{N}_{J'}. \tag{A.40}$$

At room temperature $k_{\mathrm{B}}T \approx 200\,\mathrm{cm}^{-1}$. Since $E_{J'} - E_J \approx 1900\,\mathrm{cm}^{-1}$, it is assumed $\mathscr{N}_{J'} \ll \mathscr{N}_J$. Then from (A.40) with (A.25) follows

$$f_{J'} \approx (1 - f_J)\frac{\mathscr{N}_J}{\mathscr{N}_{J'}}. \tag{A.41}$$

The steady-state ($\dot{f}_J = 0$) solution of (A.39) is

$$f_J(\nu) = \frac{1 + I\frac{\mathscr{B}}{\mathscr{A}}\frac{g_J}{g_{J'}}\mathscr{M}_q(\nu)}{1 + I\frac{\mathscr{B}}{\mathscr{A}}\left(1 + \frac{g_J}{g_{J'}}\right)\mathscr{M}_q(\nu)}, \tag{A.42}$$

and with (A.41), p [(A.35)] is modified to

$$p_q(\nu) = \frac{1}{1 + I\frac{\mathscr{B}}{\mathscr{A}}\left(1 + \frac{g_J}{g_{J'}}\right)\mathscr{M}_q(\nu)}. \tag{A.43}$$

By defining the *saturation intensity* (actually, irradiance), I_q^{sat},

$$I_q^{\mathrm{sat}}(\nu) \doteq \frac{\mathscr{A}}{\mathscr{B}\left(1 + \frac{g_J}{g_{J'}}\right)\mathscr{M}_q(\nu)}, \tag{A.44}$$

and the *saturation parameter*,

$$\begin{aligned} S_q(\nu) &\doteq \frac{I}{I_q^{\mathrm{sat}}(\nu)} \\ &= I\frac{\mathscr{B}}{\mathscr{A}}\left(1 + \frac{g_J}{g_{J'}}\right)\mathscr{M}_q(\nu) \\ &= \pi\gamma S_0 \mathscr{M}_q(\nu), \end{aligned} \tag{A.45}$$

with

$$S_0 = \frac{I}{\pi\gamma}\frac{\mathscr{B}}{\mathscr{A}}\left(1 + \frac{g_J}{g_{J'}}\right), \tag{A.46}$$

p_q [(A.43)] takes the form

$$p_q(\nu) = \frac{1}{1 + S_q(\nu)}. \tag{A.47}$$

Remark: In the high-pressure, zero-field case ($\mathscr{M} = \mathscr{L}$), the population difference at the transition centre, ν_0, is with (A.10)

$$p = \frac{1}{1 + S_0}, \tag{A.48}$$

and the saturation intensity at ν_0, I_0^{sat}, is with (A.44),

$$I_0^{\mathrm{sat}} = \pi\gamma \frac{\mathscr{A}}{\mathscr{B}\left(1 + \frac{g_J}{g_{J'}}\right)}. \tag{A.49}$$

The Einstein coefficient, $\mathscr{A}$, is inversely proportional to the upper state lifetime, $\tau^{-1} \doteq \mathscr{A}$, whereas $\mathscr{B} \sim \mathscr{S}$ is proportional to the linestrength. In the high-pressure limit considered here, the absorption cross-section at the centre of the transition is $\sigma_0 \sim \mathscr{B}/(\pi\gamma)$, and thus

$$I_0^{\mathrm{sat}} \sim \frac{1}{\sigma_0 \tau}. \tag{A.50}$$

A.5 Summary

Combining (A.47) and (A.45) with (A.38) and (A.36), the saturated refractive index and absorption coefficient become

$$n_q(\nu) = 1 + \frac{1}{4\pi\nu} \frac{\mathscr{N}\mathscr{S}\mathscr{M}'_q(\nu)}{1 + \pi\gamma S_0 \mathscr{M}_q(\nu)} \tag{A.51}$$

$$\alpha_q(\nu) = \frac{\mathscr{N}\mathscr{S}\mathscr{M}_q(\nu)}{1 + \pi\gamma S_0 \mathscr{M}_q(\nu)}. \tag{A.52}$$

The total phase-shift, $\phi_q = 2\pi\nu n_q(\nu)L$, experienced by a LHCP ($q = +1$) or RHCP ($q = -1$) wave is then

$$\phi_q(\nu) = 2\pi\nu L + \frac{\mathscr{N}\mathscr{S}L}{2} \frac{\mathscr{M}'_q(\nu)}{1 + \pi\gamma S_0 \mathscr{M}_q(\nu)}, \tag{A.53}$$

where L is the interaction length.

Bibliography

[1] O. Darrigol, *A History of Optics From Greek Antiquity to the Nineteenth Century*. Oxford: Oxford University Press, 2012.

[2] J. C. Maxwell, "Molecules," *Van Nostrand's Eclectic Engineering Magazine*, vol. 9, 1873.

[3] M. Kayton and W. R. Friend, *Terrestrial Radio-Navigation Systems*. New York: John Wiley & Sons, Ltd, 1st ed., 1997.

[4] R. A. Novelline, *Squire's fundamentals of radiology*. Harvard University Press, 6th ed., 2004.

[5] I. E. Gordon, L. S. Rothman, C. Hill, R. V. Kochanov, Y. Tan, P. F. Bernath, M. Birk, V. Boudon, A. Campargue, K. V. Chance, B. J. Drouin, J.-M. Flaud, R. R. Gamache, J. T. Hodges, D. Jacquemart, V. I. Perevalov, A. Perrin, K. P. Shine, M.-A. H. Smith, J. Tennyson, G. C. Toon, H. Tran, V. G. Tyuterev, A. Barbe, A. G. Császár, V. M. Devi, T. Furtenbacher, J. J. Harrison, J.-M. Hartmann, A. Jolly, T. J. Johnson, T. Karman, I. Kleiner, A. A. Kyuberis, J. Loos, O. M. Lyulin, S. T. Massie, S. N. Mikhailenko, N. Moazzen-Ahmadi, H. S. P. Müller, O. V. Naumenko, A. V. Nikitin, O. L. Polyansky, M. Rey, M. Rotger, S. W. Sharpe, K. Sung, E. Starikova, S. A. Tashkun, J. V. Auwera, G. Wagner, J. Wilzewski, P. Wcisło, S. Yu, and E. J. Zak, "The HITRAN2016 molecular spectroscopic database," *Journal of Quantitative Spectroscopy & Radiative Transfer Journal of Quantitative Spectroscopy & Radiative Transfer Journal of Quantitative Spectroscopy & Radiative Transfer*, vol. 14, no. 0, pp. 0–1, 2017.

[6] U. Willer, M. Saraji, A. Khorsandi, P. Geiser, and W. Schade, "Near- and mid-infrared laser monitoring of industrial processes, environment and security applications," *Optics and Lasers in Engineering*, vol. 44, no. 7, pp. 699–710, 2006.

[7] T. Fritsch, P. Hering, and M. Murtz, "Infrared laser spectroscopy for online recording of exhaled carbon monoxide -a progress report," *Journal of Breath Research*, vol. 1, no. 1, 2007.

[8] A. Somov, A. Baranov, D. Spirjakin, A. Spirjakin, V. Sleptsov, and R. Passerone, "Deployment and evaluation of a wireless sensor network for

methane leak detection," *Sensors and Actuators, A: Physical*, vol. 202, pp. 217–225, 2013.

[9] M. R. Rhoby, D. L. Blunck, and K. C. Gross, "Mid-IR hyperspectral imaging of laminar flames for 2-D scalar values," *Optics Express*, vol. 22, no. 18, p. 21600, 2014.

[10] A. Malaver, N. Motta, P. Corke, and F. Gonzalez, "Development and Integration of a Solar Powered Unmanned Aerial Vehicle and a Wireless Sensor Network to Monitor Greenhouse Gases," *Sensors*, vol. 15, no. 2, pp. 4072–4096, 2015.

[11] K. M. Manfred, G. A. D. Ritchie, N. Lang, J. Röpcke, and J. H. Van Helden, "Optical feedback cavity-enhanced absorption spectroscopy with a 3.24 μm interband cascade laser," *Applied Physics Letters*, vol. 106, no. 22, pp. 1–5, 2015.

[12] J. Wang, L. Zheng, X. Niu, C. Zheng, Y. Wang, and F. Tittel, "Mid-infrared absorption-spectroscopy-based carbon dioxide sensor network in greenhouse agriculture: Development and deployment," *Applied Optics*, vol. 55, no. 25, 2016.

[13] M. Dong, C. Zheng, S. Miao, Y. Zhang, Q. Du, Y. Wang, and F. K. Tittel, "Development and measurements of a mid-infrared multi-gas sensor system for CO, CO_2 and CH_4 detection," *Sensors (Switzerland)*, vol. 17, no. 10, 2017.

[14] C. Zheng, W. Ye, N. P. Sanchez, C. Li, L. Dong, Y. Wang, R. J. Griffin, and F. K. Tittel, "Development and field deployment of a mid-infrared methane sensor without pressure control using interband cascade laser absorption spectroscopy," *Sensors and Actuators, B: Chemical*, vol. 244, pp. 365–372, 2017.

[15] N. Pakmanesh, S. M. Cristescu, A. Ghorbanzadeh, F. J. Harren, and J. Mandon, "Quantum cascade laser-based sensors for the detection of exhaled carbon monoxide," *Applied Physics B: Lasers and Optics*, vol. 122, no. 1, pp. 1–9, 2016.

[16] W. Chen, J. Cousin, E. Poullet, J. Burie, D. Boucher, X. Gao, M. W. Sigrist, and F. K. Tittel, "Continuous-wave mid-infrared laser sources based on difference frequency generation," *Comptes Rendus Physique*, vol. 8, no. 10, pp. 1129–1150, 2007.

[17] K. E. Whittaker, L. Ciaffoni, G. Hancock, R. Peverall, and G. A. D. Ritchie, "A DFG-based cavity ring-down spectrometer for trace gas sensing in the mid-infrared," *Applied Physics B: Lasers and Optics*, vol. 109, no. 2, pp. 333–343, 2012.

[18] M. Tacke, "Lead-salt lasers," *Philosophical Transactions of the Royal Society A: Mathematical, Physical and Engineering Sciences*, vol. 359, no. 1780, pp. 547–566, 2001.

[19] R. F. Curl, F. Capasso, C. Gmachl, A. A. Kosterev, B. McManus, R. Lewicki, M. Pusharsky, G. Wysocki, and F. K. Tittel, "Quantum cascade lasers in chemical physics," *Chemical Physics Letters*, vol. 487, no. 1-3, pp. 1–18, 2010.

[20] A. Einstein, "Zur quantentheorie der strahlung," *Physikalische Zeitschrift*, 1917.

[21] T. H. Maiman, "Stimulated optical radiation in Ruby," *Nature*, vol. 187, no. 4736, pp. 493–494, 1960.

[22] M. Tacke, "New developments and applications of tunable IR Lead salt lasers," *Infrared Physics and Technology*, vol. 36, no. 1, 1995.

[23] A. Beattie and P. Landsberg, "Auger Effect in Semiconductors," *Proc. R. Soc. London, Ser. A*, vol. 249, no. 1256, pp. 16–29, 1959.

[24] R. W. Boyd, *Nonlinear Optics*. San Diego: Elsevier, 2nd ed ed., 2003.

[25] R. F. Kazarinov and R. A. Suris, "Possible amplification of electromagnetic waves in a semiconductor with a superlattice," *Soviet physics - Semiconductors*, vol. 5, no. 4, 1971.

[26] J. Faist, F. Capasso, D. L. Sivco, C. Sirtori, A. L. Hutchinson, A. Y. Cho, and Y. Cho, "Quantum Cascade Laser," *Science*, vol. 264, no. 5158, pp. 553–556, 1994.

[27] G. Duxbury, N. Langford, M. T. McCulloch, and S. Wright, "Quantum cascade semiconductor infrared and far-infrared lasers: from trace gas sensing to nonlinear optics.," *Chemical Society Reviews*, vol. 34, no. 11, pp. 921–934, 2005.

[28] O. Malis, C. Gmachl, D. L. Sivco, L. N. Pfeiffer, A. Michael Sergent, and K. W. West, "The quantum cascade laser: A versatile high-power semiconductor laser for mid-infrared applications," *Bell System Technical Journal*, vol. 10, no. 3, pp. 199–214, 2005.

[29] Y. Bai, S. R. Darvish, S. Slivken, W. Zhang, A. Evans, J. Nguyen, and M. Razeghi, "Room temperature continuous wave operation of quantum cascade lasers with watt-level optical power," *Applied Physics Letters*, vol. 92, no. 10, pp. 3–6, 2008.

[30] J. M. Hollas, *Modern Spectroscopy*. Chichester: John Wiley & Sons, Ltd, 4th ed., 2004.

[31] W. Demtroder, *Laser Spectroscopy: Basic Concepts and Instrumentation*. Berlin Heidelberg: Springer-Verlag, 3rd ed. ed., 2003.

[32] M. Abramowitz, I. A. Stegun, and D. Miller, "Handbook of Mathematical Functions With Formulas, Graphs and Mathematical Tables (National Bureau of Standards Applied Mathematics Series No. 55)," 1965.

[33] P. M. Farrell and W. R. MacGillivray, "On the consistency of Rabi frequency calculations," *Journal of Physics A: Mathematical and General*, vol. 28, no. 1, pp. 209–221, 1999.

[34] R. L. Shoemaker, "Coherent Transient Effects in Optical Spectroscopy," *Annual Review of Physical Chemistry*, vol. 30, no. 1, pp. 239–270, 1979.

[35] S. O'Hagan, T. Pinto, P. Ewart, and G. A. D. Ritchie, "Multi-mode absorption spectroscopy using a quantum cascade laser for simultaneous detection of NO and H_2O," *Applied Physics B*, vol. 122, no. 8, p. 226, 2016.

[36] A. Hugi, R. Maulini, and J. Faist, "External cavity quantum cascade laser," *Semiconductor Science and Technology*, vol. 25, no. 8, 2010.

[37] J. Faist, C. Gmachl, F. Capasso, C. Sirtori, D. L. Sivco, J. N. Baillargeon, and A. Y. Cho, "Distributed feedback quantum cascade lasers," *Applied Physics Letters*, vol. 70, no. 20, p. 2670, 1997.

[38] H. Kogelnik and C. V. Shank, "Coupled-wave theory of distributed feedback lasers," *Journal of Applied Physics*, vol. 43, no. 5, pp. 2327–2335, 1972.

[39] C. Gmachl, A. Straub, R. Colombelli, F. Capasso, D. L. Sivco, M. Sergent, and A. Y. Cho, "Single-Mode, Tunable Distributed-Feedback and Multiple-Wavelength Quantum Cascade Lasers," *IEEE Journal of Quantum Electronics*, vol. 38, no. 6, 2002.

[40] A. Wakita and K. Sugiyama, "Single-frequency external-cavity tapered diode laser in a double-ended cavity configuration," *Review of Scientific Instruments*, vol. 71, no. 1, pp. 1–4, 2000.

[41] G. P. Luo, C. Peng, H. Q. Le, S. S. Pei, W. Y. Hwang, B. Ishaug, J. Um, J. N. Baillargeon, and C. H. Lin, "Grating-tuned external-cavity quantum-cascade semiconductor lasers," *Applied Physics Letters*, vol. 78, no. 19, pp. 2834–2836, 2001.

[42] C. J. Hawthorn, K. P. Weber, and R. E. Scholten, "Littrow configuration tunable external cavity diode laser with fixed direction output beam," *Review of Scientific Instruments*, vol. 72, no. 12, pp. 4477–4479, 2001.

[43] Daylight Solutions, "www.daylightsolutions.com/home/technology/about-mid-ir-quantum-cascade-lasers/."

[44] T. Day and D. F. Arnone, "Compact external cavity mid-ir optical lasers," 2009.

[45] A. R. Goni, K. Syassen, and M. Cardona, "Effect of Pressure on the Refractive Index of Germanium and Gallium Arsenide," *Physical Review B*, vol. 41, no. 14, pp. 104–110, 1990.

[46] Isomet, "1208-6-(4)M IR Acousto-Optic Modulator user manual."

[47] A. O'Keefe and D. A. G. Deacon, "Cavity Ring-Down Optical Spectrometer for Absorption measurements using pulsed laser sources," *Review of Scientific Instruments*, vol. 59, no. 12, p. 2544, 1988.

[48] R. Engeln, G. Berden, R. Peeters, and G. Meijer, "Cavity enhanced absorption and cavity enhanced magnetic rotation spectroscopy," *Review of Scientific Instruments*, vol. 69, no. 11, pp. 3763–3769, 1998.

[49] A. O'Keefe, "Integrated cavity output analysis of ultra-weak absorption," *Chemical Physics Letters*, vol. 293, no. 5-6, pp. 331–336, 1998.

[50] A. O'Keefe, J. J. Scherer, and J. B. Paul, "cw Integrated cavity output spectroscopy," *Chemical Physics Letters*, vol. 307, no. 5-6, pp. 343–349, 1999.

[51] J. B. Paul, L. Lapson, and J. G. Anderson, "Ultrasensitive absorption spectroscopy with a high-finesse optical cavity and off-axis alignment," *Applied Optics*, vol. 40, no. 27, p. 4904, 2001.

[52] M. Mazurenka, A. J. Orr-Ewing, R. Peverall, and G. A. D. Ritchie, "Cavity ring-down and cavity enhanced spectroscopy using diode lasers," *Annual Reports Section "C" (Physical Chemistry)*, vol. 101, p. 100, 2005.

[53] G. S. Engel, W. S. Drisdell, F. N. Keutsch, E. J. Moyer, and J. G. Anderson, "Ultrasensitive near-infrared integrated cavity output spectroscopy technique for detection of CO at 1.57 microm: new sensitivity limits for absorption measurements in passive optical cavities.," *Applied Optics*, vol. 45, no. 36, pp. 9221–9229, 2006.

[54] G. Berden and R. Engeln, eds., *Cavity Ring-Down Spectroscopy: techniques and applications*. Wiley, 1st ed., 2009.

[55] G. Gagliardi and H.-p. Loock, *Cavity-Enhanced Spectroscopy and Sensing*, vol. 179. Springer, 2014.

[56] F. Trager, ed., *Springer Handbook of Lasers and Optics*. London: Springer-Verlag, 2nd ed., 2012.

[57] H. Kogelnik and T. Li, "Laser beams and resonators.," *Applied Optics*, vol. 5, no. 10, pp. 1550–1567, 1966.

[58] C. C. Davis, *Lasers and Electro-Optics: Fundamentals and Engineering*. Cambridge: Cambridge University Press, 2nd ed., 2014.

[59] A. E. Siegman, *Lasers*. Mill Valley: University Science Books, 1st ed., 1986.

[60] P. W. Atkins and R. S. Friedman, *Molecular quantum mechanics*. Oxford: Oxford University Press, 3rd ed., 1997.

[61] J. M. Brown and A. Carrington, *Rotational Spectroscopy of Diatomic Molecules*. Cambridge: Cambridge University Press, 1st ed., 2003.

[62] L. Rothman, C. Rinsland, A. Goldman, S. Massie, D. Edwards, J.-M. Flaud, A. Perrin, C. Camy-Peyret, V. Dana, J.-Y. Mandin, J. Schroeder, A. McCann, R. Gamache, R. Wattson, K. Yoshino, K. Chance, K. Jucks, L. Brown, V. Nemtchinov, and P. Varanasi, "the Hitran Molecular Spectroscopic Database and Hawks (Hitran Atmospheric Workstation): 1996 Edition," *Journal of Quantitative Spectroscopy and Radiative Transfer*, vol. 60, no. 5, pp. 665–710, 1998.

[63] L. S. Rothman, I. E. Gordon, A. Barbe, D. C. Benner, P. F. Bernath, M. Birk, V. Boudon, L. R. Brown, A. Campargue, J. P. Champion, K. Chance, L. H. Coudert, V. Dana, V. M. Devi, S. Fally, J. M. Flaud, R. R. Gamache, A. Goldman, D. Jacquemart, I. Kleiner, N. Lacome, W. J. Lafferty, J. Y. Mandin, S. T. Massie, S. N. Mikhailenko, C. E. Miller, N. Moazzen-Ahmadi, O. V. Naumenko, A. V. Nikitin, J. Orphal, V. I. Perevalov, A. Perrin, A. Predoi-Cross, C. P. Rinsland, M. Rotger, M. Šimečková, M. A. Smith, K. Sung, S. A. Tashkun, J. Tennyson, R. A. Toth, A. C. Vandaele, and J. Vander Auwera, "The HITRAN 2004 molecular spectroscopic database," *Journal of Quantitative Spectroscopy and Radiative Transfer*, vol. 110, no. 9-10, pp. 533–572, 2009.

[64] L. S. Rothman, I. E. Gordon, A. Barbe, D. C. Benner, P. F. Bernath, M. Birk, V. Boudon, L. R. Brown, A. Campargue, J. P. Champion, K. Chance, L. H. Coudert, V. Dana, V. M. Devi, S. Fally, J. M. Flaud, R. R. Gamache, A. Goldman, D. Jacquemart, I. Kleiner, N. Lacome, W. J. Lafferty, J. Y. Mandin, S. T. Massie, S. N. Mikhailenko, C. E. Miller, N. Moazzen-Ahmadi, O. V. Naumenko, A. V. Nikitin, J. Orphal, V. I. Perevalov, A. Perrin, A. Predoi-Cross, C. P. Rinsland, M. Rotger, M. A. H. Smith, K. Sung, S. A. Tashkun, J. Tennyson, R. A. Toth, A. C. Vandaele, and J. Vander Auwera, "The HITRAN 2008 molecular spectroscopic database," *Journal of Quantitative Spectroscopy and Radiative Transfer*, vol. 110, no. 9-10, pp. 533–572, 2009.

[65] L. S. Rothman, I. E. Gordon, Y. Babikov, A. Barbe, D. Chris Benner, P. F. Bernath, M. Birk, L. Bizzocchi, V. Boudon, L. R. Brown, A. Campargue, K. Chance, E. A. Cohen, L. H. Coudert, V. M. Devi, B. J. Drouin, A. Fayt, J. M. Flaud, R. R. Gamache, J. J. Harrison, J. M. Hartmann, C. Hill, J. T. Hodges, D. Jacquemart, A. Jolly, J. Lamouroux, R. J. Le Roy, G. Li, D. A. Long, O. M. Lyulin, C. J. Mackie, S. T. Massie, S. Mikhailenko, H. S. P. Müller, O. V. Naumenko, A. V. Nikitin, J. Orphal, V. Perevalov, A. Perrin, E. R. Polovtseva, C. Richard, M. A. H. Smith, E. Starikova, K. Sung, S. Tashkun, J. Tennyson, G. C. Toon, V. G. Tyuterev, and G. Wagner, "The HITRAN2012 molecular spectroscopic database," *Journal of Quantitative Spectroscopy and Radiative Transfer*, vol. 130, pp. 4–50, 2013.

[66] Y. Arita and P. Ewart, "Multi-mode absorption spectroscopy," *Optics Communications*, vol. 281, no. 9, pp. 2561–2566, 2008.

[67] P. Werle, "A review of recent advances in semiconductor laser based gas monitors," *Spectrochimica Acta Part A: Molecular and Biomolecular Spectroscopy*, vol. 54, no. 2, pp. 197–236, 1998.

[68] K. Heinrich, T. Fritsch, P. Hering, and M. Mürtz, "Infrared laser-spectroscopic analysis of ^{14}NO and ^{15}NO in human breath," *Applied Physics B: Lasers and Optics*, vol. 95, no. 2, pp. 281–286, 2009.

[69] C. Wang and P. Sahay, "Breath analysis using laser spectroscopic techniques: Breath biomarkers, spectral fingerprints, and detection limits," *Sensors*, vol. 9, no. 10, pp. 8230–8262, 2009.

[70] S. M. Cristescu, D. Marchenko, J. Mandon, K. Hebelstrup, G. W. Griffith, L. A. Mur, and F. J. Harren, "Spectroscopic monitoring of NO traces in plants and human breath: Applications and perspectives," *Applied Physics B: Lasers and Optics*, vol. 110, no. 2, pp. 203–211, 2013.

[71] T. P. J. Blaikie, J. Couper, G. Hancock, P. L. Hurst, R. Peverall, G. Richmond, G. A. D. Ritchie, D. Taylor, and K. Valentine, "Portable Device for Measuring Breath Acetone Based on Sample Preconcentration and Cavity Enhanced Spectroscopy," *Analytical Chemistry*, vol. 88, no. 22, pp. 11016–11021, 2016.

[72] T. Cai, G. Gao, M. Wang, G. Wang, Y. Liu, and X. Gao, "High-Pressure Measurements of Temperature and CO_2 Concentration Using Tunable Diode Lasers at 2 μm," *Applied Spectroscopy*, vol. 70, no. 3, pp. 474–484, 2016.

[73] D. S. Baer, R. K. Hanson, M. E. Newfield, and N. K. Gopaul, "Multiplexed diode-laser sensor system for simultaneous H_2O, O_2, and temperature measurements," *Optics Letters*, vol. 19, no. 22, pp. 1900–1902, 1994.

[74] S. A. Diddams, L. Hollberg, and V. Mbele, "Molecular fingerprinting with the resolved modes of a femtosecond laser frequency comb," *Nature*, vol. 445, no. 7128, pp. 627–630, 2007.

[75] I. Coddington, W. C. Swann, and N. R. Newbury, "Coherent multiheterodyne spectroscopy using stabilized optical frequency combs," *Physical Review Letters*, vol. 100, no. 1, pp. 11–14, 2008.

[76] G. Somesfalean, M. Sjöholm, L. Persson, H. Gao, T. Svensson, and S. Svanberg, "Temporal correlation scheme for spectroscopic gas analysis using multimode diode lasers," *Applied Physics Letters*, vol. 86, no. 18, pp. 1–3, 2005.

[77] Y. Arita, R. Stevens, and P. Ewart, "Multi-mode absorption spectroscopy of oxygen for measurement of concentration, temperature and pressure," *Applied Physics B: Lasers and Optics*, vol. 90, no. 2, pp. 205–211, 2008.

[78] Y. Arita and P. Ewart, "Infra-red multi-mode absorption spectroscopy of acetylene using an Er/Yb:glass micro-laser," *Optics Express*, vol. 16, no. 7, p. 4437, 2008.

[79] J. H. Northern, A. W. J. Thompson, M. L. Hamilton, and P. Ewart, "Multi-species detection using multi-mode absorption spectroscopy (MUMAS)," *Applied Physics B: Lasers and Optics*, vol. 111, no. 4, pp. 627–635, 2013.

[80] A. Thompson, H. Northern, B. Williams, M. Hamilton, and P. Ewart, "Simultaneous detection of CO_2 and CO in engine exhaust using multi-mode absorption spectroscopy, MUMAS," *Sensors and Actuators, B: Chemical*, vol. 198, pp. 309–315, 2014.

[81] M. L. Hamilton, G. A. D. Ritchie, Y. Arita, and P. Ewart, "Multi-mode absorption spectroscopy, MUMAS, using wavelength modulation and cavity enhancement techniques," *Applied Physics B: Lasers and Optics*, vol. 100, no. 3, pp. 665–673, 2010.

[82] H. Northern, S. O'Hagan, M. L. Hamilton, and P. Ewart, "Mid-infrared multi-mode absorption spectroscopy, MUMAS, using difference frequency generation," *Applied Physics B: Lasers and Optics*, vol. 118, no. 3, pp. 343–351, 2014.

[83] J. H. Northern, S. O'Hagan, B. Fletcher, B. Gras, P. Ewart, C. S. Kim, M. Kim, C. D. Merritt, W. W. Bewley, C. L. Canedy, J. Abell, I. Vurgaftman, and J. R. Meyer, "Mid-infrared multi-mode absorption spectroscopy using interband cascade lasers for multi-species sensing," *Optics letters*, vol. 40, no. 17, pp. 4186–4189, 2015.

[84] Thorlabs, "QF5300CM1 - Fabry-Perot Quantum Cascade Laser, 5.30 m CWL suporting documentation," 2016.

[85] S. O'Hagan, J. H. Northern, B. Gras, P. Ewart, C. S. Kim, M. Kim, C. D. Merritt, W. W. Bewley, C. L. Canedy, I. Vurgaftman, and J. R. Meyer, "Multi-species sensing using multi-mode absorption spectroscopy with mid-infrared interband cascade lasers," *Applied Physics B: Lasers and Optics*, vol. 122, no. 6, pp. 1–11, 2016.

[86] C. Gmachl, F. Capasso, D. Sivco, and A. Y. Cho, "Recent progress in quantum cascade lasers and applications," *Report on Progress in Physics*, vol. 64, pp. 1533–1601, 2001.

[87] G. Wysocki, R. Lewicki, R. F. Curl, F. K. Tittel, L. Diehl, F. Capasso, M. Troccoli, G. Hofler, D. Bour, S. Corzine, R. Maulini, M. Giovannini, and J. Faist, "Widely tunable mode-hop free external cavity quantum cascade lasers for high resolution spectroscopy and chemical sensing," *Applied Physics B: Lasers and Optics*, vol. 92, no. 3 SPECIAL ISSUE, pp. 305–311, 2008.

[88] J. Remillard, D. Uy, W. Weber, F. Capasso, C. Gmachl, A. Hutchinson, D. Sivco, J. Baillargeon, and A. Cho, "Sub-Doppler resolution limited Lamb-dip spectroscopy of NO with a quantum cascade distributed feedback laser.," *Optics Express*, vol. 7, no. 7, pp. 243–248, 2000.

[89] S. Borri, S. Bartalini, I. Galli, P. Cancio, G. Giusfredi, D. Mazzotti, A. Castrillo, L. Gianfrani, and P. De Natale, "Lamb-dip-locked quantum cascade laser for comb-referenced IR absolute frequency measurements," *Optics Express*, vol. 16, no. 15, p. 11637, 2008.

[90] M. T. McCulloch, G. Duxbury, and N. Langford, "Observation of saturation and rapid passage signals in the 10.25 micron spectrum of ethylene using a frequency chirped quantum cascade laser," *Molecular Physics*, vol. 104, no. 16-17, pp. 2767–2779, 2006.

[91] G. Duxbury, J. F. Kelly, T. A. Blake, and N. Langford, "Sub-Doppler spectra of infrared hyperfine transitions of nitric oxide using a pulse modulated quantum cascade laser: Rapid passage, free induction decay, and the ac Stark effect," *Journal of Chemical Physics*, vol. 136, no. 17, 2012.

[92] J. M. R. Kirkbride, S. K. Causier, E. A. McCormack, D. Weidmann, and G. A. D. Ritchie, "Coherent transient spectroscopy with continuous wave quantum cascade lasers.," *Physical Chemistry Chemical Physics: PCCP*, vol. 15, pp. 2684–91, feb 2013.

[93] A. L. Schawlow and C. H. Townes, "Infrared and optical masers," *Physical Review*, vol. 112, no. 6, pp. 1940–1949, 1958.

[94] C. H. Henry, "Theory of the Linewidth of Semiconductor Lasers," *IEEE Journal of Quantum Electronics*, vol. 18, no. 2, pp. 259–264, 1982.

[95] M. Yamanishi, T. Edamura, K. Fujita, N. Akikusa, and H. Kan, "Theory of the intrinsic linewidth of quantum-cascade lasers: Hidden reason for the narrow linewidth and line-broadening by thermal photons," *IEEE Journal of Quantum Electronics*, vol. 44, no. 1, pp. 12–29, 2008.

[96] S. Bartalini, S. Borri, P. Cancio, A. Castrillo, I. Galli, G. Giusfredi, D. Mazzotti, L. Gianfrani, and P. De Natale, "Observing the intrinsic linewidth of a quantum-cascade laser: Beyond the schawlow-townes limit," *Physical Review Letters*, vol. 104, no. 8, pp. 1–4, 2010.

[97] G. Di Domenico, S. Schilt, and P. Thomann, "Simple approach to the relation between laser frequency noise and laser line shape.," *Applied Optics*, vol. 49, no. 25, pp. 4801–4807, 2010.

[98] L. Tombez, S. Schilt, J. Di Francesco, T. Führer, B. Rein, T. Walther, G. Di Domenico, D. Hofstetter, and P. Thomann, "Linewidth of a quantum-cascade laser assessed from its frequency noise spectrum and impact of the current driver," *Applied Physics B: Lasers and Optics*, vol. 109, no. 3, pp. 407–414, 2012.

[99] X. Lou, Y. Dong, D. Wu, J. Wei, and Z. Lu, "Integrated cavity output spectroscopy by using a sub-centimeter short optical cavity combined with a

free-running FabryPerot diode laser," *Applied Physics B: Lasers and Optics*, vol. 121, no. 2, pp. 171–178, 2015.

[100] K. M. Manfred, L. Ciaffoni, and G. A. D. Ritchie, "Optical-feedback cavity-enhanced absorption spectroscopy in a linear cavity: model and experiments," *Applied Physics B-Lasers and Optics*, vol. 120, no. 2, pp. 329–339, 2015.

[101] A. De, G. D. Banik, A. Maity, M. Pal, and M. Pradhan, "Continuous wave external-cavity quantum cascade laser-based high-resolution cavity ring-down spectrometer for ultrasensitive trace gas detection," *Optics Letters*, vol. 41, no. 9, pp. 1949–1952, 2016.

[102] J. Morville, S. Kassi, M. Chenevier, and D. Romanini, "Fast, low-noise, mode-by-mode, cavity-enhanced absorption spectroscopy by diode-laser self-locking," *Applied Physics B: Lasers and Optics*, vol. 80, no. 8, pp. 1027–1038, 2005.

[103] I. Ventrillard, P. Gorrotxategi-Carbajo, and D. Romanini, "Part per trillion nitric oxide measurement by optical feedback cavity-enhanced absorption spectroscopy in the mid-infrared," *Applied Physics B: Lasers and Optics*, vol. 123, no. 6, pp. 1–8, 2017.

[104] X. Liu, Y. Xu, Z. Su, W. S. Tam, and I. Leonov, "Jet-cooled infrared spectra of molecules and complexes with a cw mode-hop-free external-cavity QCL and a distributed-feedback QCL," *Applied Physics B: Lasers and Optics*, vol. 102, no. 3, pp. 629–639, 2011.

[105] L. Ciaffoni, J. Couper, G. Hancock, R. Peverall, P. A. Robbins, and G. A. D. Ritchie, "RF noise induced laser perturbation for improving the performance of non-resonant cavity enhanced absorption spectroscopy," *Optics Express*, vol. 22, no. 14, p. 17030, 2014.

[106] K. M. Manfred, J. M. R. Kirkbride, L. Ciaffoni, R. Peverall, and G. A. D. Ritchie, "Enhancing the sensitivity of mid-IR quantum cascade laser-based cavity-enhanced absorption spectroscopy using RF current perturbation," *Optics Letters*, vol. 39, no. 24, pp. 6811–6814, 2014.

[107] V. L. Kasyutich and M. W. Sigrist, "Optimisation of laser linewidth and cavity alignment in off-axis cavity-enhanced absorption spectroscopy," *Infrared Physics and Technology*, vol. 71, pp. 179–186, 2015.

[108] V. L. Kasyutich and P. A. Martin, "Measurements of the linewidth of a continuous-wave distributed feedback quantum cascade laser," *Optics Communications*, vol. 284, no. 24, pp. 5723–5729, 2011.

[109] N. Mukherjee, R. Go, and C. K. N. Patel, "Linewidth measurement of external grating cavity quantum cascade laser using saturation spectroscopy," *Applied Physics Letters*, vol. 92, no. 11, p. 111116, 2008.

[110] L. B. Mercer, "1/f Frequency Noise Effects on Self-Heterodyne Linewidth Measurements," *Journal of Lightwave Technology*, vol. 9, no. 4, pp. 485–493, 1991.

[111] H. Ludvigsen, M. Tossavainen, and M. Kaivola, "Laser linewidth measurements using self-homodyne detection with short delay," *Optics Communications*, vol. 155, no. October, pp. 180–186, 1998.

[112] T. Pinto, J. Kirkbride, and G. Ritchie, "Broadening the optical bandwidth of quantum cascade lasers using RF noise current perturbations," *Optics Letters*, vol. 43, no. 8, pp. 1931–1934, 2018.

[113] T. Okoshi, K. Kikuchi, and A. Nakayama, "Novel method for high resolution measurement of laser output spectrum," *Electronics Letters*, vol. 16, no. 16, p. 630, 1980.

[114] L. E. Richter, H. I. Mandelberg, M. S. Kruger, and P. A. McGrath, "Linewidth Determination From Self-Heterodyne Measurement With Subcoherence Delay Time," *Quantum Electronics Letters*, vol. 22, pp. 2070–2074, 1986.

[115] P. Gallion and G. Debarge, "Quantum phase noise and field correlation in single frequency semiconductor laser systems," *IEEE Journal of Quantum Electronics*, vol. 20, no. 4, pp. 343–349, 1984.

[116] J. S. Melinger, S. R. Gandhi, A. Hariharan, D. Goswami, and W. S. Warren, "Adiabatic population transfer with frequency-swept laser pulses," *The Journal of Chemical Physics*, vol. 101, no. 8, p. 6439, 1994.

[117] E. Hahn, "Spin Echoes," *Physical Review*, vol. 80, no. 4, pp. 580–594, 1950.

[118] S. Zamith, J. Degert, S. Stock, B. De Beauvoir, V. Blanchet, M. Aziz Bouchene, and B. Girard, "Observation of coherent transients in ultrashort chirped excitation of an undamped two-level system," *Physical Review Letters*, vol. 87, no. 3, pp. 33001–1–33001–4, 2001.

[119] R. G. Brewer and R. L. Shoemaker, "Photon echo and optical nutation in molecules," *Physical Review Letters*, vol. 27, no. 10, pp. 631–634, 1971.

[120] R. G. Brewer and A. Z. Genack, "Optical coherent transients by laser frequency switching," *Physical Review Letters*, vol. 36, no. 16, pp. 959–962, 1976.

[121] Y.-Q. Li and M. Xiao, "Transient spectroscopy with a current-switched semiconductor diode laser," *Journal of Optics B: Quantum and Semiclassical Optics*, vol. 1, no. 5, pp. 541–545, 1999.

[122] E. A. McCormack, H. S. Lowth, M. T. Bell, D. Weidmann, and G. A. D. Ritchie, "Population transfer and rapid passage effects in a low pressure gas using a continuous wave quantum cascade laser.," *The Journal of Chemical Physics*, vol. 137, p. 034306, jul 2012.

[123] R. J. Walker, J. H. van Helden, J. Kirkbride, E. A. McCormack, M. T. Bell, D. Weidmann, and G. A. D. Ritchie, "Rapid passage signals from a vibrationally excited target molecule: a pump and probe experiment with continuous wave quantum cascade lasers," *Optics Letters*, vol. 36, no. 24, p. 4725, 2011.

[124] J. M. R. Kirkbride, S. K. Causier, A. R. Dalton, D. Weidmann, and G. A. D. Ritchie, "Pump and probe spectroscopy with continuous wave quantum cascade lasers.," *The Journal of Chemical Physics*, vol. 140, no. 5, p. 054311, 2014.

[125] G. Duxbury, N. Langford, M. T. McCulloch, and S. Wright, "Rapid passage induced population transfer and coherences in the 8 micron spectrum of nitrous oxide," *Molecular Physics*, vol. 105, no. 5-7, pp. 741–754, 2007.

[126] F. Bloch, "Nuclear induction," *Physical Review*, vol. 70, no. 7-8, pp. 460–474, 1946.

[127] C. L. Tang and H. Statz, "Optical analog of the transient nutation effect," *Applied Physics Letters*, vol. 10, no. 5, pp. 145–147, 1967.

[128] H. C. Torrey, "Bloch equations with Diffusion terms," *Physical Review*, vol. 104, no. 3, pp. 563–565, 1956.

[129] J. Kirkbride, *DPhil thesis*. PhD thesis, University of Oxford, 2014.

[130] H. Linnartz, "A remotely controllable optical Multi-Pass System," *Physica Scripta*, vol. 70, no. C24-25, p. 2, 2004.

[131] G. Hancock, S. J. Horrocks, G. A. D. Ritchie, J. H. V. Helden, and R. J. Walker, "Time-Resolved Detection of the CF_3 Photofragment Using Chirped QCL Radiation," *Journal of Physical Chemistry A*, vol. 112, pp. 9751–9757, 2008.

[132] J. H. Northern, G. A. D. Ritchie, E. P. Smakman, J. H. van Helden, J. Cockburn, and G. Duxbury, "Rapid passage signals induced by chirped quantum cascade laser radiation: K state dependent-delay effects in the $\nu 2$ band of NH_3.," *Optics letters*, vol. 35, no. 16, pp. 2750–2752, 2010.

[133] P. Atkins, *Physical Chemistry*. Oxford: Oxford University Press, 6th ed., 1998.

[134] P. J. Crutzen, "The influence of nitrogen oxides on the atmospheric ozone content," *Quarterly Journal of the Royal Meteorological Society*, vol. 96, no. 408, pp. 320–325, 1970.

[135] B. J. Finlayson-Pitts and J. N. P. Jr, "Pollution : Tropospheric Air Airborne Toxics , Ozone , Aromatic Polycyclic and Particles Hydrocarbons," *Science*, vol. 276, no. 5315, pp. 1045–1052, 1997.

[136] M. Blocquet, C. Schoemaecker, D. Amedro, O. Herbinet, F. Battin-Leclerc, and C. Fittschen, "Quantification of OH and HO_2 radicals during the low-temperature oxidation of hydrocarbons by Fluorescence Assay by Gas Expansion technique," *Proceedings of the National Academy of Sciences*, vol. 110, no. 50, pp. 20014–20017, 2013.

[137] J. P. Eiserich, M. Hristova, C. E. Cross, A. D. Jones, B. A. Freeman, B. Halliwell, and A. Van Der Vliet, "Formation of nitric oxide-derived inflammatory oxidants by myeloperoxidase in neutrophils," *Nature*, vol. 391, no. 6665, pp. 393–397, 1998.

[138] Y. A. Bakhirkin, A. A. Kosterev, C. Roller, R. F. Curl, and F. K. Tittel, "Mid-infrared quantum cascade laser based off-axis integrated cavity output spectroscopy for biogenic nitric oxide detection," *Applied Optics*, vol. 43, no. 11, p. 2257, 2004.

[139] F. A. Winiberg, S. C. Smith, I. Bejan, C. A. Brumby, T. Ingham, T. L. Malkin, S. C. Orr, D. E. Heard, and P. W. Seakins, "Pressure-dependent calibration of the OH and HO_2 channels of a FAGE HOx instrument using the Highly Instrumented Reactor for Atmospheric Chemistry (HIRAC)," *Atmospheric Measurement Techniques*, vol. 8, no. 2, pp. 523–540, 2015.

[140] G. Litfin, C. R. Pollock, R. F. Curl, and F. K. Tittel, "Sensitivity enhancement of laser absorption spectroscopy by magnetic rotation effect," *The Journal of Chemical Physics*, vol. 72, no. 12, p. 6602, 1980.

[141] M. Gianella, T. H. Pinto, X. Wu, and G. A. D. Ritchie, "Intracavity Faraday modulation spectroscopy (INFAMOS): A tool for radical detection," *Journal of Chemical Physics*, vol. 147, no. 5, 2017.

[142] R. Lewicki, J. H. Doty, R. F. Curl, F. K. Tittel, and G. Wysocki, "Ultrasensitive detection of nitric oxide at 5.33 micron by using external cavity quantum cascade laser-based Faraday rotation spectroscopy.," *Proceedings of the National Academy of Sciences of the United States of America*, vol. 106, no. 31, pp. 12587–12592, 2009.

[143] S. G. So, E. Jeng, and G. Wysocki, "VCSEL based Faraday rotation spectroscopy with a modulated and static magnetic field for trace molecular oxygen detection," *Applied Physics B: Lasers and Optics*, vol. 102, no. 2, pp. 279–291, 2011.

[144] B. Brumfield, W. Sun, Y. Wang, Y. Ju, and G. Wysocki, "Dual modulation Faraday rotation spectroscopy of HO_2 in a flow reactor," *Optics Letters*, vol. 39, no. 7, pp. 1783–1786, 2014.

[145] Y. Wang, M. Nikodem, J. Hoyne, and G. Wysocki, "Cryogen-free heterodyne-enhanced mid-infrared Faraday rotation spectrometer," *Optics Express*, vol. 21, no. 1, p. 82682F, 2013.

[146] D. Jacob, M. Vallet, F. Bretenaker, A. Le Floch, and R. Le Naour, "Small Faraday rotation measurement with a Fabry-Perot cavity," *Applied Physics Letters*, vol. 66, no. 26, pp. 3546–3548, 1995.

[147] E. Zhang, S. Huang, Q. Ji, M. Silvernagel, Y. Wang, B. Ward, D. Sigman, and G. Wysocki, "Nitric oxide isotopic analyzer based on a compact dual-modulation faraday rotation spectrometer," *Sensors (Switzerland)*, vol. 15, no. 10, pp. 25992–26008, 2015.

[148] C.-Y. Chang and J.-T. Shy, "Cavity-enhanced Faraday rotation measurement with auto-balanced photodetection," *Applied Optics*, vol. 54, no. 28, p. 8526, 2015.

[149] K. Liu, R. Lewicki, and F. K. Tittel, "Development of a mid-infrared nitrogen dioxide sensor based on Faraday rotation spectroscopy," *Sensors and Actuators, B: Chemical*, vol. 237, no. 2, pp. 887–893, 2016.

[150] D. Romanini, M. Chenevier, S. Kassi, M. Schmidt, C. Valant, M. Ramonet, J. Lopez, and H. J. Jost, "Optical-feedback cavity-enhanced absorption: A compact spectrometer for real-time measurement of atmospheric methane," *Applied Physics B: Lasers and Optics*, vol. 83, no. 4, pp. 659–667, 2006.

[151] S. G. Baran, G. Hancock, R. Peverall, G. A. D. Ritchie, and N. J. van Leeuwen, "Optical feedback cavity enhanced absorption spectroscopy with diode lasers," *Analyst*, vol. 134, no. 2, pp. 243–249, 2009.

[152] M. Gianella, S. Reuter, A. L. Aguila, G. A. D. Ritchie, and J.-P. H. van Helden, "Detection of HO_2 in an Atmospheric Pressure Plasma Jet Using Optical Feedback Cavity-Enhanced Absorption Spectroscopy," *New Journal of Physics*, vol. 18, no. 11, p. 113027, 2016.

[153] D. J. Hamilton and A. J. Orr-Ewing, "A quantum cascade laser-based optical feedback cavity-enhanced absorption spectrometer for the simultaneous measurement of CH_4 and N_2O in air," *Applied Physics B: Lasers and Optics*, vol. 102, no. 4, pp. 879–890, 2011.

[154] P. Gorrotxategi-Carbajo, E. Fasci, I. Ventrillard, M. Carras, G. Maisons, and D. Romanini, "Optical-Feedback Cavity-Enhanced Absorption Spectroscopy with a quantum-cascade laser yields the lowest formaldehyde detection limit," *Applied Physics B: Lasers and Optics*, vol. 110, no. 3, pp. 309–314, 2013.

[155] A. Hinz, J. Pfeiffer, W. Bohle, and W. Urban, "Mid-infrared laser magnetic resonance using the Faraday and Voigt effects for sensitive detection," *Molecular Physics*, vol. 45, no. 6, pp. 1131–1139, 1982.

[156] D. D. Nelson, J. H. Shorter, J. B. McManus, and M. S. Zahniser, "Sub-part-per-billion detection of nitric oxide in air using a thermoelectrically cooled mid-infrared quantum cascade laser spectrometer," *Applied Physics B: Lasers and Optics*, vol. 75, no. 2-3, pp. 343–350, 2002.

[157] B. W. M. Moeskops, S. M. Cristescu, and F. J. M. Harren, "Sub-part-per-billion monitoring of nitric oxide by use of wavelength modulation spectroscopy in combination with a thermoelectrically cooled, continuous-wave quantum cascade laser.," *Optics letters*, vol. 31, no. 6, pp. 823–825, 2006.

[158] A. A. Kosterev, A. L. Malinovsky, F. K. Tittel, C. Gmachl, F. Capasso, D. L. Sivco, J. N. Baillargeon, A. L. Hutchinson, and A. Y. Cho, "Cavity ringdown spectroscopic detection of nitric oxide with a continuous-wave quantum-cascade laser," *Applied Optics*, vol. 40, no. 30, pp. 5522 – 5529, 2001.

[159] V. I. Stsiapura, V. K. Shuali, B. M. Gaston, and K. K. Lehmann, "Detection of S-Nitroso Compounds by Use of Midinfrared Cavity Ring-Down Spectroscopy," *Analytical Chemistry*, vol. 87, no. 6, pp. 3345–3353, 2015.

[160] D. Miyakoshi, M. Aoyama, T. Tohei, A. Minoh, and M. Tsukakoshi, "Saturation effect on the lineshape of Faraday rotation spectrum in Krypton," *Japanese Journal of Applied Physics, Part 1: Regular Papers and Short Notes and Review Papers*, vol. 36, no. 12 A, pp. 7379–7382, 1997.

[161] I. O. G. Davies, P. E. G. Baird, and J. L. Nicol, "Theory and observation of Faraday rotation obtained with strong light fields," *Journal of Physics B: Atomic and Molecular Physics*, vol. 20, no. 20, pp. 5371–5386, 1999.

[162] A. P. Bogatov, P. G. Eliseev, M. A. Manko, L. P. Ivanov, A. S. Logginov, and K. Y. Senatorov, "Study of the Single-Mode Injection Laser," *IEEE Journal of Quantum Electronics*, vol. 9, no. 2, pp. 392–394, 1973.

[163] R. Lang and K. Kobayashi, "External Optical Feedback Effects on Semiconductor Injection Laser Properties," *IEEE Journal of Quantum Electronics*, vol. 16, no. 3, pp. 347–355, 1980.

[164] K. M. Manfred, *DPhil thesis*. PhD thesis, University of Oxford, 2015.

[165] W. U. W Herrmann, W Rohrbeck, "Line Shape Analysis for Zeeman Modulation Spectroscopy," *Applied Physics*, vol. 22, pp. 71–75, 1980.

[166] J. D. Jackson, *Classical Electrodynamics*. New York: Wiley, 3 ed., 1998.

[167] Y. Wang, *Development of Novel Mid-Infrared Spectrometers based on Quantum Cascade Lasers*. PhD thesis, Princeton University, 2014.

[168] J. Westberg, L. Lathdavong, C. M. Dion, J. Shao, P. Kluczynski, S. Lundqvist, and O. Axner, "Quantitative description of Faraday modulation spectrometry in terms of the integrated linestrength and 1st Fourier coefficients of the modulated lineshape function," *Journal of Quantitative Spectroscopy and Radiative Transfer*, vol. 111, no. 16, pp. 2415–2433, 2010.

[169] F. Schreier, "Optimized implementations of rational approximations for the Voigt and complex error function," *Journal of Quantitative Spectroscopy and Radiative Transfer*, vol. 112, no. 6, pp. 1010–1025, 2011.

[170] S. R. Systems, "Model SR830 DSP Lock-in Amplifier User Manual," 2011.

[171] P. Werle, R. Mücke, and F. Slemr, "The limits of signal averaging in atmospheric trace-gas monitoring by tunable diode-laser absorption spectroscopy (TDLAS)," *Applied Physics B Photophysics and Laser Chemistry*, vol. 57, no. 2, pp. 131–139, 1993.